Resolved Properties of Galaxy Mergers from the MaNGA Survey

by

Mallory D. Thorp
B.Sc., University of Washington, 2017

A Thesis Submitted in Partial Fulfillment of the
Requirements for the Degree of

MASTER OF SCIENCE

in the Department of Physics and Astronomy

University of Victoria

Resolved Properties of Galaxy Mergers from the MaNGA Survey

by

Mallory D. Thorp
B.Sc., University of Washington, 2017

Supervisory Committee

Dr. Sara Ellison, Supervisor
(Department of Physics and Astronomy, University of Victoria)

Dr. Luc Simard, Departmental Member
(Department of Physics and Astronomy, University of Victoria)

Supervisory Committee

Dr. Sara Ellison, Supervisor
(Department of Physics and Astronomy, University of Victoria)

Dr. Luc Simard, Departmental Member
(Department of Physics and Astronomy, University of Victoria)

ABSTRACT

The complex and diverse populations of galaxies observed today form hierarchically through past galactic mergers. Interactions between galaxies of similar masses will drastically alter the morphology, chemical composition, star-formation activity, and central black-hole accretion of their constituents. Though we can see the components and byproducts of galaxy mergers, these events endure over a timescale of hundreds of millions of years. Thus to understand the merging process from observations, astronomers are reliant on large spectroscopic surveys which will contain galaxy mergers at various stages of interaction, and those which have just experienced coalescence. Until recently, such surveys were limited to the global properties of each galaxy, constraining the global changes in chemical composition and star-formation activity, but overlooking how such changes vary across a galaxy. The advent of Integral Field Unit (IFU) spectroscopy surveys provides spatially resolved spectroscopic properties for thousands of galaxies for the first time. This thesis presents analysis of galaxy mergers from the Mapping Nearby Galaxies at Apache Point Observatory (MaNGA) IFU spectroscopy survey. Enhancements and deficits in star-formation rate ($\Delta\Sigma_{\rm SFR}$) and metallicity (Δ O/H), as a result of the interaction, are determined for each spatial pixel containing a spectrum (spaxel) based on well established relationships with stellar mass density. These offsets are then compressed into radial profiles to quantify how the effects of an interaction vary as a function of radius. A sample of 36 post-mergers are, on average, enhanced out to $\sim$2 effective radii, though individual galaxies can be enhanced or suppressed in the outskirts depending on the global star-formation rate of the galaxy. The metallicity is uniformly suppressed in post-merger galaxies, in concordance with the global SFR enhancement. A sample of galaxy pairs is identified with cuts in the projected separation r_p, the line of sight velocity difference Δv, and the mass ratio μ of the interaction. I develop a method to deblend close galaxy pairs that are on the same IFU observation, and remove contribution from the companion galaxy in the radial profile. Radial profiles of $\Delta\Sigma_{\mathrm{SFR}}$ and Δ O/H for the pairs sample, binned by r_p, confirm that central enhancements in SFR increase as separation decreases. Behaviour in the outskirts is more varied, and does not appear to correlate with the r_p or the μ of the interaction. Δ O/H displays a similar issue, showing no clear correlation with separation or μ. Such ambiguity implies that multiple characteristics of the interaction and its components are required to predict the spatial changes in a galaxy merger. I propose projects that could shed light on these ambiguities. The most recent release of MaNGA will double the sample size of mergers, possibly homogenizing r_p and μ bins that may be dominated by a particular population. An analysis of interacting galaxies that do not have μ measurements, but very small r_ps and highly disturbed morphologies, could provide understanding of the transition between the very end of an interaction and the state of the galaxy post-coalescence. I also propose a more complex analysis of the asymmetry of IFU spectroscopy data products, which until now have been simplified with radial profiles. Lastly, I emphasize the importance of follow up studies of the resolved molecular gas properties of merging galaxies to discern whether gas reservoir, depletion time, or both are driving the change in star-formation rate.

Contents

List of Tables

List of Figures

Acknowledgements

I would like to thank:

Sara Ellison for your wisdom, wit, and mentorship. Everyday I look forward to getting the chance to learn something new from you.

Trystyn Berg, Connor Bottrell, Maan Hani, and Joanna Woo for their indispensable counsel in academic life and beyond.

Ruth Digby, Brittany Howard, and Nick Loewen for walking this treacherous path with me.

Asa Bluck, Dave Patton, Sebastian Sánchez, Jillian Scudder, and Luc Simard for their input and support for the last two years of my MaNGA studies.

Lihwai Lin and Hsi-An Pan for advice on ALMA and the best tea shops.

The Physics and Astronomy Grads for making UVic a wonderful place to work.

The League of Astronomers for starting me on my journey in so many ways, and generally being a group of miraculous human beings (Locke Patton in particular).

Cat Stevens and Mao for welcoming me into their home.

The drop of rain maketh a hole in the stone, not by violence, but by oft falling.
Lucretius (Transl. Hugh Latimer)

Dedication

To my mother, my father, and all the orcas in the pod.

Chapter 1

Introduction

1.1 Galaxies

Galaxies are massive collections of stars, gas, and dust held together gravitationally within a cloud of dark matter. For centuries astronomers considered galaxies outside of the Milky Way to be unresolved nebulae. Improved measurements of astronomical distances with better resolution revealed these “nebulae” to be extragalactic in origin and far more similar to the Milky Way than a planetary nebula or unresolved star cluster, hence for the last century they have been more aptly dubbed “galaxies” (for the Greek word for the Milky Way, $\gamma\alpha\lambda\alpha\xi\acute{\iota}\alpha\zeta$, or “milky one”).

Upon inspection, galaxies reveal themselves to be a far more complicated and diverse population of celestial objects. It is the goal of extragalactic astronomy to uncover the relationships between these different populations of galaxies, and to better understand how so many contrasting populations are created. Edwin Hubble, in his revolutionary work classifying galaxies, categorized them as either disk-like spiral galaxies or bulge-dominated elliptical galaxies (Hubble, 1926). The Sérsic index provides a method to quantify such structure classification, measuring the shape of the light intensity recorded for a galaxy as a function of radius (Sérsic, 1963). A Sérsic index of 1 describes an exponential disk of light, whereas a Sérsic index of 4 indicates the light follows a de Vaucouleurs profile (more bulge-like) (de Vaucouleurs, 1948).

Further segregating ellipticals by their elongation and spirals by the presence of stellar arms or a bar, Hubble’s diagram inspired an evolutionary scenario where galaxies become more complex overtime (see Figure 1.1). This framework stemmed from Hubble’s classification of ellipticals as “early-type” galaxies and spirals as “late-type” galaxies, which actually refers to the increasing complexity of galaxy types, not their evolutionary stage (Hubble, 1926). Further analysis of elliptical and spiral galaxies

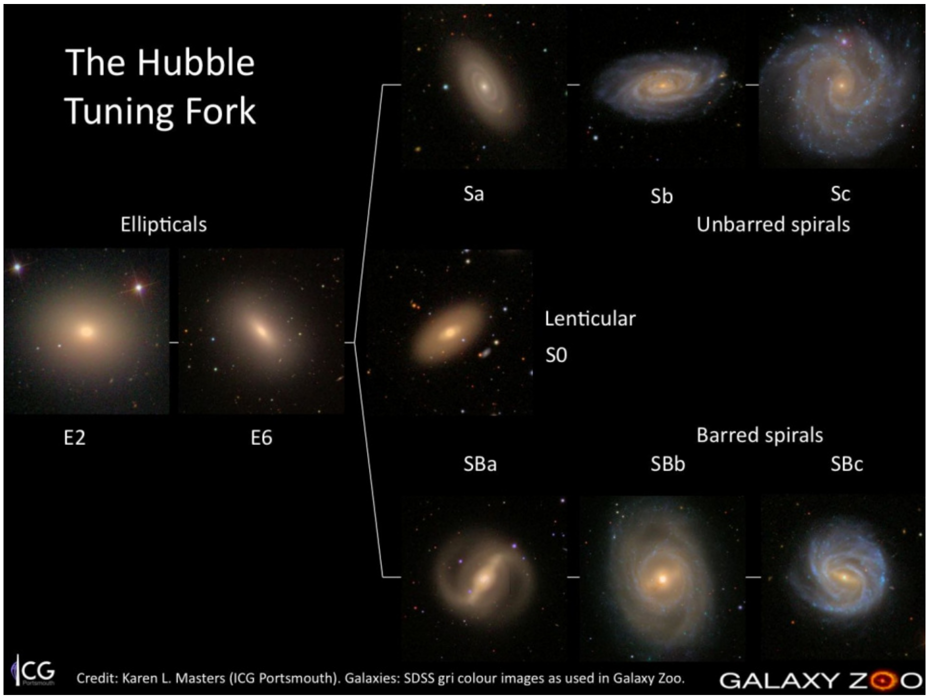

Figure 1.1: Galaxy Hubble types arranged in the original “Tuning Fork”, a preliminary attempt to connect different galaxy populations by some evolutionary track. Though not the true picture of galaxy evolution, it leads to some interesting questions about how spiral and ellipitcal galaxies relate to one another. Source: Galaxy Zoo (https://www.zooniverse.org).

would eventual expose this scenario to be the opposite of true galaxy evolution.

1.1.1 Spiral vs. Elliptical Galaxies

The colour of a galaxy is often used to inspect its nature beyond morphology alone. Blue light primarily comes from young, massive or metal-poor stars which emit shorter wavelength light, whereas red light emanates from old, low-mass, or metal-rich stars which are much cooler than their younger counterparts. A colour-mass diagram can reveal which stellar-populations dominate each type of galaxy. Figure 1.2 reveals that spiral galaxies are dominated by massive young stars, and elliptical galaxies contain older red stars (Bower et al., 1992; Bell et al., 2004; Schawinski et al., 2013).

The evolutionary theory that elliptical galaxies become spiral galaxies over time does not coincide with a scenario where elliptical galaxies have significantly older stellar populations than the spiral population. Elliptical galaxies also have significantly less angular momentum than spiral galaxies (Bertola & Capaccioli, 1975; Illingworth,

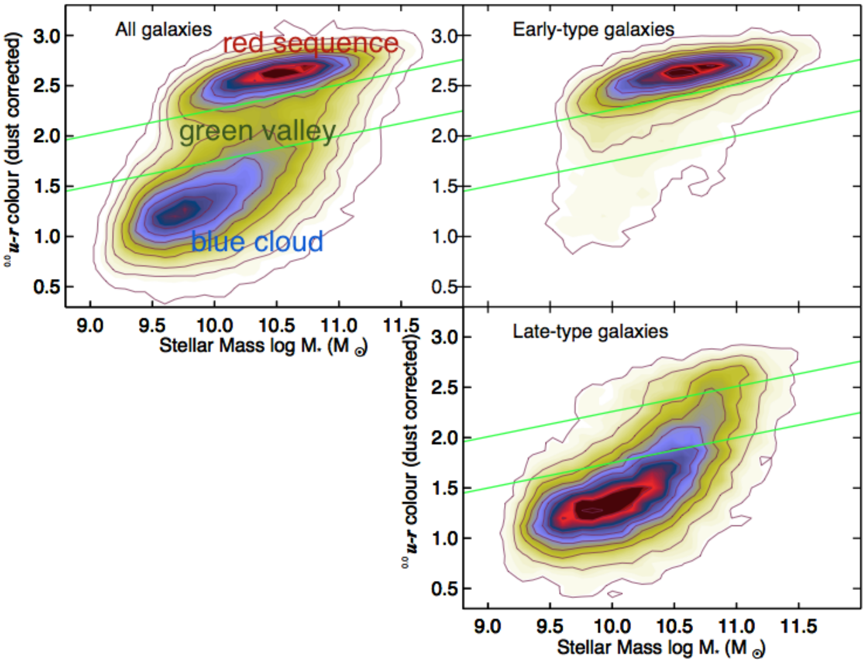

Figure 1.2: The u-r colour-mass diagram for galaxies in the Sloan Digital Sky Survey. All galaxies are shown in the top left of the diagram, whereas the top right and bottom right are divided into early-type and late-type galaxies, respectively. Green lines separate the colour space into the blue cloud (top), red sequence (bottom), and the galaxies in-between the two often called "green valley" galaxies. Source: Schawinski et al. (2013).

1977; Chiosi & Carraro, 2002), existing in dense but dynamically relaxed cluster environments (Oemler, 1974; Dressler, 1980). There is no mechanism in which ellipticals could start rotating rapidly to form spiral galaxies, implying that the reverse scenario is a more likely case. The reverse scenario is supported by the fact that the red sequence has increased in mass by a factor of 2 since z∼1, indicating that more red "early-type" galaxies are forming over time (Bell et al., 2004). [1] Elliptical galaxies do show signs of galaxy-galaxy interactions, including faint shells and asymmetries, decoupled cores, and cold gas orbiting at random inclinations (Schweizer, 1980, 1982; Malin & Carter, 1983). It is much more likely that elliptical galaxies form hierarchically from the collision of spiral galaxies, though not all products of such galaxy interactions are ellipticals (Toomre & Toomre, 1972; White & Rees, 1978; White, 1979; Baugh et al., 1996).

1.1.2 Star-Formation Activity

The diffuse interstellar medium (ISM) of galaxies is mostly neutral hydrogen (HI). Dust grains provide a sink for the binding energy that must be released for HI atoms to collide and form H_2, which constitutes molecular clouds (Carroll & Ostlie, 2007). Gravitational forces coupled with cooling and compressive forces spur over-densities in the molecular clouds, which eventually begin fusing hydrogen as new stars. Areas that are actively forming stars in this manner exist within HII regions. O and B type stars that form within the molecular cloud will emit UV radiation, which ionizes the surrounding neutral hydrogen and generates an HII region surrounding the newly formed stars.

Common nebular Hydrogen recombination lines from HII regions include Hα, Hβ, Pα, Pβ, Brα, and Brγ. The ionizing flux of these lines can be converted into a star-formation rate with the aid of evolutionary synthesis models. Star-formation rate (SFR) quantifies the mass of stars formed (in solar masses $M_\odot$) per year (Osterbrock & Ferland, 2006). Stars of mass $> 10\ M_\odot$ and lifetimes < 20 Myr contribute significantly to the ionizing emission line flux, so recombination lines measure approximately an instantaneous star-formation (Kennicutt, 1983). SFR can also be measured from the ultra-violet continuum flux, given the SFR scales linearly with luminosity if the integrated spectrum is dominated by the young stellar population. Measuring in the short UV wavelength regime (1250 - 2500Å) prevents contribution from older

---

[1] More recent studies have confirmed the increase in red sequence mass, but the magnitude of that increase can vary by up to ∼0.2 dex (Muzzin et al., 2013).

populations bound to occur in the optical regime, however this wavelength range also suffers greater dust attenuation (Kennicutt, 1998). The absorption cross-section of dust also peaks in the ultra-violet, so light from young massive stars can be traced by the far-infra-red (FIR) light re-emitted by interstellar dust (Kennicutt, 1998). However, FIR light can be contaminated by dust heated by the optical emission from older stars, a particular problem for early-type galaxies (Sauvage & Thuan, 1992; Walterbos & Greenawalt, 1996). For this work, I focus on optical emission lines as a method for measuring the star-formation rate.

Emission line luminosities trace the youngest most massive stars in a region. An initial mass function can be employed to approximate the total number of stars in a region, from all spectral types. The initial mass function (IMF) accounts for the total number of stars per unit mass interval; the mass function has to be estimated from the luminosity function, and is thus dependent on different stellar evolution theories of mass-age-luminosity relations (Chabrier, 2003). The work herein adopts the Salpeter (1955) IMF:

$$\xi(\mathrm{M}) = \xi_0 \mathrm{M}^{-2.35} \tag{1.1}$$

where ξ_0 is the constant that sets the local stellar surface density (see Figure 1.3). The Salpeter IMF assumes that most stars are low mass, that most of the galaxy's mass exists in low mass stars, and most of the galaxy's luminosity comes from high mass stars. It works best for normal disk galaxies, and is consistent with measurements of resolved stellar populations in nearby galaxies (Massey, 1998). Later investigations of the stellar populations suggest the IMF flattens at masses lower than $0.5M_\odot$ (Scalo, 1986; Kroupa, 2002; Chabrier, 2003).

Assuming a Salpeter IMF, the Schaller et al. (1993) stellar evolutionary tracks, and an exponentially declining star-formation history model, the SFR in units of $M_\odot \mathrm{yr}^{-1}$ of a galaxy can be determined from the Hα luminosity (ergs s^{-1}) using the following formula from Kennicutt et al. (1994):

$$\mathrm{SFR} = 7.9 \times 10^{-42}\ \mathrm{L(H}\alpha). \tag{1.2}$$

This method not only carries the uncertainty in the chosen IMF, but also makes the assumption that the ionizing flux traces all the massive star formation (i.e. the escape fraction of ionizing photons is less than 3%) (Leitherer et al., 1995). The Hα luminosity is often derived from the Hα flux, which first needs to be corrected for dust attenuation. Each galaxy has an intrinsic amount of dust grains which absorb

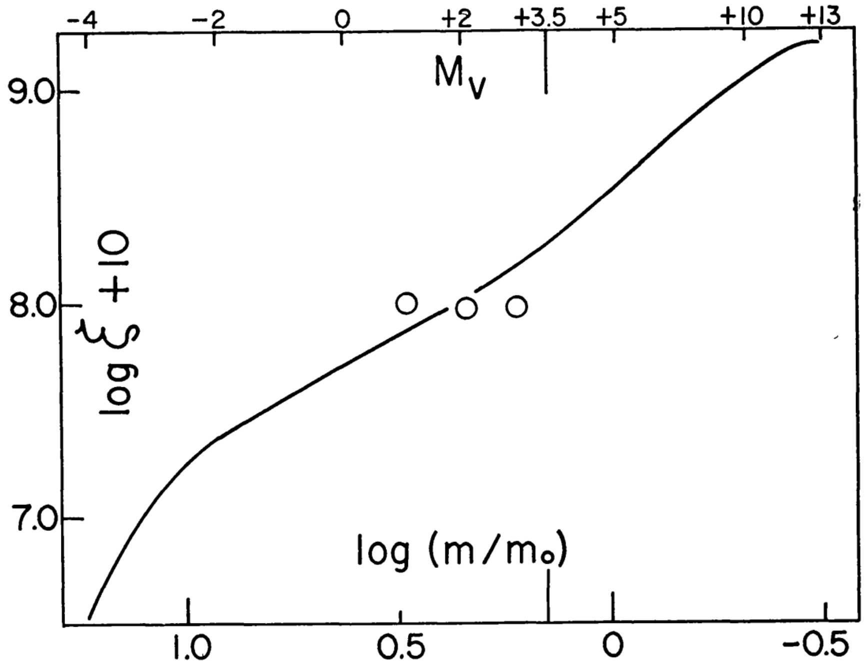

Figure 1.3: The logarithm of the initial mass function ξ in respect to solar masses. Source: Salpeter (1955).

emission flux, particularly at shorter wavelengths. The light lost can be approximated by measuring the ratio between Balmer series emission lines, such as Hα and Hβ. The ratio between these two lines should be fixed (Hα/Hβ = 2.86, Osterbrock & Ferland 2006), any decrements in that ratio are the result of reddening from dust. Thus the dust reddening effect can be accounted for by measuring a Balmer decrement, and assuming the amount of extinction changes with wavelength similarly to well established dust attenuation curves (usually the Small Magellanic Cloud, the Large Magellanic Cloud, or the Milky Way).

Figure 1.4 presents the two populations of galaxies that become apparent when examining the SFR - stellar mass (M_*) relationship. There is a population of highly star-forming galaxies for a range of masses, otherwise known as the star-forming main sequence (Brinchmann et al., 2004; Noeske et al., 2007a; Daddi et al., 2007; Elbaz et al., 2007; Pannella et al., 2009; Schreiber et al., 2015). The second population (circled in red, passive galaxies) has very weak emission lines due to the minimal star-formation activity within the galaxy, thus the measured SFR is an upper limit on the actual star-formation activity in the galaxy. Galaxies in this region are bulge dominated (have a high Sérsic index), suggesting that the SFRs of this population might be higher if the mass was distributed in a disk (Strateva et al., 2001; Bell, 2008; Wuyts et al., 2011; Mendel et al., 2013; Schawinski et al., 2013) There is a similar relationship between morphology and star-formation rate in the colour space (refer back to Figure 1.2).

The global SFR - M_* relation likely stems from relationships between surface densities on the local scale. Galaxies usually have a negative $\Sigma_{\rm SFR}$ gradient (see Figure 1.5), likely in correspondence to the negative gradient of HII region density observed in most galaxies (Pagel & Edmunds, 1981; Evans, 1986; Garnett & Shields, 1987; Shields, 1990). Observational studies have revealed that there is also a tight correlation between the star-formation surface density ($\Sigma_{\rm SFR}$) and the stellar mass surface density (Σ_*), where regions with higher Σ_* have a corresponding increase in $\Sigma_{\rm SFR}$ (Rosales-Ortega et al., 2012; Sánchez et al., 2013; Cano-Díaz et al., 2016; González Delgado et al., 2016; Hsieh et al., 2017). Resolved studies have demonstrated that most galaxies have a negative gradient in $\Sigma_{\rm SFR}$, following this notion (see Figure 1.5).

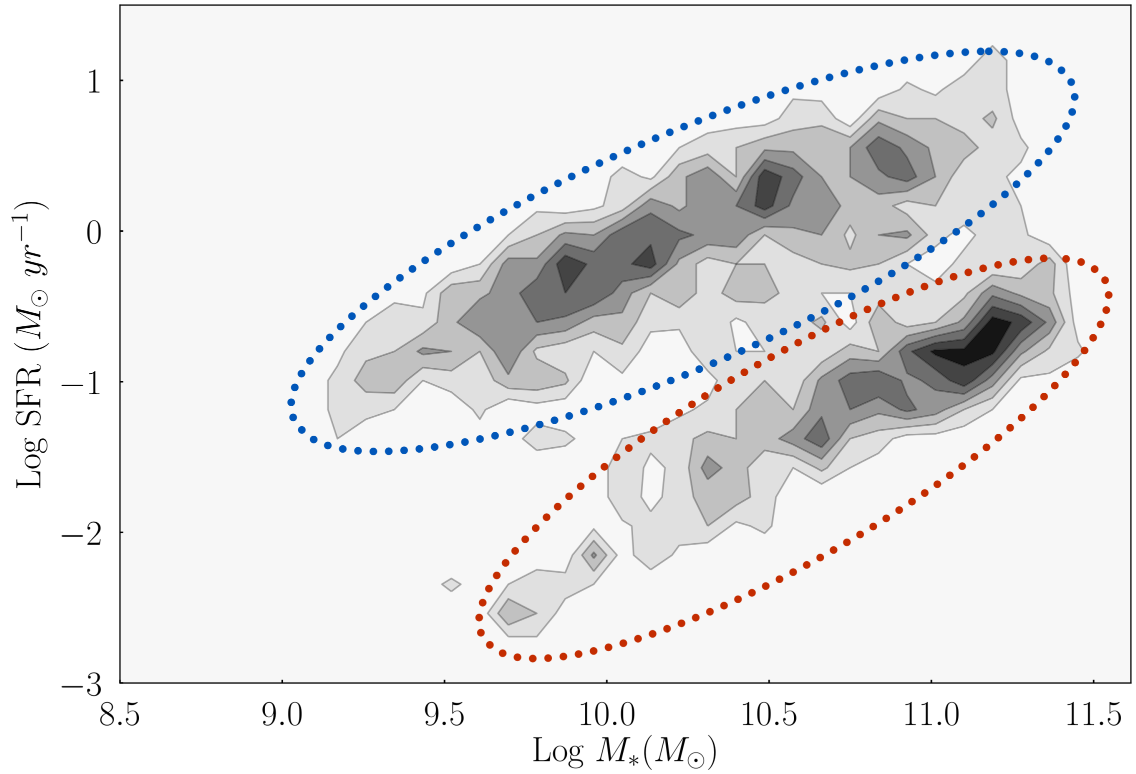

Figure 1.4: SFR plotted against M_* for all DR14 MaNGA galaxies (contours represent the number of galaxies in the sample), the approximate shapes of the star-forming main sequence and passive population are circled with dotted blue and red lines, respectively. SFR and M_* are collected from the PIPE3D VAC (see section 2.1.1 for exact calculation methods used).

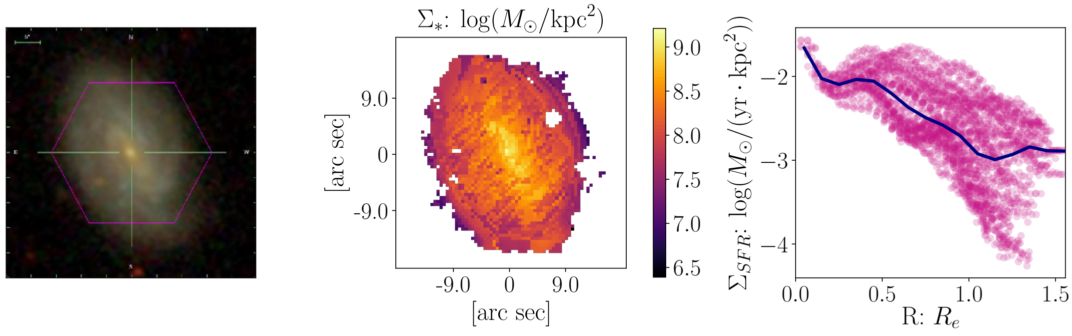

Figure 1.5: From left to right: the gri-image of a MaNGA spiral galaxy, the stellar mass surface density map for the galaxy provided by MaNGA, and the two dimensional median profile of SFR surface density, which demonstrates how both $\Sigma_{\rm SFR}$ and Σ_* decrease with radius.

1.1.3 Galaxy Metallicity

Star formation is one of the main processes to increase the metallicity of an HII region. Over time stars produce heavier elements than the primordial matter that made up the universe after the Big Bang (mostly hydrogen and helium-4, with smaller amounts of deuterium, helium-3, and lithium scattered throughout). The heavy nuclei are eventually injected into the ISM by supernova explosions, stellar winds, and planetary nebulae ejection. Metallicity refers to the fraction of the total mass which consists of elements heavier than hydrogen and helium, conventionally oxygen for gas metallicity, or iron for stellar metallicity. From here, the metallicity will refer to the gas-phase oxygen abundance of a galaxy or region.

To measure the oxygen abundance, the electron temperature (T_e) from faint auroral or nebular emission lines must be determined. However, these lines are intrinsically weak, and become weaker as metallicity increases. Thus metallicity measurements require indirect abundance measurements from strong emission lines. Strong line calibrators usually rely on ratios between strong emission lines that estimate the oxygen abundance, including [NII]λ6583/Hα, [OIII]λ5007/Hβ, [NII]λ6583/[OII]λ3727, [OIII]λ5007/[OII]λ3727 and more (Mcgaugh, 1991; Zaritsky et al., 1994; Kewley & Dopita, 2002; Pettini & Pagel, 2004; Kobulnicky & Kewley, 2004; Marino et al., 2013b)

Three major physical processes impact the metallicity values and distribution in a galaxy: chemical enrichment from star-formation (as mentioned previously), gas inflows, and galactic outflows in the form of winds. Galactic winds created by a starburst or triggered AGN transport metals from the centre of the galaxy to the intergalactic medium (Garnett, 2002; Veilleux et al., 2005). Gas can also flow into the centre of the galaxy, triggered by non-axisymmetric structures (see Section 1.2.1 for further discussion), and dilute the central metallicity (Barnes & Hernquist, 1991, 1996; Kewley et al., 2006, 2010)

Generally the metallicity of a galaxy increases with the global stellar mass, though this increase dampens at the largest M_* values (see Figure 1.6 for an example). This correlation is commonly referred to as the mass-metallicity relation (Lequeux et al., 1979; Tremonti, 2004). There are varying interpretations for why this empirical relationship exists. It could be that in lower-mass galaxies, with comparatively low gravitational potentials, metals are more easily ejected by galactic outflows (Larson, 1974; Tremonti, 2004). Conversely, high mass galaxies are able to trap the galactic winds which would otherwise transport metals outside of the galaxy. It might also be the case that high mass galaxies begin to form their stars earlier than low mass galaxies, allowing for more time to enrich the gas reservoir with metals (Noeske et al., 2007b). Other studies have suggested that low mass galaxies are simply less efficient at converting gas into stars (Brooks et al., 2007; Calura et al., 2009; Mouhcine et al., 2008).

Galaxies with high specific star-formation rates (the SFR divided by the total stellar mass, sSFR) have relatively lower metallicities than those with low sSFRs at the same mass interval. This relationship between mass, gas-phase metallicity, and sSFR has been dubbed the Fundamental Metallicity Relationship (FMR) (Ellison et al., 2008b; Mannucci et al., 2010; Lara-López et al., 2010). The FMR is controlled by the infall of intergalactic medium gas (thus SFR is dependent on metallicity) and the outflow of enriched gas (the metallicity becomes dependent on mass). The existence of a FMR is still contested. It is possible the FMR is an artifact of aperture effects in the single fibre spectroscopic surveys that have identified it, or it is a local effect limited to the central regions of galaxies (Sanders et al., 2017).

More contemporary work has demonstrated analytically that the FMR observed likely stems from a local anti-correlation between star-formation rate surface density (Σ_{SFR}) and metallicity at fixed mass; this analytic model implies that any local relation between two properties would lead to a global relationship (Sánchez Almeida & Sánchez-Menguiano, 2019). There is also a strong correlation between the gas-phase metallicity and stellar mass surface density, implying that the global mass-metallicity relationship stems from a local mass-density-metallicity relationship (Sánchez et al., 2013; Barrera-Ballesteros et al., 2016).

1.2 Galaxy Mergers

Many of the qualities of galaxies described previously, from morphology to star-formation activity, can be drastically altered by interactions between two galaxies. Dynamical friction experienced during a close encounter can eventually lead to one galaxy falling into another and the two coalescing. Dynamical friction is the consequence of a series of small gravitational tugs on each star in a galaxy from the stars in a neighbouring galaxy, overtime resulting in a transfer of energy from the target stars to the acceleration of the neighbouring stars (Chandrasekhar, 1943). Simplifying the process to the effects of a star in a passing galaxy (m_*) on another galaxy (mass

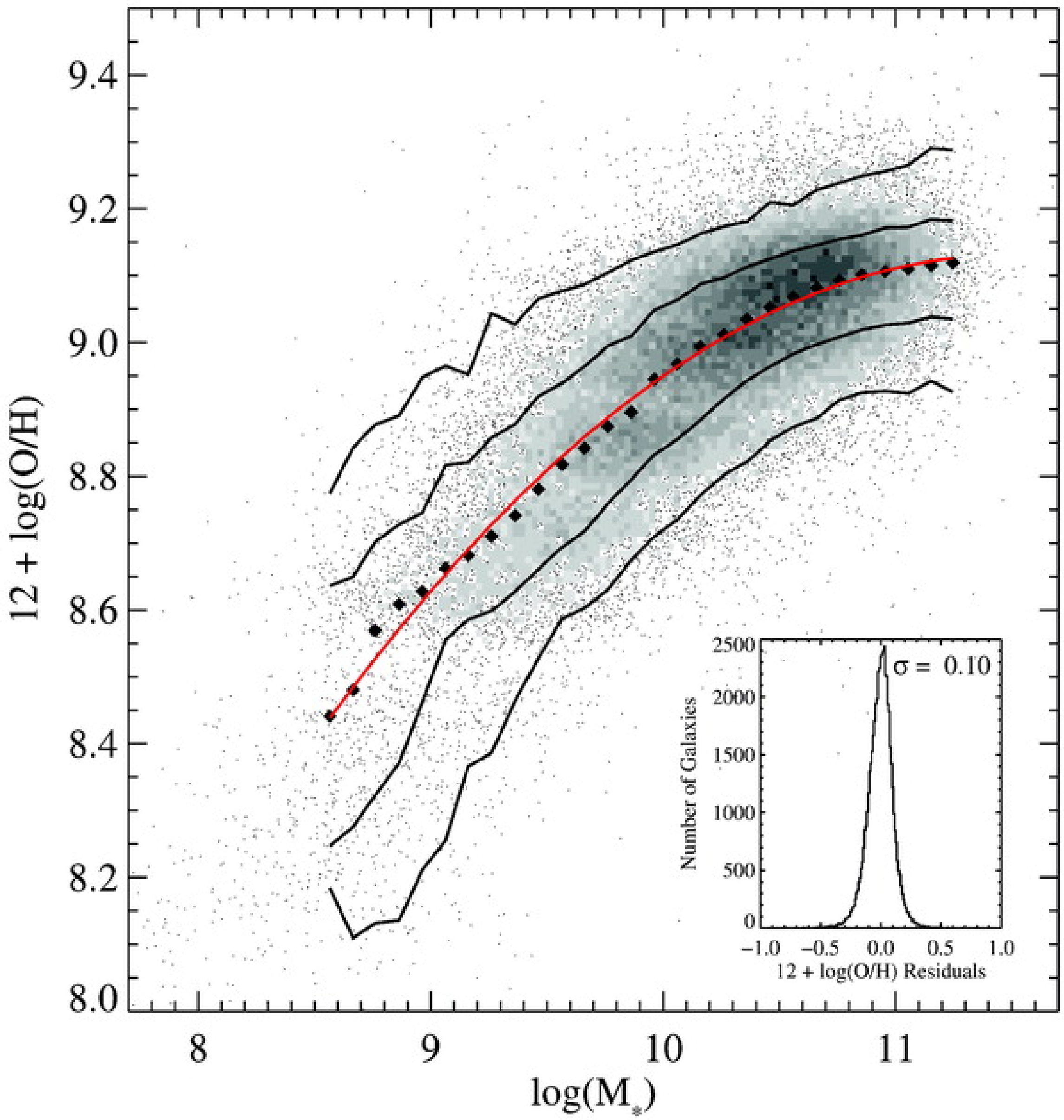

Figure 1.6: Gas-phase oxygen abundance metallicity plotted against total stellar mass for ∼53,400 star-forming galaxies from SDSS. Solid black lines represent contours that hold 68% and 95% of the data. Black diamonds represent the median metallicity for bins of 0.1 dex in M_* , with a red line displaying a polynomial fit to the data. Source: Tremonti (2004).

M_g), that galaxy will experience an acceleration perpendicular to its current forward velocity v resulting from the perpendicular attractive force of the star:

$$\frac{dv_{_\perp}}{dt} = \frac{Gm_*b}{(b^2 + v^2t^2)^{3/2}}, \tag{1.3}$$

where $(b^2 + v^2t^2)$ is the distance between the star and the galaxy at time t, with b as the impact parameter. The perpendicular change in velocity can be computed by integrating 1.3 from $t = -\infty$ to $t = \infty$, resulting in a change in perpendicular velocity of $\Delta v_{_\perp g} = \frac{2Gm_*}{bv}$, or a change in the galaxy's momentum of $\frac{2Gm_*M_g}{bv}$. Given the conservation of momentum, the star will also experience a change in perpendicular momentum of the same amount, resulting in a perpendicular change in the velocity of the star $\Delta v_{_\perp *} = \frac{2GM_g}{bv}$. The change in perpendicular velocity for both the galaxy and the star can be used to determine the change in perpendicular kinetic energy of the system:

$$\Delta K_\perp = \frac{M_g \Delta v^2_{_\perp g}}{2} + \frac{m * \Delta v^2_{_\perp *}}{2} = \frac{2G^2 m_* M_g (m_* + M_g)}{b^2 v^2}. \tag{1.4}$$

The energy of the system must be conserved, implying that the larger mass (the galaxy) will lose some of its forward motion, and that energy will be transferred to the smaller mass (the star). The kinetic energy from the forward motion, $\frac{M_g v^2}{2}$, should be equal to the kinetic energy lost by the galaxy when v decreases by Δv, plus the perpendicular change in kinetic energy and the kinetic energy gained by the star $\frac{m_* \Delta v_*}{2}$. Employing the conservation of momentum in the system, $M_g \Delta v = m_* \Delta v_*$, such that the star's change in forward velocity is $\Delta v_* = \frac{M_g \Delta v}{m_*}$, the conservation of energy can be met as follows:

$$\frac{M_g v^2}{2} = \frac{M_g (v - \Delta v)^2}{2} + \frac{m_*}{2}\Big(\frac{M_g \Delta v}{m_*}\Big)^2 + \frac{2G^2 m_* M_* (M_* + M_g)}{b^2 v^2}. \tag{1.5}$$

Assuming the mass of the star is significantly less than the galaxy ($m_* \ll M_g$, thus $m_* + M_g \simeq M_g$), and the change in the galaxy's forward motion is a small fraction of its current velocity ($\Delta v \ll v$) such that the Δv^2 terms can be dropped, equation 1.3 becomes

$$\frac{M_g v^2}{2} \simeq \frac{M_g (v^2 - 2v\Delta v)}{2} + \frac{2G^2 m_* M_* M_g}{b^2 v^2}, \tag{1.6}$$

which can be rearranged to solve for the change of velocity on the galaxy:

$$\Delta v \simeq \frac{2G^2 m_* M_g}{b^2 v^3}. \tag{1.7}$$

The total change in velocity for the galaxy can be determined by integrating Δv over all impact parameters, assuming an n number density of stars and the cylindrical volume at the impact parameter covered in time dt is $vdt2\pi b$:

$$\frac{dv}{dt} = -\int_{b_{min}}^{b_{max}} \frac{2G^2 m_* M_g}{b^2 v^3}(nv2\pi bdb) = \frac{4\pi G^2 m_* M_g n}{v^2} ln(b_{max}/b_{min}). \tag{1.8}$$

Assuming b_{min} is approximately the radius of the galaxy and b_{max} is approximately 3 galactic radii (the edge of the other side of the passing galaxy), $ln(b_{max}/b_{min})$ is approximately one. Given the mass density in stars (ρ_*) is equal to the number of stars n multiplied by the mass of each star m_*, the deceleration experienced by one galaxy due to the close passing of another is:

$$\frac{dv}{dt} \simeq -\frac{4\pi G^2 M_g \rho_*}{v^2}. \tag{1.9}$$

Equation 1.9, also called the Chandrasekhar formula, can be used to approximate how long it will take for the smaller galaxy to be consumed by the larger after a number of close passages: the merger timescale t_{merger}.

$$t_{merge} \sim \frac{v}{dv/dt} \sim \frac{v^3}{4\pi G^2 M_g \rho_*} \tag{1.10}$$

If one assumes a galaxy mass of 10^{10}M$_\odot$, moving at 200 km/s, passes a galaxy with a stellar mass surface density of 10^6M$_\odot$/kpc^3, the approximate merger timescale is $\sim 10^8$ years. Modern simulations of galaxy interactions show similar merger timescales, measuring on average 0.6 Gyr for the time in the pair stage (separation $<$ 30 kpc) for galaxies with mass ratios between 1:1 and 4:1 (Lotz et al., 2010a). However, real galaxies experience multiple close encounters before coalescence, existing in an "interacting" stage for up to $\sim$1Gyr (Jian et al., 2012). Visual indicators of an interaction, such as a perturbed morphology, can emerge as soon as this first close approach (pericentric passage) occurs, and last up to 0.1 - 1.2 Gyr depending on the parameter used to quantify the perturbed morphology (Lotz et al., 2008). Of the galaxies within z $<$ 1, 4 - 6% have the perturbed morphology that indicates a recent interaction (within the last 1 Gyr or less) (Darg et al., 2010), and 9% of present day ultra-luminous galaxies have undergone a major merger since z=1.2 (Lin et al., 2004). N-body simulations suggest that a typical galaxy at z$\sim$3 ($M_* > 10^{10} M_\odot$) undergoes over 4 mergers before z=1 (Conselice, 2006; Rodriguez-Gomez et al., 2015). Despite the ubiquitous nature of galaxy mergers, only a small fraction of mergers which are currently ongoing can be observed.

1.2.1 Simulations of Galaxy Interactions

Given the process of galaxies merging can take $\sim$2 Gyr, galaxy simulations provide the best method for understanding how one stage of an interaction leads directly to another for a particular progenitor case. Early N-body simulations, which model the gravitational forces between particles in a galaxy, were initially used to demonstrate how tidally interacting galaxies evolve into elliptical galaxies (Toomre & Toomre, 1972; White, 1978, 1979). To understand the effects on a galaxy outside of structure and dynamics, one must consider the more complicated radiative processes which govern the gas-dynamics of a galaxy interaction. Pioneering works which combined N-body simulations with hydrodynamics code provided the opportunity to study both the structural changes (such as the creation of tidal tails and bars) along with physical effects of those changes (Hernquist, 1989; Barnes & Hernquist, 1991). Simulations without hydrodynamics included also generally underestimate the merging time scale predicted by the Chandrasekhar theory of dynamical friction (Boylan-Kolchin et al., 2008).

Galaxy-galaxy interactions continuously alter their constituents morphologies, as described above, such that various merger stages have their own unique morphological affects (Toomre, 1977; Bournaud et al., 2005; Lotz et al., 2008; Hopkins et al., 2009; Rodriguez-Gomez et al., 2017). Tidal gravitational forces lead to the creation of extended features (Arp, 1966; Toomre & Toomre, 1972) and stellar tidal arms (Barnes, 1988; Barnes & Hernquist, 1996; Mihos & Dubinski, 1998). The growth of non-axisymmetric structures results in gravitational torques that cause gas to lose angular momentum and fall into the centre of the galaxy (Toomre & Toomre, 1972; Barnes & Hernquist, 1991; Iono et al., 2004). These structures occur both at large radii (0.1 - 1 kpc) with bar-like stellar modes created by strong perturbations in the gravitational potential, and small radii (10 pc) where an eccentric or lopsided disk dominates the potential (Hopkins & Quataert, 2011). The resulting misalignment between the stellar bar and gaseous bar cause the stellar component to exert a torque on the gaseous component (Barnes & Hernquist, 1996; Hopkins et al., 2009). The gaseous component loses the angular momentum to stay at its current radius and falls inward.

The inflow of low-metal gas also produces a dilution in central metallicity (Kewley et al., 2006; Ellison et al., 2008a; Michel-Dansac et al., 2008). Hydrodynamic simulations have been used to demonstrate how merging events flatten the metallicity gradient, with a central suppression directly proportional to the strength of the central starburst triggered by the gas inflow (Rupke et al., 2010; Montuori et al., 2010; Perez et al., 2011). Interacting galaxies have an excess of cold-dense gas and host gas, both of which are prominent in the star-forming process, resulting in a period of enhanced SFR up to 4 Gyr after the first pericentric passage (Moreno et al., 2019). Subsequent supernova chemical production will eventually temper the metallicity dilution resulting from gas inflows (Perez et al., 2011).

Gas inflows then fuel an increase in central star-formation, as supported by both observations (e.g. Donzelli & Pastoriza 1997; Barton Gillespie et al. 2000; Lambas et al. 2003; Alonso et al. 2004; Ellison et al. 2008a, 2010; Darg et al. 2010) and simulations (e.g. Barnes & Hernquist 1996; Mihos & Hernquist 1996; Cox et al. 2006; Di Matteo et al. 2007; Montuori et al. 2010; Torrey et al. 2012). Correspondingly, merging galaxies tend to be bluer in colour than their isolated counterparts (Larson & Tinsley, 1978; Patton et al., 2011). The SFR gradient is always negative, but the SFR behaviour in the outskirts varies greatly depending on the galaxy mass and the orientation of the interaction (see Figure 1.7).

Consequently, galaxy mergers, and their subsequent effects, are inherently sensitive to the qualities and orientation of their progenitors. There are direct interactions, where the target galaxy's disk spin is aligned with the orbital angular momentum vector, and retrograde interactions where the galaxy's spin is oriented in the opposite direction to the orbital angular momentum. Retrograde interactions result in smaller gas depletion times compared to direct interactions, most likely in concordance with the lessened tail development for an interaction of this orientation (Di Matteo et al., 2007; D'Onghia et al., 2010). There are also greater perturbations in a merging galaxy when its rotation speed is similar to the peak angular speed of the encounter (D'Onghia et al., 2010). The orientation of the interaction matters as well; the angle at which two galaxies approach each other can alter the strength of the ensuing central starburst, and whether the galaxy outskirts have suppressed or enhanced star-formation (Moreno et al., 2015). Galaxies that are initially aligned before they

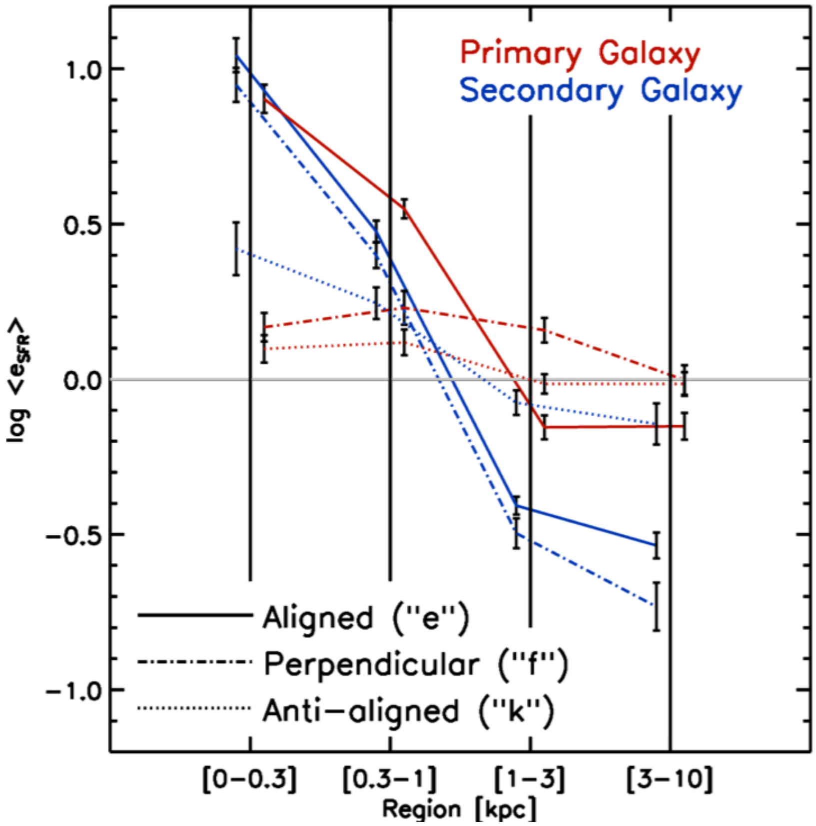

Figure 1.7: SFR efficiency as a function of radius for the larger (red line) and smaller (blue line) galaxy in interactions of different orientations (solid, dashed, and dotted). Source: Moreno et al. (2015).

interact have a greater suppression in their outskirts after first pericentric passage, compared to galaxies that approach anti-aligned (refer again to Figure 1.7).

Figure 1.7 also demonstrates how the mass of the interaction mitigates the influence of the interaction. The more massive of the two galaxies always has less SFR suppression in the outskirts, even experiencing an enhanced SFR in the outskirts of a primary galaxy perpendicular to its companion (Moreno et al., 2015). Observational and theoretical studies demonstrate stronger gas inflows for interactions between galaxies of similar/equal mass (Cox et al., 2006). The closer to two galaxies are in size, the stronger the subsesquent SFR enhancement (Woods & Geller, 2007; Cox et al., 2008; Ellison et al., 2010; Lambas et al., 2012).

The gas fraction of the interacting galaxy disks can also lead to variable central starburst strength. Interacting galaxies with high gas fractions are predicted to have weak and short-lived enhancements in star-formation (Bournaud et al., 2011; Perez et al., 2011; Scudder et al., 2015; Fensch et al., 2017), or no enhancement at all (Perret et al., 2014). The gas inflow can also trigger an active galactic nucleus (AGN) (Cattaneo et al., 2005; Di Matteo et al., 2005; Capelo et al., 2015; Ellison et al., 2019). The effects of a merger event are not always centrally focused either. Interactions can increase the compressive tidal forces across a galaxy, increasing the compressive turbulence to create an excess of dense gas and increased star-formation in the outskirts (Renaud et al., 2014).

1.3 Observations of Galaxy Mergers

1.3.1 Global Studies of Mergers

Photometry can be used to measure the distribution of galaxies in the U-B/B-V plane, and indicate whether a galaxy is "redder" or "bluer". Recent or strong starburst activity is seen as a bluer U-B colour for a given B-V colour. Galaxies with peculiar morphology have a greater scatter in the U-B/B-V plane compared to well-behaved galaxies, indicating that interactions trigger starburst activity (Larson & Tinsley, 1978). The fraction of red galaxies is greater for pairs than for isolated galaxies, given they exist in denser environments (Ellison et al., 2010; Patton et al., 2011; Alonso et al., 2012). However, pair colour becomes bluer as the separation between interacting galaxies decreases (Barton Gillespie et al., 2003; Patton et al., 2011; Tonnesen & Cen, 2012), the bluest galaxies being those with prominent tidal features (Lambas et al., 2012).

An equally common method for determining SFR is employing spectroscopy to measure Hα flux. This can be done with a long-slit spectrograph, which gathers the spectral information along a fixed position angle on the sky, or with a fibre which collects the light within an aperture to be sent to a spectrograph. If the galaxy extends outside of the fibre or slit, imaging can help correct for the flux lost outside the fibre (Brinchmann et al., 2004). The global SFR values are greatest for galaxy interactions with low mass ratios and small projected separations (r_p) (Nikolic et al., 2004; Woods et al., 2010; Ellison et al., 2008a; Scudder et al., 2012; Yuan et al., 2012). By comparing the SFR of galaxy mergers to a control sample of isolated galaxies, one can determine a value ΔSFR that quantifies any offset in SFR as a result of the interaction. Similar to the increase in SFR with decreasing r_p, ΔSFR is greatest with smallest r_p (see Figure 1.8). Galaxies experience the greatest enhancement in SFR at the moment of coalescence (Ellison et al., 2013).

Observational studies found a slight positive correlation between SFR enhancement and gas fraction, but such correlation is likely caused by high gas fraction galaxies having a generally high SFR before the interaction (Scudder et al., 2015). It is important to note that galaxies with a higher gas fraction actually have longer lasting morphological disturbances, so many visually selected observational studies could be biased towards gas rich interactions with shorter lived (by up to a factor of 10) starbursts (Lotz et al., 2008, 2010b).

Offset in metallicity, ΔO/H, can be computed in a similar manner to demonstrate the corresponding suppression in metallicity at smallest separation (see Figure 1.8). Unlike ΔSFR, ΔO/H approaches zero beyond r_p ~60 kpc, indicating behaviour consistent with the control sample (Scudder et al., 2012). The metallicity offsets are also of a much smaller magnitude compared to the SFR offsets, which is expected given metallicity changes are expected to be of the order of 0.3 - 0.5 dex (Cooper et al., 2008; Ellison et al., 2008a).

1.3.2 Integral Field Spectroscopy

Global spectroscopic studies have the drawback of only collecting one value to describe an entire galaxy. The resulting integrated properties are biased, considering information was sampled from only the centre, or a particular axis if a slit was used. For interacting galaxies at varying separation, the ΔSFR measurements outside of the fibre (fibre SFR subtracted from the total aperture corrected SFR) is less than that

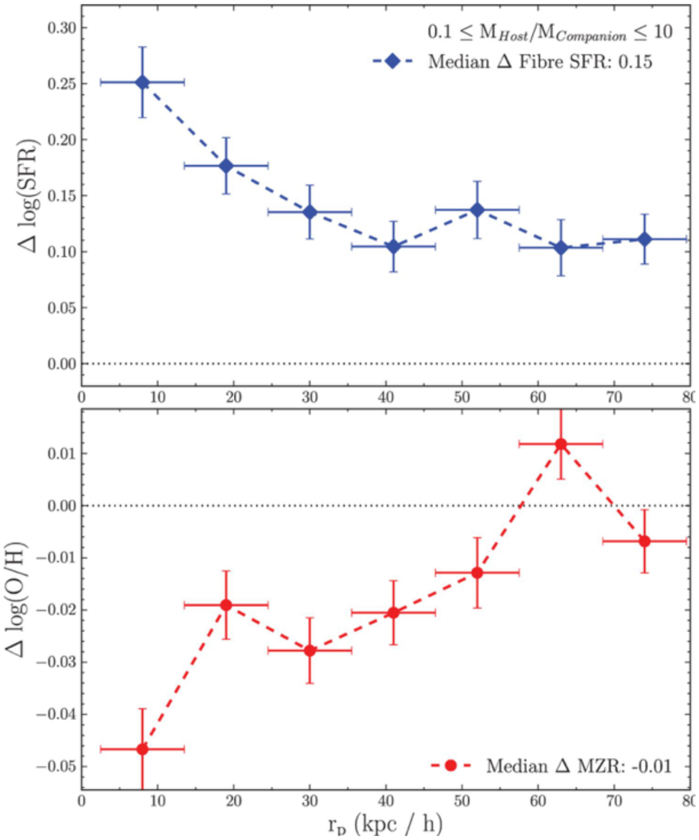

Figure 1.8: SFR offset (ΔSFR) and metallicity offset (ΔO/H). A positive Δ value indicates an enhancement, whereas a negative Δ value indicates suppression. Source: Scudder et al. (2012).

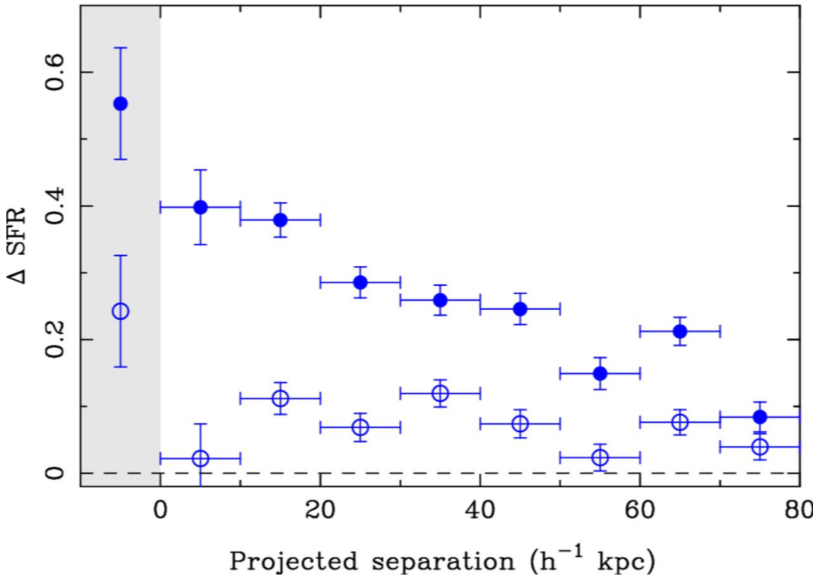

Figure 1.9: SFR enhancement (ΔSFR) for post-mergers and pair galaxies. Filled circles represent the fibre SFR, and the empty circles represent SFR outside of the fibre. Source: Ellison et al. (2013).

within the fibre, indicating there is radial variation in ΔSFR overlooked by global spectroscopic studies (see Figure 1.9).

Two dimensional spatially resolved spectroscopy, on the other hand, can reveal to us the distribution of star-formation, indications for particular quenching mechanisms, disk and bulge growth over time, and much more. Desire for spatially resolved spectroscopic studies for a survey of galaxies, rather than singular case studies, motivated the advancement of integral field units (IFUs) as a tool for spectroscopic studies.

The Spectroscopic Areal Unit for Research on Optical Nebulae (SAURON) was a trail blazer for large Integral Field Spectroscopy (IFS) surveys, collecting spectra for 72 galaxies (Tim De Zeeuw et al., 2002). Building on results concerning early type galaxies made by SAURON, the ATLAS^{3D} survey combined IFS observations with those in the radio and millimeter to create a multiwavelength study of 260 E/S0 K-band selected galaxies (Cappellari et al., 2011). The DiskMass Survey followed up on the dynamical studies SAURON completed, analyzing the mass-to-light ratios of disk-like galaxies to understand the dark matter fractions of Milky Way - like galaxies (Bershady et al., 2010).

The success of these early studies led to countless more IFS surveys with their own particular science goals. The VENGA (VIRUS-P Exploration of Nearby Galaxies)

Survey focused on high spatial resolution and deep observations to constrain star-formation in nearby spirals (Blanc et al., 2013). The SLUGGS Survey (SAGES Legacy Unifying Globulars and GalaxieS) obtained IFU data for 25 early-type galaxies out to $\sim 8R_e$, to probe the chemical composition and kinematics at the outermost radii (Brodie et al., 2014). A sample of some of the largest galaxies ($M_* \gtrsim 10^{11.5} M_\odot$) were investigated with the MASSIVE Survey (Ma et al., 2014) using IFU spectroscopy.

Recently, more massive IFS surveys have observed on the order of $\sim$ 1000s rather than $\sim$ 10s of galaxies to provide a holistic sample on which more focused studies can be performed. The first of these surveys to be launched was the Calar Alto Legacy Integral Field Area Survey (CALIFA), with the goal to observe $\sim$ 600 galaxies between 2011 and 2016 (Sánchez et al., 2012a). The next large IFS survey, the Sydney-Australian Astronomical-Observatory Multi-object Integral-Field Spectrograph (SAMI), more than tripled their sample with the goal to observe $\sim$3000 galaxies (Allen et al., 2015). The Mapping Nearby Galaxies at Apache Point Observatory (MaNGA) survey has the largest collection of IFS targets so far, with $\sim$4500 observations so far of a $\sim$10,000 galaxy goal by 2020 (Bundy et al., 2015; Law et al., 2015).

1.3.3 IFS Studies of Mergers

Case studies examining nearby merging galaxies with integral field spectroscopy effectively illustrate the importance of resolved properties when studying interactions. The 10:1 stellar mass ratio galaxy pair NGC 7771 + NGC 7770 was examined with Potsdam Multi-Aperture Spectrograph fibre package (PMAS/PPAK), the same spectrograph used with the CALIFA survey, to demonstrate the extended starburst experienced by the smaller of the interacting galaxies (Alonso-Herrero et al., 2012). The official CALIFA survey was employed to examine the MICE interacting system, uncovering a lack of both central and extended star-formation enhancement for galaxies just experiencing first pericentric passage (Wild et al., 2014). IFS surveys like CALIFA are now large enough to collect a statistically significant samples of galaxy mergers to study their spatially resolved properties.

The CALIFA survey was the first to collect a a large sample (103 galaxies) of IFS observations at different stages of the merging process, each galaxy possessing a companion within r_p <160 kpc and line-of-sight velocity difference Δv <600 km/s, or the disturbed morphology indicating the galaxy is post-coalescence (Barrera-Ballesteros et al., 2015). The CALIFA data is then split into "central"(5 arcseconds) and "extended"(30 arcseconds) apertures to quantify the behaviour of merging galaxies as a function of position within the galaxy. This method has the benefit of simplifying galaxy behaviour to central and outskirt, quickly identifying how interactions influence different regions. The equivalent width (EW) of Hα, a proxy for specific star-formation rate, is higher in the central aperture for interacting galaxies compared to a control sample (see Figure 1.10). However, this Hα EW behaviour in the extended apertures of interacting galaxies is similar to, or even suppressed compared to, the control sample (depending on how the control sample of star-forming galaxies was selected).

Figure 1.11 show the metallicity offsets for the same sample of interacting CALIFA galaxies. On average the central metallicity of these galaxies is consistent with the control sample, but when extended apertures are accounted for a suppression in the outer metallicity becomes apparent (Barrera-Ballesteros et al., 2015). The metallicity gradients of interacting galaxies are flattened in comparison to a non-interacting sample (Sánchez et al., 2014), which would suggest an inflow of low-metal gas to homogenize the galaxy's metallicity. The seemingly contradictory points of these two studies highlights the importance of examining the stages of interaction contributing to offset measurements.

Metallicity measurements can provide approximations for how an interaction affects the low-metal gas in a galaxy, but the true nature of gas within a galaxy is better understood by measuring the molecular gas distribution. The Combined Array for Research in Millimeter-wave Astronomy (CARMA) Extragalactic Database for Galaxy Evolution (EDGE) survey, which collected global CO information for a sample of CALIFA targets, revealed that interacting galaxies with this central Hα EW enhancement had the same concentration of molecular gas as those which did not have a central burst of recent star-formation activity (Chown et al., 2019). The CO measurements complicate a scenario where merger-induced gas inflows trigger a central starburst.

1.4 Thesis Objectives

IFS surveys have provided the novel opportunity to measure the spatially resolved properties of a population of interacting galaxies, rather than studies of galaxy mergers on a case by case basis. CALIFA, SAMI, and MaNGA have verified the central

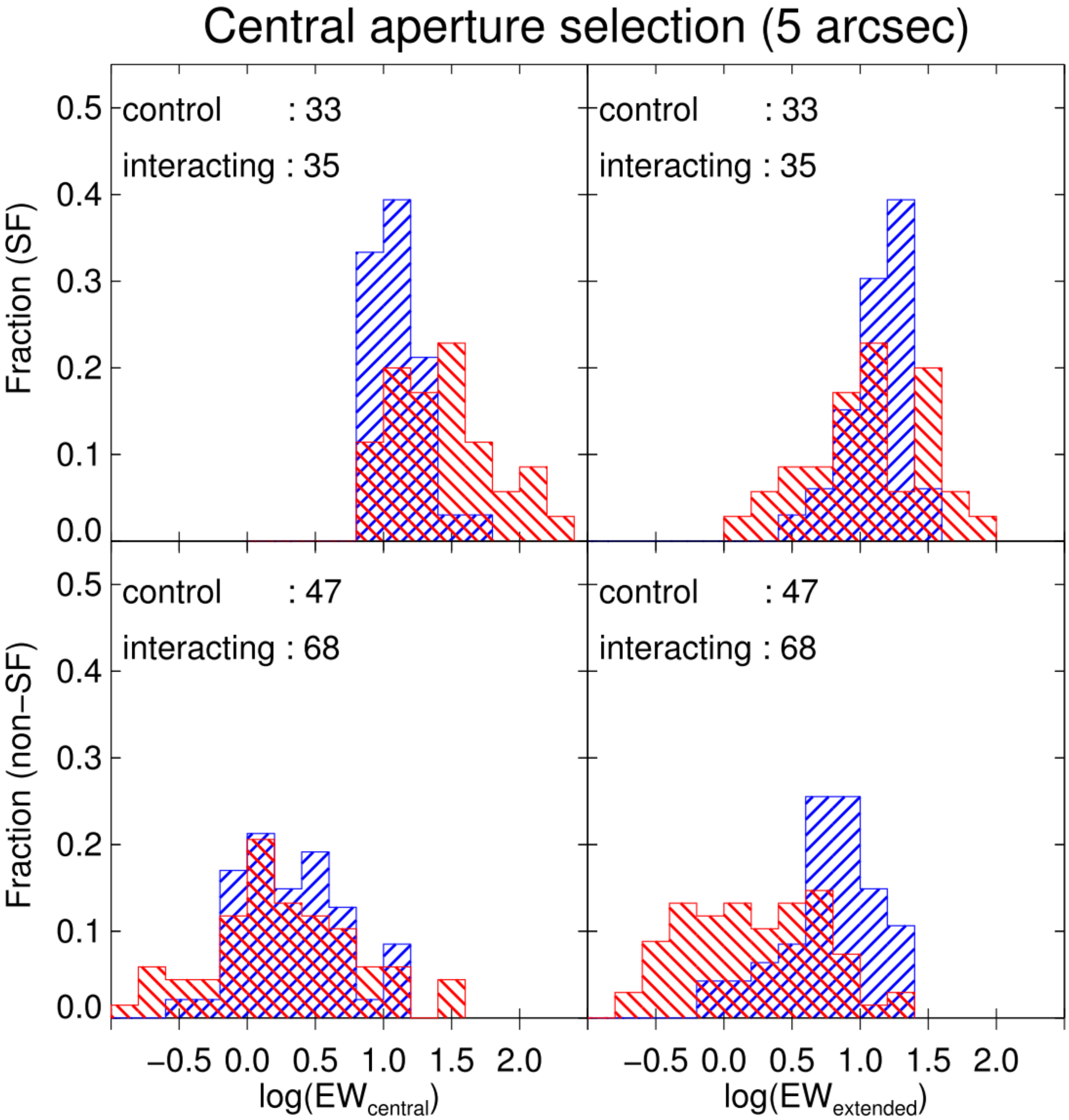

Figure 1.10: Integrated Hα EW for interacting (red) and control (blue) galaxies in CALIFA. The left and right panels show the distribution of integrated Hα EW in the "central" and "extended" apertures, respectively. The top (bottom) panel shows the distribution for star-forming (non-star-forming) sample, classified using a 5 arcsecond aperture. Source: Barrera-Ballesteros et al. (2015).

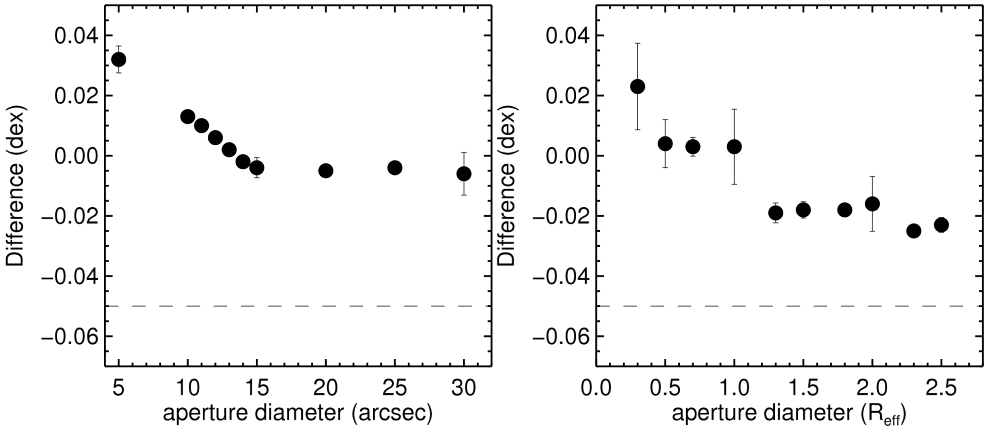

Figure 1.11: The difference in metallicity for interacting galaxies with respect to a control (isolated) galaxy sample at different aperture sizes. There is a slight difference depending on how you define the radius (arcseconds are an independent measurement method, R_e is dependent on the light profile of the galaxy), however both show a suppression in the outskirts. Source: Barrera-Ballesteros et al. (2015).

starbursts observed in global studies of galaxy mergers, as well as unveiling new questions to be answered concerning the more nuanced behaviour of mergers at the galaxy outskirts.

None of the current IFS studies of galaxy mergers have performed separate analysis on targets based on interaction stage. Post-merger galaxies demonstrate significantly stronger nuclear enhancement of SFR compared to galaxy pairs (Ellison et al., 2013), yet more often than not post-mergers are grouped together in pair samples. Chapter 2 will investigate the spatially resolved properties of only post-merger galaxies using IFS spectroscopy, and investigate the variable distributions of star-formation enhancement and metallicity deficit for galaxies supposedly in a very similar merger stage. Unlike other IFS studies, which utilize apertures to define central and extended behaviour (Barrera-Ballesteros et al., 2015), this work is the first to construct full radial profiles of offsets in SFR and metallicity.

Many global studies of galaxy mergers have focused on the stage of the galaxy interaction (Ellison et al., 2008a; Scudder et al., 2012; Patton et al., 2016; Pan et al., 2018), using r_p as a proxy for merger stage. No such analysis has been made for interacting galaxies with IFS observations, and could reveal how the distribution of star-formation enhancements varies as the merger progresses. Mass ratio can also be used to characterize a set of interacting galaxies, and though plenty of effort has gone into measuring how global offsets change as a function of mass ratio (Cox et al., 2006; Ellison et al., 2008a; Pan et al., 2018) no such study has been replicated with an IFS survey. Chapter 3 explores how interaction stage and progenitor characteristics shape the spatially resolved properties of interacting galaxy pairs.

Chapter 4 will introduce new routes for galaxy merger analysis that could answer some remaining questions left by the studies herein. More nuanced analysis of galaxy pairs needs to be completed, and investigation into the asymmetry of spatially resolved properties could greatly improve such analysis. The molecular gas content of galaxy mergers also warrants further exploration, particularly in juxtaposition to spatially resolved optical information.

Chapter 2

Post-Mergers in MaNGA

A focused analysis of a population of post-merger galaxies using integral field spectroscopy, from a large survey such as MaNGA, has never been completed. Section 2.1 will review the finer details concerninging the MaNGA survey instrumentation and science goals, along with the spectral reduction and analysis pipeline, PIPE3D. A handful of dataproducts were computed separately from PIPE3D, and are explained in Section 2.2. $\Delta\Sigma_{\rm SFR}$ and Δ O/H values are used to quantify offsets in galaxy behaviour as a result of the recent interaction; calculation of these values is described in Section 2.3. Finally, the visual classification of post-merger galaxies from the MaNGA sample is recounted in Section 2.4, followed by results from the analysis of those post-mergers (Section 2.5).

2.1 Mapping Nearby Galaxies at Apache Point Observatory (MaNGA)

The Mapping Nearby Galaxies at Apache Point Observatory (MaNGA) survey was launched on July 1st 2014 as one of the core programs of the fourth-generation Sloan Digital Sky Survey (SDSS-IV). MaNGA makes dithered observations with 17 fibre-bundle IFUs, each a hexabundle that ranges in diameter from 19 fibres (12”) to 127 fibres (32”) where each fibre has a diameter of 2”, to cover a wide range of angular sizes (see Figure 2.1) (Bundy et al., 2015). The MaNGA team designed a metal ferrule housing that begins as a wide circle and tapers into the desired hexagonal shape, making it easier to quickly manufacture many IFUs (more than 200 separate IFUs were created) (Drory et al., 2015). Fibres are attached to aluminium plug-plates, which have been drilled for specific fields and targets, that are mounted onto the 2.5 m Sloan Telescope at the Apache Point Observatory (see Gunn et al. 2006). These fibres then feed light into the dual-channel Baryon Oscillation Spectroscopic

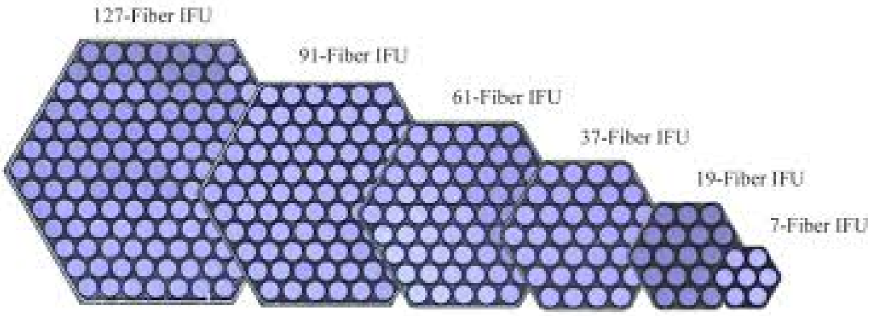

Figure 2.1: All hexabundle IFU sizes, including the seven-fibre bundle used for flux calibration. Source: Bundy et al. (2015).

Survey (BOSS) spectrograph, which covers a wavelength range of 3600 - 10300 Å, with an average spectral resolution of R$\sim$2000 (Smee et al., 2013). To minimize the calibration errors on the SFR and nebular metallicity measurements, the MaNGA survey requires a spectrophotometry accuracy better than 7% from [OII]λ3727 to Hα, and better than 2.4% between Hβ and Hα (Bundy et al., 2015).

Observations from MaNGA need to be corrected for flux lost to the atmosphere, and corrected for system throughput. A seven-fibre "mini-bundle" is used to measure the fraction of light covered by the central fibre as a function of wavelength; given an initial estimate of the seeing PSF provided by the guide camera, the flux loss due to system throughput can be measured and accounted for (Bundy et al., 2015). Sky subtraction is performed by locating sky-fibres near the science IFUs on the plate, and co-located along the slit with the same science fibres. Two sky-fibres are then placed at the end of each science IFU V-groove block (the positioned end of the fibres that compose one IFU, which directs light to the spectrograph), to minimize any bright source contamination. The total number of sky-fibres per IFU ranges from 2 (for the 19-fibre bundles) to 8 (for the 127-fibre bundles) (see Figure 2.2 for a simplified example of fibre placement). Based on the BOSS reduction pipeline (Bolton et al., 2012), MaNGA reaches $\sim$1% level sky subtraction from the continuum

MaNGA has a larger wavelength range (3600 - 10300 Å) than both CALIFA's 3750 - 7000 Å and SAMI's 3700 - 5700 Å range (Sánchez et al., 2012b; Allen et al., 2015). It also has the benefit of continuous wavelength coverage, unlike surveys such as SAMI which have split wavelength ranges of 3700 - 5700 Å and 6250 - 7350 Å. MaNGA's sample size goal is also an order of magnitude larger than any current IFU survey, aiming to observe $\sim$10,000 galaxies in 6 years. The targets were required to have principal components which define a galaxy (stellar mass, SFR, environment) that could

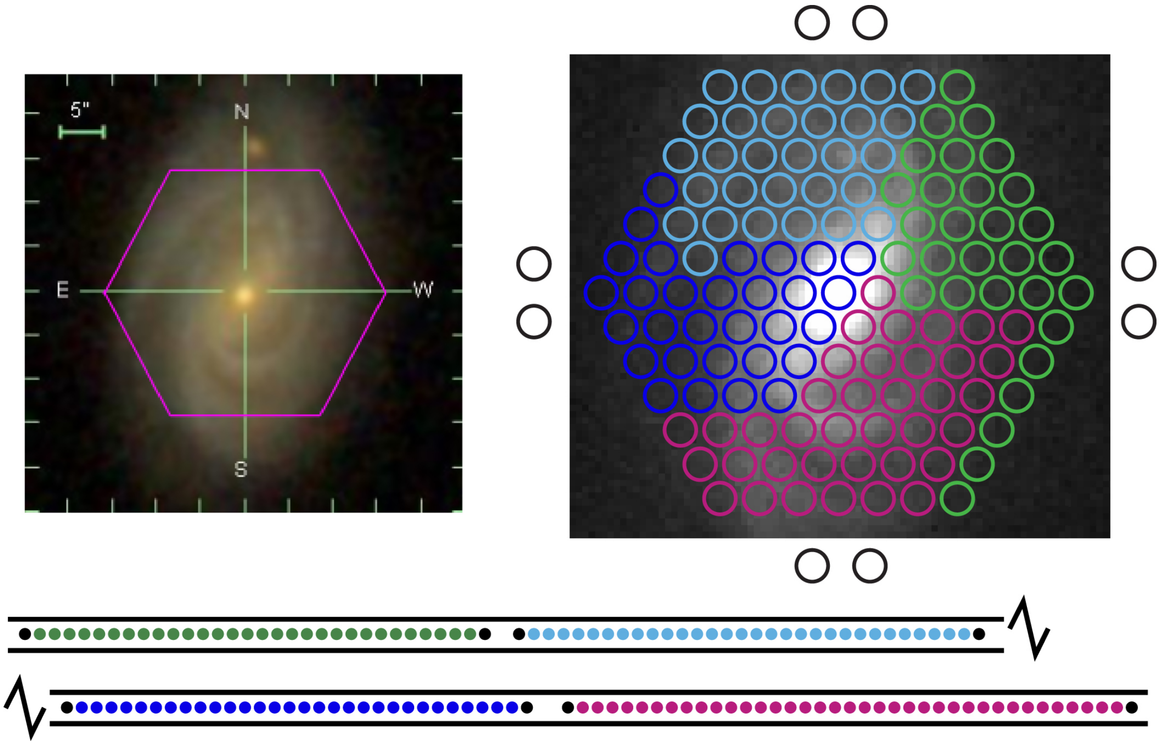

Figure 2.2: Example of the MaNGA IFU fibre placement. The left panel shows the SDSS gri-image of a MaNGA galaxy, with the IFU footprint overlain in pink. The right panel shows a zoomed in g-band image in gray scale, with circles representing the 127 overlain fibres. The black circles at the edge of the image are the 8 sky fibres. The schematic diagram at the bottom models how all fibres are grouped into four physical blocks on the spectrograph entrance slit. Source: Law et al. (2016).

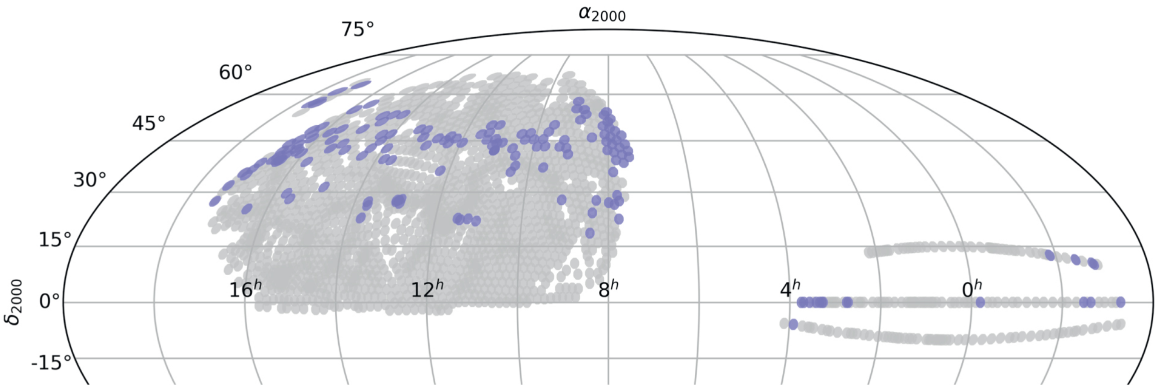

Figure 2.3: The distribution of possible MaNGA plates on the sky (grey), with plates released as part of DR14 in purple. Source: Abolfathi et al. (2018).

be divided into 6 bins in which the single measurement precision is approximately equal to the expected difference in signal from bin to bin (see Appendix A.1 for a detailed calculation of sample size). The survey size also provides the opportunity to collect a relatively large sample (more than 100 targets) of more rare populations like major galaxy mergers, post-starbursts, and galaxies with strong galactic outflows. The MaNGA sky distribution overlaps with the SDSS Main spectroscopic sample footprint (see Figure 2.3), a total of ∼2700 deg^2 coverage (Bundy et al., 2015).

The work herein uses primarily the 14th Data release of MaNGA, which was made available to the public on July 31st 2017 (Abolfathi et al., 2018). This included spectra datacubes for ∼2600 galaxies. Rather than use the raw datacubes, which supply the flux for each spatial pixel containing a spectrum (spaxel) as a function of wavelength (calibrated and reduced by Law et al. 2016), datacubes which had already been through a spectral analysis pipeline (see Section 2.1.1) are used to move directly to analysis.

2.1.1 PIPE3D

A galaxy's optical spectrum is a combination of multiple emitting sources, mostly stars and ionized gas. To study stars and gas individually from spectral information, they need to first be decoupled. Luckily most emitting sources have clear observational distinctions. For example, ionized gas emits as a set of distinct emission lines at fixed wavelength defined by atomic physics, whereas stellar populations dominate the continuum. To decouple the two, one must assume that the stellar emission is the result of a single (or a combination of several different single) stellar populations (SSP).

It is possible to generate synthetic stellar populations based on principal properties (such as star-formation rate, initial mass function , stellar isochrones, etc.) to try to determine what theoretical populations make up the observed spectral energy distribution. However, variations in the factors that direct stellar population evolution can lead to degeneracies, particularly as a result of age, metallicity, and extinction (Worthey, 1994; Gil de Paz & Madore, 2002). Most galaxies have complex star-formation histories, with complex dust distributions and episodes of activity leading to multiple populations with differing ages and metallicities. A wide wavelength range can help probe different populations of stars and minimize any degeneracies, another benefit of the MaNGA survey compared to other IFS surveys. Lastly, the stellar continuum needs to be redshifted to account for kinematic affects, as well as smoothed and broadened for any velocity dispersion affects and corrected for dust attenuation (Sánchez et al., 2016a). The completed modelled stellar spectrum is subtracted from the observed spectrum, leaving only emission from the ionized gas.

PIPE3D is a spectroscopic analysis pipeline that uses FIT3D to fit SSP models to spatially resolved data from IFS surveys, including CALIFA (Sánchez et al., 2012b), SAMI (Croom et al., 2012), and MaNGA (Bundy et al., 2015). FIT3D[1] is an SSP analysis tool introduced in Sánchez et al. (2006), updated for PIPE3D to use a Monte-Carlo (MC) procedure to iterate over randomized versions of the input spectrum, providing mean weights for different populations in the stellar component. By using MC, FIT3D can also provide uncertainties on the weights and the final model (Sánchez et al., 2016a). Kinematics are derived prior to the linear combination of stellar populations, using a pre-defined range of possible values. See Sánchez et al. (2016a,b) for a thorough description of FIT3D procedure.

Every emission line in the clean spectrum is fit with a Gaussian function and a low order polynomial to fit the continuum. The Gaussian function accounts for the velocity, velocity dispersion, and intensity of the emission line. The polynomial function is a combination of linear components. The non-linear components are fit using a random exploration of a range of values with an initial guess value for each. During this pseudo-random exploration, a least-squares linear regression is used to derive the linear parameters of the Gaussian (intensity) and the polynomial. As a result of these methods, PIPE3D provides both the emission line parameters needed to generate SFR and metallicity (see Section 2.2 for further discussion), as well as stellar population properties like stellar mass surface density (Σ_*), which are crucial

---

[1] http://www.astroscu.unam.mx/sfsanchez/FIT3D

to our analysis. A summary of the average stellar population properties is provided in Table 2.1.

Average Stellar Population Properties per spaxel	Units
V-band image	10^{-16}erg/s/cm^2
Continuum segmentation map	none
Continuum dezonification	none
Median intensity within full analyzed wavelength range	10^{-16}erg/s/cm^2
Standard deviation from median intensity	10^{-16}erg/s/cm^2
Luminosity weighted age of stellar population	Gyr
Mass weighted age of the stellar population	Gyr
Error of the age of the stellar population	Gyr
Luminosity weighted metallicity of the stellar population	none
Mass weighted metallicity of the stellar population	none
Error of the metallicity of the stellar population	none
Average dust attenuation of the stellar population	mag
Error of the average dust attenuation of the stellar population	mag
Velocity of the stellar population	km/s
Error in the velocity of the stellar population	km/s
Velocity dispersion of the stellar population	km/s
Error in the velocity dispersion of the stellar population	km/s
Average mass-to-light ratio of the stellar population	$\log M_\odot/L_\odot$
Stellar mass surface density per pixel without dust correction	$\log M_\odot$/spaxels
stellar mass surface density per pixel with dust correction	$\log M_\odot$/spaxels

Table 2.1: The average stellar population properties derived from multi-SSP analysis on the stellar continuum, using PIPE3D. Source: `https://data.sdss.org/datamodel/files/MANGA_PIPE3D/MANGADRP_VER/PIPE3D_VER/PLATE/manga.Pipe3D.cube.html`.

2.2 Custom Dataproduct Extension

The majority of dataproducts used in this study are taken from the PIPE3D spectral analysis datacubes (see Section 2.1.1 for details), although Σ_{SFR}, metallicities, and half-light radii are determined outside the PIPE3D framework.

SFRs are computed for each spaxel as part of a custom PIPE3D extension produced by Sebastian Sánchez, in which the flux intensity of Hα provided by PIPE3D is converted to a luminosity (ergs/sec) using the following equation:

$$L_{H\alpha} = F_{H\alpha} \cdot 4 \cdot \pi \cdot D_L^2 \tag{2.1}$$

where D_L is the luminosity distance and $F_{H\alpha}$ is the dust-corrected flux intensity of Hα. The attenuation by dust is computed using the Cardelli et al. (1989) Milky-Way-like extinction curve (assuming Hα/Hβ is 2.86, Osterbrock & Ferland 2006). The derived attenuation, along with the Cardelli et al. (1989) extinction curve, are used to correct for dust attenuation in emission lines at every wavelength. $L_{H\alpha}$ is then converted to SFR using the Salpeter IMF (see Section 1.1.2 for details). The star-formation rate surface density ($\Sigma_{\rm SFR}$ $M_\odot$yr^{-1}kpc^{-2}) in each spaxel is calculated by dividing SFR$_{H\alpha}$ by the area of each spaxel in kpc^2 (first converting the area of each spaxel in arcseconds squared (0.25 arcsec^2) to the area in kpc^2 assuming an arcsecond to kpc conversion based on the galaxy's redshift).

The customized PIPE3D extension also computes the metallicity of each spaxel using the Marino et al. (2013a) O3N2 technique, which minimizes extinction affects while still using strong lines in the optical ([OIII]λ5007/Hβ)/([NII]λ6583/Hα). O3N2 was first introduced by Pettini & Pagel (2004). However, the Marino et al. (2013b) calibration uses estimations for the oxygen abundance based on photoionization models made for the high-metallicity range (Kewley & Ellison, 2008). The Marino et al. (2013b) O3N2 was re-calibrated using direct measurements of oxygen abundances of HII regions (Pilyugin et al., 2012; Pérez-Montero & Contini, 2009) and integral field spectroscopy.

The r-band half-light radius, i.e. the effective radius (R_e), for each target is collected from the Simard et al. (2011) catalogue of bulge+disk decompositions for SDSS. The Simard et al. (2011) catalogue introduced the GIM2D pipeline, which first deblends galaxies from the SDSS r-band photometric image using the source extraction software SExtractor . Bulge and disk decomposition is then performed on the g-band and r-band deblended images, and a semimajor half-light radius is generated by collapsing the bulge and disk components onto their major axes and summing them into a one-dimensional profile.

2.3 Defining $\Delta\Sigma_{\rm SFR}$ and Δ O/H

To quantify offsets in quantities such as $\Sigma_{\rm SFR}$ and O/H within each spaxel that are the result of an interaction, a set of control samples is required for comparison. As a result of the strong correlation between total stellar mass and both SFR and O/H (e.g. Brinchmann et al. 2004; Tremonti et al. 2004), it is already common procedure to measure global offsets in SFR and O/H at fixed M_* (e.g. Ellison et al. 2008a;

Scudder et al. 2012; Patton et al. 2013). However, there are also “resolved” relations on the kpc-scale between Σ_* and both $\Sigma_{\rm SFR}$ (e.g. Sánchez et al. 2013; Cano-Díaz et al. 2016; González Delgado et al. 2016; Hsieh et al. 2017) and O/H (e.g. Rosales-Ortega et al. 2012; Sánchez et al. 2013; Barrera-Ballesteros et al. 2016). Therefore, offsets in $\Sigma_{\rm SFR}$ and O/H can be computed for individual spaxels, using a similar method to the global offset calculations. The spaxel offset method was introduced by Ellison et al. (2018a), in which MaNGA was utilized to examined SFR enhancement and deficit profiles as a function of main sequence offset.

In order to compute offsets, a sample of star-forming spaxels from MaNGA is selected using the Kauffmann et al. (2003) criteria for classifying star-forming vs AGN emission based on the relationship between emission line ratios [NII]λ6584/Hα and [OIII]λ5007/Hβ (column 1 of Figure 2.4). Spaxels are also required to have a signal-to-noise ratio greater than 3 in all four emission lines to ensure reliable measurements of O/H and Σ_{SFR}. There are ~900,000 spaxels in MaNGA DR14 that satisfy these criteria (Fig. 2.5). There are other popular methods for determining whether an emission in a spectrum is star-forming or not. For instance, Kewley et al. (2001) establishes an extreme starburst classification line (Figure 2.4, column 1, red dashed line) which is inclusive of all starbursts galaxies, even if they have a mix of AGN contribution as well as star-forming emission. One can also use other emission lines besides [NII]λ6584, such as [SII]λ6717 and [OI]λ6300 (Kewley et al., 2006). The [SII]λ6717 and [OI]λ6300 helps distinguish Seyfert emission (lower luminosity AGN) and LINER emission (low-ionization nuclear emission-line region, similar to Seyfert emission but with much stronger low-ionization lines), as well as segregate the star-forming emission from these two categories. Though the Kauffmann et al. (2003) criteria are adopted for this study, checks were made throughout analysis that the results could be reproduced with other emission line diagnostics.

A collection of control spaxels, to be used for comparison to a particular spaxel of interest, is then chosen to match Σ_* within 0.1 dex (Fig. 2.5), which defines the resolved star-forming main sequence and resolved mass-metallicity relation. The resolved mass-metallicity relation is independent of the total stellar mass, except for the lowest mass galaxies ($M_* \lesssim 10^{9.5}$) where the relation is biased towards lower metallicities (Barrera-Ballesteros et al., 2016). To account for these exceptions, the control sample is also matched to M_* within 0.1 dex. Finally, the control sample is matched within 0.1 R_e, given that within each galaxy there is gradient of $\Sigma_{\rm SFR}$ and O/H dependent on the radius (Rupke et al., 2010; Montuori et al., 2010; Perez et al.,

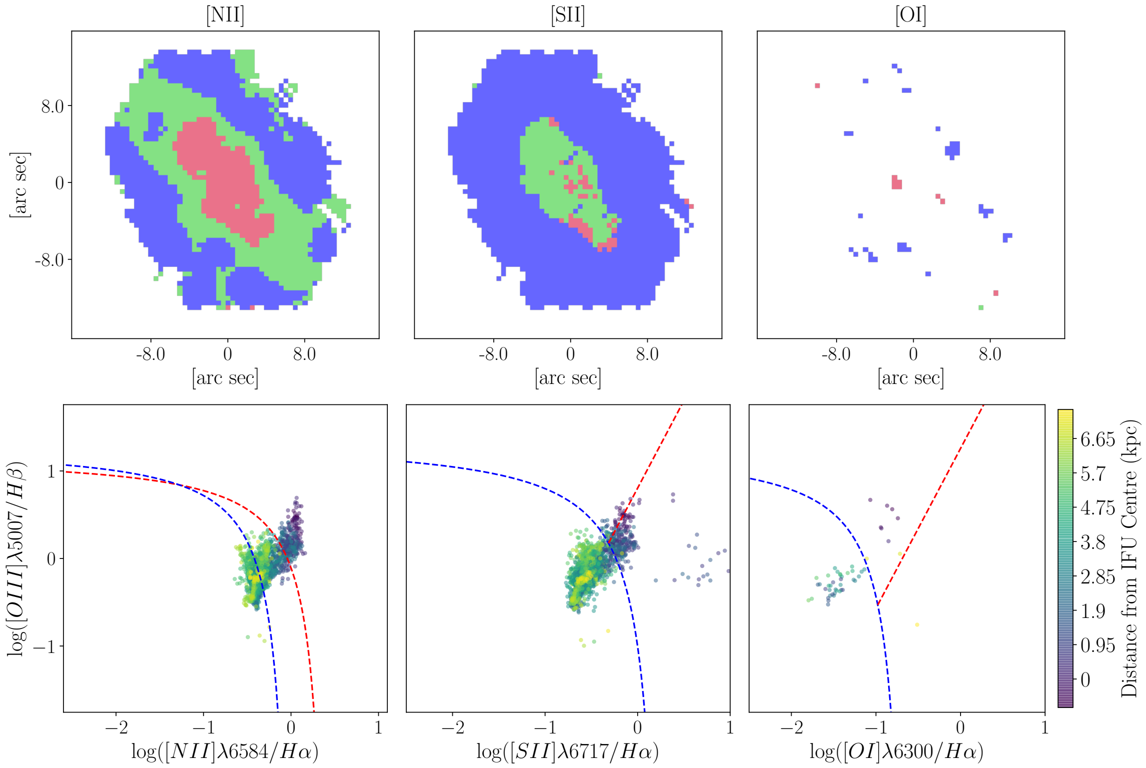

Figure 2.4: The top row shows the [NII], [SII], and [OI] flux (10^{-16}erg/s/cm^2) coloured by the source of the emission flux (blue spaxels are star-forming, red and green spaxels have contribution from AGN). The bottom row shows the three Baldwin, Phillips & Telervich (BPT) diagrams used to classify emission sources, with each spaxel plotted based on emission line ratios and colour-coded by the distance from the centre of the IFU. Column 1: BPT classification based on the (Kauffmann et al., 2003)(blue-dashed) and (Kewley et al., 2001)(red-dashed) lines, where emission originates from star-formation (blue), AGN (red), or a combination of the two (green); Column 2: BPT classification based on the [SII]λ6717/Hα ratio, with the red line differentiating between Seyfert (left, red spaxels) and LINER (right, green spaxels) emission (Kewley et al., 2006); Column 3: BPT classification based on the [OI]λ6300/Hα ratio, with the red line differentiating between Seyfert (left, red spaxels) and LINER (right, green spaxels) emission (Kewley et al., 2006).

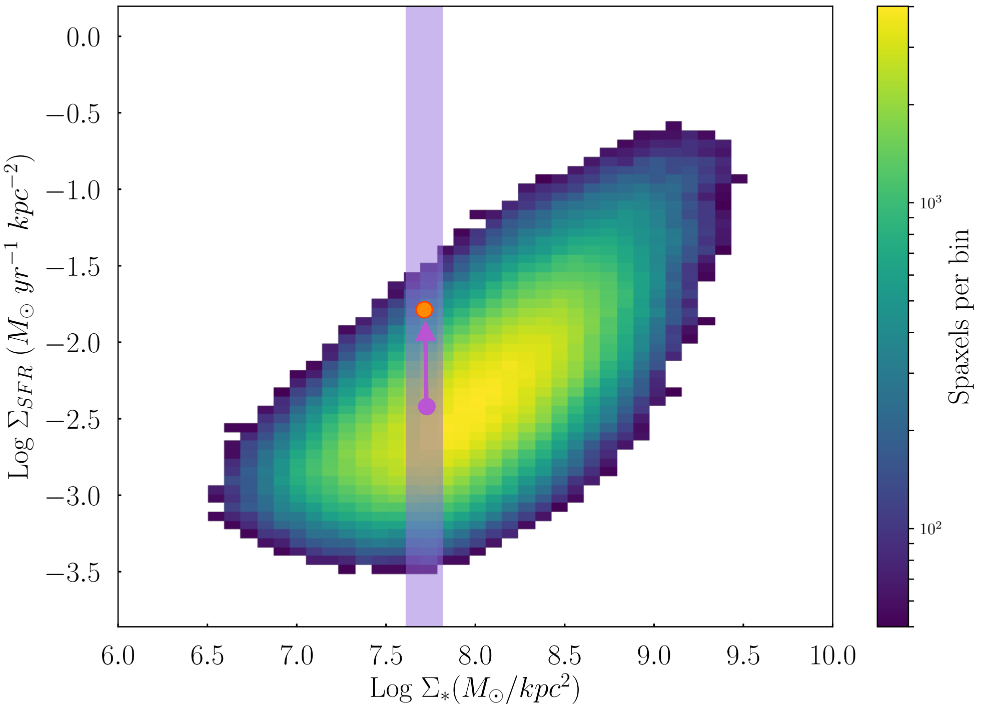

Figure 2.5: The Σ_{SFR} - Σ_* relationship for all star-forming spaxels in MaNGA. An example control median spaxel (purple circle) is determined for a target spaxel (orange circle) within a M_* bin, with the purple arrow representing the enhancement of the target spaxel from the control ($\Delta\Sigma_{\mathrm{SFR}}$).

2011). The median of the control sample of galaxies is then computed, and used to determine any enhancement or suppression in Σ_{SFR} and O/H for the spaxel of interest (see Figure 2.5).

Thus any enhancement or suppression in SFR (compared to a control matched in Σ_*, M_* , and R_e) is quantified as

$$\Delta\Sigma_{\mathrm{SFR}} = \log \Sigma_{\mathrm{SFR,spaxel}} - \log \Sigma_{\mathrm{SFR,control}}, \tag{2.2}$$

and enhancement or suppression in O/H as

$$\Delta\mathrm{O/H} = \log \Sigma_{\mathrm{O/H,spaxel}} - \log \Sigma_{\mathrm{O/H,control}}. \tag{2.3}$$

2.4 Galaxy Merger Classification

Galaxy Classification is a very subjective process, and can be highly dependent on the classification methodology, the quality of the sample, and the classifier themselves. There are quantitative methods of merger classification often used to automate any selection by morphology. Conselice et al. (2003) invented a method to calculate the concentration (C), asymmetry (A), and smoothness (S) of a galaxy to quantify galaxy morphology from flux information. A particular sub-volume of CAS space is highly probable to contain post-merger or merging galaxies. However, CAS parameters are strongly correlated with (B-V) colour and Hubble type, and are biased towards galaxies that just underwent first passage or final coalescence (Lotz et al., 2008; Hambleton et al., 2011). Shape asymmetry is a similar morphological parameter, but optimized to measure faint features that don't contribute significantly to the flux. Instead of the light distribution, a binary detection mask is used to measure the asymmetry in the shape alone (Pawlik et al., 2016). The Gini (G) coefficient, originally developed in economics to measure wealth disparity, measures the relative distribution of flux intensity within a galaxy (Abraham et al., 2003). It is similar to concentration in this way, but does not assume the geometric centre is the centre of the distribution. G is often paired with the morphology parameter M_{20}, which quantifies the second order moment of the brightest 20% of the galaxy (Lotz et al., 2004). Tidal features and more than one nuclei in an object result in a larger M_{20}, making it the ideal parameter for identifying galaxies in the late stages of an interaction (Lotz et al., 2004). The combination of G and M_{20} is more sensitive to interactions with large mass ratio than the asymmetry parameter (Lotz et al., 2010b).

Visual classification can also be done by hand if the sample is reasonably sized, or many volunteers are willing to classify thousands of galaxies. Galaxy Zoo[2] utilizes crowd sourcing for classification, providing a brief tutorial to volunteers for how mergers are visually distinct, and then showing one target to many volunteers to collect a sample of classifications. A weighted merger vote fraction f_m is determined for each galaxy, which quantifies the confidence that the galaxy of interest is currently undergoing an interaction ($f_m =$ the number of merger classifications / the total number of classifications) (Darg et al., 2010). Galaxy Zoo faces many of the same struggles an individual classifier would: How strongly perturbed must a galaxy be to still qualify as a merger? How does one account for the depreciating image quality as redshift

---

[2] https://www.zooniverse.org

increases? As a result Galaxy Zoo has a significant number of borderline cases where $0 < f_m < 0.4$.

There is growing interest in using machine learning to identify galaxy mergers. Machine learning has already been employed to differentiate galaxy Hubble types (De La Calleja & Fuentes, 2004; Banerji et al., 2010). Convolutional Neural Networks (CNN) have also been used to identify irregulars, disks, and spheroids more effectively than CAS methods (Huertas-Company et al., 2015). The training set provided to a CNN determines the success of the classifications. CNN's can be trained on one survey and applied to another with some fine-tuning, but in order to attain the vast test sample size necessary, many turn to galaxy simulations to assist in CNN training (Domínguez Sánchez et al., 2019).

A CNN trained on SDSS data can identify mergers in an SDSS test sample with 91.5% accuracy, but when the SDSS test sample is passed through a network trained on EAGLE simulations only 64.6% of galaxies are correctly classified (Pearson et al., 2019). Though there is still much to be explored and optimized concerning CNN merger classification, recent studies are optimistic that future surveys could forgo individual classifiers and morphology parameters in favour of a machine learning network.

Training a CNN to select galaxy mergers from MaNGA could be a separate project within itself, while utilizing a catalogue of classifications like that in Galaxy Zoo would require individual review to handle borderline cases. Given the approachable size of the 14th data release (DR14) of MaNGA, I chose to visually classified all ∼2700 galaxies in MaNGA, identifying post-merger galaxies using the following criteria:

1. Tidal features, such as a tail, connected to no obvious companion.
2. Multiple shells around the nucleus.
3. Catastrophically asymmetric morphology.
4. Drastic colour and morphology variation within the galaxy.

Out of the 2680 galaxies in MaNGA DR14, only those with global properties computed in the PIPE3D value added catalogue are considered (Sánchez et al., 2016a,b), of which there were 2642. The others encounter critical failures where global properties could not be computed. Of this subset, I identified 48 post-merger galaxies

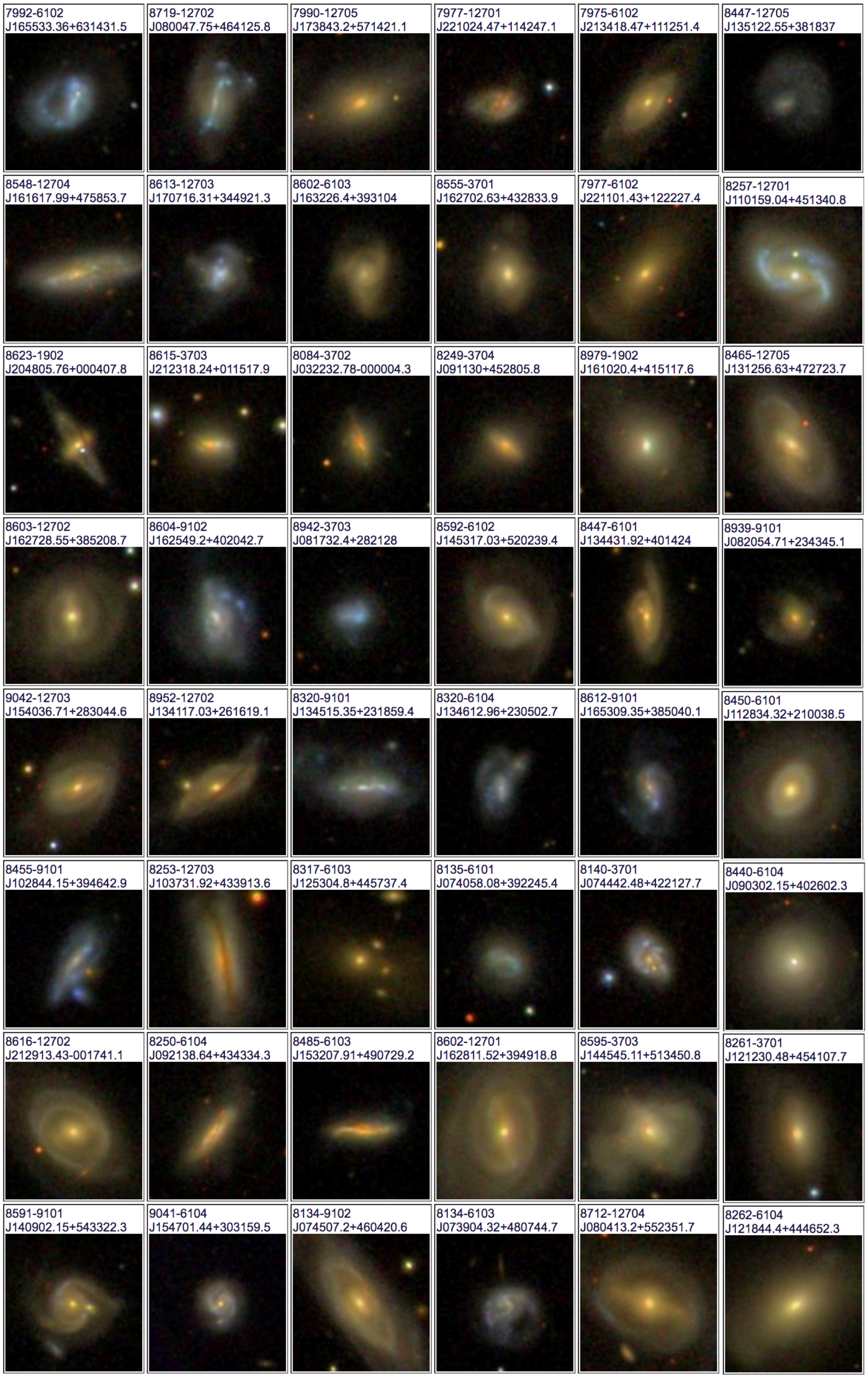

Figure 2.6: All post-merger galaxies identified in data release 14 of MaNGA. Source: http://skyserver.sdss.org/dr15/en/tools/chart/list.aspx.

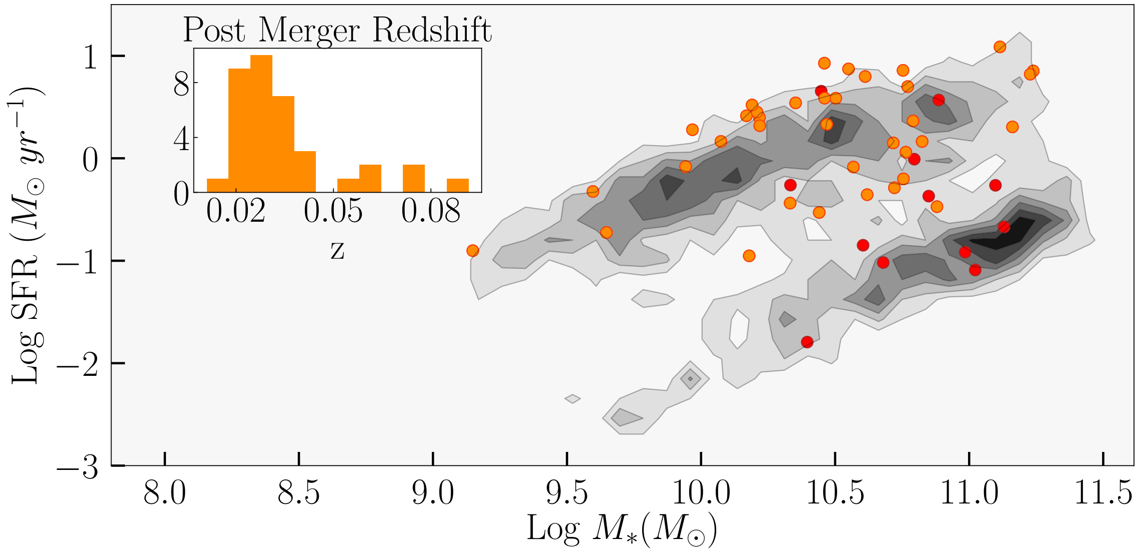

Figure 2.7: SFR-mass distribution of the full DR14 MaNGA data set (grey contours), with the post-merger galaxies overlaid as orange points (red points represent post-mergers that were dropped due to incomplete $\Delta\Sigma_{\mathrm{SFR}}$ or Δ O/H maps). The redshift distribution of the final post-merger sample is provided in the inset.

(1.8% of the original sample). An image of all post-merger galaxies is provided in Figure 2.6.

Twelve of the 48 post-merger galaxies were removed because they had no star-forming spaxels (defined by the Kauffmann et al. (2003) star-forming emission criteria) for which viable Σ_{SFR} could be measured. The distribution of the final sample of 36 post-merger galaxies (as well as the 12 withdrawn), with respect to the rest of the MaNGA sample, is provided in Figure 2.7. It is unfortunate that the 12 removed galaxies represent some of the lowest SFR values in the post-merger sample. This could limit our understanding of a particular class of mergers (between two passive galaxies, or representing a merger-triggered quenching process) (Patton et al., 2013).

2.5 Results

Maps of $\Delta\Sigma_{\mathrm{SFR}}$ and Δ O/H are generated for all post-merger galaxies, a sample of which is shown in Figure 2.8. The majority of post-mergers exhibit a central enhancement in star-formation, as expected from global spectroscopic studies (Ellison et al., 2013). The star formation enhancement is clumpy, and often distributed asymmetrically across a galaxy's surface, similar to the SFR distribution.

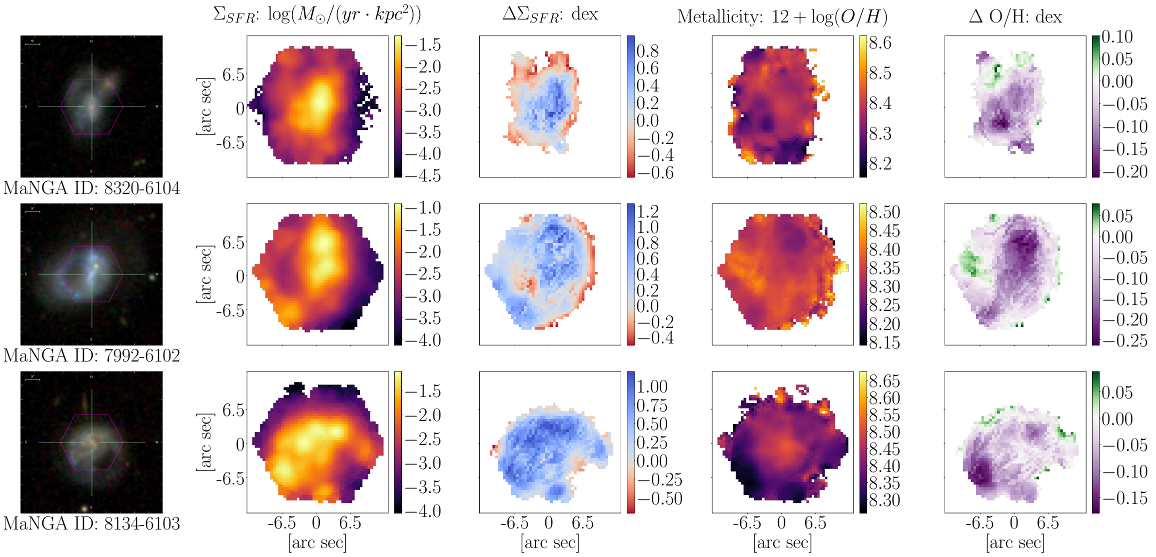

Figure 2.8: MaNGA data products and offset maps for 3 example post-merger galaxies. Column 1: SDSS gri-image with MaNGA IFU footprint overlaid in magenta. Column 2: Map of Σ_{SFR} as determined by PIPE3D. Column 3: Offset in Σ_{SFR} ($\Delta\Sigma_{\mathrm{SFR}}$) from the resolved main sequence; enhancements are shown in blue and deficits in red. Column 4: Map of O/H measurements from O3N2 diagnostic. Column 5: Offset in metallicity from the resolved mass-metallicity relation (Δ O/H); enhancements are shown in green and deficits in purple. Some spaxels are lost in the matching process for offset maps.

2.5.1 $\Delta\Sigma_{\mathrm{SFR}}$ Profiles

My objective for the post-mergers study is to quantify the spatially resolved variations in post-mergers, compared to "regular" star-forming galaxies. Although maps of $\Delta\Sigma_{\mathrm{SFR}}$ and Δ O/H provide fascinating insights into the distribution of starbursts and low-metal regions of post-mergers, it is difficult to combine spatial distribution maps for all post-mergers into a more generalized behaviour. To determine the azimuthally average behaviour of a post-merger, the spatially resolved properties of all 36 targets must be combined. A common method for averaging behaviour with resolved surveys is to create radial profiles: averaging IFS maps azimuthally to examine each case, and then combining all post-merger spaxels into one radial profile to generalize behaviour (e.g. Barrera-Ballesteros et al. 2015; Chown et al. 2019; Ellison et al. 2018a; Spindler et al. 2018).

In Figure 2.9 displays radial profiles for each post-merger galaxy (coloured according to the global ΔSFR). Profiles are constructed out to the radius at which point less than 5% of the total spaxel count would be beyond that R_e (see appendix A.2 for details). As the sample of $\Delta\Sigma_{\mathrm{SFR}}$ maps showed, the majority of post-mergers are centrally enhanced, as expected from theoretical work such as Barnes & Hernquist (1991); Mihos & Hernquist (1996); Di Matteo et al. (2005); Springel & Hernquist (2005); Cox et al. (2006); Montuori et al. (2010); Torrey et al. (2012). This is always true for galaxies with a $\Delta\mathrm{SFR} > 0$. However, the keen eye will notice that for galaxies where $\Delta\mathrm{SFR} < 0$, there is no information about the profile until $\sim 0.3R_e - 0.5R_e$. The central spaxels for $\Delta\mathrm{SFR} < 0$ galaxies tend to be dominated by AGN or composite emission, so no trustworthy SFR measurements can be made (see Figure 2.10 as an example).

Figure 2.9 clearly demonstrates that even though the majority of post-mergers are centrally enhanced, there is more variable behaviour at the very outer edges. Each of the bold profiles represents one of the post-mergers in Figure 2.8. The galaxy in the first row of Figure 2.8 shows an enhancement in SFR in the centre of the galaxy, and a suppression in SFR in the very outer radii. This behaviour is reflected in its radial profile, which has $\Delta\Sigma_{\mathrm{SFR}}$ >0 until $R_e \sim 1$, where $\Delta\Sigma_{\mathrm{SFR}}$ dips to below zero. A handful of other galaxies behave in a similar fashion. Some of the post-mergers have $\Delta\Sigma_{\mathrm{SFR}} > 0$ out to $2R_e$, such as the third row of Figure 2.8. It could be that $\Delta\Sigma_{\mathrm{SFR}}$ profiles that are enhanced to the furthest measurable radii represent galaxies that have undergone an interaction more recently, given the starburst is predicted to

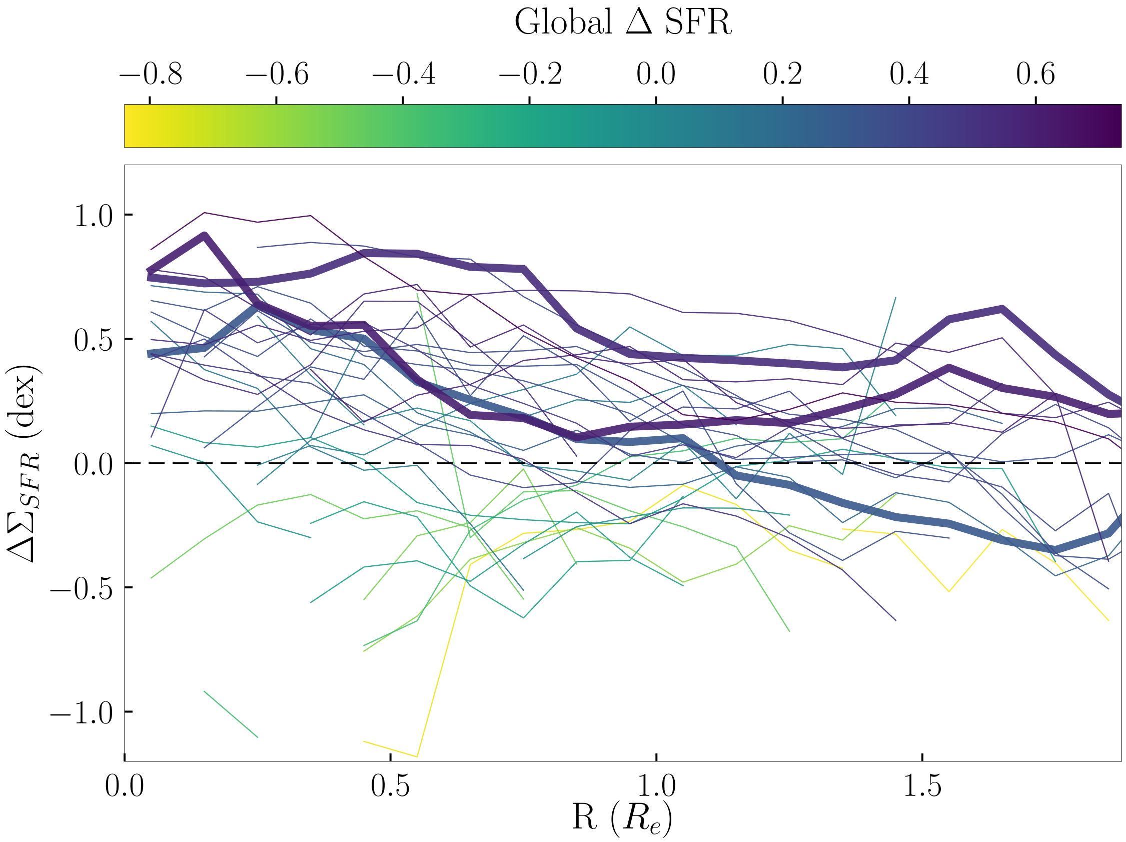

Figure 2.9: All $\Delta\Sigma_{\mathrm{SFR}}$ profiles as a function of effective radius, coloured according to the global ΔSFR of the host galaxy. Bold lines represent galaxies from Fig.2.8 (Column 1: suppressed at 1.5 R_e; Column 2: slightly enhanced at 1.5 R_e; Column 3: greatly enhanced at 1.5 R_e).

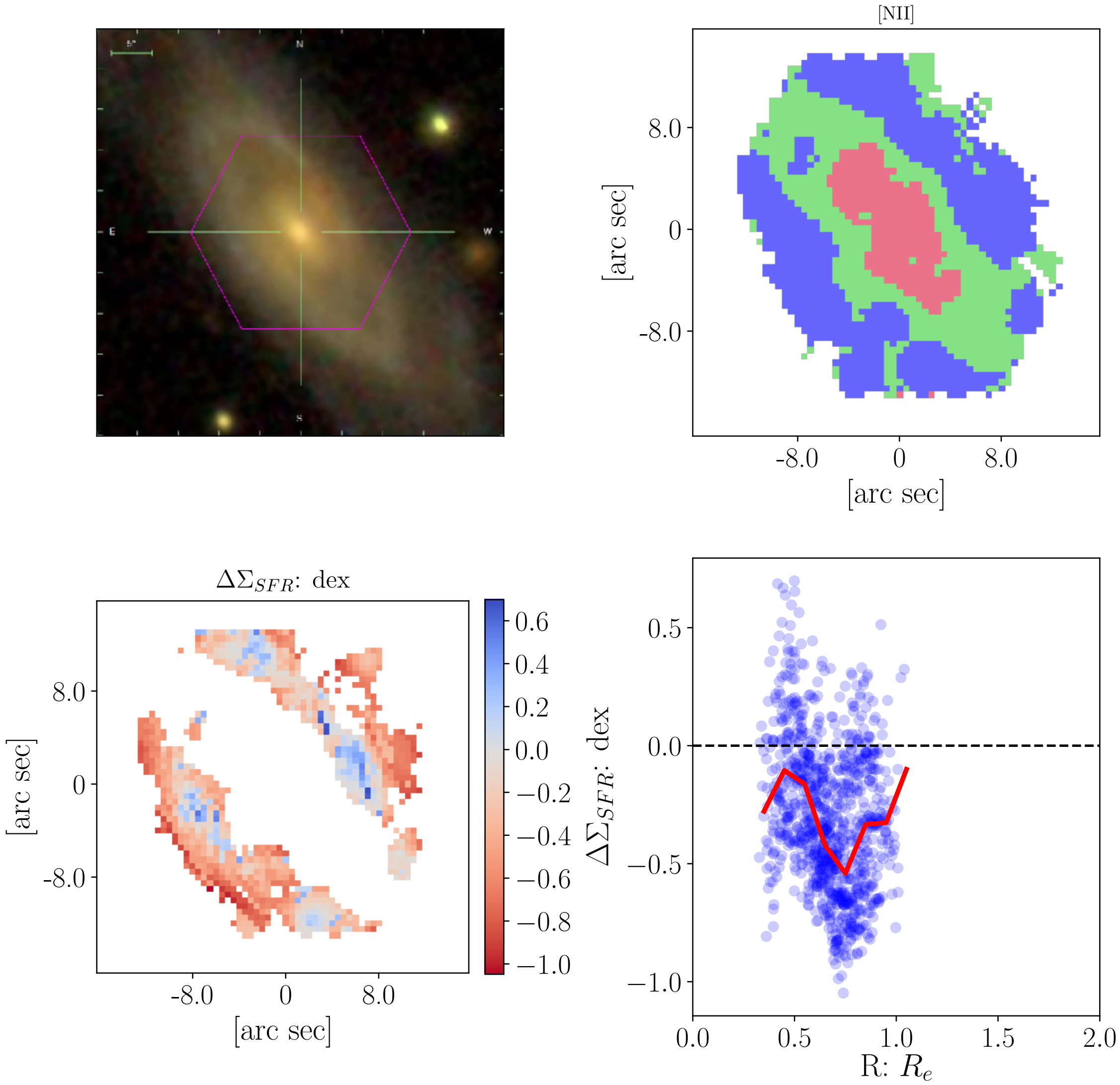

Figure 2.10: Column 1: the gri-image of the target galaxy provided by SDSS; column 2: BPT segmentation of the galaxy based on the Kauffmann et al. (2003) criteria, red is AGN dominated, green is composite, and blue is star-forming; column 3: $\Delta\Sigma_{\rm SFR}$ for star-forming spaxels, blue represents an enhancement in SFR, red a deficit; column 4: All spaxel $\Delta\Sigma_{\rm SFR}$ values plotted against R_e, with the radial profile fit over those points.

be strongest just at the moment of coalescence (Cox et al., 2008; Torrey et al., 2012; Moreno et al., 2019). It could also be that variations in the extended radial profile are the result of averaging post-merger with different progenitor qualities. As discussed previously, mass ratio (Cox et al., 2006, 2008; Scudder et al., 2012), gas fraction (Bournaud et al., 2011; Perez et al., 2011; Scudder et al., 2015; Fensch et al., 2017), and interaction orientation (Di Matteo et al., 2007; D'Onghia et al., 2010; Moreno et al., 2015) are predicted to influence the strength of a post-coalescence starburst.

The galaxy in row 2 of Figure 2.8 exhibits odd behaviour in its radial profile where the centre has enhanced SFR, the profile dips towards $1 \sim R_e$ as if the star-formation is returning to normal, but then increases from $\sim 1.2R_e - 2R_e$. This is due to the highly disturbed morphology of the post-merger. Examining the gri-image of this highly disturbed galaxy (Figure 2.8, row 2, column 1), there is an extended tidal tail on one side of the galaxy. This leads to a highly asymmetric SFR map (Figure 2.8, row 2, column 2), indicating that the tidal disturbance is a major location for star-formation activity. This is reflected in the $\Delta\Sigma_{\mathrm{SFR}}$ map (Figure 2.8, row 2, column 3), where the starburst nature of the tail can be seen at the very edge of the IFU. However, upon examination of the other side of the galaxy, there is clearly a suppression at the very outer edge of the galaxy where the tidal feature does not exist.

The complexity of the morphology and star-formation activity is lost when a map is compressed (including radial and azimuthal information) into a radial profile. Post-mergers are a particularly problematic case for radial profiles, given their highly disturbed morphologies there are bound to be many cases like that of 7992-6102. This complexity must be considered when interpreting the median radial profiles.

The general behaviour of post-merger galaxies is exhibited using spaxels from all of the post-merger galaxies in the construction of one radial profile (the teal profile in Figure 2.11). The profile extends to the point where less than 5% of the total spaxel count would be beyond that R_e (see appendix A.2 for details). Generally, post-mergers are enhanced in the central region up to ~ 0.5 dex, that enhancement decreases to ~ 0.1 dex but is present out to $2R_e$.

The median post-merger behaviour is dominated by galaxies where $\Delta\mathrm{SFR} > 0$, which make up approximately two-thirds of the entire post-mergers sample. The smaller sample of $\Delta\mathrm{SFR} < 0$ galaxies generally have $\Delta\Sigma_{\mathrm{SFR}} < 0$, which is consistent with the assumption that local relationships shape global relationships (Barrera-Ballesteros et al., 2016). Galaxies that are above the star-forming main sequence have enhanced SFR throughout, whereas galaxies that are generally below the star-

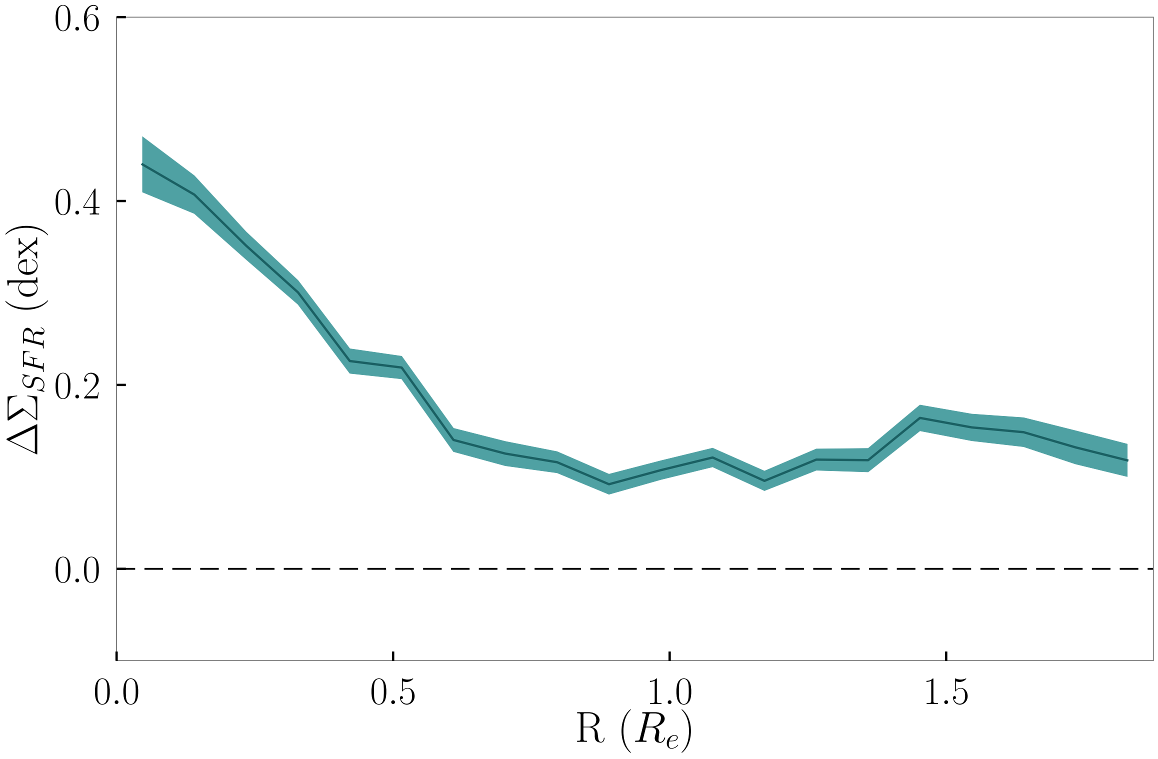

Figure 2.11: Median $\Delta\Sigma_{\mathrm{SFR}}$ profile of all post-merger spaxels. The width of the line represents the standard deviation in $\Delta\Sigma_{\mathrm{SFR}}$ in that radius bin, divided by the square root of the number of spaxels in that bin.

forming main sequenced have a deficit in SFR compared to main-sequence galaxies. Galaxies with ΔSFR < 0 are expected to have central $\Delta\Sigma_{\rm SFR}$ either similar to or less than the $\Delta\Sigma_{\rm SFR}$ at outer radii, an effect of the inside-out quenching experienced by nearby galaxies (Ellison et al., 2018b). Contrary to what is expected, post-mergers with ΔSFR < 0 have central $\Delta\Sigma_{\rm SFR}$ equal to zero, such that all post-mergers have a greater SFR in the centre than in the outskirts. The variation between $\Delta\Sigma_{\rm SFR}$ profiles for isolated and merging ΔSFR < 0 may indicate that galaxies in the final stage of coalescence experience a different quenching process, from the outside in. However, such a conclusion comes with a caveat that galaxies with the lowest ΔSFR tend to be dominated by AGN in the centre, and thus do not contribute to the central radial profile. Thus the central $\Delta\Sigma_{\rm SFR}$ behaviour may be dominated by galaxies with the highest ΔSFR for that bin, and not represent the spaxels at $\sim 1R_e$ that belong to galaxies with lower ΔSFR.

Radial profiles are constructed as a function of effective radius (R_e), a Petrosian quantity that translates well between different sized galaxies. The halfway point between the centre and what we may define as the "edge" of a galaxy is always $2R_e$ based on a Sérsic fit to the galaxy, in physical units anywhere between 2 - 25 kpc depending on the galaxy. When the radial profiles are recomputed using physical units, or arcseconds, the results differ slightly. At the outer most radii, the SFR can be suppressed (see Figure 2.12a), or at least have $\Delta\Sigma_{\rm SFR}$ =0 (see Figure 2.12b). The radial profile as a function of physical units differs because the outermost radii are dominated by the largest galaxies, which extend to the largest kiloparsecs, leading to a greater uncertainty beyond 10 kpc. Combining spaxels by arcseconds leads to similar issues, where differences in galaxy redshift leads to the same arcsecond value corresponding to varying physical units and R_e values. Similar arguments can be made for variable behaviour in the Δ O/H profiles (see Figure 2.13), though the variations in the Δ O/H profiles are not as drastic. The only place radius values in kpc/arcseconds are trustworthy is in the very centre of the galaxy, where there is an enhancement in SFR similar to that produced using R_e.

Our findings are in conflict with the results from the CALIFA mergers study by Barrera-Ballesteros et al. (2015), who found enhanced central SFRs, but mild to suppressed SFRs over extended scales. There are several possible sources for this disparity, most of which stem from the different methods of our studies. First of all, Barrera-Ballesteros et al. (2015) select mergers over a large timescale, from pairs with separations as large as $\sim$ 150 kpc, to post-mergers. In contrast, my study is limited

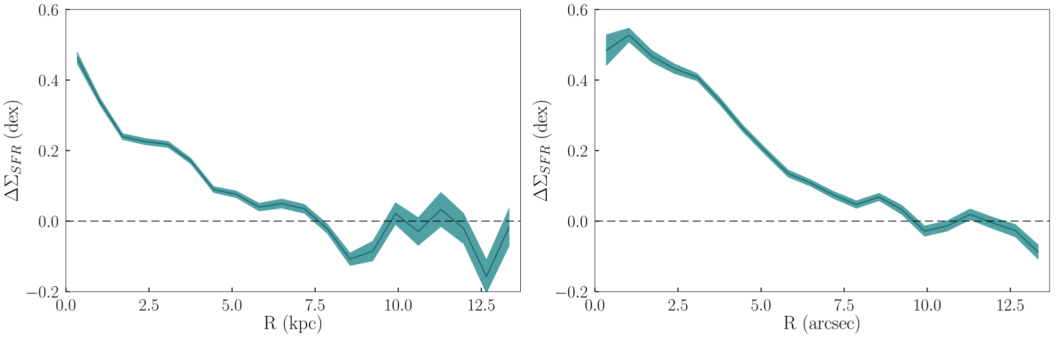

(a) kpc

(b) arcsec

Figure 2.12: Alternative radial bins for $\Delta\Sigma_{\mathrm{SFR}}$, the width of the line represents the standard deviation in $\Delta\Sigma_{\mathrm{SFR}}$ in that radius bin, divided by the square root of the number of spaxels in that bin.

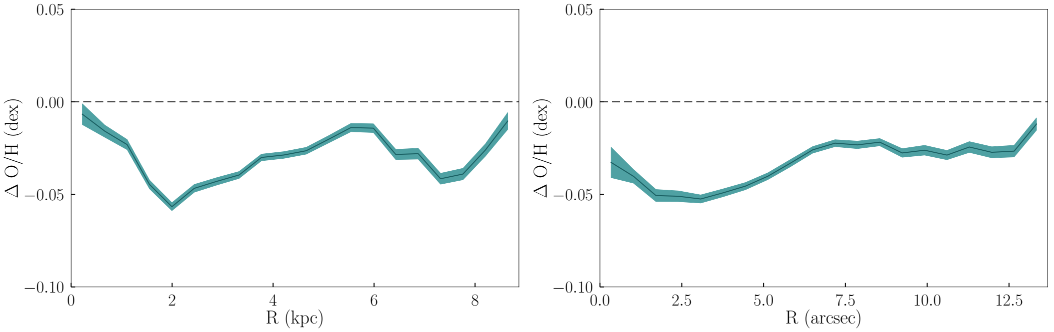

(a) kpc

(b) arcsec

Figure 2.13: Alternative radial bins for Δ O/H , the width of the line represents the standard deviation in Δ O/H in that radius bin, divided by the square root of the number of spaxels in that bin.

to one evolutionary stage to restrict the timescale of the interaction, focusing on galaxies with still-visible tidal features, to indicating a recent interaction. There can be different spatial distributions of star-formation in the pre- and post-coalescence phase (e.g. García-Marín et al. 2009) that would lead to different results between our respective studies. Barrera-Ballesteros et al. (2015) also measure spatial distributions differently, rather than using radial profiles they bin their IFU data into two apertures to study the central and extended star-formation. Lastly, CALIFA also has a different spatial coverage than MaNGA, with observations extending out to 2.5 R_e (Sánchez et al., 2012b).

My results are in agreement with smaller studies such as Cortijo-Ferrero et al. (2017) and García-Marín et al. (2009), who found extended enhanced SFR in interacting pairs. The work herein shows, for the first time, that this enhancement persists beyond the pairs phase and is measurable well into coalescence. Smaller studies have also predicted that star-formation in mergers would be clumpy and often offset from the centre (Elmegreen et al., 2006), which is the case for the most morphologically disturbed galaxies. Most simulations have predicted enhanced and extended star-formation activity as well (Powell et al., 2013; Renaud et al., 2014). The alignment of the simulated interaction, and whether the galaxy was the more/less massive in a pair, influences whether the galaxy experienced suppression, regular, and slightly enhanced star-formation between ~ 1 kpc and ~ 10 kpc (see Figure 1.7). Perhaps the variable behaviour seen in the outskirts of my post-merger sample is capturing multiple progenitor scenarios like those described in simulations (Moreno et al., 2015).

2.5.2 Δ O/H Profiles

Until recently only simulations were able to examine changes in metallicity at outer radii. Theoretical studies like those performed by Rupke et al. (2010), Perez et al. (2011), and Sillero et al. (2017) showed that metallicity dilution in mergers can extend out to 2-3 disk scale lengths. These studies also suggest that metallicity can be enhanced on larger scales (leading to a flattened gradient overall). MaNGA does not extend far enough to check the largest scales, however it can be used to validate metallicity dilution to 2 R_e.

The analysis used in Section 2.5.1 is repeated with the Δ O/H values, first constructing radial profiles for each post-merger individually (Figure 2.14). Most galaxies appear to have a suppression in metallicity, which correlates with an inflow of low-metal gas to fuel the central star-formation activity seen in Figure 2.9. The median Δ O/H behaviour is then computed for all post-merger spaxels in the same method as $\Delta\Sigma_{\mathrm{SFR}}$ (Figure 2.15). On average post-mergers have Δ O/H values that are suppressed by ~ -0.04 dex out to $2R_e$. The uncertainty on the individual spaxel metallicities are ~ -0.1 dex (Marino et al., 2013a), however the statistical error on the median of all spaxels is quite small in comparison (given each radius bin has ~ 1000 spaxels in it), making this ~ -0.04 dex offset significant. The general dilution agrees with observational studies of global spectra, which established that metallicities are diluted in a merging event (Ellison et al., 2008b; Michel-Dansac et al., 2008; Scudder et al., 2012). Much like the $\Delta\Sigma_{\mathrm{SFR}}$ profiles, the the smaller population of $\Delta\mathrm{SFR} < 0$ galaxies varies pretty significantly compared to the median profile and the $\Delta\mathrm{SFR} > 0$ population. The metallicity enhancement experienced by $\Delta\mathrm{SFR} < 0$ post-mergers, particularly in the outskirts, is likely a consequence of low sSFR galaxies having enhanced metallicity compared to high sSFR galaxies of the same total mass (Ellison et al., 2008b; Mannucci et al., 2010).

My results are in direct contrast with the CALIFA mergers study performed by Barrera-Ballesteros et al. (2015), which found similarly suppressed metallicity in the outskirts, but revealed normal metallicities in the centre of merging galaxies. To reiterate, discrepancies with the Barrera-Ballesteros et al. (2015) study probably stems from differences in the sample selection (particularly the inclusion of interacting pairs) and analysis methodologies. The radial profile shows a slight trend towards Δ O/H=0 for the smallest radii, which would be in more agreement with Barrera-Ballesteros et al. (2015) (see Figure 2.15). However this bin is at the resolution limit of the MaNGA survey (~ 1 kpc, depending on the redshift of the galaxy), so no concrete conclusions can be drawn from this uptick. If Δ O/H=0 for the smallest radii is a real characteristic of the post-merger sample, it could be the result AGN triggered by galaxy interactions. If the inflow of low-metal gas triggers AGN activity in merging galaxies (as suggessted by Ellison et al. 2008a, 2011; Scudder et al. 2012; Patton et al. 2016, and Pan et al. 2018), then spaxels with low metallicity in the centre would be removed due to AGN contribution, leaving only galaxies with normal metallicity where AGN has not been triggered. An examination of the molecular gas distributionuion for these galaxies would help determine whether this was the case, or whether galaxy mergers have regular nuclear metallicity as described by Barrera-Ballesteros et al. (2015), which would suggest gas enrichment at the centre of the galaxy due to the nuclear starburst triggered by the merger event (see Chapter 4 for further discussion).

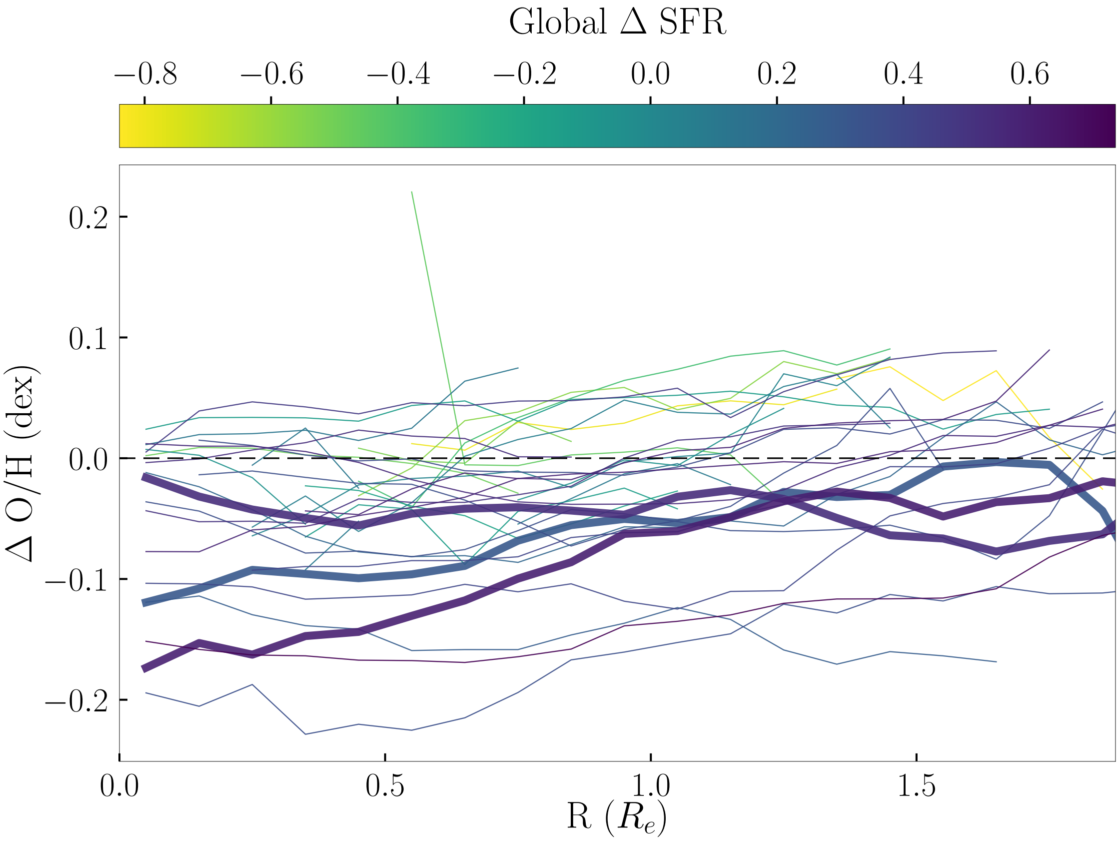

Figure 2.14: All Δ O/H profiles as a function of effective radius, coloured according to the global ΔSFR of the host galaxy. Bold lines represent galaxies from Fig.2.8.

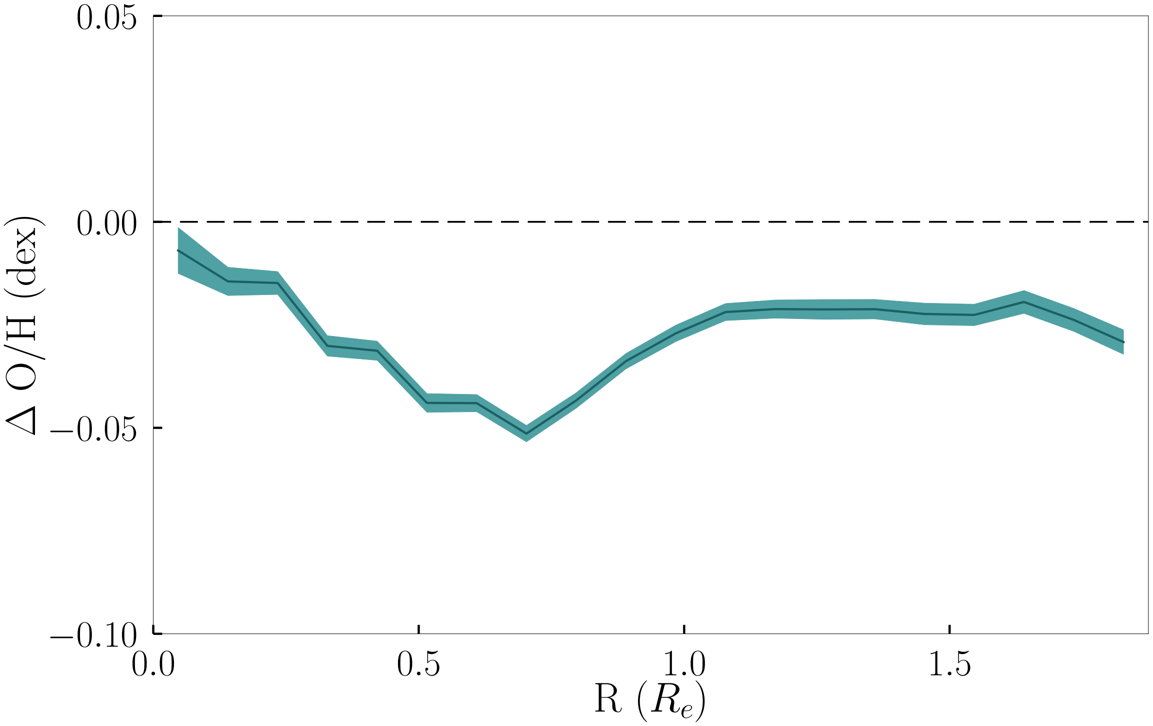

Figure 2.15: Median Δ O/H profile of all post-merger spaxels (teal line), also broken into bins of ΔSFR < 0 (yellow line) and ΔSFR > 0 (purple line). The width of the line represents standard deviation in $\Delta\Sigma_{\rm SFR}$ in that radius bin, divided by the square root of the number of spaxels in that bin.

Chapter 3

Interacting Pairs in MaNGA

The pairs stage of a galaxy interaction allows us to look at the progenitors of possible post-merger scenarios, and to approximate how the components of a galaxy merger change as the interaction progresses. Galaxy simulations have the benefit of "rewinding the clock" on a merger event, and can analyze the same interacting pair at different times over the interaction. Observational studies of galaxy pairs are dependent on large surveys to create a diverse sample of galaxies at different stages of the interaction process. The method with which galaxy pairs from such surveys are identified varies on the purpose of the study. Section 3.1 describes the pairs selection process used for the work herein. IFS surveys have the additional complexity of multiple galaxies being observed by one IFU in some cases, which provides the opportunity to study the spectroscopic qualities of close pairs. Section 3.2.1 explains the Source-Extractor program used to deblend such close pairs, and Section 3.2.2 outlines the successes and failures of this method. Radial profiles of $\Delta\Sigma_{\mathrm{SFR}}$ and Δ O/H, similar to those utilized in Chapter 2, are constructed for the pairs sample and binned by principal characteristics of the galaxy pair (such as r_p and Δv).

3.1 Identifying Interacting Pairs

The previous chapter examined the final stage of a galaxy interaction, the clearly defined post-merger phase. Conversely, the galaxy pairs phase captures a much longer time span of the interaction process. Simulations predict that at the first close approach of two galaxies (pericentric passage), both components of the system experience a burst of star-formation activity triggered by the tidal forces of the interaction (Barnes & Hernquist, 1996; Mihos & Hernquist, 1996; Di Matteo et al., 2007; Cox et al., 2008; Montuori et al., 2010; Torrey et al., 2012). Star-formation returns to normal as the galaxies move past each other, but when gravitational forces pulls them back together for a second pericentric passage, SFR is enhanced again, with the greatest period of star-formation occurring at coalescence (Mihos & Hernquist, 1996; Springel & Hernquist, 2005; Montuori et al., 2010; Torrey et al., 2012; Moreno et al., 2019). Observations of galaxies at multiple interaction stages have corroborated simulated predictions for SFR evolution with interaction time, observing an increase in star-formation as the projected separation between pairs decreases (Barton Gillespie et al., 2000; Lambas et al., 2003; Ellison et al., 2008a; Jogee et al., 2009; Robaina et al., 2009; Woods et al., 2010; Scudder et al., 2012; Patton et al., 2013), and a greater episode of star-formation post-coalescence (Ellison et al., 2013). In actuality, not all pairs show an enhancement in SFR: although the larger (primary) galaxy in a pair generally experiences an SFR enhancement (independent of companion mass), the smaller (secondary) galaxy can experience a suppression in SFR if its mass is one third the primary mass (Davies et al., 2015).

There are several ways to identify galaxy pairs in a survey, and the method can vary depending on the goal of the project and the available data. Galaxy asymmetry often stems from an interaction and is anti-correlated with the projected separation between pairs (r_p), making it an excellent tool to approximate merger stage (Patton et al., 2016). However, morphological changes resulting from an interaction are short lived in comparison to the corresponding SFR enhancement (Lotz et al., 2008), and could bias the sample to more recent interactions. Asymmetrical features can last ten times longer for galaxies with large mass ratios compared to mass ratios less than 4:1, and these features are longer lasting for higher gas fraction in all mass ratio regimes Lotz et al. (2010a,b). Thus methods of visual classification are biased towards high gas-fraction, large mass ratio, recently interacting galaxies

Many observational studies simply use r_p in concordance with the line of sight velocity differences (Δv) to approximate merger stage as a function of separation (Barton Gillespie et al., 2000; Alonso et al., 2004; Ellison et al., 2008a; Patton et al., 2011; Scudder et al., 2012; Fu et al., 2018). Galaxies can experience the effects of a companion out to ~150 kpc (see Figure 3.1), though this is likely due to fly-by's or galaxies that have already undergone first-pericentric passage. Most studies agree that companions within 50 - 100 kpc will influence the primary galaxy even on a first encounter, although the r_p at which merger affects start to occur will vary per galaxy (Barton et al., 2000; Wong et al., 2011; Scudder et al., 2012; Patton et al., 2013; Ellison et al., 2013).

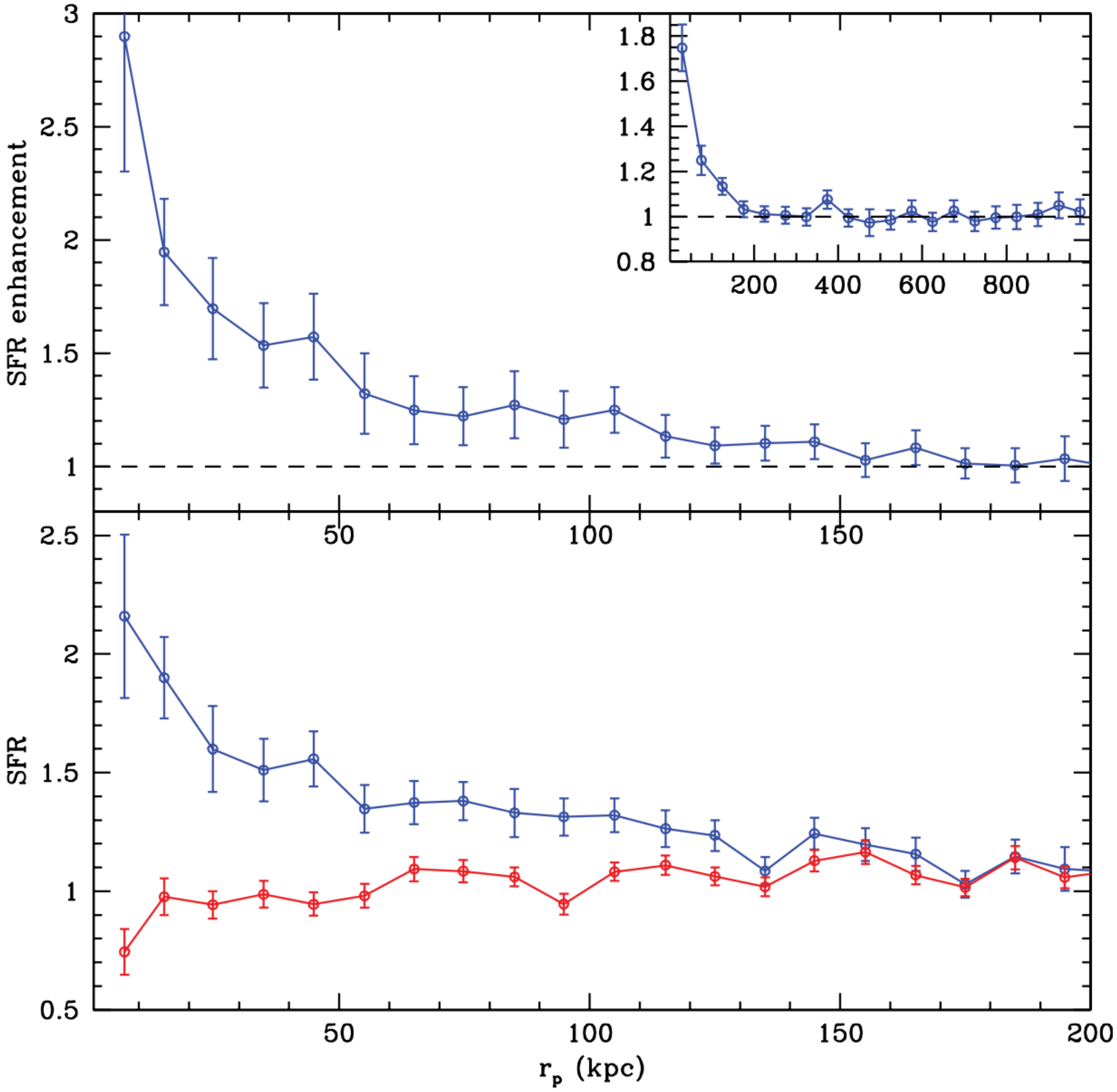

Figure 3.1: Lower Panel: Mean SFR for interacting galaxies (blue) and the respective control isolated galaxies (red) as a function of projected separation r_p. Top Panel: The ratio of pair SFR to control SFR as a function of r_p, with a dashed black line representing zero enhancement. The inset shows this plot extended to 1000 kpc. All error bars show the standard error in the mean. Source: Patton et al. (2013).

A Δv limit prevents contribution from foreground or background galaxies into a pairs sample. The likelihood of an interaction increases as Δv decreases, with regular star-formation activity being prominent once $\Delta v < 100$ - 300 km/s (depending on the r_p value) (Yang et al., 2007; Von Der Linden et al., 2007). However, separations less than 20 h^{-1}kpc, galaxies with $\Delta v < 500$ km/s still show morphological disturbances indicating a merger event (Lin et al., 2004). Simulations confirm that galaxies with such separation will merge in less than 1 Gyr (Kitzbichler & White, 2008; Jian et al., 2012). Galaxies must also have enough mass to assert significant gravitational influence on a each other to be considered "interacting". Thus many theoretical and observational simulations use a mass ratio (μ = primary galaxy mass / secondary galaxy mass) to constrain a sample of pairs to those undergoing a major merger (simulations: Cox et al. 2008; Lotz et al. 2010b; observations: Barton Gillespie et al. 2000; Lambas et al. 2003; Patton et al. 2011).

In my work, I combine different but complimentary methods for identifying pairs in the MaNGA sample. One sample of galaxy pairs is collected from the Patton et al. (2016) catalogue, which identifies the closest companion for each galaxy in SDSS data release 7, with a companion boundary at $r_p = 1$ Mpc and $\Delta v = 1000$ km/s. MaNGA galaxies are matched to the Patton et al. (2016) catalogue based on right ascension (RA) and declination (DECL) for all targets, with the closest match in RA and DECL being determined by Astropy[1] match_to_catalog_sky package (The Astropy Collaboration et al., 2013, 2018). If the positions of a galaxy in MaNGA and in Patton et al. (2016) match within 2 arcseconds, they are treated as the same object. Not all of the spectroscopic pairs are necessarily interacting given the extensive range of possible r_p and Δv values. An additional cut of $r_p < 100$ kpc, $\Delta v < 500$ km/s, and $0.1 < \mu < 10$ is made to ensure that galaxies are beginning the interaction process (r_p and Δv cuts), and that each component is massive enough to adequately influence the other (μ cut).

SDSS DR7 targets have a minimum separation of 55" due to the size of the fibre plugs preventing any closer placement. This can constitute anywhere between 10 kpc and 100 kpc depending on the redshift of the target. Thus spectroscopic pairs identified in DR7 will be biased towards larger r_p, missing many galaxies at first pericentric passage, or those just before coalescence. The design of MaNGA IFUs can help address this issue. IFU sizes range from 12" - 32", capturing the closest galaxy pairs that may not appear in the Patton et al. (2016) catalogue within

---

[1] http://www.astropy.org

the IFU footprint. These pairs are selected from the MaNGA sample with a visual classification, performed in conjunction with the post-merger classification described in Section 2.4. Any object that had two distinct galactic nuclei within the IFU footprint is considered an "IFU pair". Based on results from simulations, the outskirts hold crucial variability depending on the interaction progenitors (Moreno et al., 2019), and the results for post-mergers presented in Chapter 2 exhibit some of the most diverse behaviour at the outskirts.

Combining the two classification methods, there are 258 spectroscopic pairs from the Patton et al. (2016) catalogue, and 92 visually classified IFU pairs. Eighteen of the IFU pairs are also in the Patton et al. (2016) catalogue; thus the final number of unique interacting pairs in MaNGA is 332, each with measured redshifts, Δv's, and mass ratios. This method does disregard galaxies which are visually interacting with a companion (tidal bridges connecting the two or clear morphological disturbances), but that companion is neither on the IFU nor in the Patton et al. (2016) catalogue. In this case the companion would not have mass ratios available from Patton et al. (2016), nor the MaNGA data available to approximate a mass ratio. Thus they are excluded from the following analysis where mass ratio is prominently considered. The following section outlines the methods used to measure μ, Δv, and r_p for IFU pairs to confirm whether they fit within the designated cuts.

3.2 IFU Pairs

IFU pairs can create issues with the azimuthally averaged radial profiles used to analyze merging galaxies in MaNGA. The two nuclei within the IFU have individual profiles in SFR and metallicity that contribute to the azimuthally averaged profile. Given that radius measurements are made from the centre of the target galaxy, the nucleus of the companion galaxy will contribute at larger radii and lead to misinterpretations of offsets in SFR and metallicity as the result of an interaction. The companion nucleus, and any spaxels belonging to the companion, must be masked when considering offset profiles for the target galaxy. The following section describes the software developed to mask IFU companions, and the subsequent μ, Δv, and r_p measurements computed.

3.2.1 SExtractor

To ascertain which spaxels belong with which galaxy on an IFU, I use the source extraction software SExtractor [2], a computer program originally designed to automatically detect and perform photometry on sources in a fits image, in particular images from large galaxy surveys (Bertin & Arnouts, 1996). Although not ideal for completing highly detailed photometry on a few objects with known locations, SExtractor is optimized to create a catalogue of all objects in an image for which photometry can be performed. With the capacity to handle massive fits files, SExtractor allows the user to process many files extremely quickly for any input parameters desired. The quality of these input parameters is crucial to proper target detection. SExtractor is optimized to create a catalogue of all objects in an image for which photometry can be performed.

SExtractor completes the following steps to deblend multiple galaxies on an image. The package first determines whether pixels belong to the background of the image based on a detection threshold set by the user (DETECT_THRESH). The background (and its RMS) is determined such that background values can be subtracted from images for photometry. However, given the work herein requires only deblending, not photometry, the background subtraction and other photometry components are ignored. Pixels are then grouped into candidate objects based on three criteria: each pixel has a value above the detection threshold (DETECT_THRESH), all pixels belonging to the object have corners or sides adjacent to each other, and the number of pixels in the object is above the minimum pixel count for a detected object (DETECT_MINAREA). There may be many detections above DETECT_THRESH next to each other in one area; thus this area must be deblended into separate objects. SExtractor accomplishes this by creating a "tree" of detections, with a branch for every detection above a minimum pixel threshold (set by DETECT_THRESH). The user defines the number of levels between this threshold and the maximum detection with the parameter DEBLEND_NTHRESH. Within these levels, objects are deblended by having counts above a fraction of the total count in the area (DEBLEND_MINCONT), and on the condition that there is at least one other branch in that level above DEBLEND_MINCONT (see Figure 3.2 for further illustration).

The 92 IFU pairs require some fine-tuning to create a proper mask, by adjusting the four following input parameters: DETECT_THRESH, DETECT_MINAREA,

---

[2] https://www.astromatic.net/software/sextractor

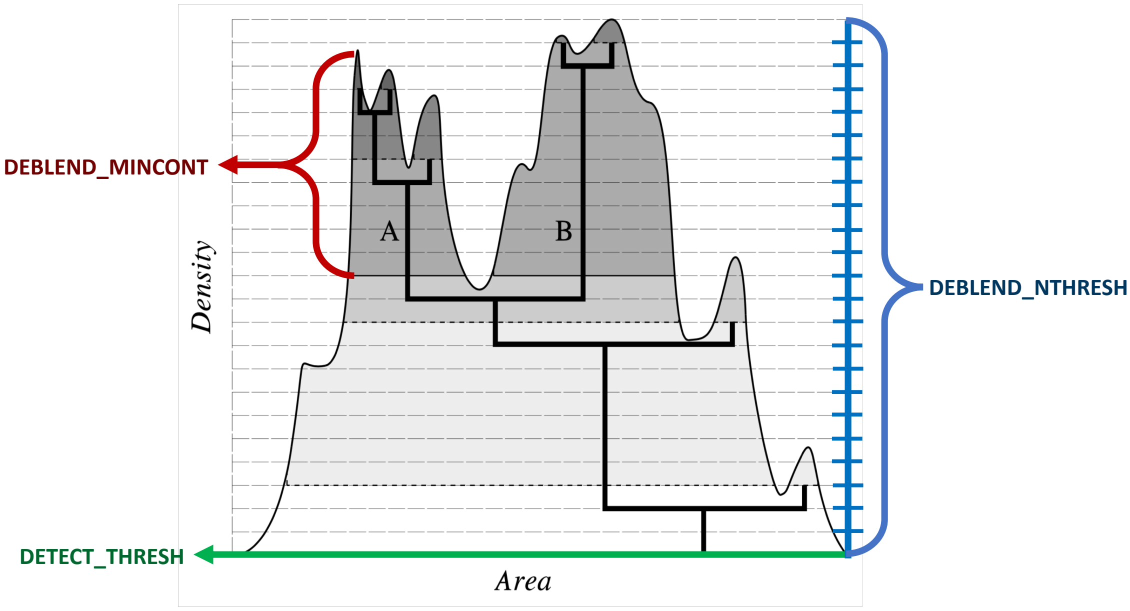

Figure 3.2: Schematic for the “tree” deblending method for multiple objects above DETECT_THRESH. Different branches occurs when detections above the threshold are separated by one or more pixels (dark black lines). The two branches are only determined to be separate objects if both integrated intensities of each branch are greater than DEBLEND_MINCONT. The two objects identified here are labeled “A” and “B”. Source: Bertin & Arnouts (1996).

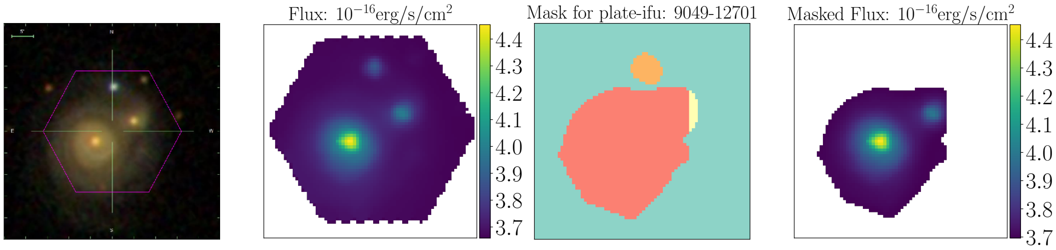
Flux: 10^{-16}erg/s/cm^2

Mask for plate-ifu: 9049-12701

Masked Flux: 10^{-16}erg/s/cm^2

Figure 3.3: Example of a galaxy pair whose white light image is not successfully deblended by SExtractor . From left to right: SDSS gri-image of galaxy pair, the white-light image of galaxy, the mask created by SExtractor, and the white-light image masked based on SExtractor deblending. Notice a nearby star is identified as an object, but the true companion is considered a component of the target galaxy.

DEBLEND_NTHRESH, and DEBLEND_MINCONT. The SExtractor output includes a mask file for the input image which assigns each spaxel to an identified galaxy or to the background. SExtractor also produces a catalogue file that identifies the centre of each identified "object" within the mask.

3.2.2 Differentiating Galaxies

The first attempt at using SExtractor to differentiate IFU pair galaxies was run on the MaNGA white light images. White light images were created by compressing the flux at all wavelength values of the datacube into a single fits image with a summed flux value for each spaxel. Although SExtractor can easily differentiate pairs isolated within the IFU, nearby stars or bright clumps of star-formation can hinder SExtractor's ability to identify the desired galaxies (see Figure 3.3 for an example).

The stellar mass surface density (Σ_*) maps produced by PIPE3D provide an excellent alternative to the white light image. Σ_* maps mask out contribution from stars, and prioritize galaxies over less massive clumps of star-formation. A set of default input parameters are initially run for all IFU pairs, where DETECT_MINAREA = 20, DETECT_THRESH = 0.000005, DEBLEND_NTRHESH = 64, and DEBLEND_MINCONT = 0.00001. DEBLEND_NTRHESH is at a particularly large value to distinguish very close objects, such as interacting nuclei. DETECT_THRESH and DEBLEND_MINCONT are initially set at very small values to capture any possible pairs, even if they are relatively low mass. DETECT_MINAREA is relatively large value to avoid deblending a

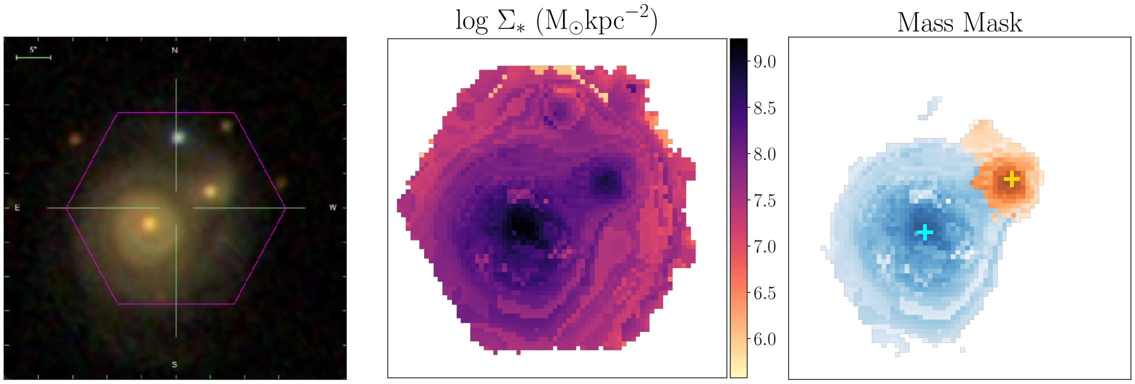

Figure 3.4: Example of a galaxy pair whose mass map is successfully deblended by SExtractor . From left to right: the SDSS gri-image of the galaxy pair, the PIPE3D stellar mass surface density map, and the stellar mass surface density masked based on SExtractor deblending. Compared to the mask created by a white light image of the same galaxy in Figure 3.3, here the target and companion galaxy are properly distinguished based on the gri-image.

small collection of high mass pixels, but not so large as to exclude small companions. For most galaxy pairs, SExtractor easily finds a companion after tweaking the input parameters once or twice (see Figure 3.4 for an example).

There are some cases where, even when Σ_* maps are used, SExtractor fails to deblend the IFU pair. Failures occur when no visually flagged companion is identified, or the mask poorly represents the light from the gri-image. Only 26 of the 92 IFU pairs fail in this manner, only 8 of which fail to identify any companion. The other 18 are visually identified as having poor masks compared to the gri-image, and in most cases the galaxies are so intertwined no clear line could be used to separate the two.

3.2.3 Extracting IFU Pair Properties

Total stellar mass (M_*) and total SFR values are computed by summing the Σ_* and $\Sigma_{\rm SFR}$ spaxels assigned to each galaxy by the SExtractor mask. Visual inspection of the mask reveals that they tend to underestimate the galaxy coverage of the IFU, in turn underestimating M_* and SFR. Figure 3.5 provides an example of both an underestimation of the Σ_* coverage, and the $\Sigma_*/\Sigma_{\rm SFR}$ coverage differences not be accounted for in the mass mask. To account for such underestimations, pixels that belong to neither the target nor the companion mask are reassigned to the closest galaxy mask (see Figure 3.6 for an example).

To test the accuracy of the masked M_* of the IFU pair, comparisons to both the PIPE3D integrated M_* and the independently computed NASA-Sloan Atlas (NSA) Sérsic mass are made to validate the new masses. The NSA Sérsic mass is determined independently from photometry (Blanton et al., 2011): the mass-to-luminosity ratio is determined from the spectral energy distribution of the galaxy, then the luminosity is determined from flux and redshift to measure a total mass (Brinchmann & Ellis, 2000). Different methodologies are used to compute NSA Sérsic M_* and the PIPE3D M_*, in particular different IMFs are used. Appendix A.3 outlines the particular steps of how NSA Sérsic M_* can be converted to values comparable with PIPE3D M_*. Figure 3.7 demonstrates how the initial integrated masses from the PIPE3D value added catalogue (blue dots) are systemically greater than the NSA Sérsic mass(once the correction detailed in Appendix A.3 and eqn. A.1 has been applied), likely due to contribution from the IFU companion in the PIPE3D masses. The integrated masses computed from the masked Σ_* spaxels exhibit a more random variation from the NSA Sérsic mass (Figure A.2b). Neither the PIPE3D nor NSA Sérsic mass are inherently better, particularly for close pairs. For example, the SDSS detectors are more to r - sensitive, resulting in deeper r-band images than in other filters, which creates more overlap between the isophotes of close companion galaxies, and thus greater contribution from the companion galaxy (Simard et al., 2011). Companion contribution thus complicate photometric masses, like those provided by the NSA catalogue, just like it complicates the PIPE3D integrated mass. This is likely why many of the cases where the masked integrated mass is significantly different from the NSA Sérsic mass occur at small r_p (see Figure A.2b for details). To ensure the consistency of this project it is simplest to measure M_* from integrated Σ_* provided by PIPE3D, which is why I chose to use the PIPE3D VAC masses and my own masked masses, computed in the same method except for the pixel count.

With verified M_* values for each galaxies in an IFU pair, mass ratios can be computed for each pair to remove those which do not fit the desired μ limit. A subset of the IFU pairs have $\mu < 0.1$ or $\mu > 10$, and are thus outside the limit of my mass ratio cut. To ensure no minor mergers contribute to the sample, these IFU pairs are removed. To summarize, IFU galaxy pairs which have two targets identified by SExtractor , a reasonable mass mask based on the gri-image, and $0.1 < \mu < 10$ are kept for the interacting pairs analysis: all other IFU pairs are dropped from the sample (26 with bad masks, 7 cut for mass ratio). Figure 3.9 provides a visual for how

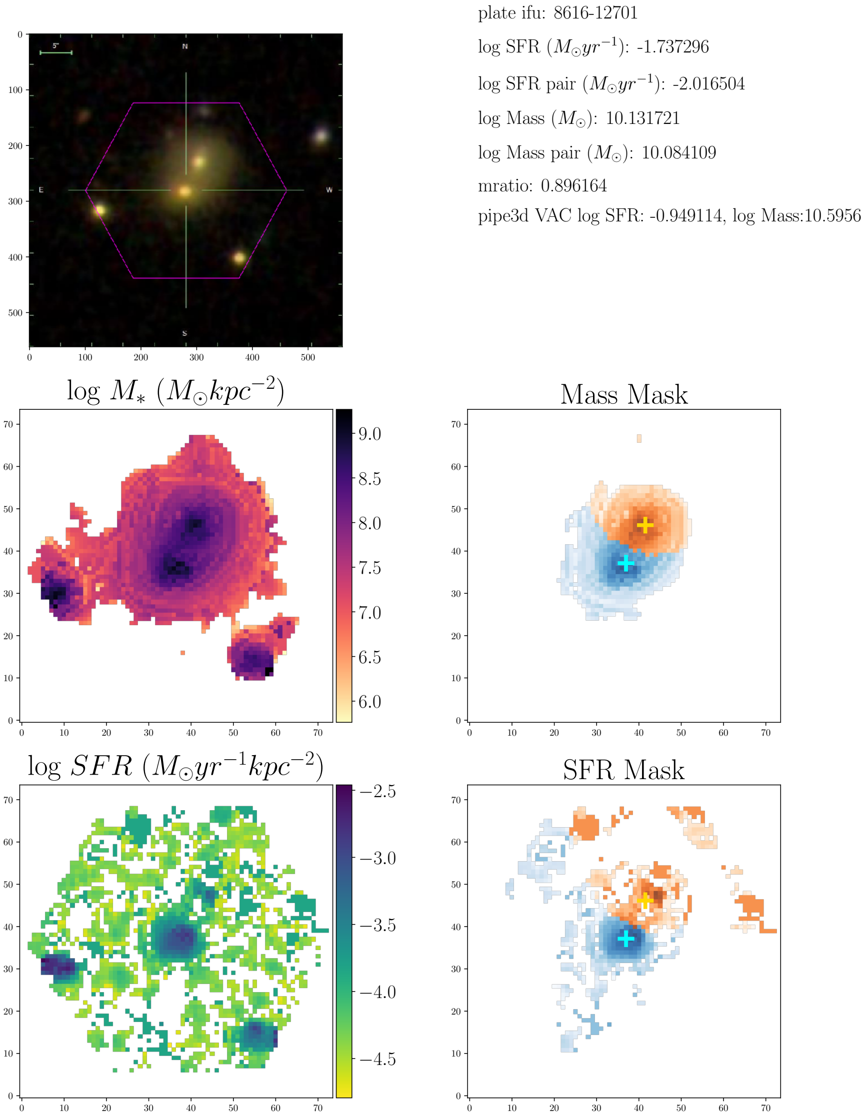

plate ifu: 8616-12701

log SFR ($M_\odot yr^{-1}$): -1.737296

log SFR pair ($M_\odot yr^{-1}$): -2.016504

log Mass ($M_\odot$): 10.131721

log Mass pair ($M_\odot$): 10.084109

mratio: 0.896164

pipe3d VAC log SFR: -0.949114, log Mass:10.5956

Figure 3.5: An example of a properly deblended galaxy pair. Top left: SDSS gri-image of the target. Middle left: PIPE3D mass map. Middle right: SExtractor mask created from the mas map. Bottom left: PIPE3D SFR map. Bottom right: masked SFR. The mask excludes spaxels at the very edge of each galaxy, particularly for the companion.

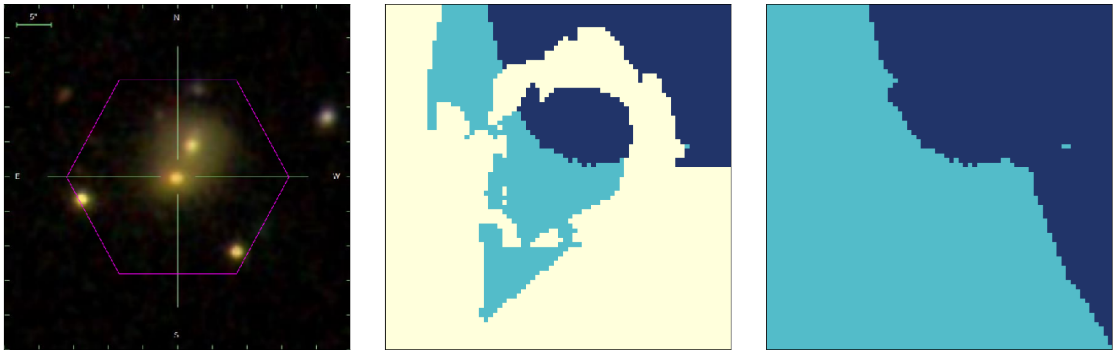

Figure 3.6: From left to right: the SDSS gri-image of MaNGA target, the mask created by SExtractor based on mass map, and the masks extended to include pixels assigned to neither mask previously.

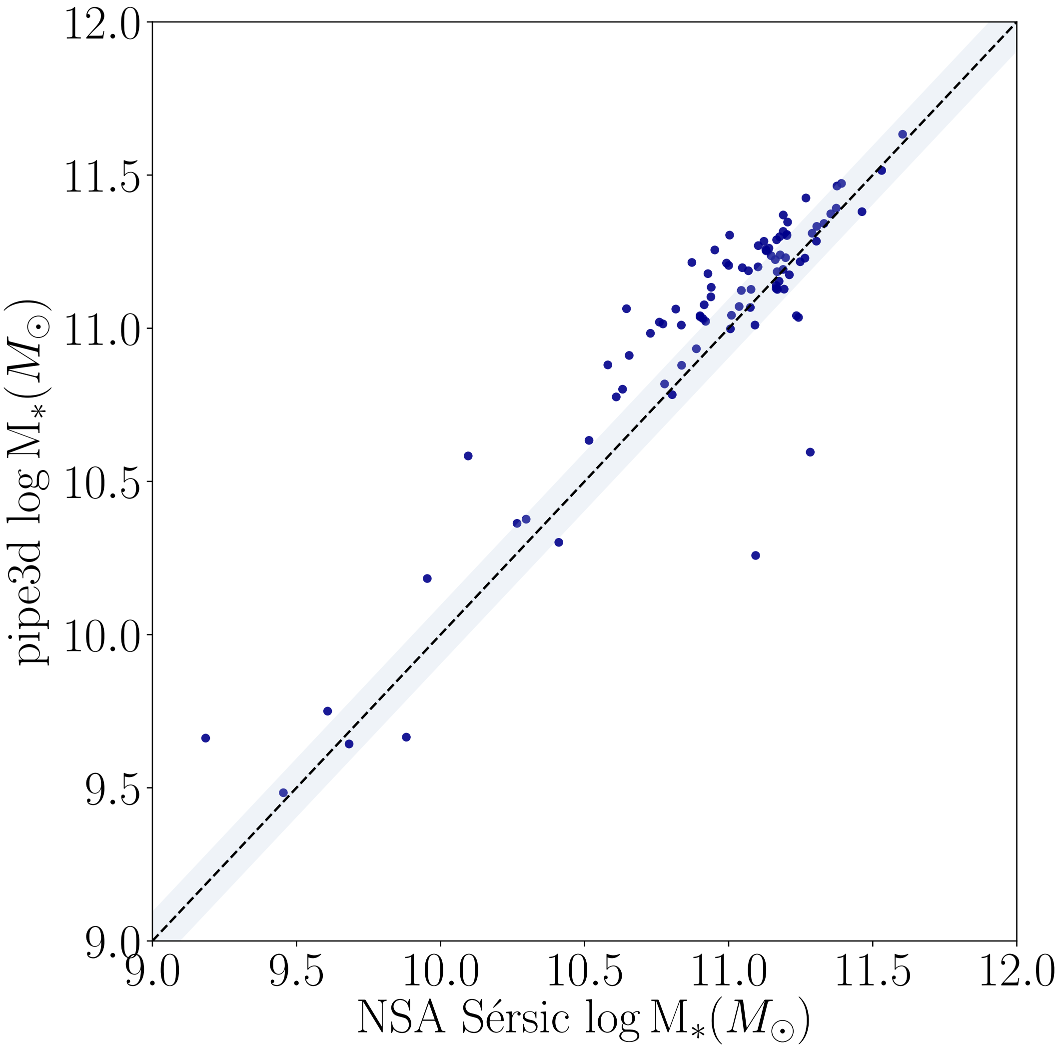

Figure 3.7: Comparison of the integrated PIPE3D M_* and NSA Sérsic M_* (corrected per appendix A.3) for IFU pairs. The black dashed line represents where the two are equal, and the gray area around this bar represents the average uncertainty in the pipe3d mass. Note the integrated PIPE3D M_* is systemically larger, likely as a result from contribution from the companion galaxy.

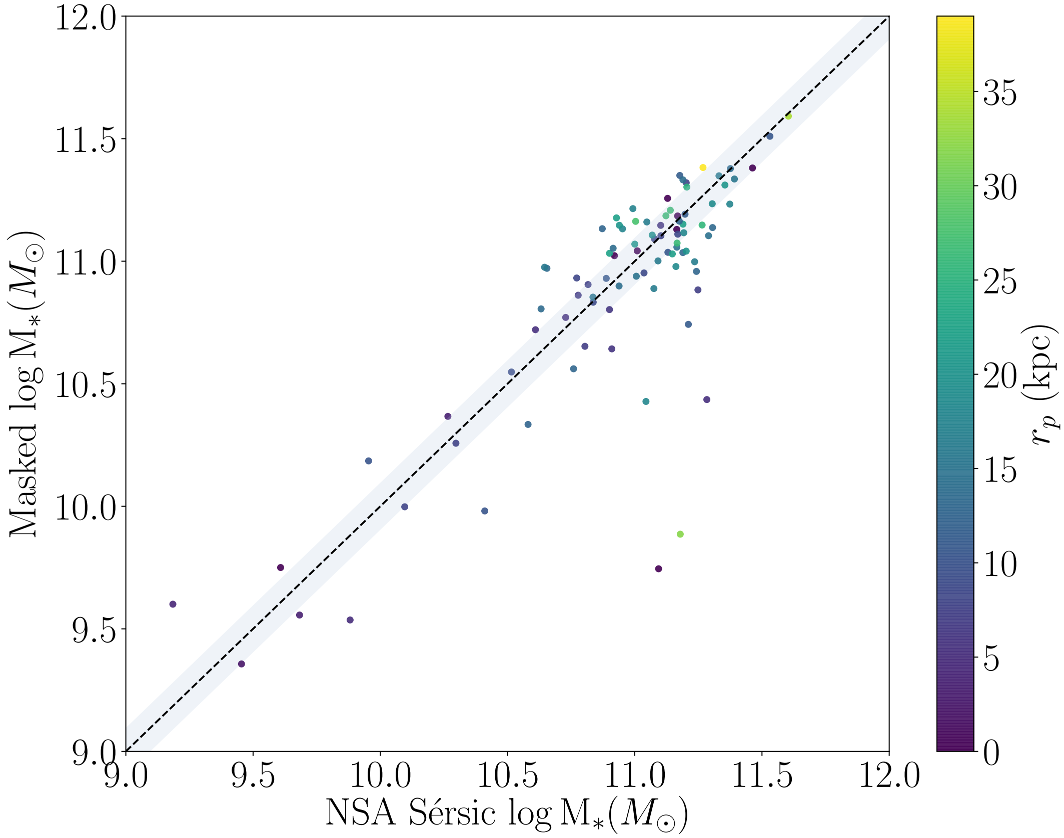

Figure 3.8: Comparison of the masked PIPE3D M_* and NSA Sérsic M_* (corrected per appendix A.3) for IFU pairs. The black dashed line represents where the two are equal, and the gray area around this bar represents the average uncertainty in the pipe3d mass. Note the masses now have an more random scatter about the line of equality. The cases where the two masses are significantly different are often the closest pairs, where the NSA Sérsic M_* overestimates the target galaxy mass, probably from close companion contribution.

successful IFU pairs are determined, and what sort of cases constitute the galaxy being dropped from the mergers sample. Fourteen cases fail the pair classification based on Figure 3.9, but still have the disturbed morphology indicative of an interaction. These galaxies are worth examining to investigate the effects on the most tidally disturbed galaxies. However, they do not fit in with my analysis using r_p and μ, and are thus save for future work (see Section 4.2 for details). Of the IFU pairs, only the spaxels assigned to the central galaxy are used for analysis. To properly analyze the spatially resolved properties of the companions, new radius values (in particular R_e) would need to be determined for the companion galaxies, which is beyond the scope of this work and saved for future investigation. Thus, of the 92 IFU pairs there are only the central galaxy is analyzed, of those 58 are kept in the interacting galaxies sample based on the decision tree.

The projected separation between the IFU pairs is computed based on the "centre" of each galaxy determined by SExtractor. This can be slightly different than the initial r_p determined during visual classification with the SDSS image tool[3]. Comparing the r_p initially calculated (by visual inspection, or from the Patton et al. (2016) catalogue) to the new r_p reveals no drastic difference between the two (see Figure 3.10). In all cases the r_p computed from the mask is used for the analysis of interacting galaxies.

The Δv values are determined by computing the mean stellar velocity within a 3" aperture centered on the each galaxy (see Figure 3.11 for an example), and calculating the difference between the two mean velocities.. The redshift can also be determined for each galaxy using the mean stellar velocity. For the 18 IFU pairs that are also in Patton et al. (2016), the new Δv is approximately the same as the original, unless r_p is very large. If the r_p is very large the Patton et al. (2016) companion is not on the IFU, so the Δv is referring to a different companion entirely.

To demonstrate the importance of handling IFU pairs properly, Figure 3.12 shows the median radial profile in $\Delta\Sigma_{\mathrm{SFR}}$ and Δ O/H for the IFU pairs spaxels (the 58 selected after μ and mask cuts), and for the IFU pairs spaxels masked to discard companion spaxels. Both masked and unmasked $\Delta\Sigma_{\mathrm{SFR}}$ have different radial distributions, but most of the variable behaviour occurs beyond $R = 1R_e - 1.5R_e$. Interestingly, the $\Delta\Sigma_{\mathrm{SFR}}$ and Δ O/H profiles vary at different radii, although both vary more at extended radii. This is likely due to the distribution of available verifiable SFR and O/H measurements.

---

[3] http://skyserver.sdss.org/dr14/en/tools/chart/navi.aspx

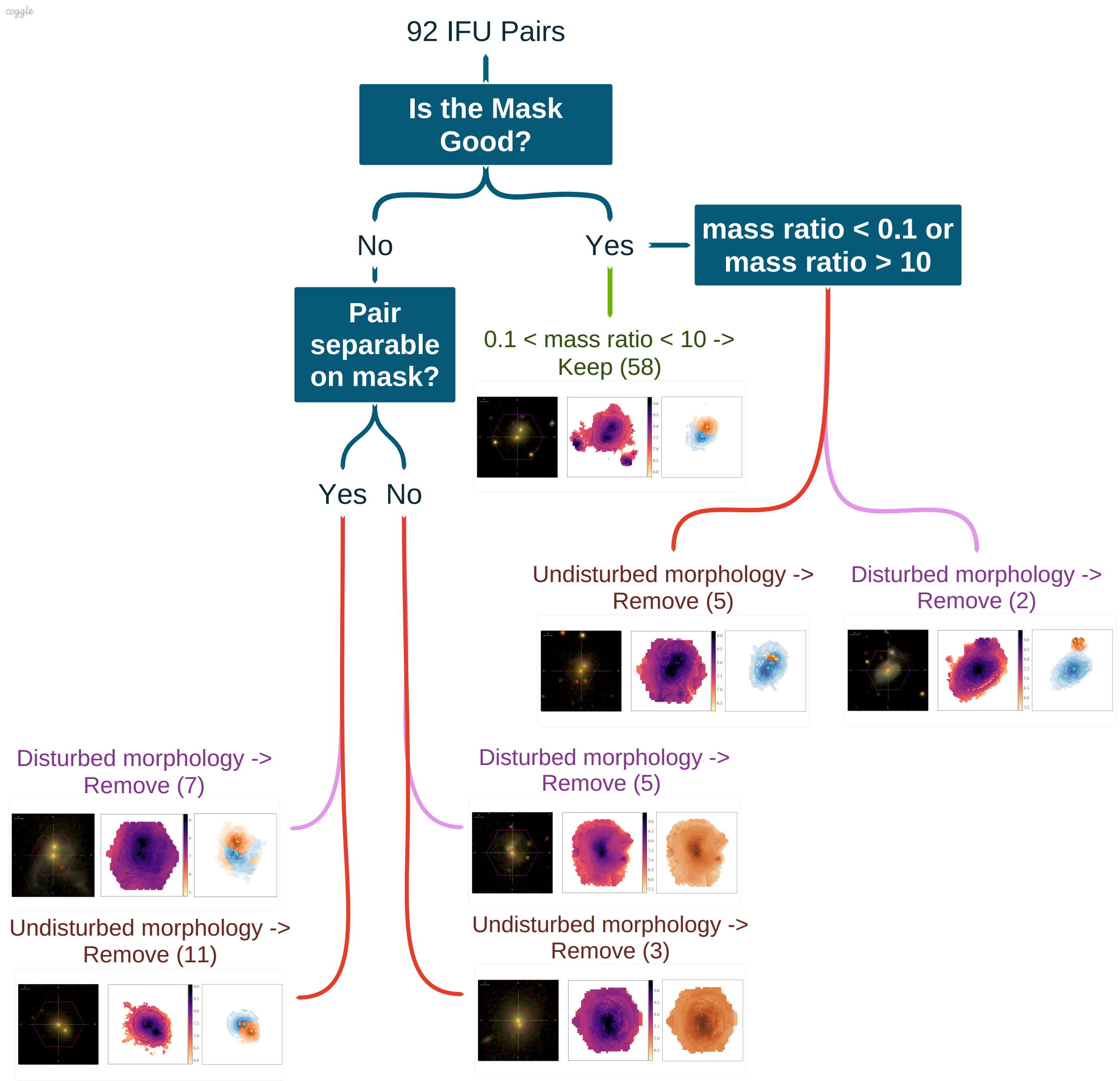

Figure 3.9: The decision tree for whether an IFU pair is including in the interacting galaxies sample. Examples of each case are shown within the decision tree.

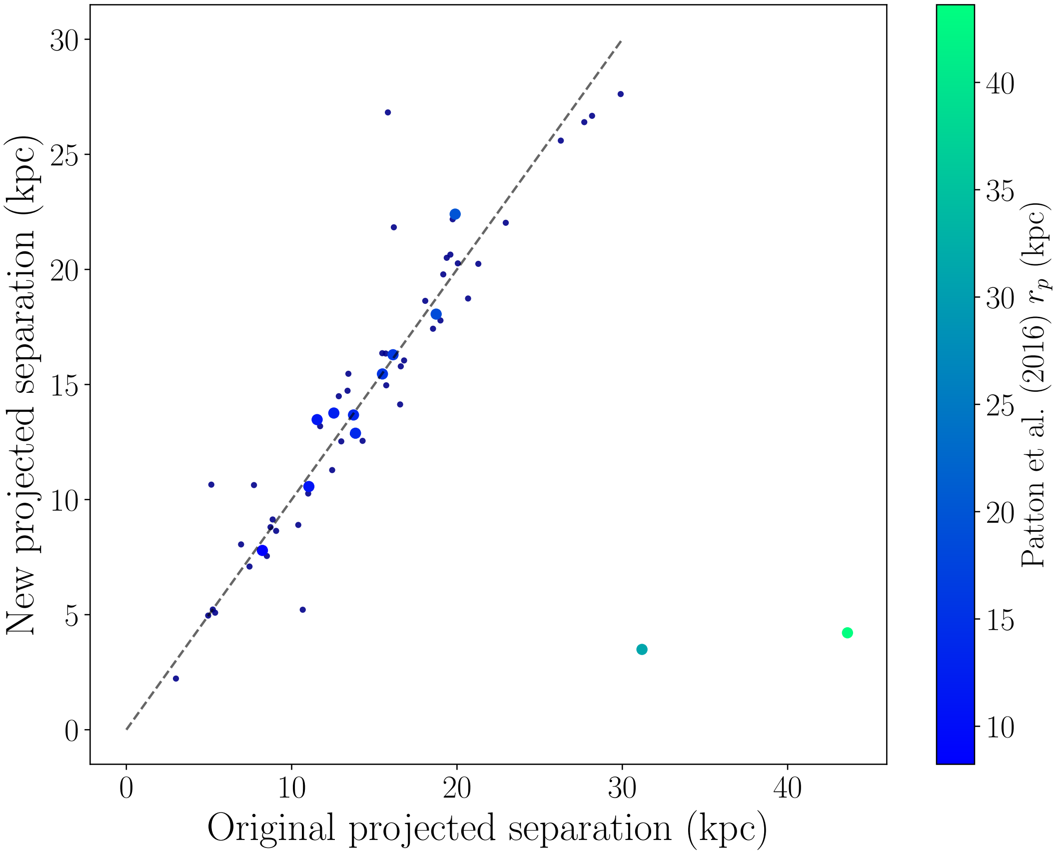

Figure 3.10: r_p based on SExtractor galaxy centres of IFU pairs, compared to the original r_p calculated from visual inspection, or spectroscopic pairs with their own RA and DECL. Galaxies that have spectroscopic companions are larger circles colour coded by their r_p provided in Patton et al. (2016). The only galaxies with significant deviation between the new and old r_p are those from Patton et al. (2016), indicating that the spectroscopic pair is a different galaxy from the IFU companion.

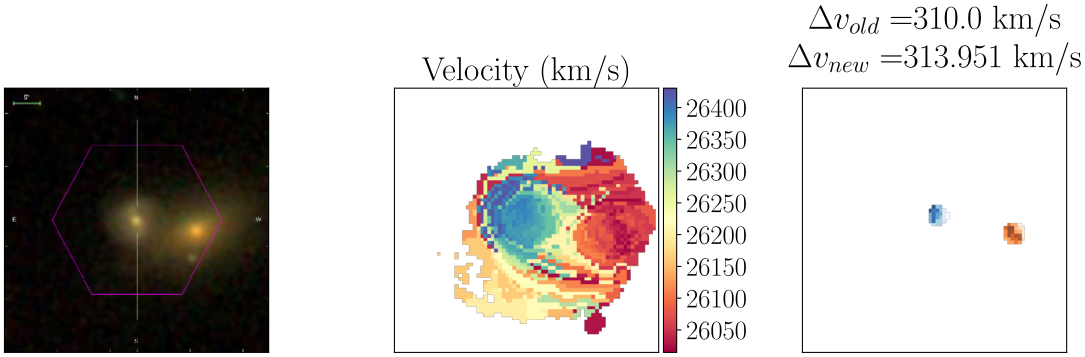

Figure 3.11: An example of a spectroscopic pair where both galaxies are on the IFU. From left to right: the gri-image of the galaxy, the velocity map computed by PIPE3D, and the masked velocity map used for calculation of Δv. Notice that the previous Δv value from Patton et al. (2016) and the newly computed Δv are practically identical.

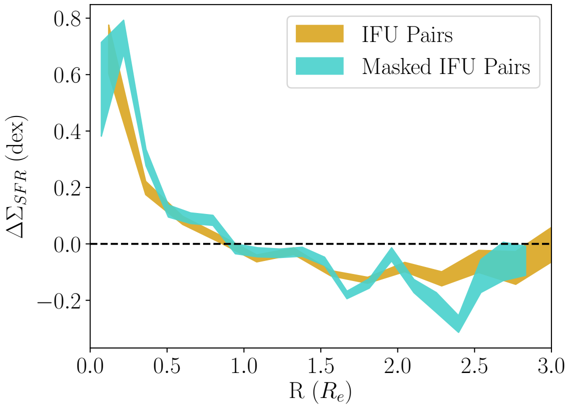

(a) Median $\Delta\Sigma_{\rm SFR}$ profile for unmasked (yellow) and masked(blue) interacting galaxies in an IFU pair.

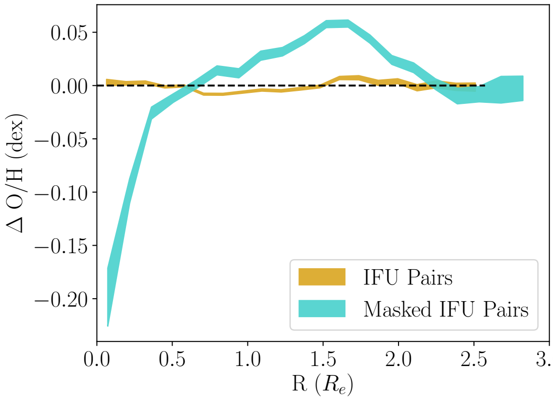

(b) Median Δ O/H profile for unmasked (yellow) and masked(blue) interacting galaxies in an IFU pair.

Figure 3.12: Demonstration of how median radial profiles vary once the IFU companions spaxels have been excluded. The width of the line represents the standard deviation in $\Delta\Sigma_{\rm SFR}$ or Δ O/H in that radius bin, divided by the square root of the number of spaxels in that bin.

3.2.4 Interacting Pairs Sample

In the final sample there are 58 IFU pairs and 240 spectroscopic pairs from Patton et al. (2016), for a final sample of 298 interacting galaxies. None of the IFU galaxies are outside the $r_p < 100$ kpc and $\Delta v < 500$ km/s cuts. The final distribution for global properties of the pairs sample (both spectroscopic and IFU pair) are included in Figure 3.13. The majority of galaxies with $r_p < 30$ kpc are IFU pairs, demonstrating how crucial the inclusion of visually classified IFU pairs is to creating a holistic sample of interacting galaxies.

Interestingly, the IFU pairs under-sample the $\mu < 1$ range. If there is a companion on the IFU, it is much more likely to be offset from the centre and thus have less allotted spaxels than the central galaxy, hence IFU pairs tend to have mass ratios greater than 1. The distribution on the SFR-M_* plane of the interacting pairs provided in Figure 3.14 shows the generally even distribution of galaxies and their r_p values for different total masses and SFRs, though there tend to be slightly more close pairs in the passive sample as expected (Patton et al., 2011).

3.3 Preliminary Results

The following section presents radial profiles of $\Delta\Sigma_{\mathrm{SFR}}$ and Δ O/H for the interacting sample, using a similar analysis method as in Section 2.5. Of the IFU pairs, only the primary galaxy is used in the analysis. The interacting pairs sample has the advantage of know the r_p of the pair, constraining the interaction stage, and μ to specify the interaction progenitors. Previous IFU studies have examined the spatial properties of merging galaxies with differentiating galaxy stage in this manner (see Barrera-Ballesteros et al. 2015).

3.3.1 $\Delta\Sigma_{\mathrm{SFR}}$ Profiles

$\Delta\Sigma_{\mathrm{SFR}}$ values, similar to those computed in Chapter 2, are calculated for all interacting pairs and separated into bins of r_p (see Figure 3.15). As discussed previously, the projected separation is a decent approximation for merger stage (De Propris & Melnick, 2014; Scudder et al., 2012; Patton et al., 2013, 2016; Pearson et al., 2019). On average, interacting galaxies at any stage experience a central SFR enhancement, although the greatest enhancement is experienced by those with $r_p <$ 20kpc. Interestingly, the central enhancement of the closest galaxy pairs is on par with (if not

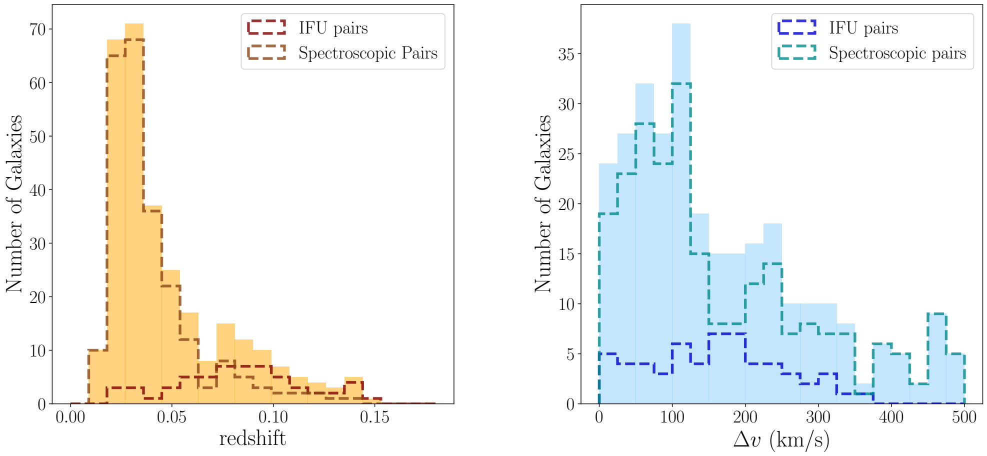

(a) Redshift distribution.　(b) Δv distribution.

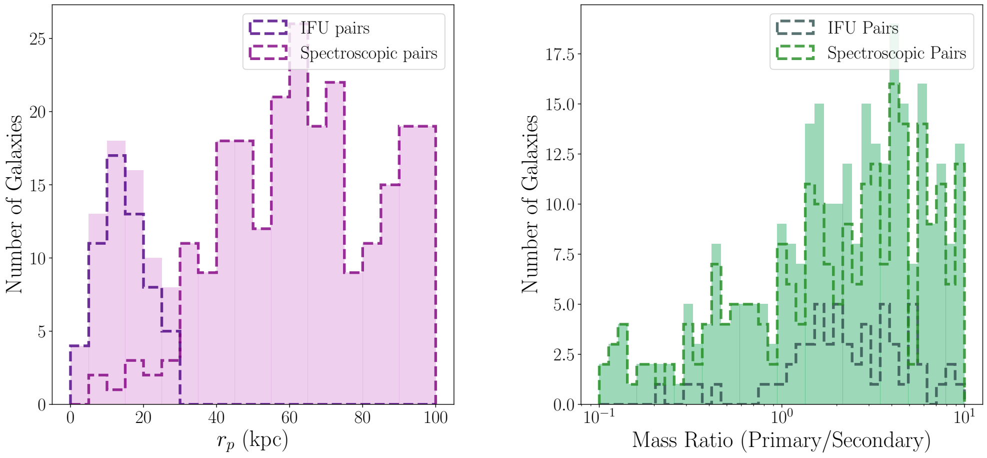

(c) r_p distribution.　(d) μ distribution.

Figure 3.13: The IFU pairs and Spectroscopic pairs are plotted as different colour dashed lines. The filled in histogram represents the distribution of the combined pairs sample.

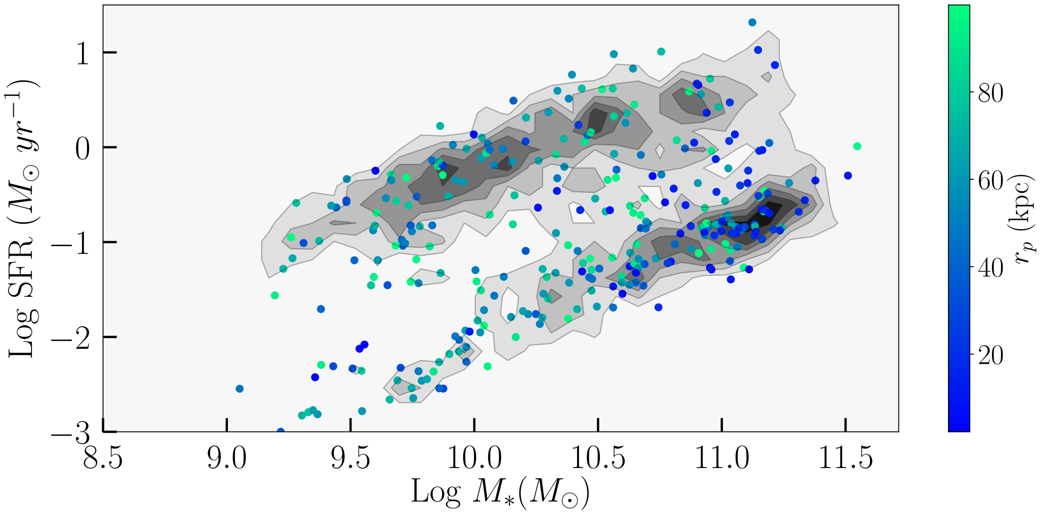

Figure 3.14: The distribution of SFR and M_* for the entire DR14 MaNGA sample (gray contours), with the interacting pairs represented over this distribution as dots. Each dot is colour-coded according to the r_p of the pair.

greater than) the central enhancement experienced by post-merger galaxies (green profile). Galaxies experience the greatest burst of star-formation at coalescence, the close pairs may be probing a subsample of galaxies at the cusp of coalescence (Cox et al., 2008; Torrey et al., 2012; Moreno et al., 2019). It is also likely that the median post-merger enhancement is diluted by galaxies that coalesced much longer ago, given morphological features of a merger can last longer than the starburst (Lotz et al., 2008, 2010a). Pairs with $r_p > 40$kpc experience a central enhancement $\sim$0.3 dex less than the closest pairs, implying that the starburst experienced at first pericentric passage is short-lived. Significant enhancement out to $2R_e$ is unique to the post-merger stage, suggesting that the central starburst triggered at small r_p can trigger a global enhancement in SFR that only materializes post-coalescence. Global studies indicate that r_p dependence is weak beyond 50 kpc, in agreement with the minor central enhancements and outer suppression exhibited by galaxies where $r_p >$ 40 kpc in Figure 3.15. Generally the interacting pairs are slightly suppressed in the outskirts, in agreement with other IFS studies of galaxy mergers (Barrera-Ballesteros et al., 2015). The variation in outskirt behaviour beyond 40 kpc is unclear in origin.

Although both simulations and observations have demonstrated how decreasing r_p correlates with increased SFR (Barton Gillespie et al., 2000; Lambas et al., 2003; Ellison et al., 2008a; Jogee et al., 2009; Robaina et al., 2009; Woods et al., 2010; Scudder et al., 2012; Patton et al., 2013), other parameters can greatly influence the strength of the starburst. Qualities of the progenitors galaxies, such as mass ratio, gas fraction, and orbital parameters drastically alter the lasting effects of the merger (Cox et al., 2006; Scudder et al., 2015; Moreno et al., 2015; Fensch et al., 2017). To investigate the effects of progenitors, $\Delta\Sigma_{\rm SFR}$ profiles are reproduced, but binned by mass ratio (μ) rather than r_p (see Figure 3.16)

Galaxies with the smallest μ, where the target galaxy is the smaller of the two, experience minimal SFR enhancement in the centre, and suppression beyond 0.5 R_e down to -0.5 dex. For a similar mass ratio range, except where the primary galaxy is the larger of the pair ($5 < \mu < 10$), the pair experiences twice as much SFR enhancement in the centre compared to the $0.0 < \mu < 0.2$ range, which lessens but is still enhanced out to 1.5 R_e. Similar results were uncovered with global studies of mergers, where the more massive galaxy in a pair experiences a stronger starburst than the less massive galaxies, for small r_p (Scudder et al., 2012).

Galaxies with the smallest mass in comparison to their companion generally have greater SFR suppression in the outskirts, despite any central SFR enhancement. Be-

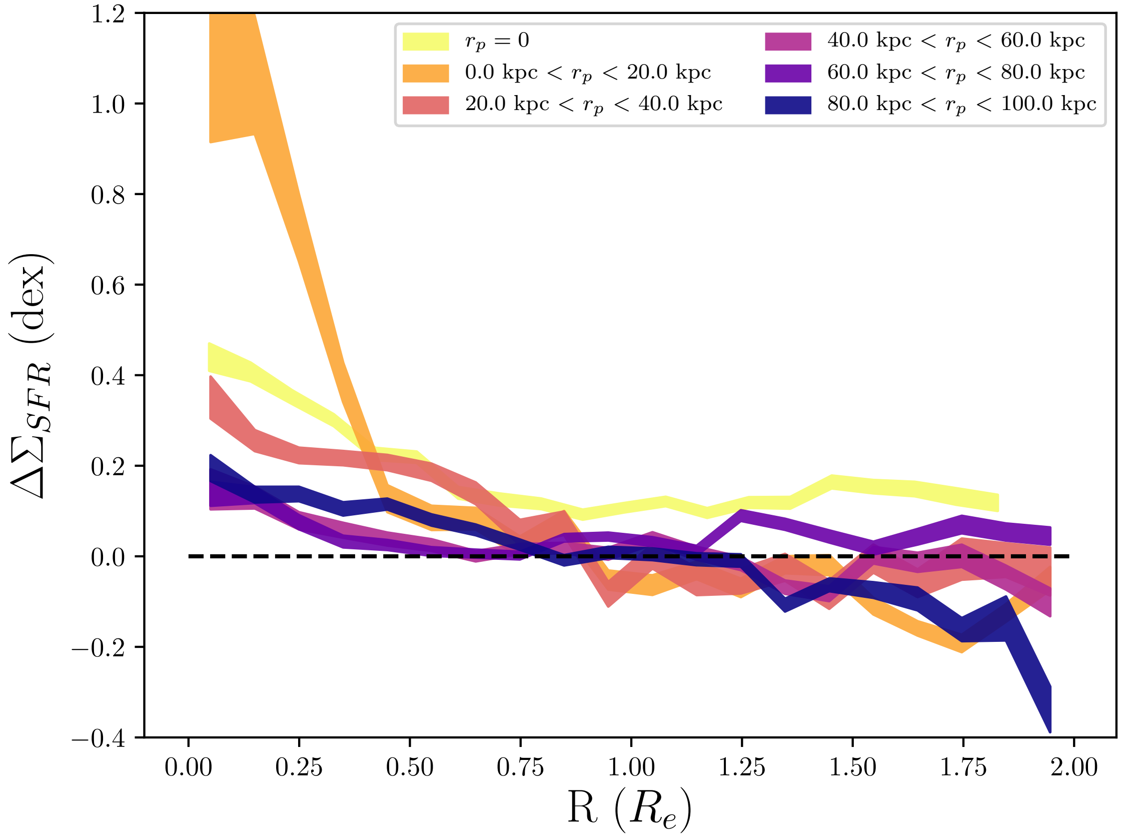

Figure 3.15: Radial profiles of $\Delta\Sigma_{\rm SFR}$ for all galaxy pairs, separated into bins of projected separation. IFU pairs are masked to remove contribution from the nearby companion. $r_p = 0$ kpc represents the post-merger sample. The width of the line represents the standard deviation in $\Delta\Sigma_{\rm SFR}$ in that radius bin, divided by the square root of the number of spaxels in that bin.

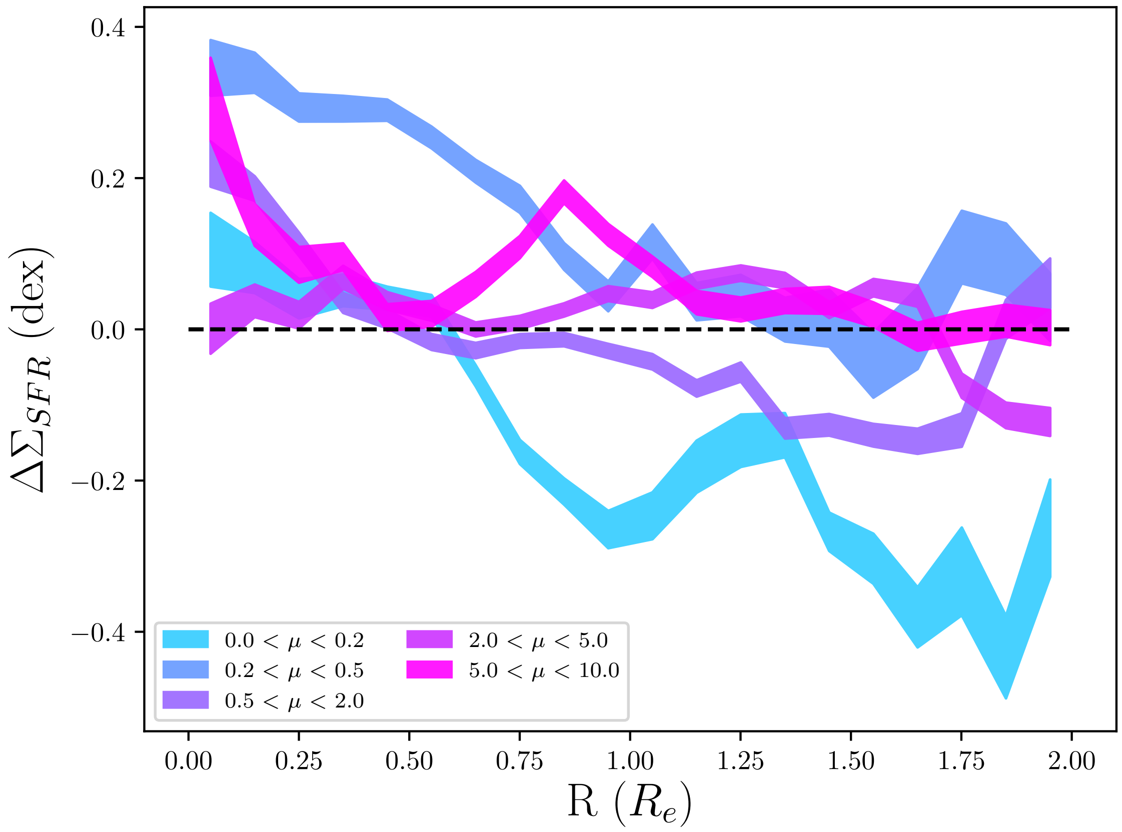

Figure 3.16: Radial profiles of $\Delta\Sigma_{\mathrm{SFR}}$ for all galaxy pairs, separated into bins of mass ratio. IFU pairs are masked to remove contribution from the nearby companion. The width of the line represents the standard deviation in $\Delta\Sigma_{\mathrm{SFR}}$ in that radius bin, divided by the square root of the number of spaxels in that bin.

yond that, however, there is no clear trend between μ and ΔSFR. Clearly both μ and r_p are influencing $\Delta\Sigma_{\mathrm{SFR}}$, however the current sample size is too limited to create a plot that separates mergers based on two parameters, that also has statistically significant results.

3.3.2 O/H Profiles

Post-merger galaxies experience a suppression in metallicity that corresponds to the enhanced SFR (see Figure 3.16). Profiles of Δ O/H are constructed for the interacting pairs to see if a similar relationship exists in the earlier stage of the interaction. Figure 3.17 displays Δ O/H profiles binned by r_p to examine the different interaction stages. Galaxies with 0 kpc $< r_p <$ 20 kpc have a significant metallicity suppression (Δ O/H~ -0.2) in the inner regions, in correlation with the strong central starburst experienced by galaxies at this r_p. This suggests that, as with post-merger galaxies, the inflow of low-metal gas fuels the central starburst. Interestingly, despite the central enhancement in SFR for galaxies with 20 kpc $< r_p <$ 40 kpc, the metallicity is actually enhanced in the centre (both Δ O/H and $\Delta\Sigma_{\mathrm{SFR}}$ are enhanced to $0.5R_e$). The variation could be indicative of more complex gas distribution across the galaxys surface. The interacting galaxies have consistently larger Δ O/H values than post-merger galaxies, beyond $0.5R_e$, although the cause is unclear given there is no correlation with Δ O/H enhancement in r_p.

Radial profiles are also binned by mass ratio to disclose the ramifications of progenitor qualities, see Figure 3.18. Despite having continuous enhancement in SFR, galaxies with $0.2 < \mu < 0.5$ experience both enhancements and suppression in metallicity. There is no clear correlation between Δ O/H and $\Delta\Sigma_{\mathrm{SFR}}$ for mass ratio bins, implying that mass ratio does not influence the metallicity offset either. A more useful comparison would be the gas fraction offset of spaxels, which would truly trace the low metal gas that fuels the merger.

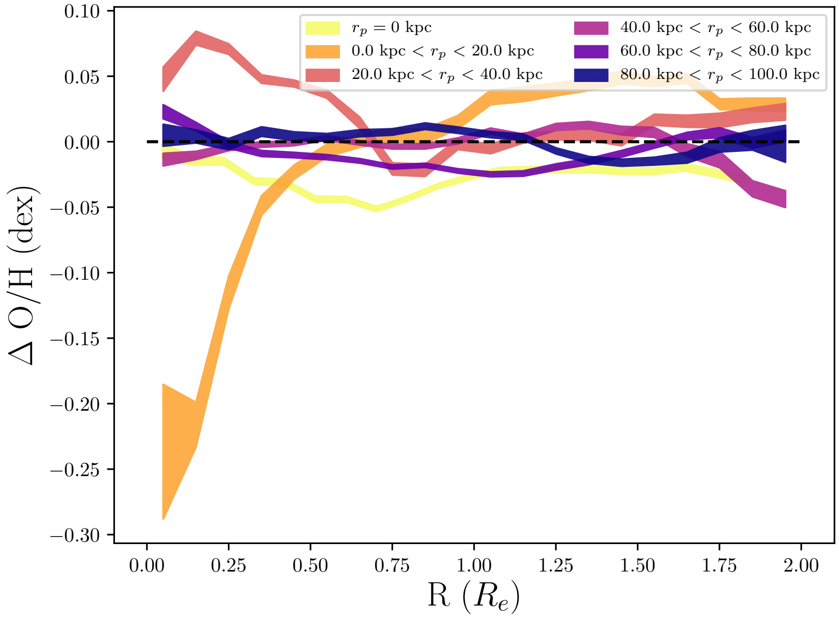

Figure 3.17: Radial profiles of Δ O/H for all galaxy pairs, separated into bins of projected separation. $r_p = 0$ kpc represents the post-merger sample. The width of the line represents the standard deviation in Δ O/H in that radius bin, divided by the square root of the number of spaxels in that bin.

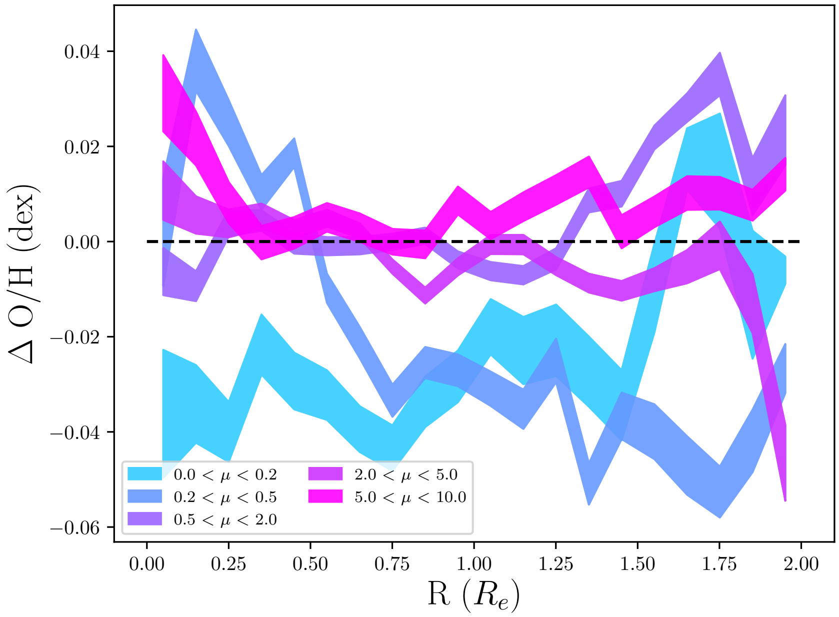

Figure 3.18: Radial profiles of Δ O/H for all galaxy pairs, separated into bins of mass ratio. The width of the line represents the standard deviation in Δ O/H in that radius bin, divided by the square root of the number of spaxels in that bin.

Chapter 4

Future Work

Chapter 3 presented a preliminary analysis of $\Delta\Sigma_{\mathrm{SFR}}$ and Δ O/H profiles for galaxy pairs. There are trends for enhanced central SFR with decreasing r_p, but the outskirts show no clear trend with r_p beyond being generally suppressed. No obvious trend in radial changes with μ exists either, though there are some hints that the smaller galaxy ina pair experiences greater effects. Global spectroscopic studies of mergers find correlation between enhancements in SFR and suppression in metallicity as a function of r_p and μ (Ellison et al., 2008a; Scudder et al., 2012; Patton et al., 2013). In this chapter I outline further tests that help further explore the results presented here, but which are beyond the scope of this work. Section 4.1 outlines how I will continue the pairs study using the 15th data release from MaNGA, almost doubling the sample size. Section 4.2 addresses the clearly disturbed galaxies pairs on an IFU that SExtractor failed to deblend, and how they may be included in future analysis of a pairs sample. One of the main obstacles to creating radial profile for merging galaxies is the dataproducts are at times asymmetric, so plotting a dataproduct as a function of a circular, uniform radius is misleading. Section 4.3 suggests a follow up project based on the study of galaxy mergers completed herein, mainly a more in depth look at merger morphology. Finally, Section 4.4 introduces the benefit of resolved molecular gas properties for understanding mergers, and the advantages of combined MaNGA - Atacama Large Millimeter Array (ALMA) observations to constrain the gas fraction and star-formation efficiency of merging galaxies.

4.1 Work with DR15

In December 2018, the 15th data release from SDSS was made public, along with ∼2000 new galaxies observed by MaNGA (Aguado et al., 2019). Given the time vi-

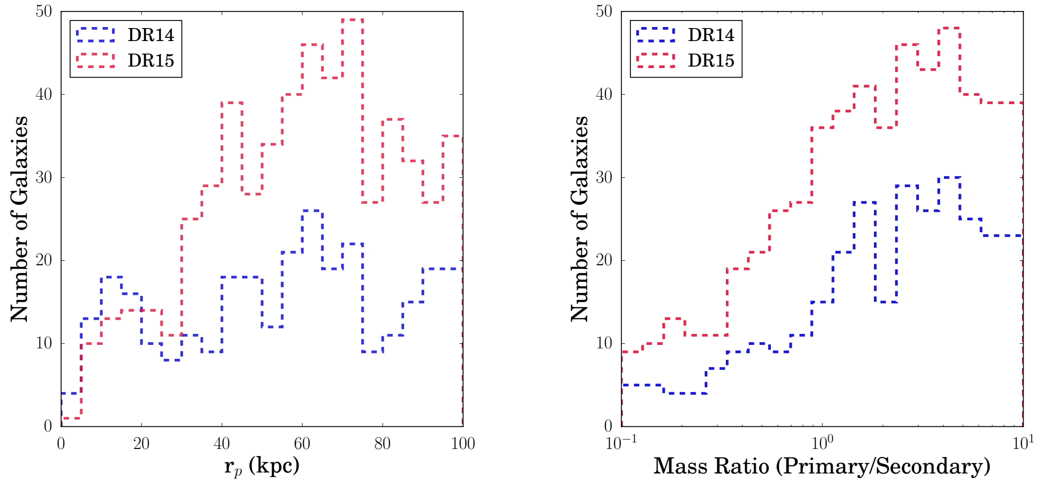

(a) r_p distribution of DR14(blue) and DR15(red)

(b) μ distribution

Figure 4.1: Spectroscopic pairs in DR15 (red) compared to the complete interacting pairs sample from DR14 (blue) adopted in Chapter 3.

sual classification and mass masking required for DR14, and the timing of the data release in respect to the end date of this project, sufficient time was not available to incorporate DR15 into this thesis. However, given the percentage of galaxy mergers in the DR14 study, I can estimate the size of the merger sample including new DR15 galaxies. Selecting a sample of spectroscopic galaxy pairs by matching galaxies within the Patton et al. (2016) to those in MaNGA DR15 is easily done with current information from both catalogues. Implementing a $0.1 < \mu < 10$, $\Delta v < 500$ km/s, and $r_p < 100$ kpc cut yields a sample of 554 spectroscopic galaxy pairs in DR15, almost twice as many as in DR14. Figure 4.1 presents the distribution in r_p and μ for this sample of DR15 spectroscopic pairs in comparison to the DR14 spectroscopic and IFU pairs sample identified in Chapter 2. The r_p distribution of DR15 is about the same as that in DR14 for $r_p < 30$ kpc, but significantly greater for all other r_p (see Figure 4.1a). This offset is created by IFU pairs in DR15 that are not included in Patton et al. (2013), and need to be visually classified from DR15 and properly deblended before any proper pairs analysis can be performed. Post-merger galaxies could also be visually classified from DR15, and based on the fraction of new spectroscopic pairs it is likely the post-merger sample would double in size.

The larger sample size could help mitigate particular populations dominating the behaviour in r_p and μ bins. Figures 3.15 and 3.17 both display sharp peaks in $\Delta\Sigma_{\rm SFR}$

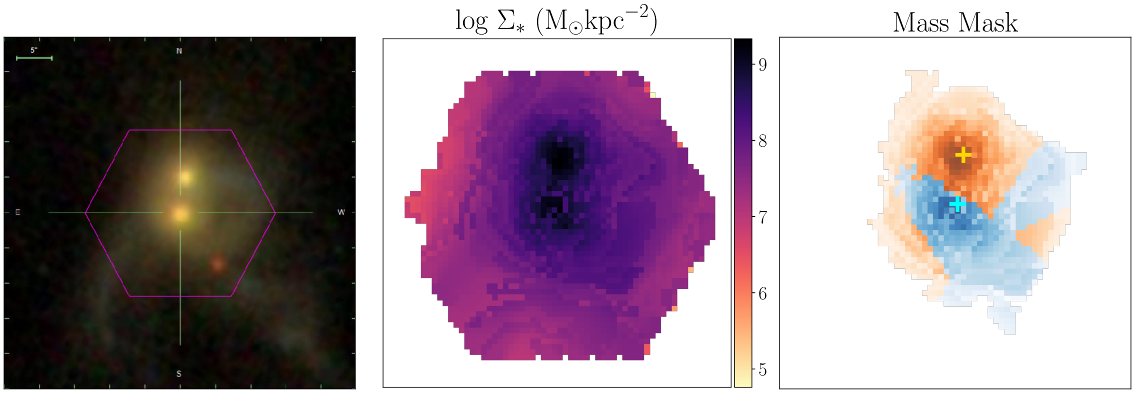
$\log \Sigma_* \ (\mathrm{M}_\odot \mathrm{kpc}^{-2})$

Mass Mask

Figure 4.2: An example of a highly disturbed galaxy where an accurate mask cannot be made. From left to right: the gri-image of the galaxy, the mass map of the galaxy, and the mask crated by SExtractor from this map.

and Δ O/H for galaxy pairs where $r_p < 20$ kpc, showing offset even greater than those in the post-merger sample. Likely a handful of highly star-forming galaxies dominate the spaxel contribution at very small R_e, contributing to unexpected peaks in offset that may decrease once the sample size at those R_e and r_p increases. At the smallest radial bin for $r_p < 20$ kpc, the median specific star formation is -9.85 $\log \mathrm{yr}^{-1}$, compared to the median specific star formation is -10.35 $\log \mathrm{yr}^{-1}$ beyond that radial bin. The bias in sSFR is further evidence that more variables need to be analyzed in conjunction (such as μ, r_p, ΔSFR and more) rather than individually.

4.2 Interacting Galaxies Without Mass Ratios

In Chapter 3 a small sample (14) of galaxies with clear morphological indicators of an interaction failed to be properly masked by SExtractor. Either the mass ratio of the interacting pair was too small to be included in the analysis sample, or the mask did not properly represent the gri-image of the galaxy. Some of these failed mask cases could not be properly discerned even by the human eye: although there are two clear nuclei on the galaxy, the two galaxies are so mixed and disturbed it is not clear which spaxels belong to which galaxy (see Figure 4.2 for an example). It is likely there will be twice as many cases like this once the new DR15 MaNGA observations are included.

The tidal disturbances of both the target and companion galaxy in failed mask pairs indicates that an interaction has recently occurred; intuitively the pair either just experienced a first or second pericentric passage. The stage right before coalescence is most likely dominated by galaxies so highly disturbed SExtractor fails to construct a reliable mass map, and represents a crucial step in the interaction process. Although r_p could be measured to include these galaxies in the analysis, results could be misleading if spaxels from these cases were combined with close pairs approaching their first interaction. This is especially difficult considering the closest pairs approaching interaction are properly deblended, whereas contribution from the companion galaxy for the disturbed cases could not be removed. A metric to quantify merger stage beyond projected separation would greatly benefit such a pairs study, but is a complex enough problem to warrant its own study.

4.3 Intricacies of Morphology

Radial profiles such as the ones employed here are commonly used for statistical studies of IFS data, so that spatially resolved data for hundreds of galaxies can be analyzed in a cohesive manner (Chown et al., 2019; Ellison et al., 2018a; Spindler et al., 2018). However, such studies hinge on the assumption that the information being compressed into a radial profile is axisymmetric. No analysis has been completed to check if IFS dataproducts such as SFR and metallicity are axisymmetric and conform to this assumption. The post-mergers in MaNGA are an example of where this assumption fails, where highly disturbed post-mergers have asymmetric distribution of $\Delta\Sigma_{\rm SFR}$ and Δ O/H (see Figure 2.8). Great benefit would come from checking which dataproducts fail to be axisymmetric, how many galaxies in a spatially resolved survey such as MaNGA adhere to this assumption, and what is unique about galaxies with asymmetries in particular dataproducts.

One possible route to scrutinize the spatial homogeneity of IFS data products is the measure their asymmetry. Many parameters have been designed to quantify the asymmetry of a galaxy. The simplest method measures an asymmetry parameter A calculated by computing the difference between the image of a galaxy $(I(i, j))$ and a duplicate of the image rotated 180 degrees around a central spaxel $(I_{180}(i, j))$ (Schade et al., 1995; Abraham et al., 1996; Bershady et al., 2000; Conselice et al., 2000). Translated to a mathematical formula, asymmetry (A) can be quantified with in the following manner:

$$A = \sum_{i,j} \frac{|I(i,j) - I_{180}(i,j)|}{|I(i,j)|} - B_{180} \tag{4.1}$$

where B_{180} is the asymmetry in the background. Merging galaxies tend to have a high asymmetry (A >0.35) compared to related spiral and elliptical galaxies (A <0.2) (Lotz et al., 2008).

Simard et al. (2002) implement a different method for quantifying asymmetry, R_A, which measures the fraction of light left in an image after a single component Sérsic fit is subtracted from the image to leave only the asymmetric component. Both A and R_A utilize flux measurements from all locations in a galaxy. However, asymmetries which result from interactions are often faint features at large radii that contribute less to the flux. In order to represent these fainter, outer features, Pawlik et al. (2016) adopt a method to measure the shape asymmetry (A_s) from a binary detection mask of the galaxy, such that all intensity regions contribute evenly to the image. A_s can only measure the overall shape of the object, not any asymmetry in the light distribution. However, it more easily picks up faint features like shells and tidal tails. A_s more accurately selects galaxy mergers, with A_s >0.2 selecting 95% of galaxy mergers, compared to the 35% identified by A (Pawlik et al., 2016).

Combining A with another morphological parameter can improve the selection completeness of galaxy mergers (Lotz et al., 2004). The distribution of A with the concentration index C is very different for major galaxy mergers in comparison to isolated galaxies, and can also help distinguish late-type and early-type galaxies (Conselice et al., 2003). Concentration index C measures the ratio of light within an inner aperture in respect to the light in an outer aperture, the sizes of which can vary depending on the purpose of the study. Galaxies with a large concentration ($C \sim 4 - 6$), tend to be bulge-dominated, early type galaxies (Lotz et al., 2008). A common method for measuring C uses an inner aperture that is 20% the Petrosian radius, and an outer aperture that is 80% the Petrosian radius (see equation 4.2) (Bershady et al., 2000).

$$C = 5 \log \frac{r_{80}}{r_{20}} \tag{4.2}$$

The Gini (G) coefficient is similar to the concentration index in that it measures the relative distribution of flux intensity within a galaxy, however it does not assume the geometric centre of the target is the centre of the distribution (Lotz et al., 2004). G is often paired with the morphology parameter M_{20}, which quantifies the second order moment of the brightest 20% of the galaxy and identifies tidal features or multiple nuclei (Lotz et al., 2004, 2010b).

The asymmetry of a galaxy tends to increase as the separation from a nearby companion decreases (De Propris et al., 2007; Ellison et al., 2010; Casteels et al., 2014; Patton et al., 2016). Once $r_p > 50$ kpc, R_A becomes enhanced compared to a control sample and increases until R_A is twice as large in a merger than an isolated galaxy at $r_p = 5$ kpc (Patton et al., 2016). It is possible that the asymmetry - r_p anti-correlation is also present in $\Delta\Sigma_{\rm SFR}$. Galaxies in pairs have occasionally shown asymmetry in the distribution of anomalously low metallicity regions (equivalent to Δ O/H << 0 regions), such that the side of the galaxy closer to the companion has generally lower metallicity than on the opposite side of the galaxy (Hwang et al., 2018). This is a good indicator that the asymmetry-r_p anti-correlation could exist in other properties of the galaxy, particularly those properties most impacted by merging events (see figure 4.3 for an example).

Chapters 2 and 3 demonstrate that galaxy mergers have central enhancements in $\Delta\Sigma_{\rm SFR}$, which could result in a larger concentration index for $\Delta\Sigma_{\rm SFR}$ of interacting galaxies. However, starburst galaxies (even those not in interactions), have been shown to contain similar central SFR enhancements (Ellison et al., 2018a). In future work I will use a variety of morphological metrics, such as those described above, to test whether the distribution of enhanced star-formation is similar between general starbursts and interaction-induced starbursts. With this information I could test whether radial $\Delta\Sigma_{\rm SFR}$ profiles for starbursts and mergers show more variety once complex spatial distributions are taken into account.

4.4 Benefits of Molecular Gas Studies

The central enhancement in $\Delta\Sigma_{\rm SFR}$ for interacting galaxies, observed in Chapter 2 and 3, is presumed to result from the gas inflow created by the gravitational torque of non-axisymmetric structures created in the interaction (Barnes & Hernquist, 1991; Mihos & Hernquist, 1996), and the subsequent increase in central gas supply to fuel the starburst. Although most simulations agree with a merger induced central starburst, some simulations have demonstrated that the efficiency at which gas forms stars drives the star-formation rate, in particularly stellar feedback efficiency regulates whether

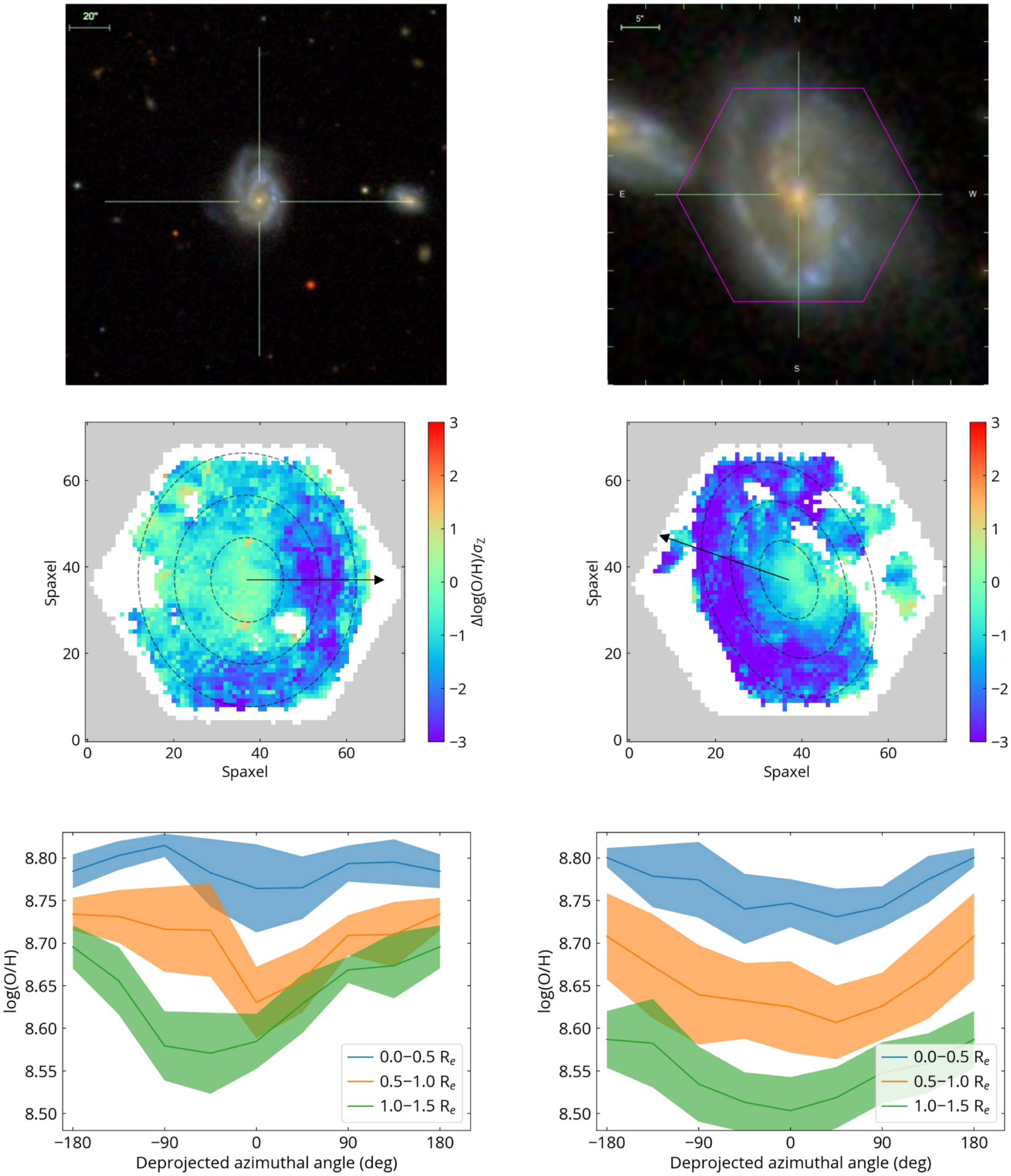

Figure 4.3: $\Delta O/H$ maps for two galaxies in close pair systems. Anomalously Low Metallicity (ALM) regions tend to be on the side closer to the companion galaxy, indicating that the interaction is already affected the host metallicity. Unlike post-merger galaxies, the metallicity in the centre is about regular. Source: Hwang et al. (2018).

gas regions reach star-forming densities (Cox et al., 2006; Di Matteo et al., 2007). The star-formation efficiency (SFE) is measured by dividing the star-formation rate by the molecular gas mass, proving the inverse of depletion time for the gas content in a galaxy. Shocks and flows created in a merger event increase the gas turbulence such that gas clouds become denser, decreasing the free fall time and, as a result, the depletion time. The same shocks and flows could also trigger HI to transition to H_2, leading to an increase in the molecular gas fraction (Powell et al., 2013). The relationship between gas fraction and SFE, and which/both regulate SFR, is still contested.

Single dish radio telescopes have been used to examine the total molecular gas fraction and SFE of merger galaxies, but small sample sizes have led studies to draw conflicting conclusions about which mechanism is the dominant regulator of SFR (Braine & Combes, 1992; Casasola et al., 2004; Huchtmeier et al., 2008). Global studies have demonstrated that the gas fraction in both galaxy pairs and post-mergers is enhanced compared to a control star-forming sample (Pan et al., 2018; Ellison et al., 2018b). Other global studies found increased gas fraction and SFE in interacting galaxies, but these enhancements were consistent with non-mergers with elevated SFRs, indicating that both external forces and internal processes regulate gas fraction and SFE (Violino et al., 2018).

Spatially resolved studies of molecular gas and SFE can shed light on the internal processes that regulate star-formation, as well as the spatially resolved effects on an interaction on molecular gas and SFE. The EDGE-CALIFA survey combines IFS data from CALIFA with molecular gas measurements from the Combined Array for Research in Millimeter-wave Astronomy (CARMA) observatory (Bolatto et al., 2017). Utomo et al. (2017) identified a small (14 galaxies) sample of EDGE-CALIFA galaxies that had greater central SFE than that in the disk, the majority of which were morphologically disturbed (indicating the presence of a bar, or recent interaction). Observations of early type galaxies with particularly low star-formation efficiencies, made with the Atacama Large Millimeter Array (ALMA), revealed spatial asymmetries such as gas clouds and kinematic warps (van de Voort et al., 2018). These create dynamical effects which prevent the gas reservoir from collapsing, consequently the star-formation efficiency is very low.

I am a co-investigator on an ALMA cycle-6 observation, which collected molecular gas information for 16 local starburst galaxies, 2 of which are post-mergers. Both post-mergers, along with their MaNGA Σ_{SFR} measurements, molecular gas surface density, and SFE are displayed in Figure 4.4, in comparison to an undisturbed starburst galaxy. Molecular gas surface density is derived from the CO luminosity measurement observed by ALMA using the constant conversion factor $\alpha = 4.3\ \mathrm{M}_{\odot}\mathrm{pc}^{-2}$ (though determining the "best" conversion factor for varying galaxies can be complicated (Bolatto et al., 2013)). Interestingly, the distribution of SFE is highly asymmetric in both post-mergers, whereas the isolated galaxy displays an axisymmetric SFE distribution. Further work is required to analyze the SFE and gas fraction of these galaxies (in particular, defining an offset as the result of the merger event), but the initial difference between the post-mergers and isolated galaxy foretells the interesting results that could come from a larger, more diverse sample of post-merger galaxies observed with ALMA.

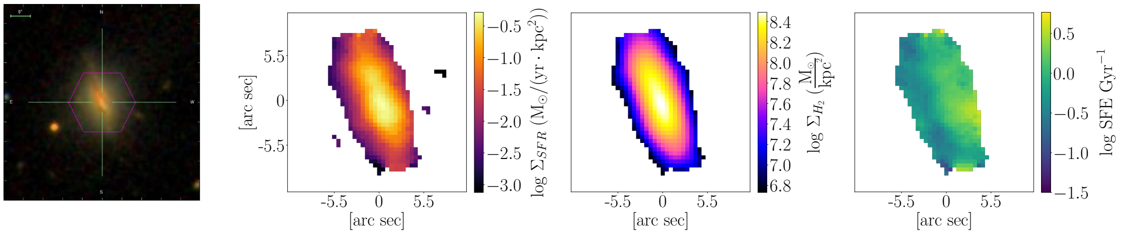

(a) Post-Merger

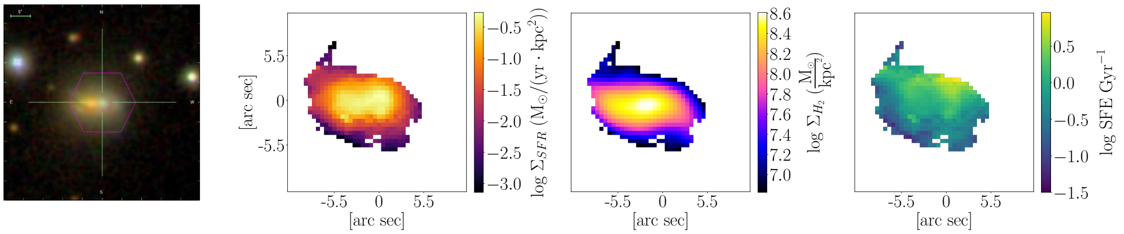

(b) Post-Merger

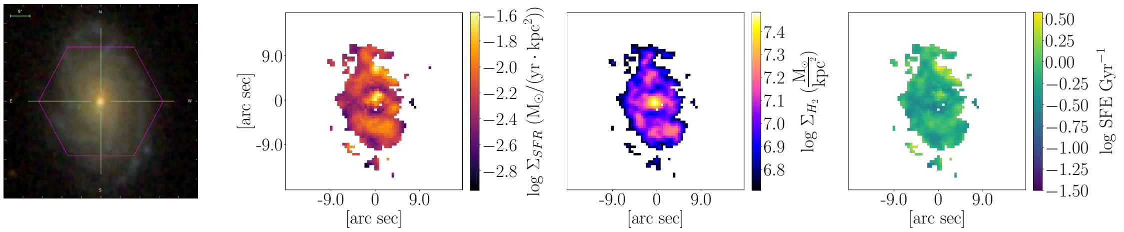

(c) Undisturbed Starburst Galaxy

Figure 4.4: MaNGA and ALMA observations for two post-mergers (top two rows) and one starburst galaxy (bottom row). From left to right: the gri-image of the galaxy, Σ_{SFR} computed from MaNGA, H_2 surface density measured from ALMA, and SFE for each spaxel, computed by dividing the Σ_{SFR} in each spaxel by Σ_{H_2} in each spaxel.

Chapter 5

Conclusions

I have presented the first analysis of full radial profile information for a statistically significant post-merger sample (Chapter 2). Using PIPE3D dataproducts, enhancements/deficits in SFR and O/H were quantified for ∼20,000 spaxels in post-merger galaxies in MaNGA. Enhancements/deficits were defined by the offset from the well established relationships between O/H, Σ_{SFR}, and Σ_{*}. On average post-mergers are enhanced in SFR, both in the centres predicted by simulations and global spectroscopic studies, and extended to 1.9 R_e (Figure 2.11). However, both enhancements and deficits in SFR can occur in the outer regions (Figure 2.9), which could be connected to the time since coalescence or the progenitor qualities. In correlation with the central starburst, the metallicities of post-mergers are generally suppressed by ~ -0.4 dex (Figure 2.15). Analysis of the post-merger sample reveals that star-formation can be clumpy, centrally offset, and asymmetric, which influence the outer $\Delta\Sigma_{\mathrm{SFR}}$ values in particular. These results motivate development of a more complex analysis of the spatial distribution of post-merger galaxies than the currently implemented radial profiles.

Chapter 3 extends the mergers sample to include galaxy pairs, defined as interacting based on r_p, Δv, and μ cuts. A sample of spectroscopic pairs is collected from the Patton et al. (2016) catalogue, and a second sample of IFU pairs is visually classified as having two galaxies on the IFU. I address the obstacle of analyzing IFU pairs, where MaNGA observations contain contribution from two galaxies rather than one, by using SExtractor to deblend the two galaxies and assign each spaxel to the target or companion galaxy. This method both removes contribution from the bright centre of the companion in the profile, as well as produces a better representation of the target total stellar mass (Figure 3.7). As noted in global spectroscopic observations, the SFR enhancement is greatest for the smallest r_p (Barton et al., 2000; Lambas et al., 2003; Ellison et al., 2008a; Jogee et al., 2009; Robaina et al., 2009; Woods et al., 2010; Scudder et al., 2012; Patton et al., 2013). This trend is reproduced by the $\Delta\Sigma_{\rm SFR}$ profiles, which exhibit a central SFR enhancement that is largest for the smallest r_p. There is also a distinct trend towards suppressed SFR in the outskirts of the interacting galaxies, though no trend with the strength of the suppression and r_p is apparent. The analysis is repeated using bins of μ, where no clear relationship between $\Delta\Sigma_{\rm SFR}$ distribution and μ is apparent. The central $\Delta\Sigma_{\rm SFR}$ has no correlation with μ either, despite observational studies finding that larger galaxies in a pair experience a stronger starburst. Radial profiles of Δ O/H are equally ambiguous.

I have outlined prospective tests that could further investigate the spatial distribution of $\Delta\Sigma_{\rm SFR}$ and Δ O/H, and their relation to r_p and μ. The 15th data release of MaNGA will double the current sample size, mitigating any small number statistics in particular r_p and μ, as well as homogenizing the galaxy populations in each bin. I also address the hindrance of non-axisymmetric dataproducts, the finer effects of which are lost in radial profile analysis of post-merger and pair galaxies. No analysis of the asymmetry or concentration has been completed for the dataproducts of IFS observations, yet radial profiles are widely used in contemporary spatially resolved studies. Not only would symmetry tests check the validity of radial profile analysis, it could also identify merging galaxies at different stages of the interaction.

Finally, I propose an analysis of ALMA observations of MaNGA galaxies such that spectroscopic properties can be examined in conjunction with molecular gas. Throughout Chapters 2 and 3, I briefly mention how metallicity can reflect the movement and distribution of low-metal gas that fuels star-formation. To acquire a true understanding of the molecular gas content of a galaxy, and how efficiently it is fuelling star-formation, radio observations are required to measure CO and calculate the H_2 surface density distribution for an interacting galaxy sample. CO measurements for local galaxies with ALMA can take anywhere from 40 minutes to 5 hours, so collecting a large sample of diverse galaxies is observationally expensive. However, the benefit a $\sim$20 galaxy merger sample with Σ_{H_2} and $\Sigma_{\rm SFR}$ down to $\sim$1.5 kpc would be indispensable to our current understanding of how interaction influence different galaxy populations.

Appendix A

Additional Information

A.1 MaNGA Sample Size

The MaNGA sample size was designed with the goal that each principal component of galaxy population (stellar mass, SFR, environment) could be divided into 6 bins, each with a number of galaxies in each bin to assure that the single-measurement precision is approximately equal to the expected difference in the signal from bin to bin. The significance of a detected difference between bins is $\sqrt{n/2}$, with n representing the number of galaxies in the bin of interest. As an example, let us consider a measurement of stellar age. The desired precision for the stellar age gradient, based on variation in the quantity among currently studied galaxies (Kuntschner et al., 2010; Spolaor et al., 2010), is 0.1 dex per decade in R_e. Thus, to achieve a 5σ detection we need 50 galaxies in each bin for our three principal components. We then multiply n=50 by the number of bins to sample all galaxy populations (6^3), resulting in a sample size of 10,800 galaxies.

A.2 Radial Profile Distributions

Radial profiles are constructed for spaxel dataproducts by determining the median spaxel value within a set radius bin (R_e in most cases). To determine the extent of the radial profiles, the spaxel count distribution as a function of radius is plotted, a Gaussian profile is computed for that distribution using SCIPY STATS[1] function NORM, which outputs a σ value that can be used to limit the radial profile to 2σ. Figure A.1 reproduces the $\Delta\Sigma_{\mathrm{SFR}}$ profile for post-merger galaxies, overlain with the spaxel count distribution and the appropriate radius cut at 2σ.

---

[1] `http://www.scipy.org/`

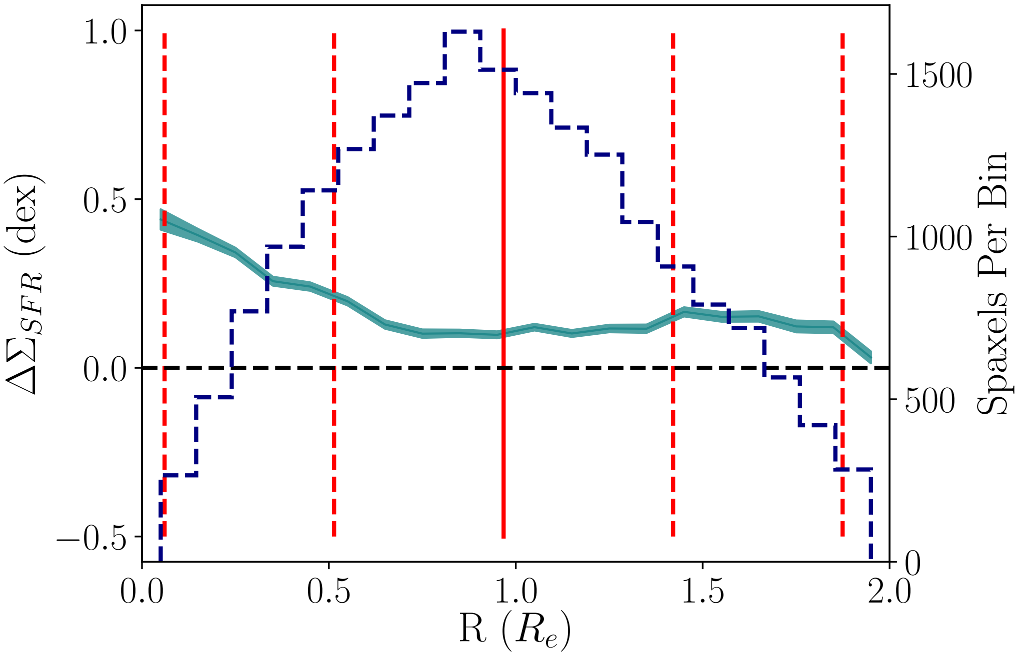

Figure A.1: $\Delta\Sigma_{\rm SFR}$ profile for post-merger galaxies as a function of R_e in teal. The blue dashed histogram represents the spaxel count in each radial bin. The mean R_e value is represented by a solid red line, and the median plus/minus 1σ and 2σ are represented with dashed red lines.

A.3 NSA Sérsic M_* and PIPE3D M_* Comparison

PIPE3D and the NSA catalogue use different initial mass function (IMFs), the Salpeter IMF (Salpeter, 1955) and the Chabrier IMF (Chabrier, 2003), respectively. Chabrier masses can be converted to Salpeter masses by dividing by 0.61 (Madau & Dickinson, 2014). Figure A.2a compares the NSA Sérsic M_* and PIPE3D M_* once the NSA Sérsic M_* has been converted to Salpeter. The offset in the lower and higher mass galaxies has been previously noted in the PIPE3D literature (see `https://www.sdss.org/dr14/manga/manga-data/manga-pipe3d-value-added-catalog/` for details). A linear fit is applied to this sample to quantify these offsets. NSA Sérsic masses are further corrected to match the PIPE3D masses by adding or subtracting a set value based on this fit. The final NSA Sérsic M_*s used as comparisons are exhibited in Figure A.2b. Equation A.1 outlines the method to convert the NSA Sérsic M_* for comparison with PIPE3D.

$$\log M_{\mathrm{NSA,\ converted}} = 0.775230 \log \left(M_{\mathrm{NSA}}/0.61 \right) + 2.329139 \tag{A.1}$$

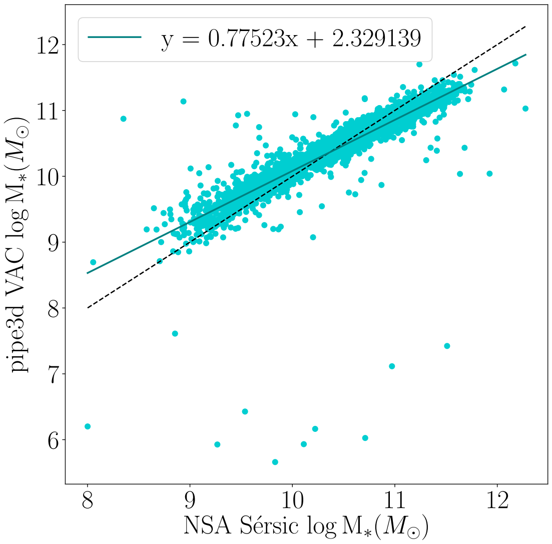

(a) Comparison of the PIPE3D M_* and NSA Sérsic M_* converted to the Salpeter IMF, with a dashed black line representing where the two are equal. A linear function is fit to the data to quantify any remaining differences between the two, with the slope and intercept of this fit provided in the legend.

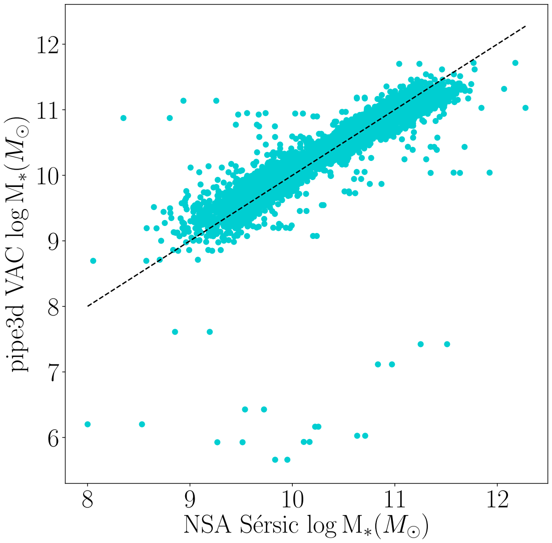

(b) Comparison of the PIPE3D M_* and NSA Sérsic M_* converted to the Salpeter IMF and corrected based on the fit in Figure A.2a.

Figure A.2: NSA Sérsic M_* to PIPE3D M_* conversion process.

A.4 MaNGA Post-Mergers Catalogue

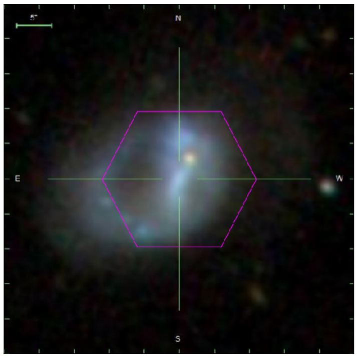

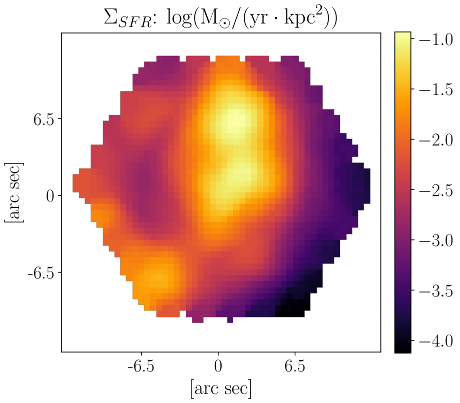
Σ_{SFR}: log(M$_\odot$/(yr · kpc^2))

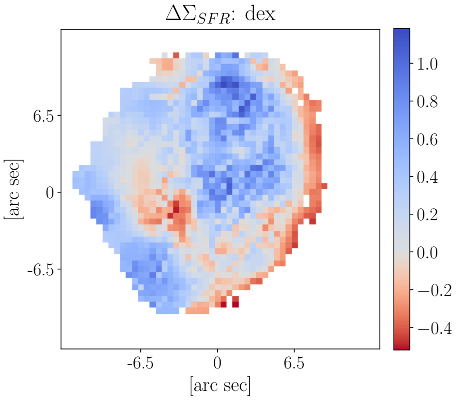
$\Delta\Sigma_{SFR}$: dex

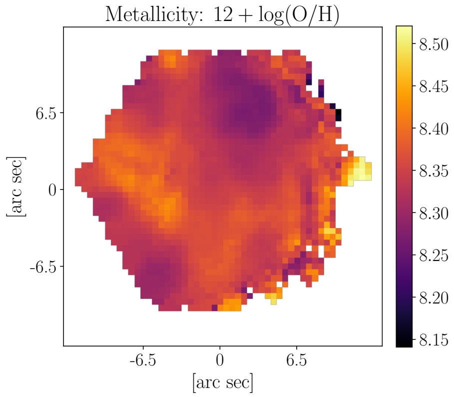
Metallicity: 12 + log(O/H)

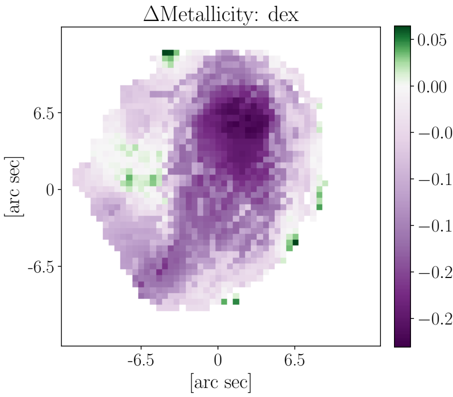
ΔMetallicity: dex

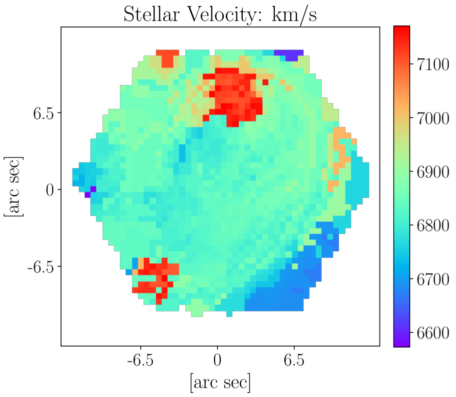
Stellar Velocity: km/s

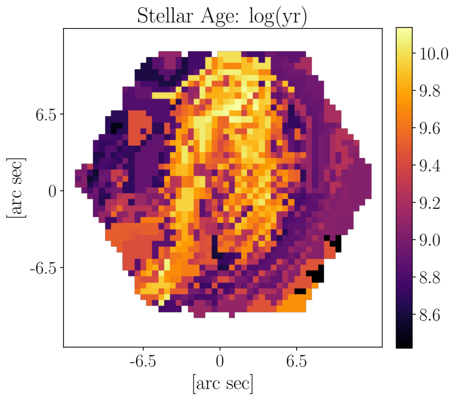
Stellar Age: log(yr)

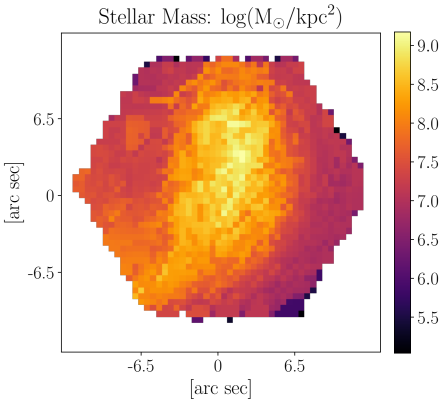
Stellar Mass: log(M$_\odot$/kpc^2)

Galaxy objID: 587725503945048077

plate-ifu: 7992-6102

RA: 253.889°

Decl: 63.2421°

z: 0.0227762

K03: SF

$\log \mathrm{M}_*$: 9.96784 $\log \mathrm{M}_\odot$

$\log \mathrm{SFR}$: 0.278572 $\log(\mathrm{M}_\odot/\mathrm{yr})$

O/H(KE08): 8.90902

Δ SFR: 0.67576

manga-id: 1-634299

Match separation: 0.328731"

Companion Flag: 0

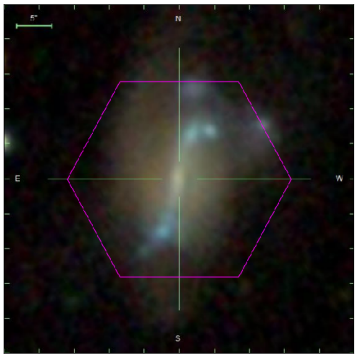

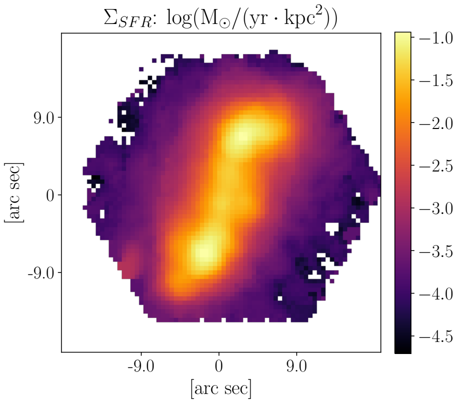

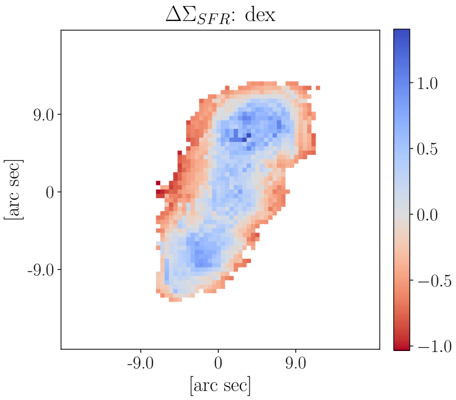

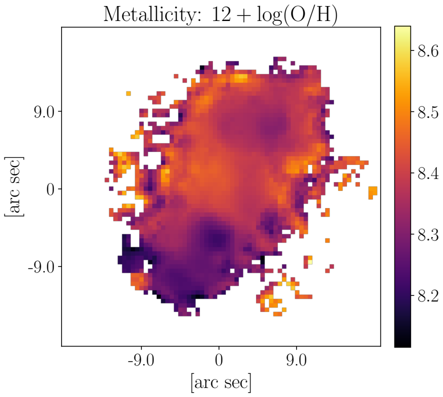

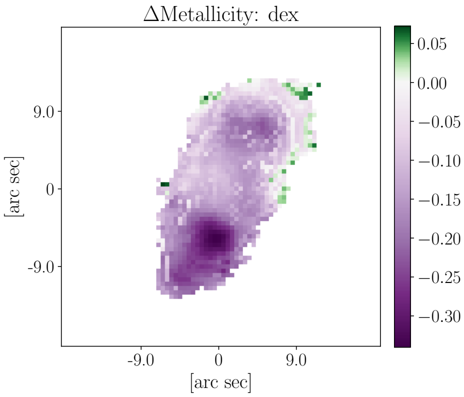

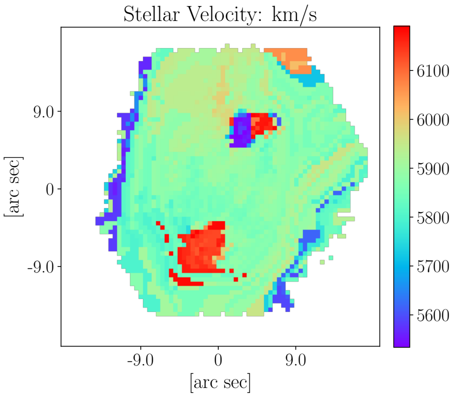

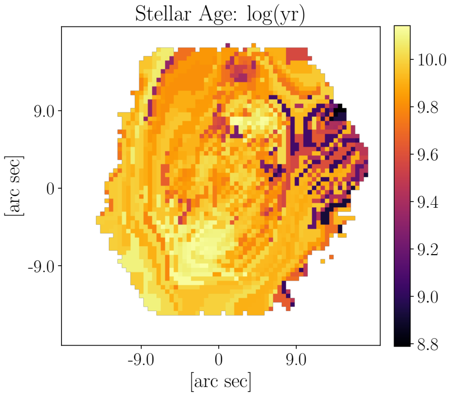

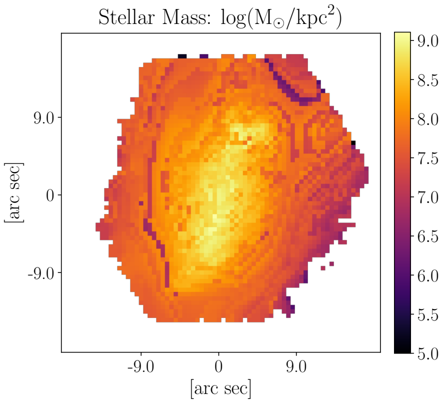

Galaxy objID: 587725552269459549
plate-ifu: 8719-12702
RA: 120.199°
Decl: 46.6905°
z: 0.0195836
K03: NULL
$\log M_*$: 10.0741 $\log M_\odot$
$\log SFR$: 0.164431 $\log(M_\odot/yr)$
O/H(KE08): nan
Δ SFR: 0.29223
manga-id: 1-44745
Match separation: 0.243406”
Companion Flag: 0

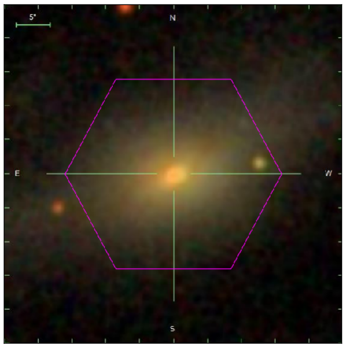

Σ_{SFR}: log(M$_\odot$/(yr · kpc^2))

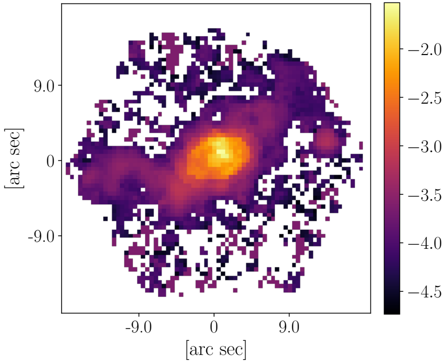

$\Delta\Sigma_{SFR}$: dex

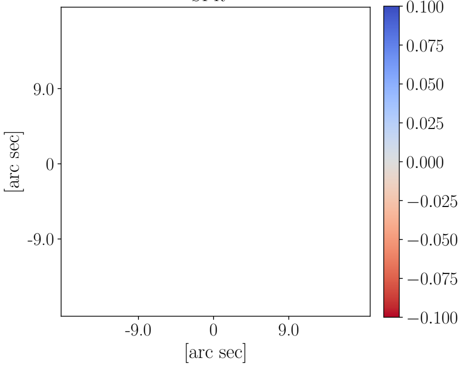

Metallicity: $12 + \log(\mathrm{O/H})$

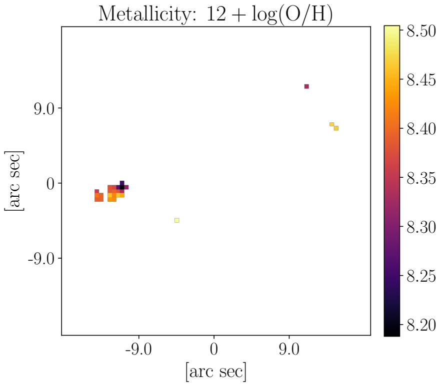

ΔMetallicity: dex

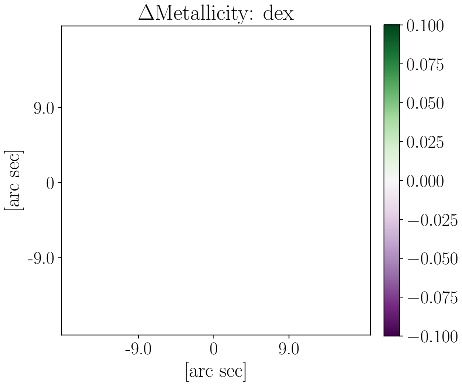

Stellar Velocity: km/s

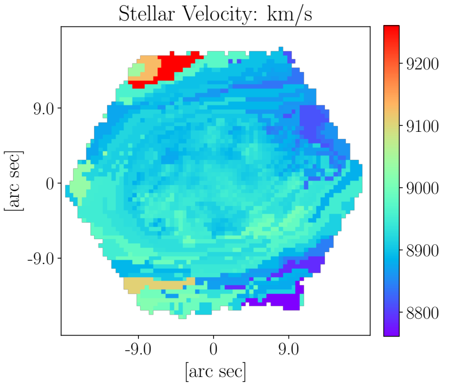

Galaxy objID: 587725578037231676

plate-ifu: 7990-12705

RA: 264.68°

Decl: 57.2392°

z: 0.0297794

K03: NULL

$\log \mathrm{M}_*$: 10.6043 $\log \mathrm{M}_\odot$

$\log \mathrm{SFR}$: -0.848922 $\log(\mathrm{M}_\odot/\mathrm{yr})$

O/H(KE08): nan

Δ SFR: nan

manga-id: 1-24476

Match separation: 0.151054”

Companion Flag: 0

Stellar Age: log(yr)

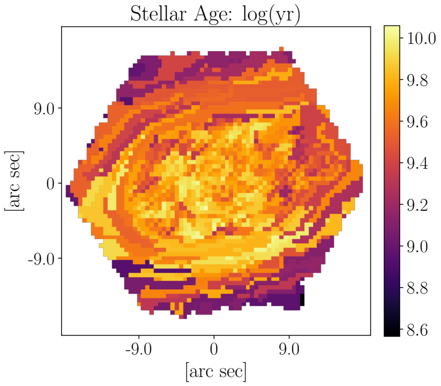

Stellar Mass: log(M$_\odot$/kpc^2)

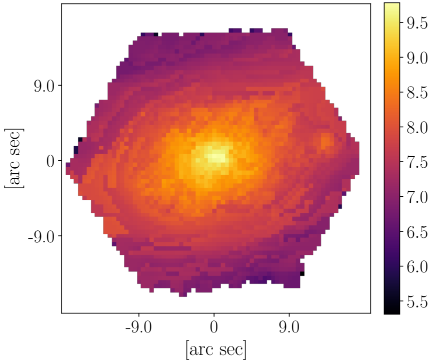

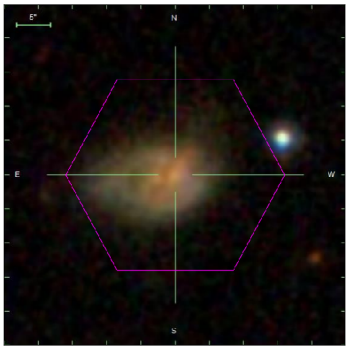

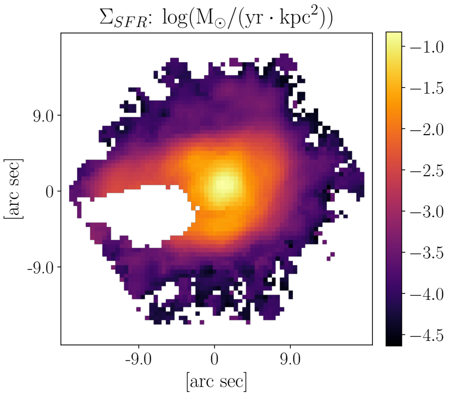
Σ_{SFR}: log(M$_\odot$/(yr · kpc^2))

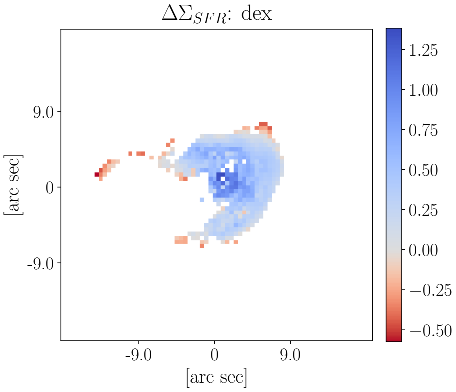
$\Delta\Sigma_{SFR}$: dex

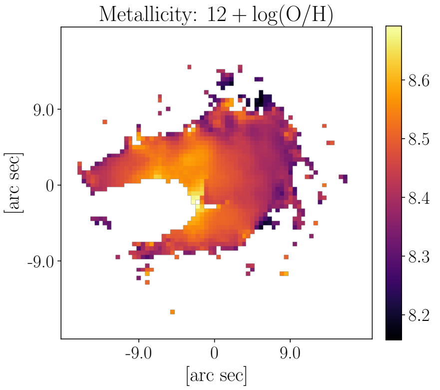
Metallicity: $12 + \log(\mathrm{O/H})$

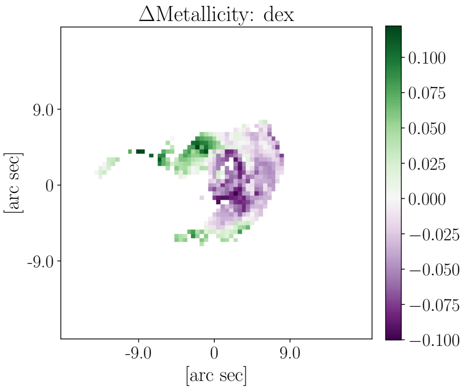
ΔMetallicity: dex

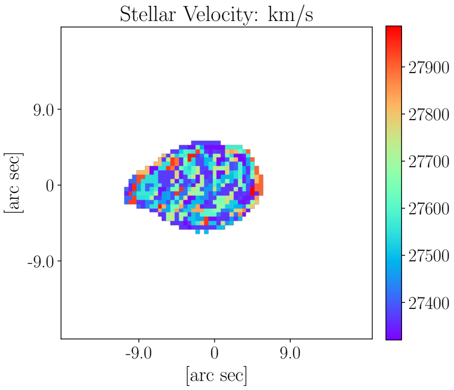
Stellar Velocity: km/s

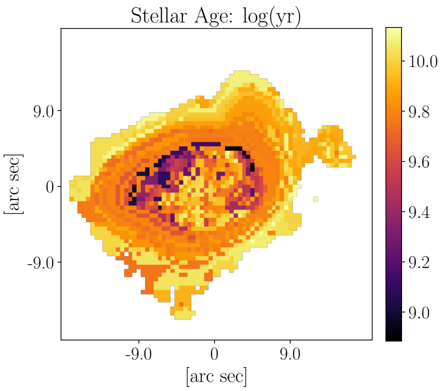
Stellar Age: log(yr)

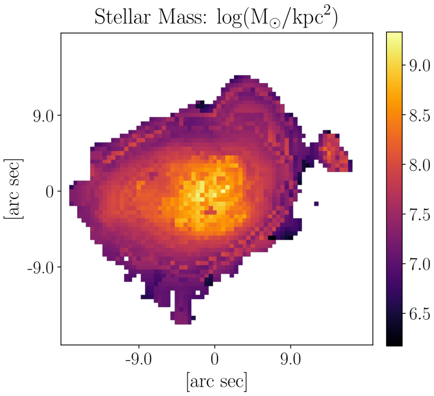
Stellar Mass: log(M$_\odot$/kpc^2)

Galaxy objID: 587727220864909648

plate-ifu: 7977-12701

RA: 332.602°

Decl: 11.7131°

z: 0.0915773

K03: SF

log M_* : 11.1148 log M$_\odot$

log SFR : 1.08718 log(M$_\odot$/yr)

O/H(KE08): 8.96443

Δ SFR: 0.17989

manga-id: 1-114955

Match separation: 0.171674"

Companion Flag: 0

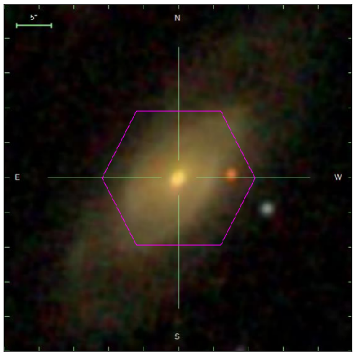

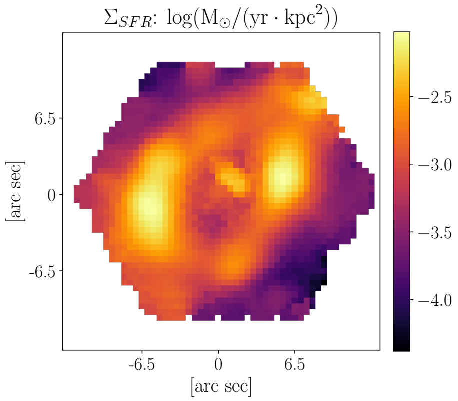
Σ_{SFR}: log(M$_\odot$/(yr · kpc^2))

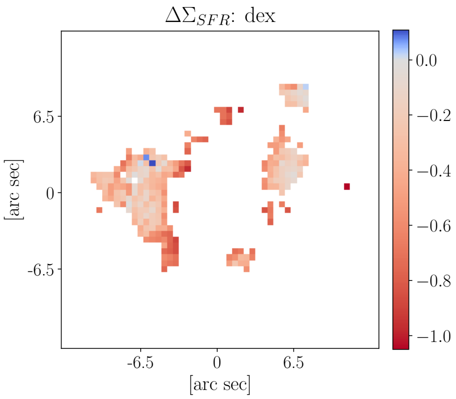
$\Delta\Sigma_{SFR}$: dex

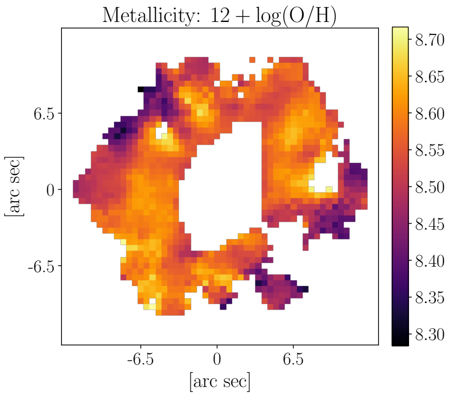
Metallicity: $12 + \log(\mathrm{O/H})$

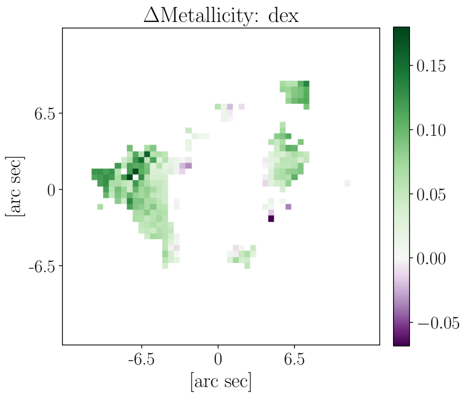
ΔMetallicity: dex

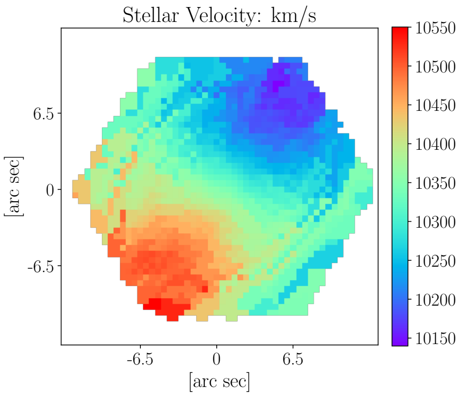
Stellar Velocity: km/s

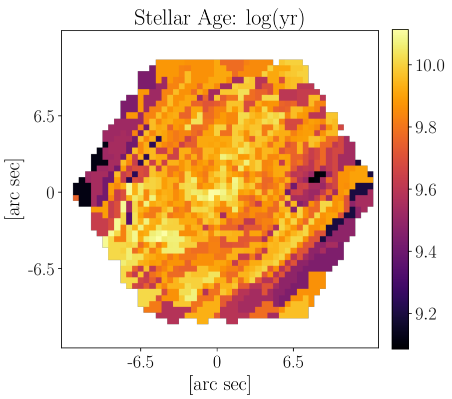
Stellar Age: log(yr)

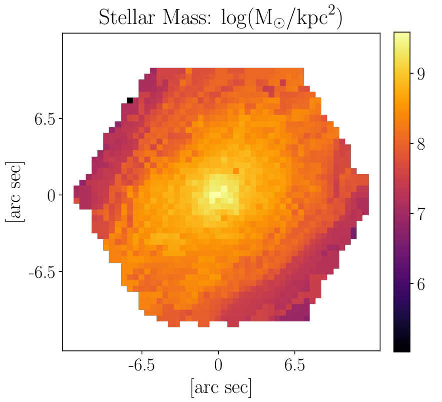
Stellar Mass: log(M$_\odot$/kpc^2)

Galaxy objID: 587727221934785112

plate-ifu: 7975-6102

RA: 323.577°

Decl: 11.2143°

z: 0.0344683

K03: NULL

$\log \mathrm{M}_*$: 10.6196 $\log \mathrm{M}_\odot$

$\log \mathrm{SFR}$: -0.355243 $\log(\mathrm{M}_\odot/\mathrm{yr})$

O/H(KE08): nan

Δ SFR: nan

manga-id: 1-114145

Match separation: 0.11308"

Companion Flag: 0

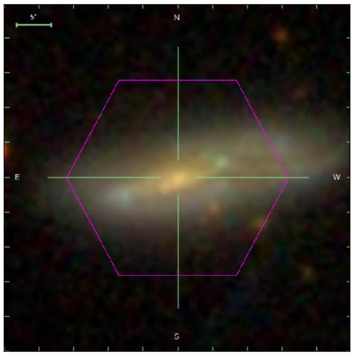

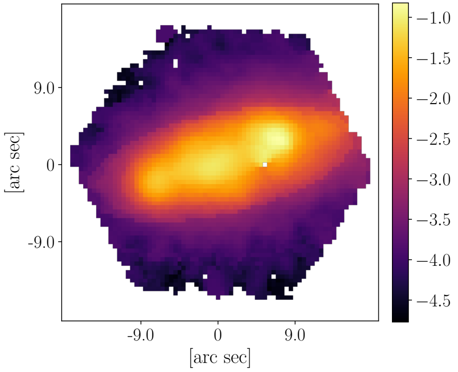
Σ_{SFR}: log(M$_\odot$/(yr · kpc^2))

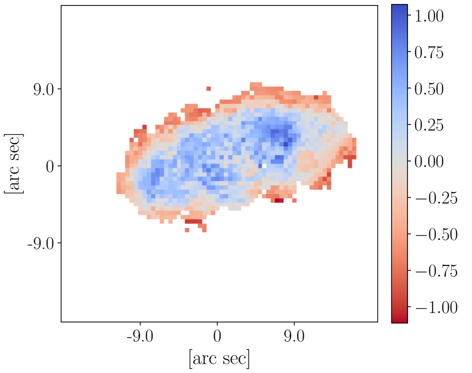
$\Delta\Sigma_{SFR}$: dex

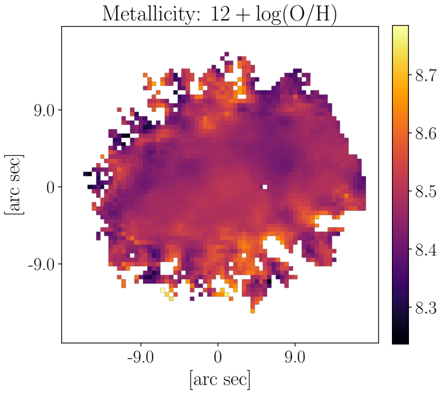
Metallicity: $12 + \log(\mathrm{O/H})$

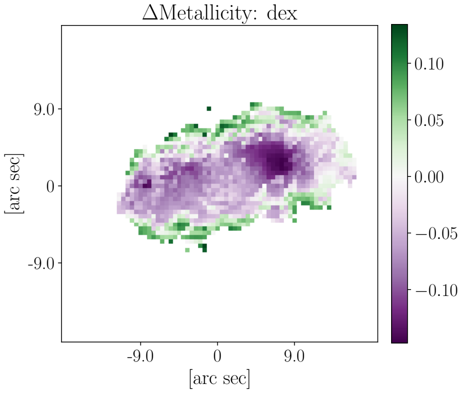
ΔMetallicity: dex

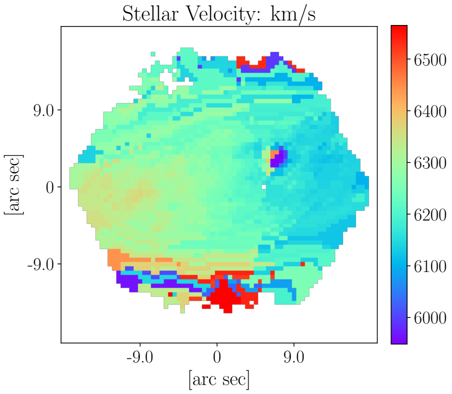
Stellar Velocity: km/s

Galaxy objID: 587729408612237365

plate-ifu: 8548-12704

RA: 244.075°

Decl: 47.9816°

z: 0.0208447

K03: SF

$\log \mathrm{M}_*$: 10.2178 $\log \mathrm{M}_\odot$

$\log \mathrm{SFR}$: 0.397506 $\log(\mathrm{M}_\odot/\mathrm{yr})$

O/H(KE08): nan

Δ SFR: 0.0

manga-id: 1-633839

Match separation: 0.0800341”

Companion Flag: 0

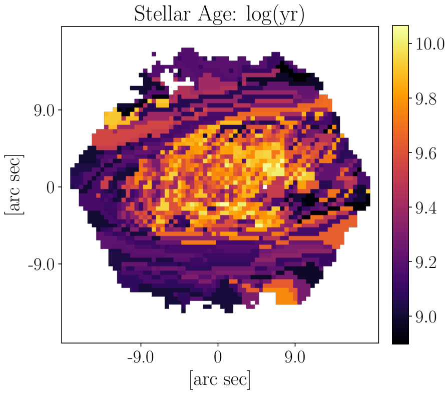
Stellar Age: log(yr)

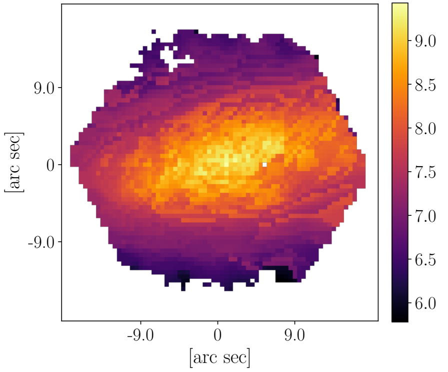
Stellar Mass: log(M$_\odot$/kpc^2)

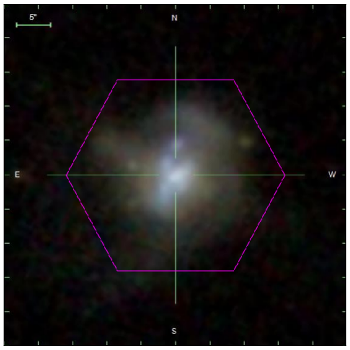

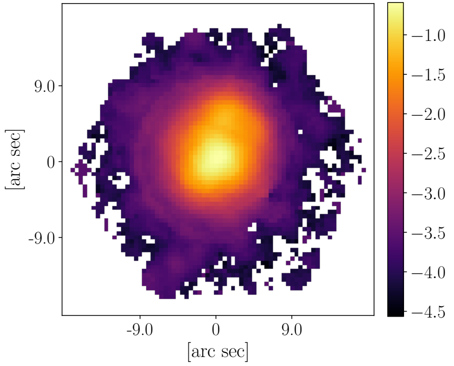
Σ_{SFR}: log(M$_\odot$/(yr · kpc^2))

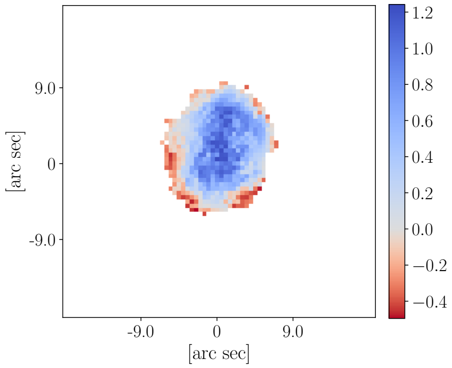
$\Delta\Sigma_{SFR}$: dex

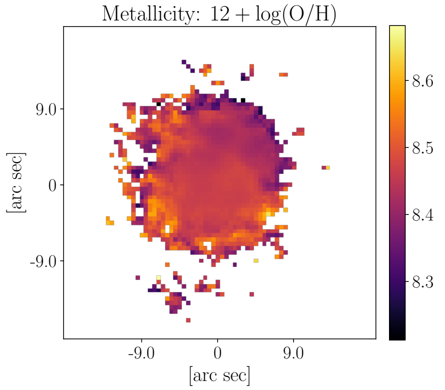
Metallicity: 12 + log(O/H)

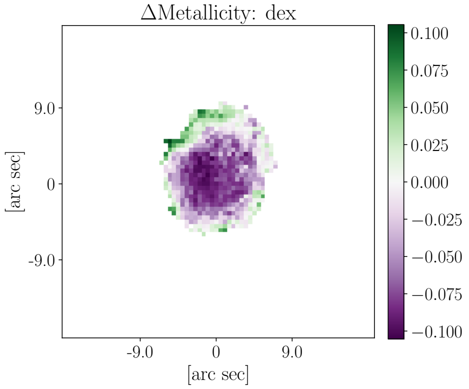
ΔMetallicity: dex

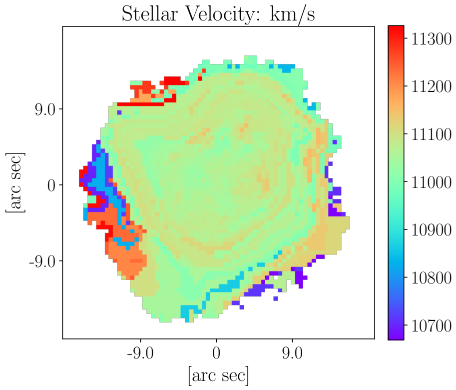
Stellar Velocity: km/s

Galaxy objID: 587729409156186207

plate-ifu: 8613-12703

RA: 256.818°

Decl: 34.8226°

z: 0.0368594

K03: SF

log M$_*$: 10.3526 log M$_\odot$

log SFR : 0.540645 log(M$_\odot$/yr)

O/H(KE08): 8.89889

Δ SFR: 0.594544

manga-id: 1-177270

Match separation: 0.0770626”

Companion Flag: 0

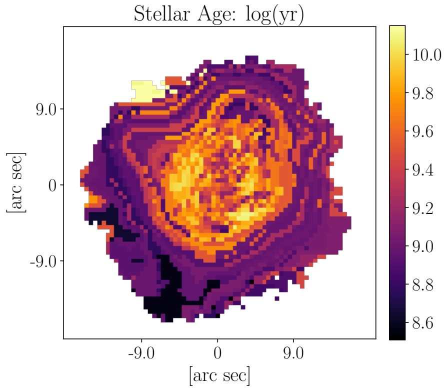
Stellar Age: log(yr)

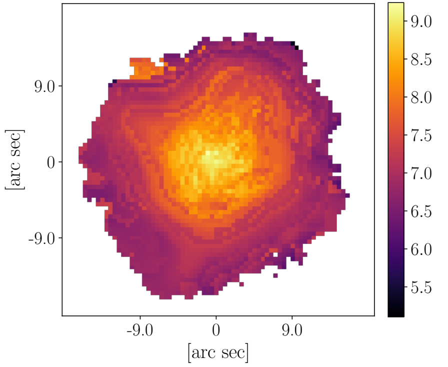
Stellar Mass: log(M$_\odot$/kpc^2)

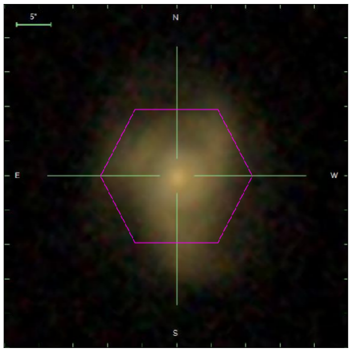

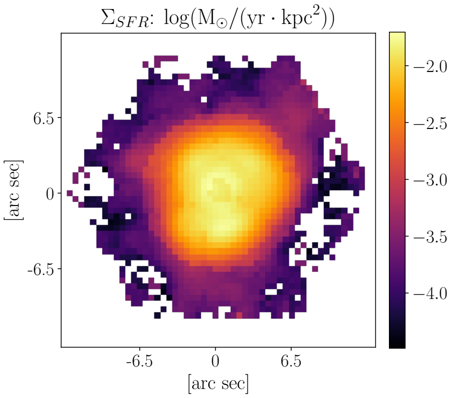
Σ_{SFR}: log(M$_\odot$/(yr · kpc^2))

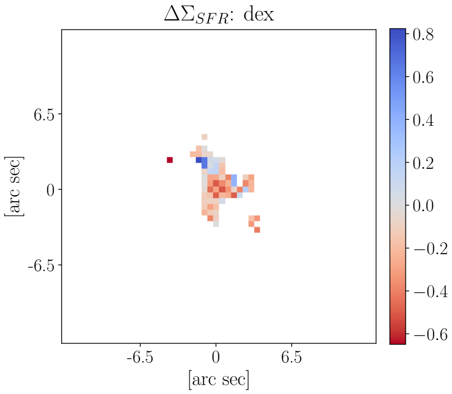
$\Delta\Sigma_{SFR}$: dex

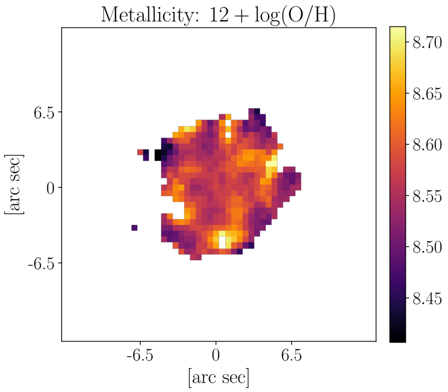
Metallicity: $12 + \log(O/H)$

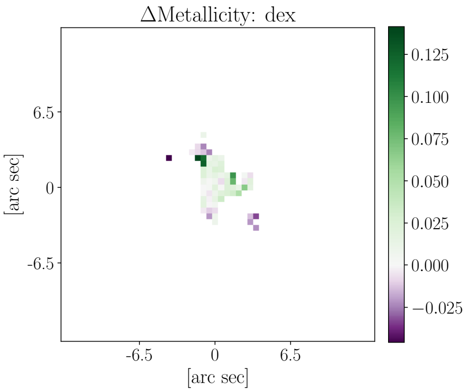
ΔMetallicity: dex

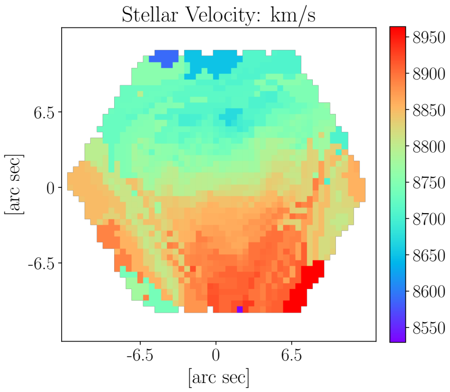
Stellar Velocity: km/s

Galaxy objID: 587729651811877012

plate-ifu: 8602-6103

RA: 248.11°

Decl: 39.5178°

z: 0.0293573

K03: NULL

$\log M_*$: 10.3322 $\log M_\odot$

log SFR : -0.437749 log(M$_\odot$/yr)

O/H(KE08): nan

Δ SFR: nan

manga-id: 1-135520

Match separation: 0.0806571"

Companion Flag: 0

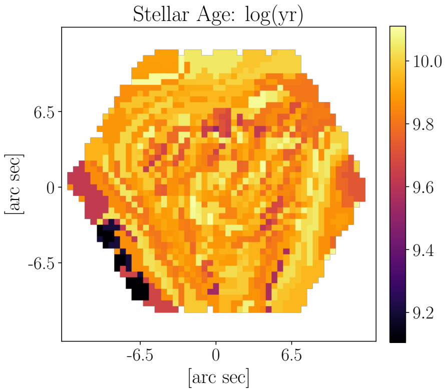
Stellar Age: log(yr)

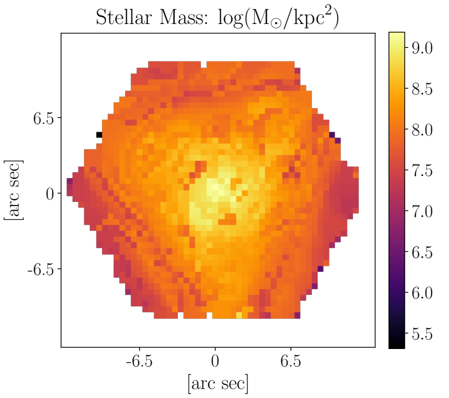
Stellar Mass: log(M$_\odot$/kpc^2)

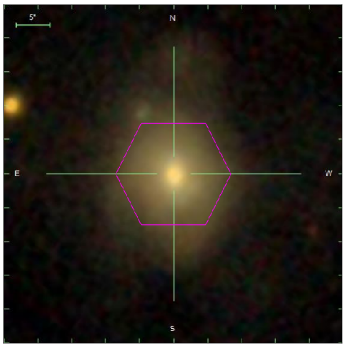

Σ_{SFR}: $\log(\mathrm{M}_\odot/(\mathrm{yr}\cdot\mathrm{kpc}^2))$

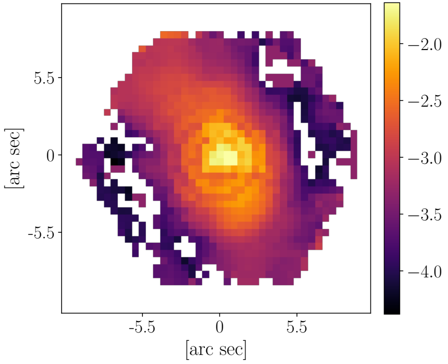

$\Delta\Sigma_{SFR}$: dex

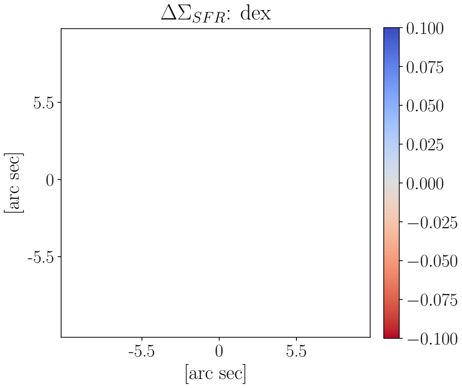

Metallicity: $12 + \log(\mathrm{O/H})$

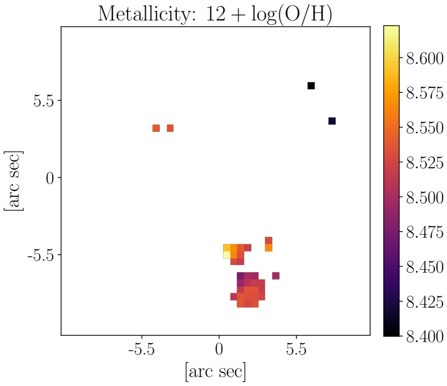

ΔMetallicity: dex

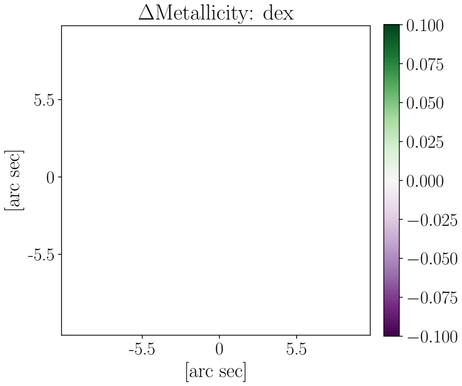

Stellar Velocity: km/s

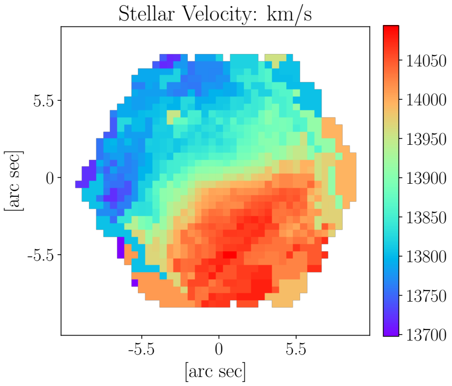

Galaxy objID: 587729653957722238

plate-ifu: 8555-3701

RA: 246.761°

Decl: 43.4761°

z: 0.046516

K03: NULL

$\log \mathrm{M}_*$: 10.8491 $\log \mathrm{M}_\odot$

$\log \mathrm{SFR}$: -0.369477 $\log(\mathrm{M}_\odot/\mathrm{yr})$

O/H(KE08): nan

Δ SFR: nan

manga-id: 1-134964

Match separation: 0.10833”

Companion Flag: 0

Stellar Age: $\log(\mathrm{yr})$

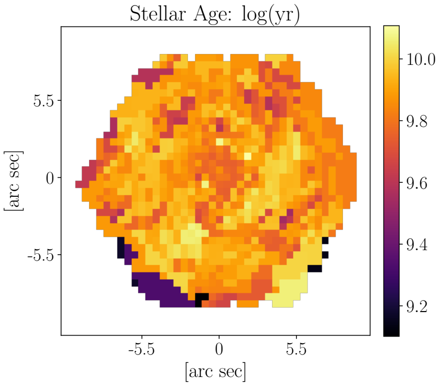

Stellar Mass: $\log(\mathrm{M}_\odot/\mathrm{kpc}^2)$

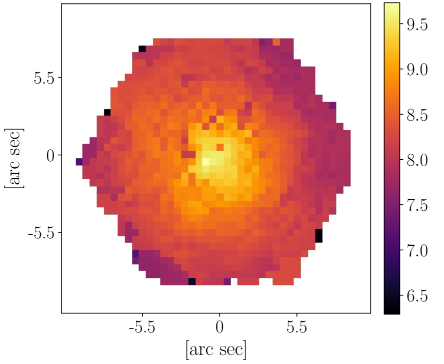

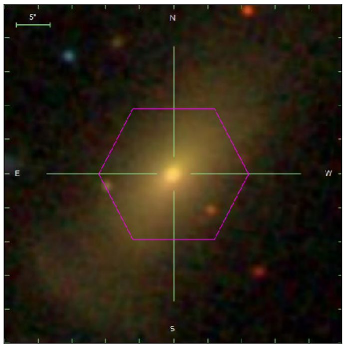

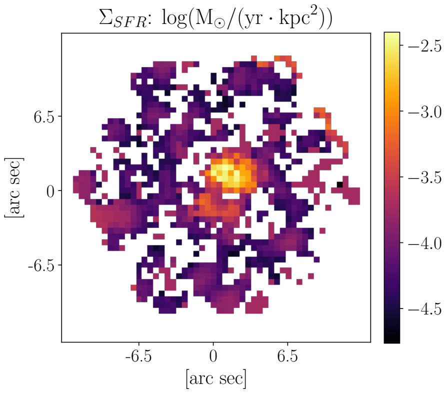

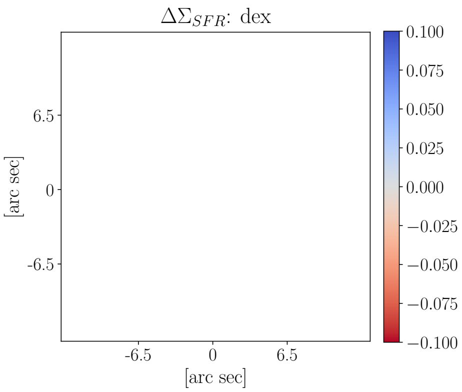

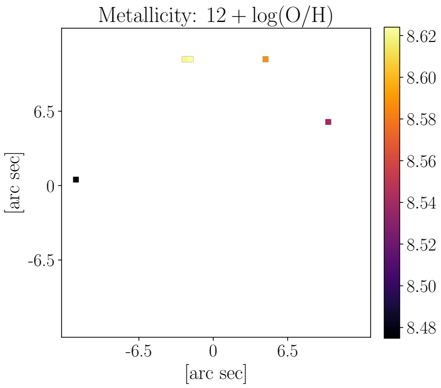

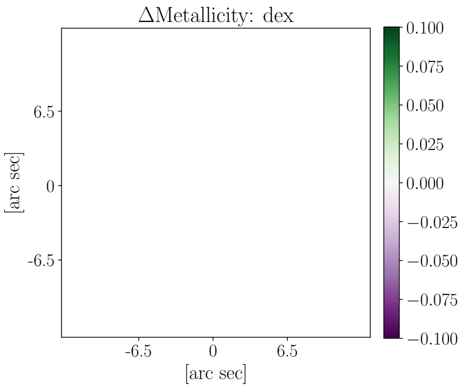

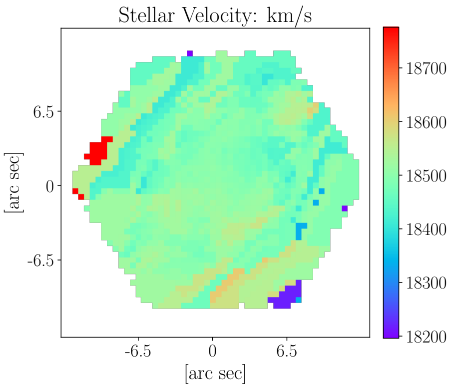

Galaxy objID: 587730773877129334

plate-ifu: 7977-6102

RA: 332.756°

Decl: 12.3743°

z: 0.0616801

K03: NULL

$\log \mathrm{M}_*$: 11.0227 $\log \mathrm{M}_\odot$

$\log \mathrm{SFR}$: -1.0903 $\log(\mathrm{M}_\odot/\mathrm{yr})$

O/H(KE08): nan

Δ SFR: nan

manga-id: 1-114998

Match separation: 0.112744”

Companion Flag: 0

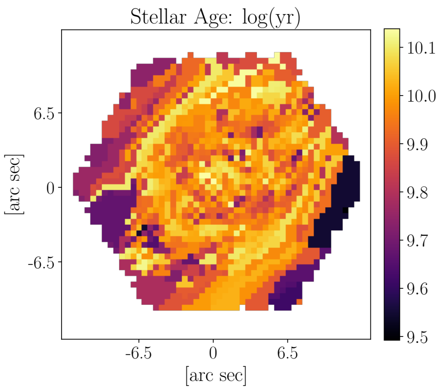

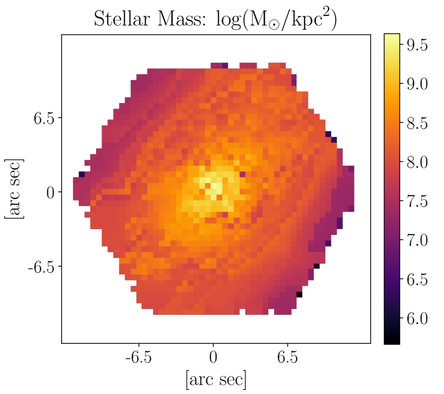

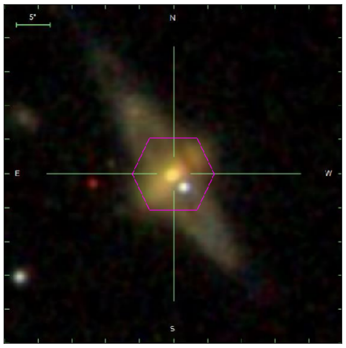

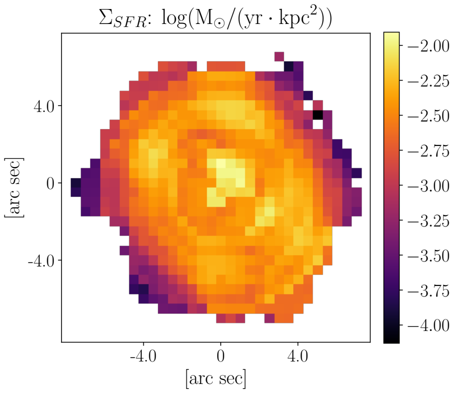
Σ_{SFR}: log(M$_\odot$/(yr · kpc^2))

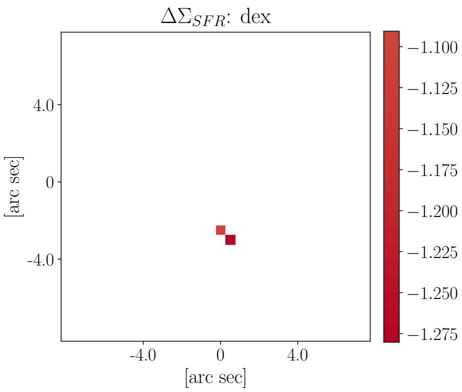
$\Delta\Sigma_{SFR}$: dex

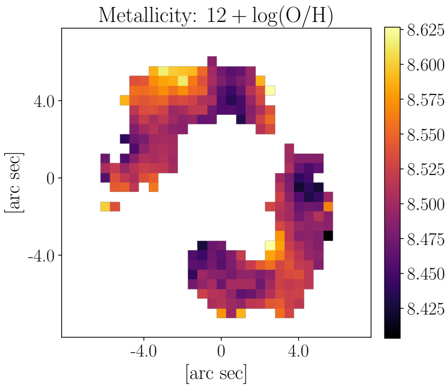
Metallicity: $12 + \log(\mathrm{O/H})$

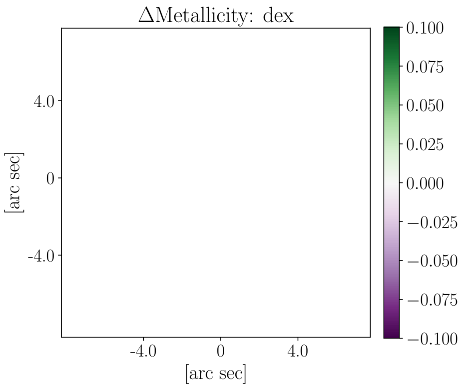
ΔMetallicity: dex

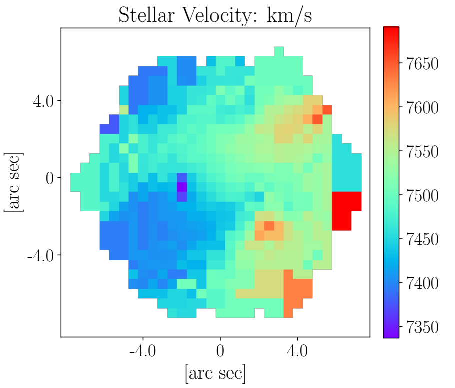
Stellar Velocity: km/s

Galaxy objID: 587730847423791750

plate-ifu: 8623-1902

RA: 312.024°

Decl: 0.0688414°

z: 0.0249126

K03: NULL

$\log \mathrm{M}_*$: 10.1795 $\log \mathrm{M}_\odot$

$\log \mathrm{SFR}$: -0.952148 $\log(\mathrm{M}_\odot/\mathrm{yr})$

O/H(KE08): nan

Δ SFR: nan

manga-id: 1-178838

Match separation: 0.0115274”

Companion Flag: 0

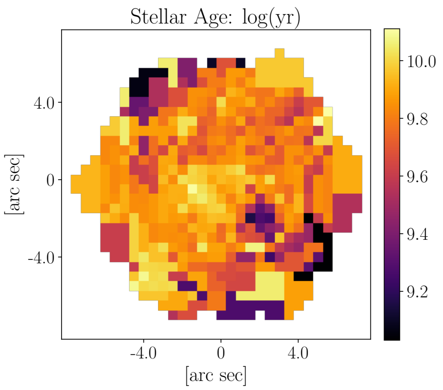
Stellar Age: log(yr)

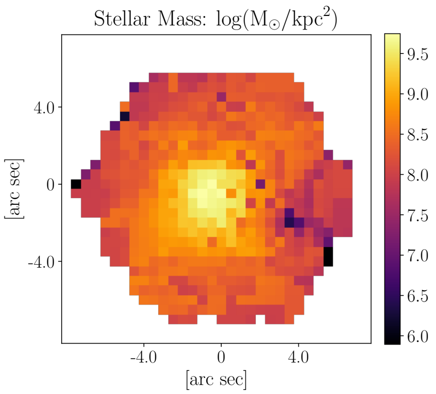
Stellar Mass: log(M$_\odot$/kpc^2)

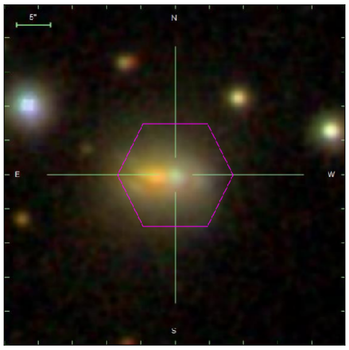

Σ_{SFR}: log(M$_\odot$/(yr · kpc^2))

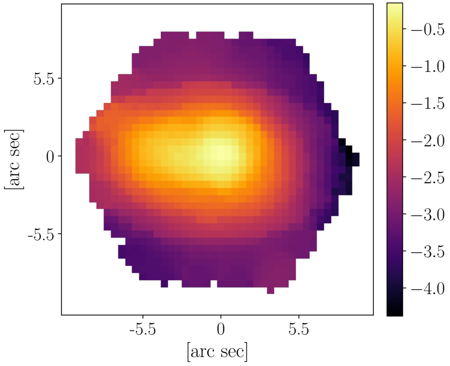

$\Delta\Sigma_{SFR}$: dex

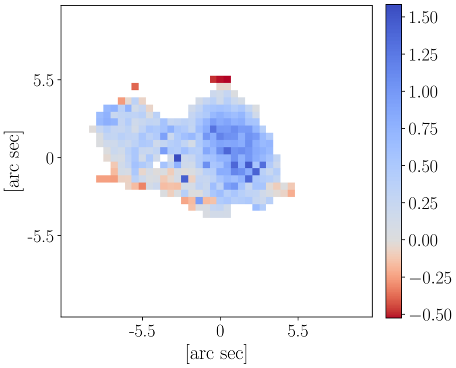

Metallicity: 12 + log(O/H)

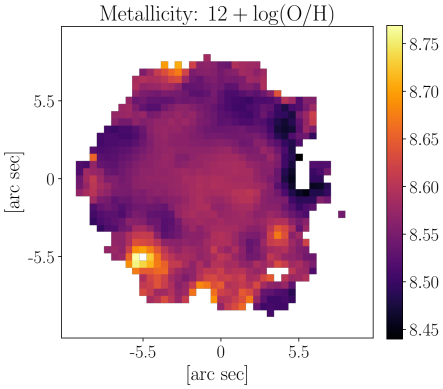

ΔMetallicity: dex

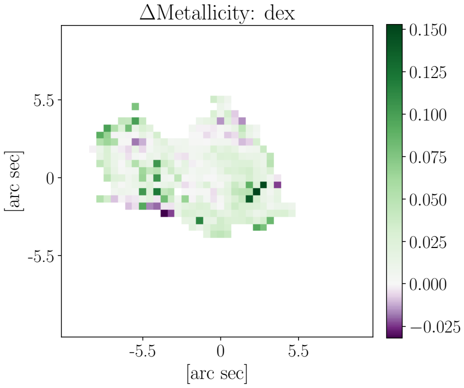

Stellar Velocity: km/s

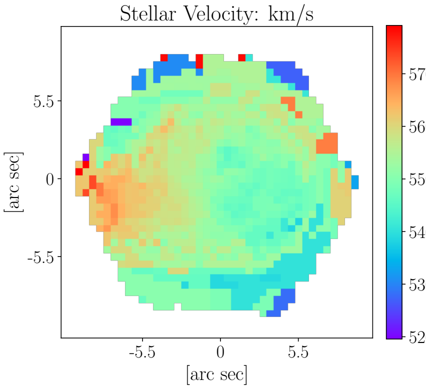

Galaxy objID: 587731187797393472

plate-ifu: 8615-3703

RA: 320.826°

Decl: 1.25498°

z: 0.0183638

K03: NULL

log M$_*$: 10.1694 log M$_\odot$

log SFR : 0.414822 log(M$_\odot$/yr)

O/H(KE08): nan

Δ SFR: nan

manga-id: 1-180028

Match separation: 0.55422"

Companion Flag: 0

Stellar Age: log(yr)

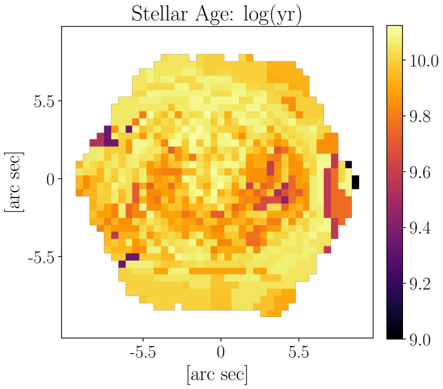

Stellar Mass: log(M$_\odot$/kpc^2)

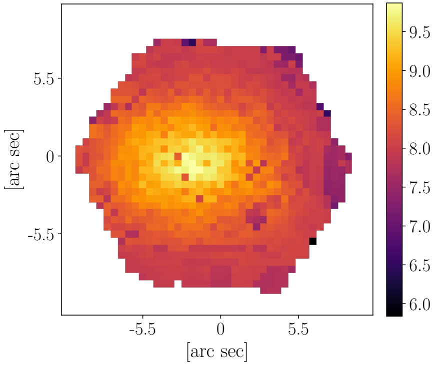

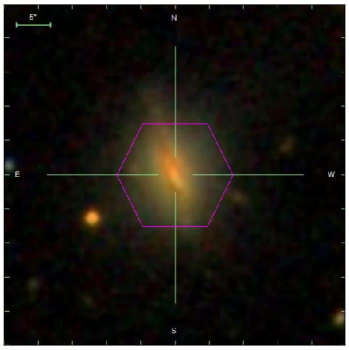

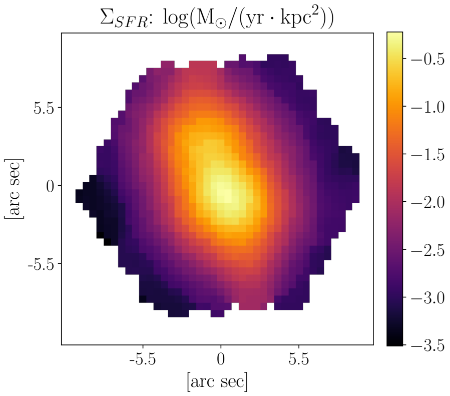
Σ_{SFR}: log(M$_\odot$/(yr · kpc^2))

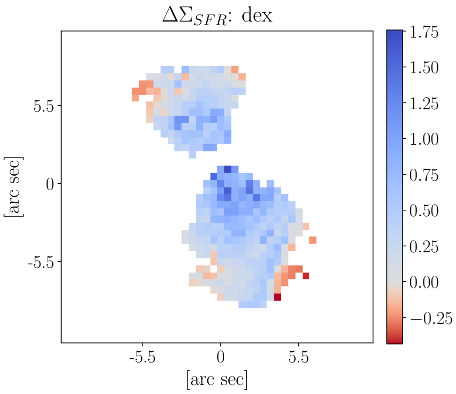
$\Delta\Sigma_{SFR}$: dex

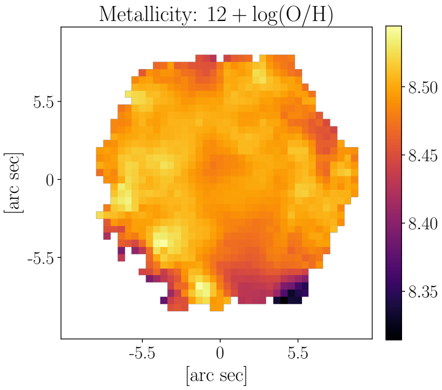
Metallicity: 12 + log(O/H)

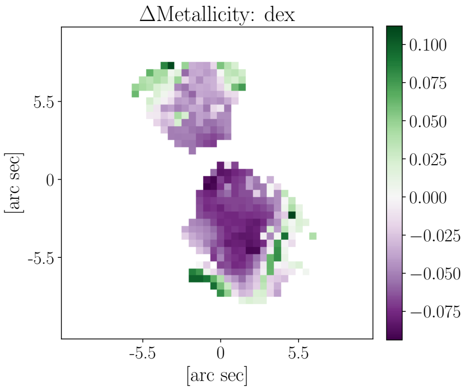
ΔMetallicity: dex

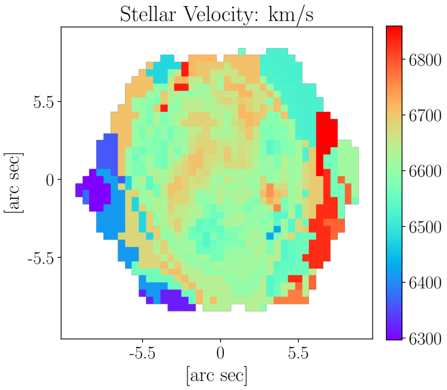
Stellar Velocity: km/s

Galaxy objID: 587731512619696292

plate-ifu: 8084-3702

RA: 50.6366°

Decl: -0.00121269°

z: 0.0221195

K03: SF

log M_* : 10.2088 log $M_\odot$

log SFR : 0.450692 log($M_\odot$/yr)

O/H(KE08): nan

Δ SFR: 0.277312

manga-id: 1-604052

Match separation: 0.198665"

Companion Flag: 0

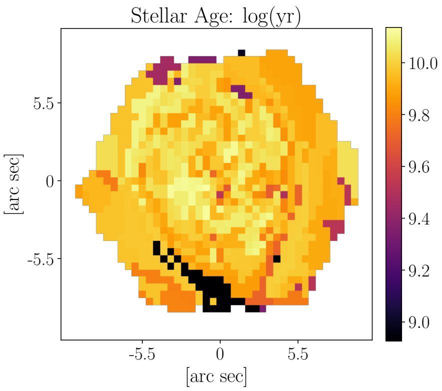
Stellar Age: log(yr)

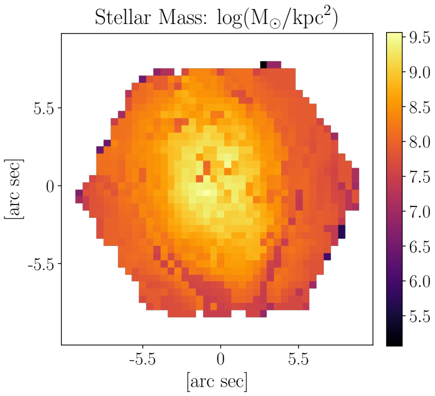
Stellar Mass: log(M$_\odot$/kpc^2)

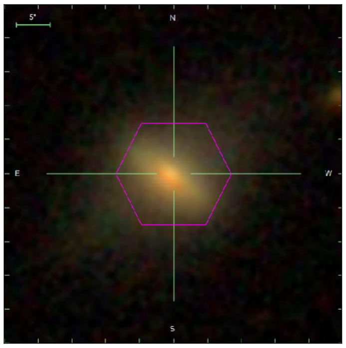

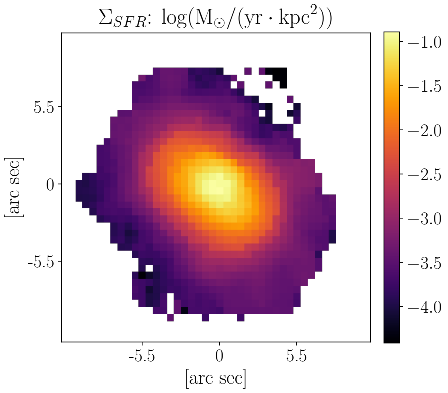
Σ_{SFR}: $\log(\mathrm{M}_\odot/(\mathrm{yr}\cdot\mathrm{kpc}^2))$

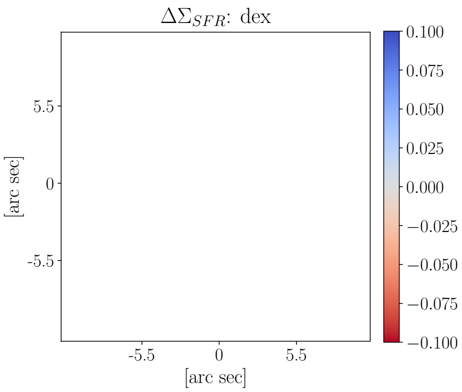
$\Delta\Sigma_{SFR}$: dex

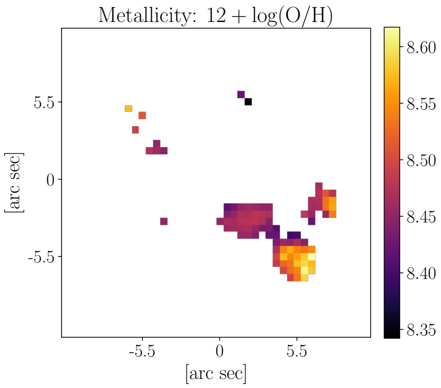
Metallicity: $12+\log(\mathrm{O/H})$

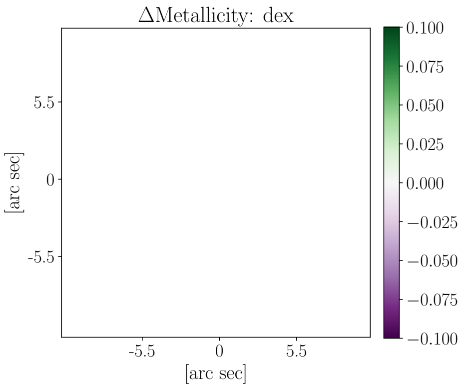
ΔMetallicity: dex

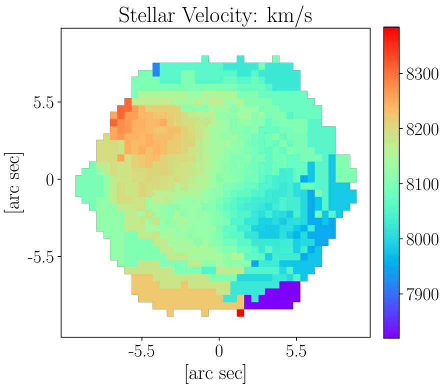
Stellar Velocity: km/s

Galaxy objID: 587731522818670711

plate-ifu: 8249-3704

RA: 137.875°

Decl: 45.4683°

z: 0.02709

K03: AGN

$\log \mathrm{M}_*$: 10.3334 $\log \mathrm{M}_\odot$

$\log \mathrm{SFR}$: -0.261716 $\log(\mathrm{M}_\odot/\mathrm{yr})$

O/H(KE08): nan

Δ SFR: nan

manga-id: 1-137883

Match separation: 0.244584"

Companion Flag: 0

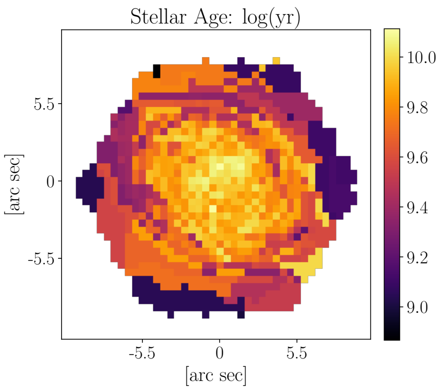
Stellar Age: log(yr)

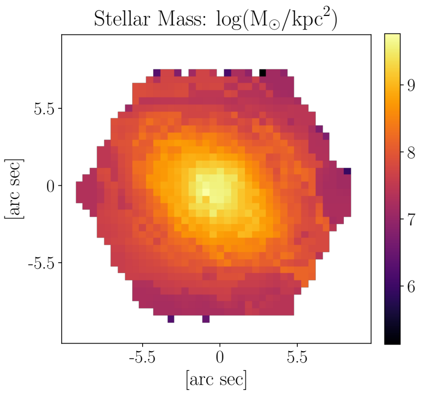
Stellar Mass: $\log(\mathrm{M}_\odot/\mathrm{kpc}^2)$

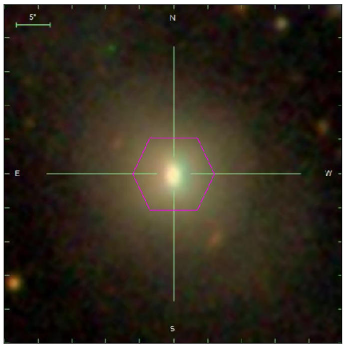

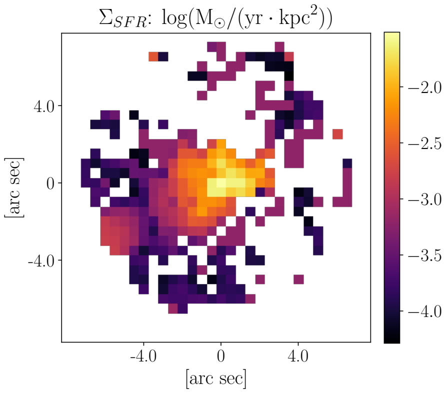

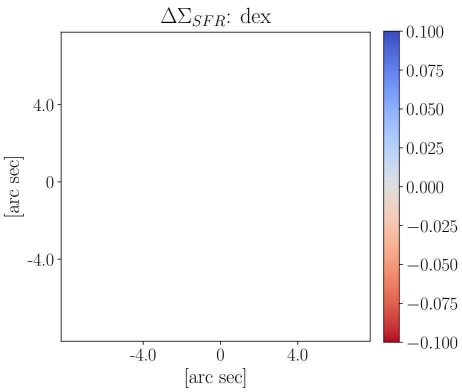

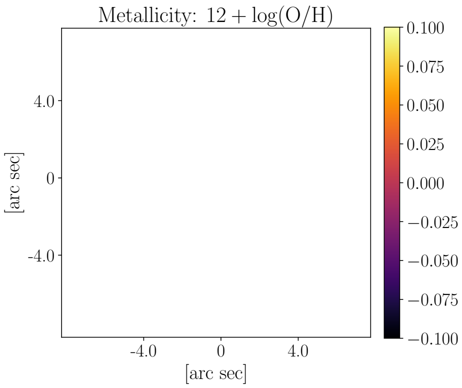

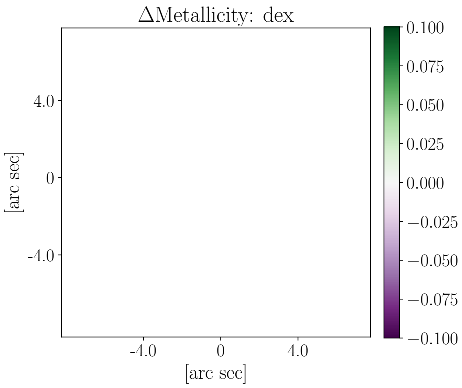

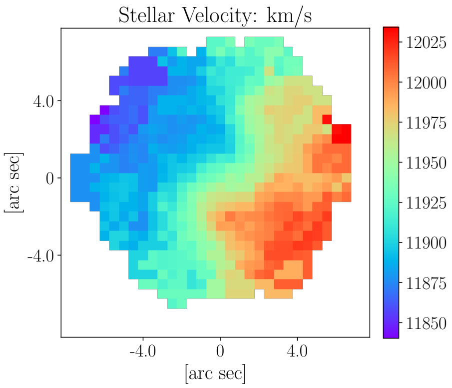

Galaxy objID: 587733608014872696

plate-ifu: 8979-1902

RA: 242.585°

Decl: 41.8549°

z: 0.0398023

K03: NULL

$\log \mathrm{M}_*$: 10.6795 $\log \mathrm{M}_\odot$

log SFR : -1.01794 log(M$_\odot$/yr)

O/H(KE08): nan

Δ SFR: nan

manga-id: 1-210114

Match separation: 0.0924927”

Companion Flag: 0

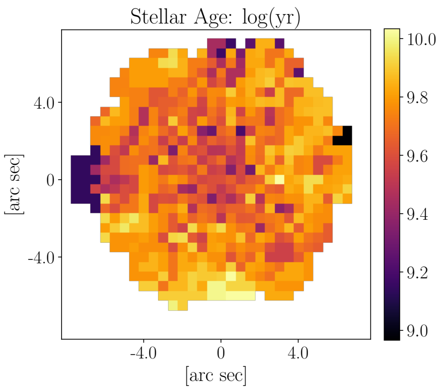

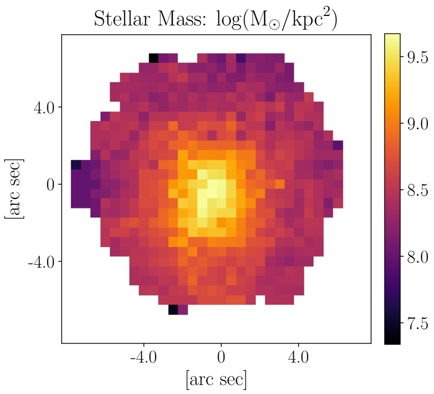

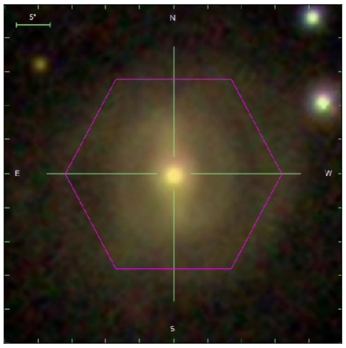

Σ_{SFR}: log(M$_\odot$/(yr · kpc^2))

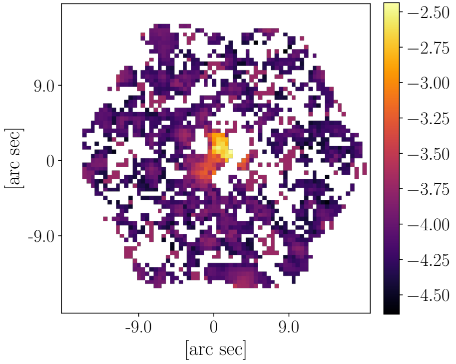

$\Delta\Sigma_{SFR}$: dex

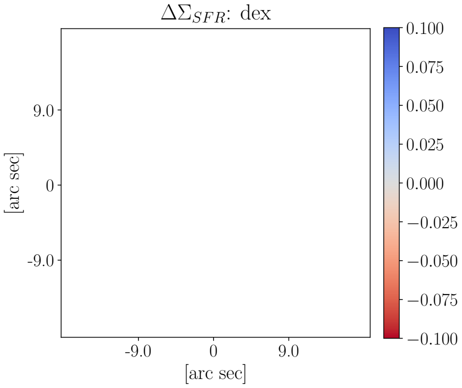

Metallicity: 12 + log(O/H)

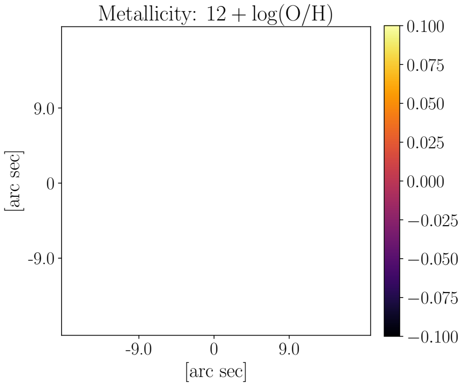

ΔMetallicity: dex

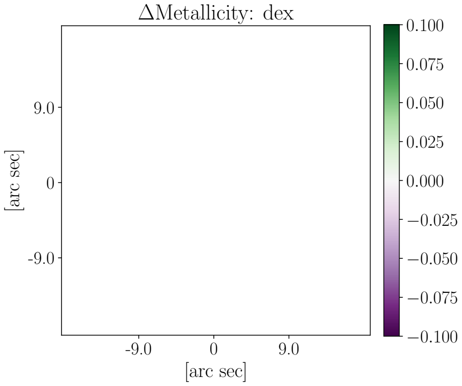

Stellar Velocity: km/s

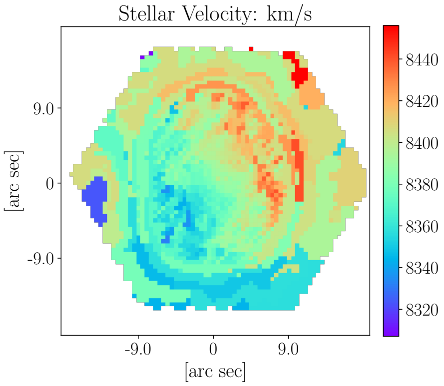

Galaxy objID: 587733608553709617

plate-ifu: 8603-12702

RA: 246.869°

Decl: 38.8691°

z: 0.0279484

K03: NULL

$\log \mathrm{M}_*$: 10.396 $\log \mathrm{M}_\odot$

$\log \mathrm{SFR}$: -1.79414 $\log(\mathrm{M}_\odot/\mathrm{yr})$

O/H(KE08): nan

Δ SFR: nan

manga-id: 1-211227

Match separation: 0.0522375”

Companion Flag: 0

Stellar Age: log(yr)

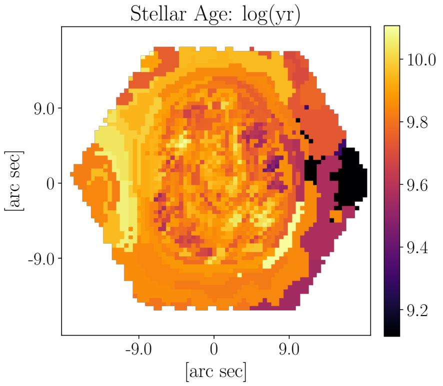

Stellar Mass: log(M$_\odot$/kpc^2)

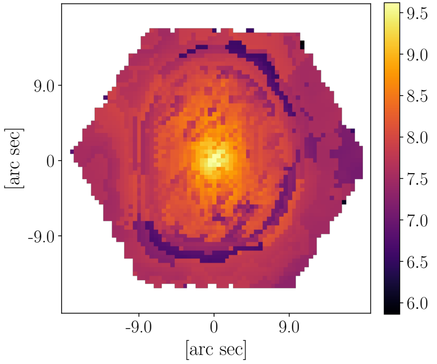

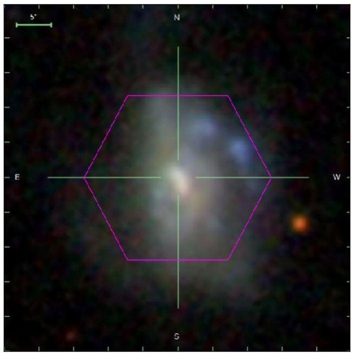

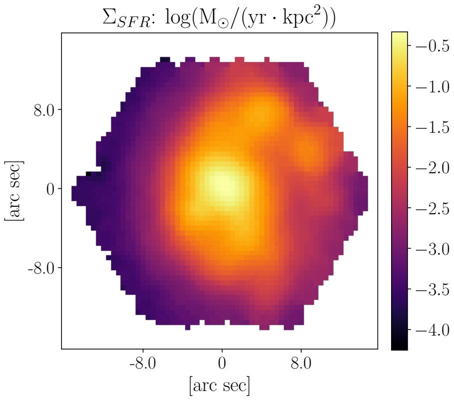

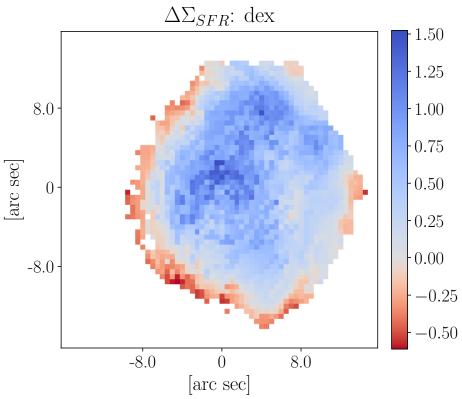

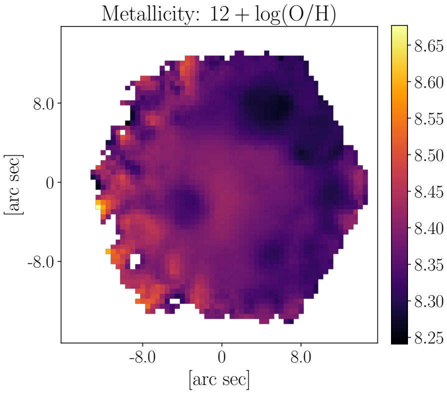

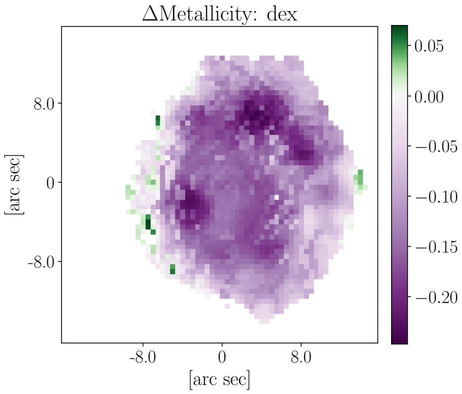

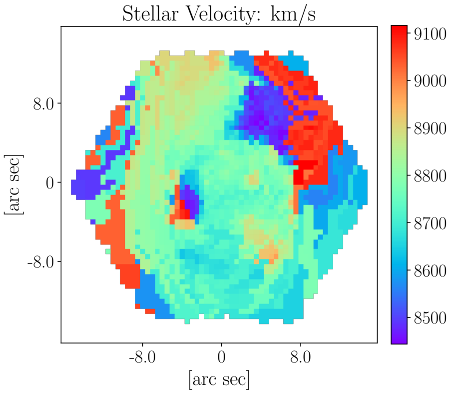

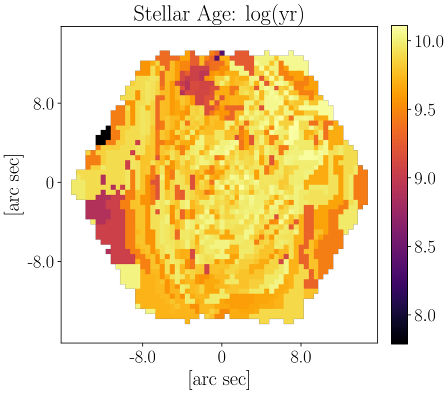

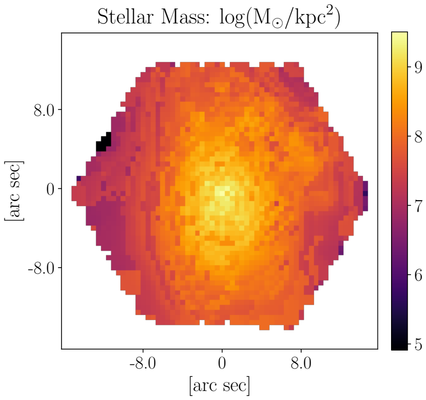

Galaxy objID: 587733609626861608
plate-ifu: 8604-9102
RA: 246.455°
Decl: 40.3452°
z: 0.029182
K03: SF
$\log M_*$: 10.46 $\log M_\odot$
$\log \mathrm{SFR}$: 0.928379 $\log(M_\odot/\mathrm{yr})$
O/H(KE08): 8.73526
Δ SFR: 0.664058
manga-id: 1-210971
Match separation: 0.28527"
Companion Flag: 0

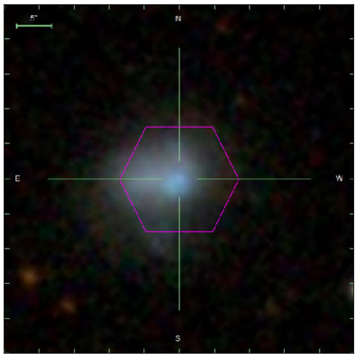

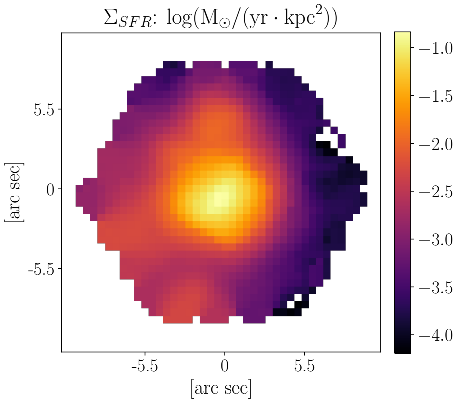
Σ_{SFR}: $\log(M_\odot/(\mathrm{yr}\cdot\mathrm{kpc}^2))$

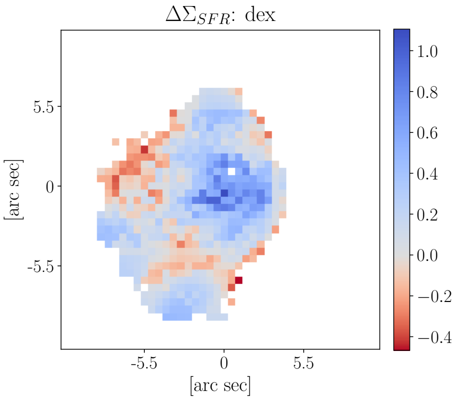
$\Delta\Sigma_{SFR}$: dex

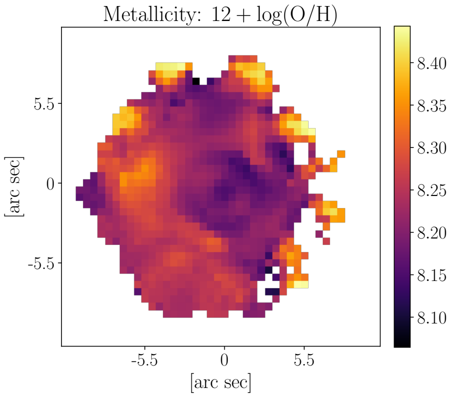
Metallicity: $12 + \log(\mathrm{O/H})$

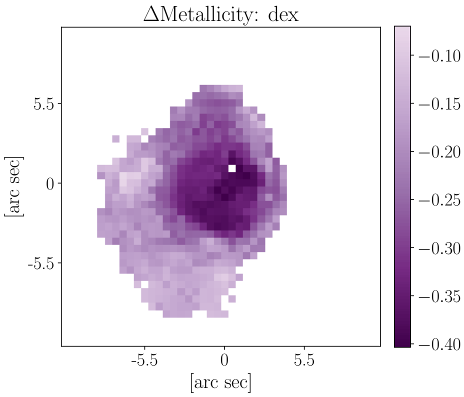
ΔMetallicity: dex

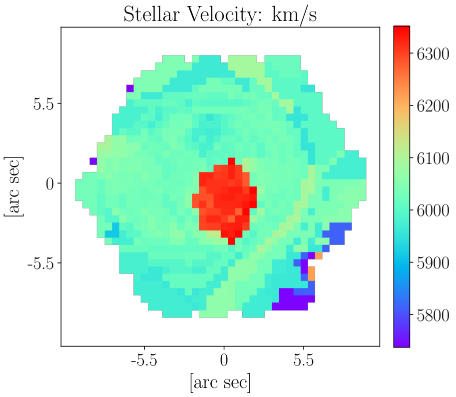
Stellar Velocity: km/s

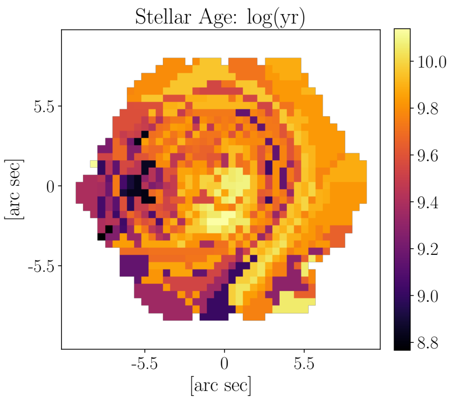
Stellar Age: log(yr)

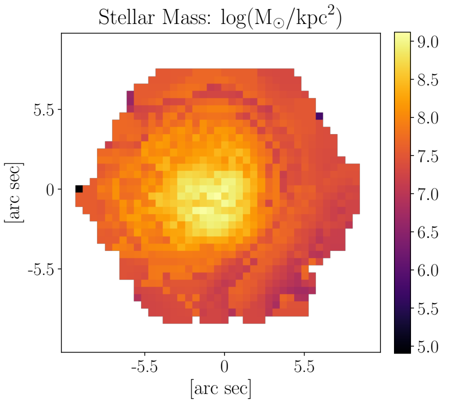
Stellar Mass: $\log(M_\odot/\mathrm{kpc}^2)$

Galaxy objID: 587734622702600263

plate-ifu: 8942-3703

RA: 124.385°

Decl: 28.3578°

z: 0.0210097

K03: NULL

$\log M_*$: 9.59663 $\log M_\odot$

$\log \mathrm{SFR}$: -0.324089 $\log(M_\odot/\mathrm{yr})$

O/H(KE08): nan

Δ SFR: 0.593549

manga-id: 1-218435

Match separation: 0.719319”

Companion Flag: 0

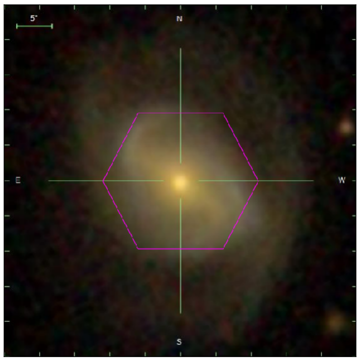

Σ_{SFR}: $\log(\mathrm{M}_\odot/(\mathrm{yr}\cdot\mathrm{kpc}^2))$

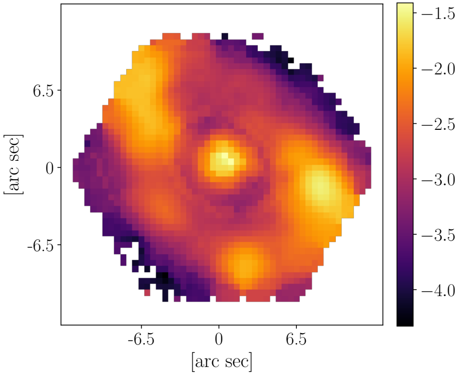

$\Delta\Sigma_{SFR}$: dex

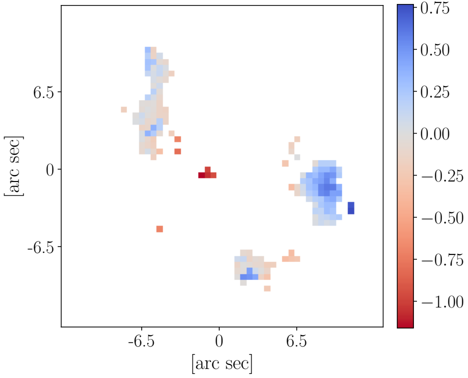

Metallicity: $12 + \log(\mathrm{O/H})$

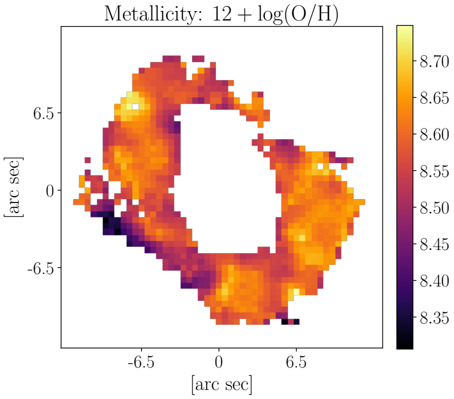

ΔMetallicity: dex

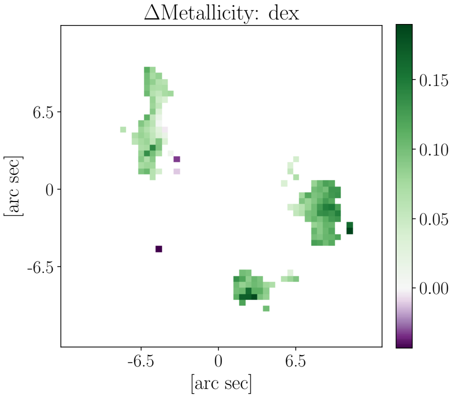

Stellar Velocity: km/s

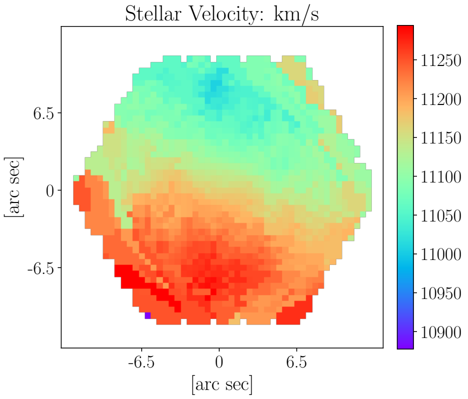

Stellar Age: log(yr)

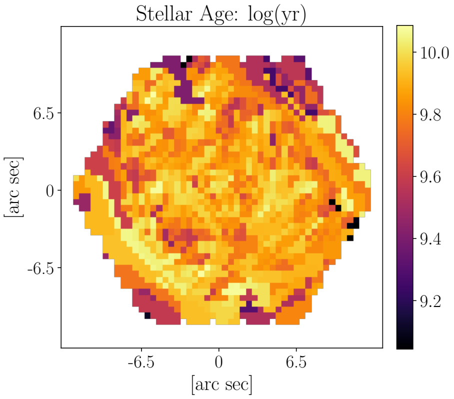

Stellar Mass: $\log(\mathrm{M}_\odot/\mathrm{kpc}^2)$

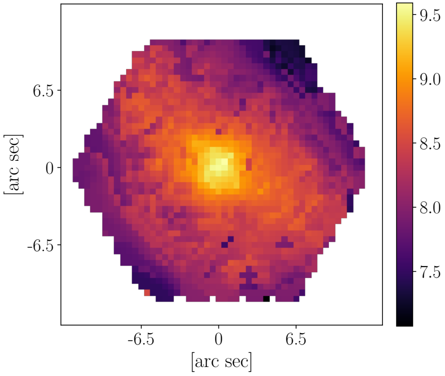

Galaxy objID: 587735697527341202
plate-ifu: 8592-6102
RA: 223.321°
Decl: 52.0443°
z: 0.0372022
K03: NULL
$\log \mathrm{M}_*$: 10.7638 $\log \mathrm{M}_\odot$
$\log \mathrm{SFR}$: 0.0593922 $\log(\mathrm{M}_\odot/\mathrm{yr})$
O/H(KE08): nan
Δ SFR: nan
manga-id: 1-246470
Match separation: 0.0136335”
Companion Flag: 0

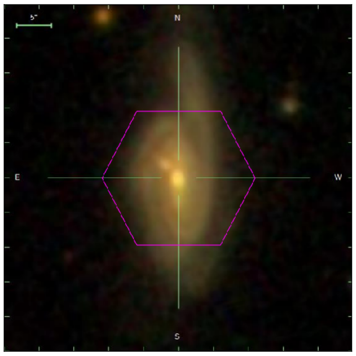

Σ_{SFR}: log(M$_\odot$/(yr · kpc^2))

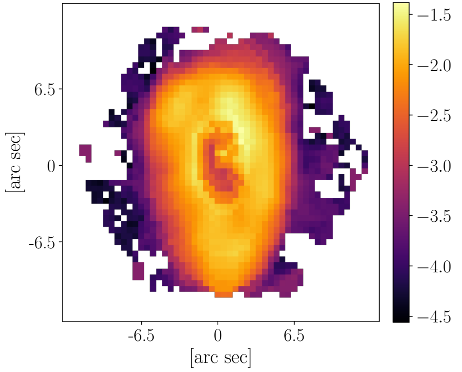

$\Delta\Sigma_{SFR}$: dex

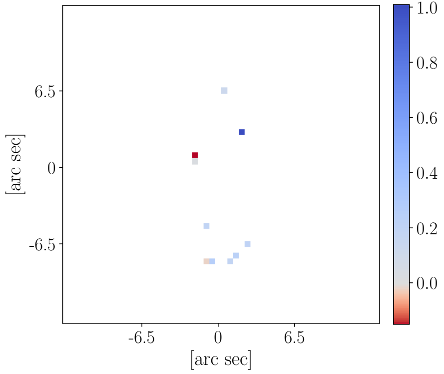

Metallicity: $12 + \log(\text{O/H})$

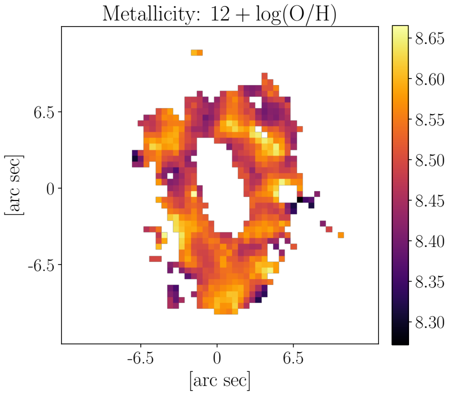

ΔMetallicity: dex

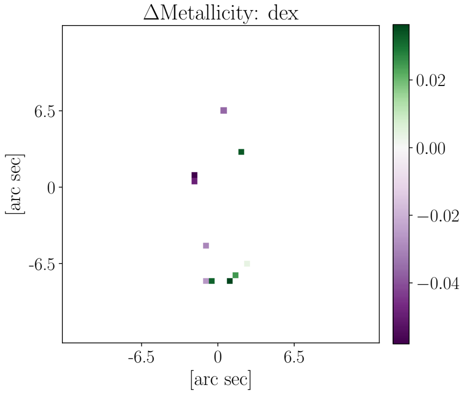

Stellar Velocity: km/s

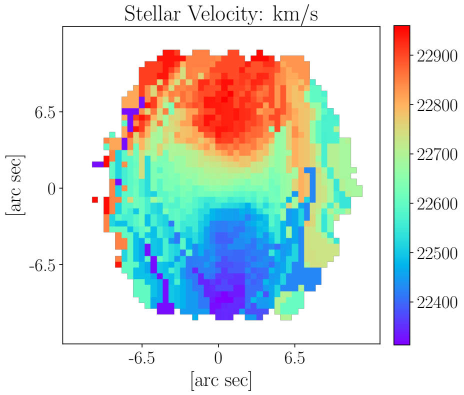

Stellar Age: log(yr)

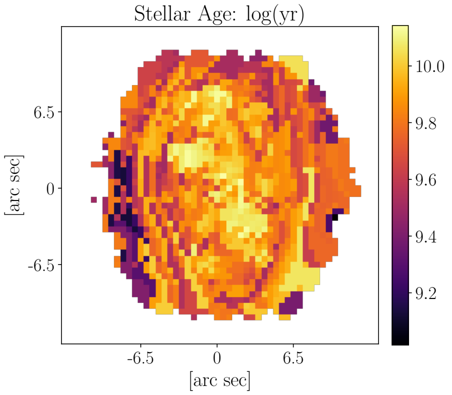

Stellar Mass: log(M$_\odot$/kpc^2)

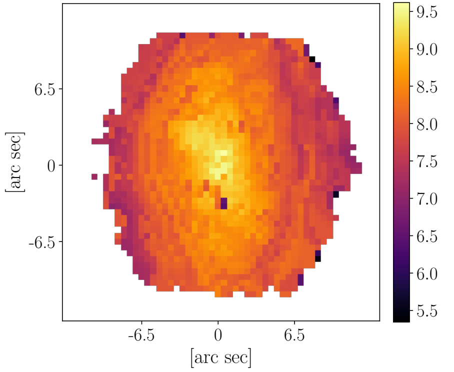

Galaxy objID: 587736584961523819

plate-ifu: 8447-6101

RA: 206.133°

Decl: 40.24°

z: 0.0755124

K03: NULL

$\log \text{M}_*$: 11.239 $\log \text{M}_\odot$

$\log \text{SFR}$: 0.852139 $\log(\text{M}_\odot/\text{yr})$

O/H(KE08): nan

Δ SFR: nan

manga-id: 1-260446

Match separation: 0.0634748"

Companion Flag: 0

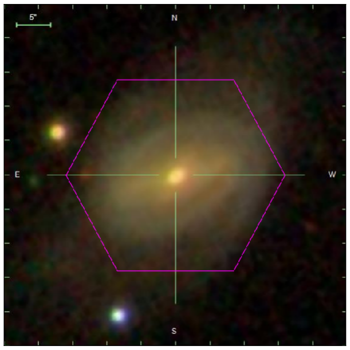

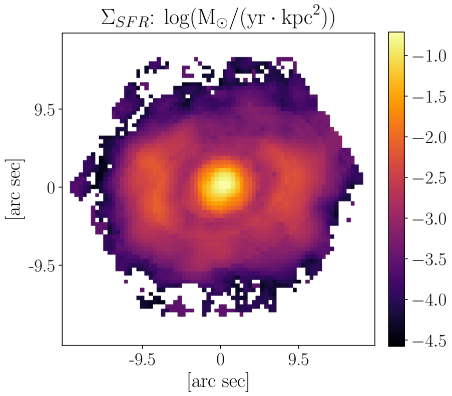
Σ_{SFR}: $\log(M_{\odot}/(yr \cdot kpc^2))$

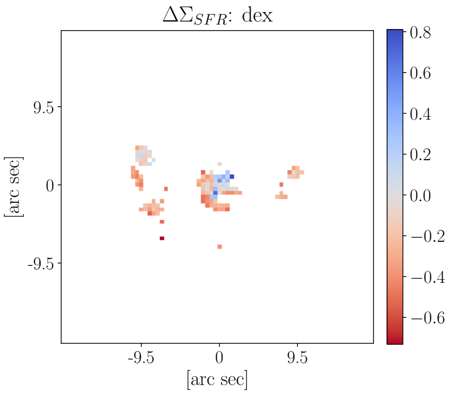
$\Delta\Sigma_{SFR}$: dex

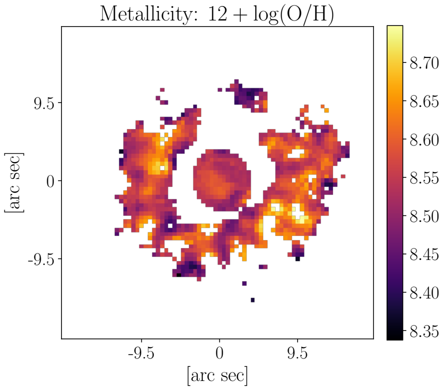
Metallicity: $12 + \log(O/H)$

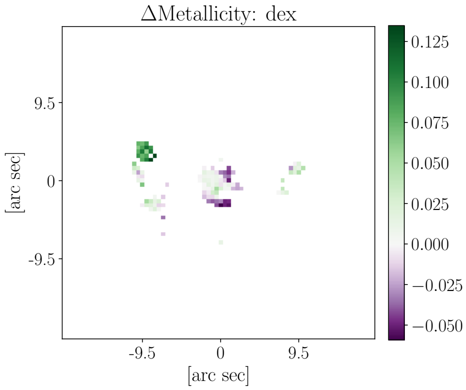
ΔMetallicity: dex

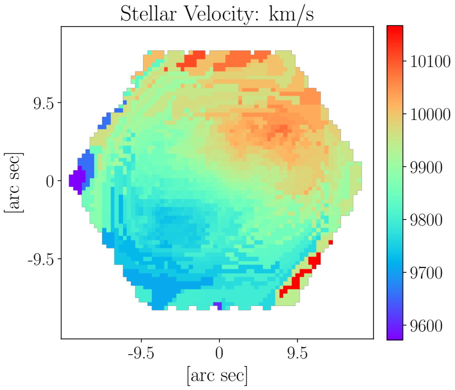
Stellar Velocity: km/s

Galaxy objID: 587736941989920863

plate-ifu: 9042-12703

RA: 235.153°

Decl: 28.5124°

z: 0.0329293

K03: SF

$\log M_*$: 10.7169 $\log M_{\odot}$

$\log SFR$: 0.149726 $\log(M_{\odot}/yr)$

O/H(KE08): nan

Δ SFR: 0.170175

manga-id: 1-316872

Match separation: 0.146526”

Companion Flag: 0

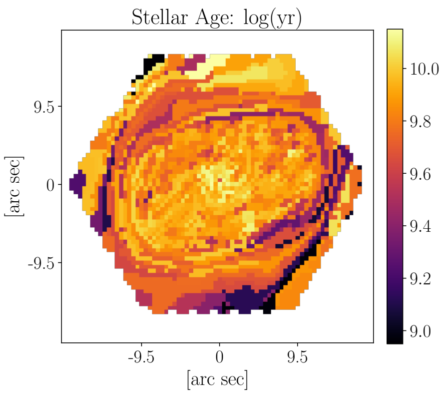
Stellar Age: log(yr)

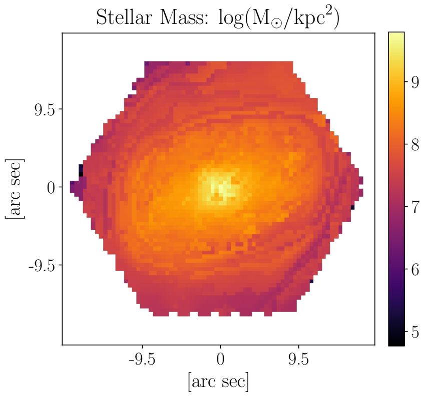
Stellar Mass: $\log(M_{\odot}/kpc^2)$

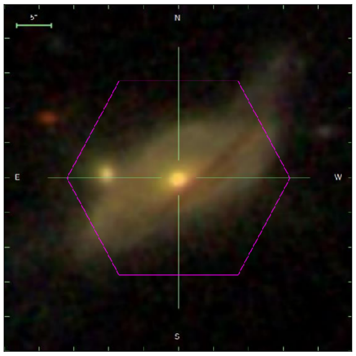

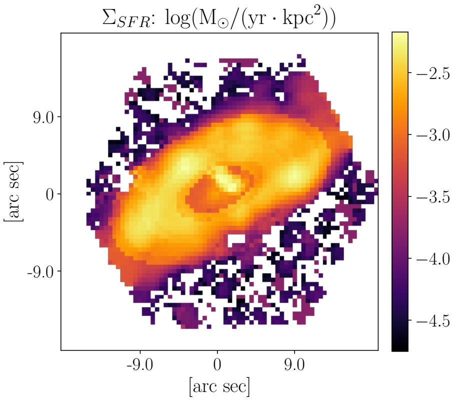
Σ_{SFR}: log(M$_\odot$/(yr · kpc^2))

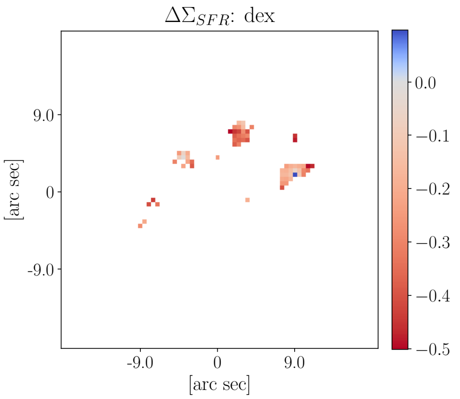
$\Delta\Sigma_{SFR}$: dex

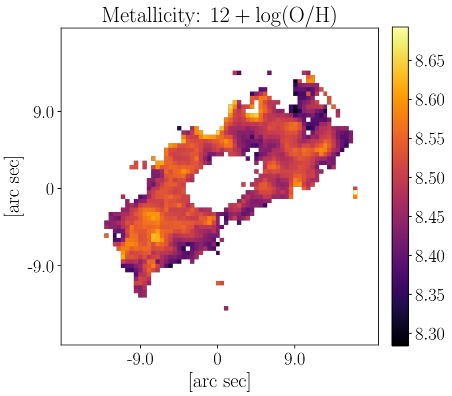
Metallicity: $12 + \log(\mathrm{O/H})$

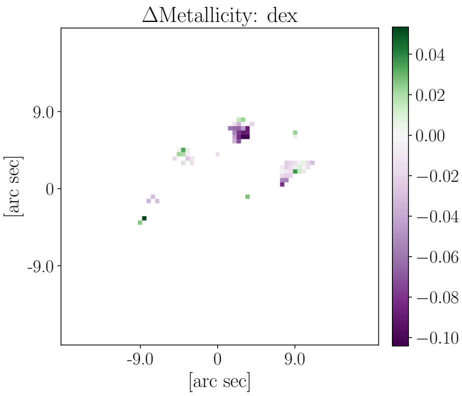
ΔMetallicity: dex

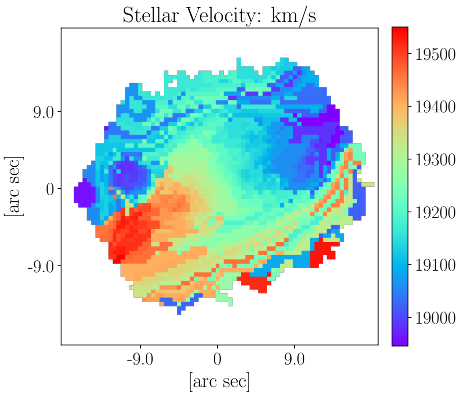
Stellar Velocity: km/s

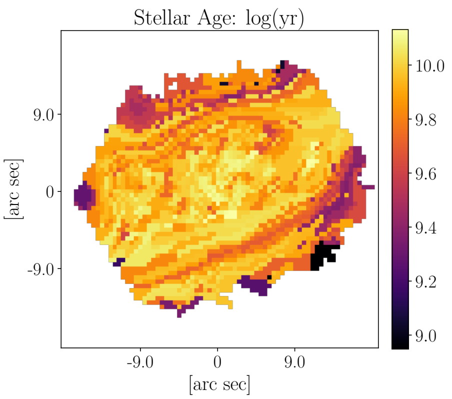
Stellar Age: log(yr)

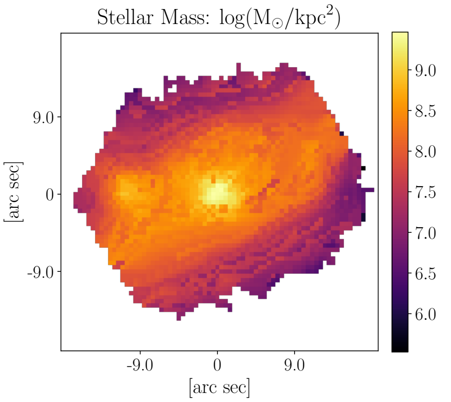
Stellar Mass: log(M$_\odot$/kpc^2)

Galaxy objID: 587739811020341405
plate-ifu: 8952-12702
RA: 205.321°
Decl: 26.272°
z: 0.0642608
K03: NULL
$\log \mathrm{M}_*$: 11.1615 $\log \mathrm{M}_\odot$
$\log \mathrm{SFR}$: 0.306261 $\log(\mathrm{M}_\odot/\mathrm{yr})$
O/H(KE08): nan
Δ SFR: nan
manga-id: 1-627000
Match separation: 0.0940311”
Companion Flag: 1

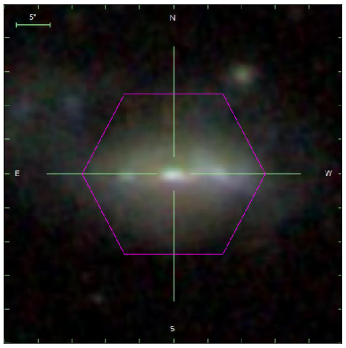

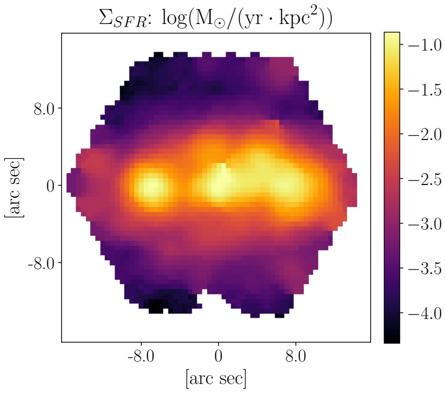
Σ_{SFR}: log(M$_\odot$/(yr · kpc^2))

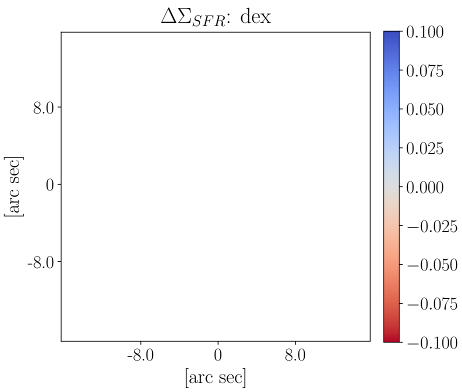
$\Delta\Sigma_{SFR}$: dex

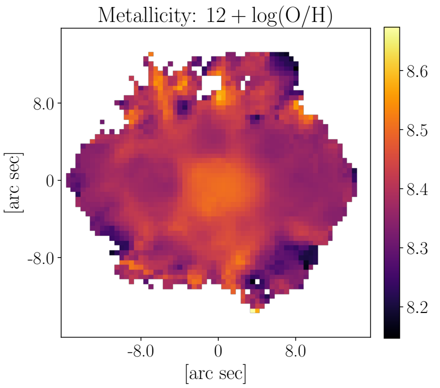
Metallicity: $12 + \log(\mathrm{O/H})$

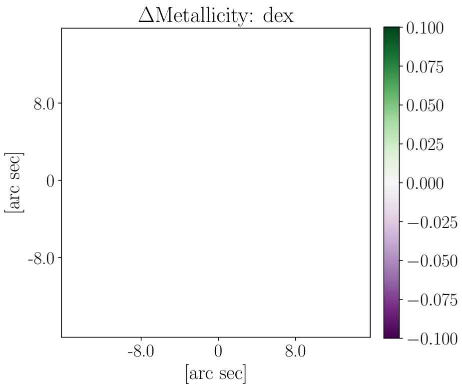
ΔMetallicity: dex

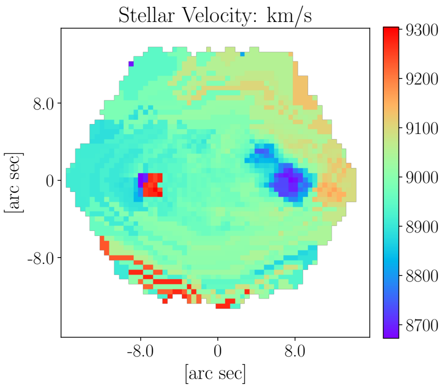
Stellar Velocity: km/s

Galaxy objID: 587741726050353203

plate-ifu: 8320-9101

RA: 206.314°

Decl: 23.3165°

z: 0.0298928

K03: NULL

$\log \mathrm{M}_*$: 10.4481 $\log \mathrm{M}_\odot$

$\log \mathrm{SFR}$: 0.654801 $\log(\mathrm{M}_\odot/\mathrm{yr})$

O/H(KE08): nan

Δ SFR: nan

manga-id: 1-523050

Match separation: 0.0929047"

Companion Flag: 0

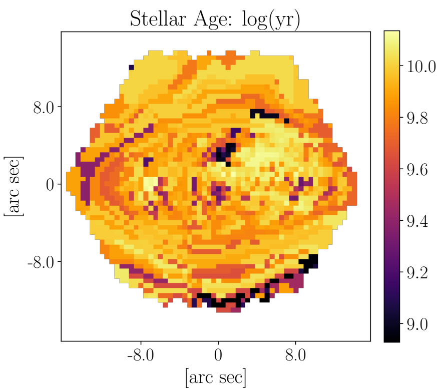
Stellar Age: log(yr)

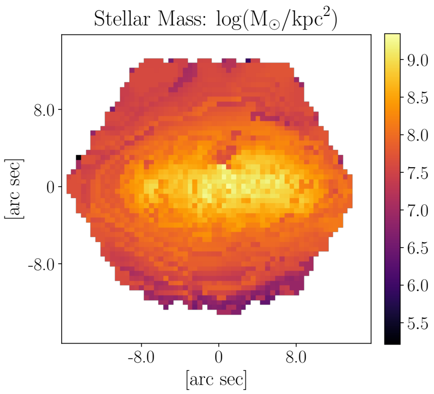
Stellar Mass: log(M$_\odot$/kpc^2)

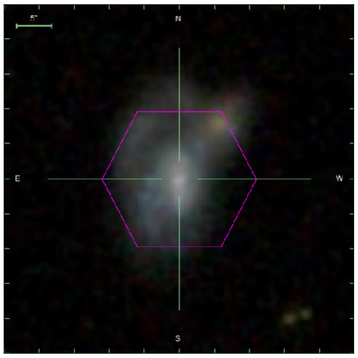

Σ_{SFR}: $\log(\mathrm{M}_\odot/(\mathrm{yr}\cdot\mathrm{kpc}^2))$

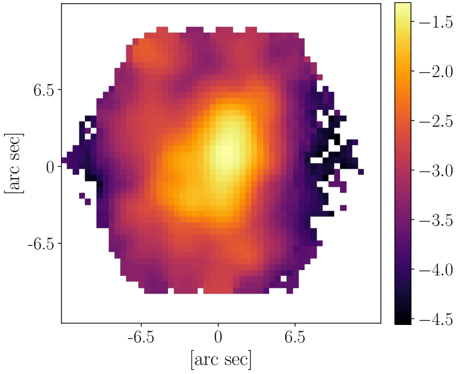

$\Delta\Sigma_{SFR}$: dex

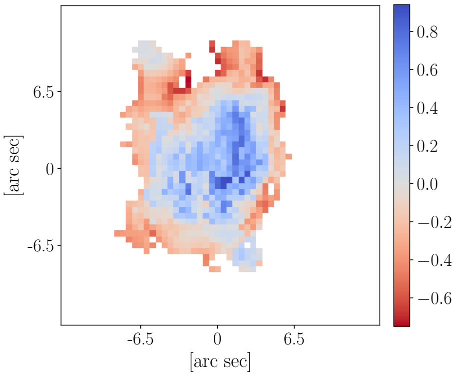

Metallicity: $12 + \log(\mathrm{O/H})$

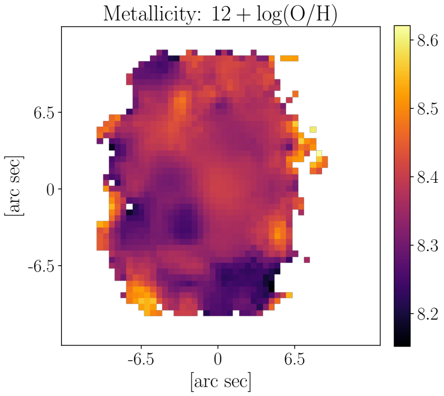

ΔMetallicity: dex

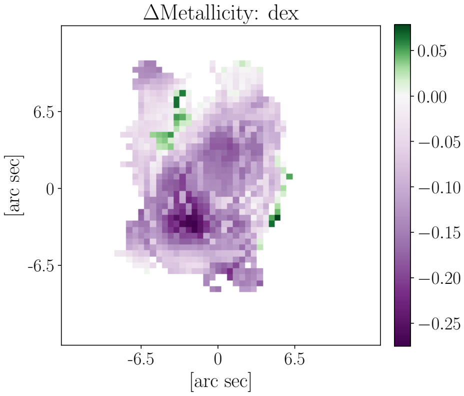

Stellar Velocity: km/s

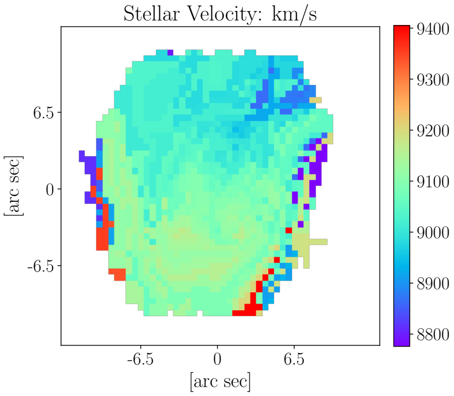

Stellar Age: log(yr)

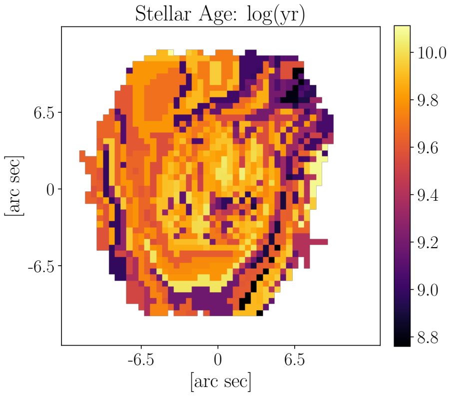

Stellar Mass: $\log(\mathrm{M}_\odot/\mathrm{kpc}^2)$

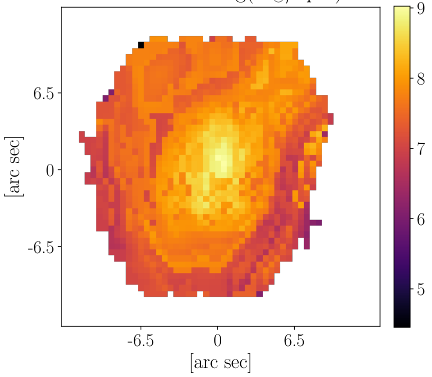

Galaxy objID: 587742189913833708

plate-ifu: 8320-6104

RA: 206.554°

Decl: 23.0841°

z: 0.030233

K03: SF

$\log \mathrm{M}_*$: 9.94244 $\log \mathrm{M}_\odot$

$\log \mathrm{SFR}$: -0.0819313 $\log(\mathrm{M}_\odot/\mathrm{yr})$

O/H(KE08): 8.77594

Δ SFR: 0.490707

manga-id: 1-627332

Match separation: 0.10813"

Companion Flag: 1

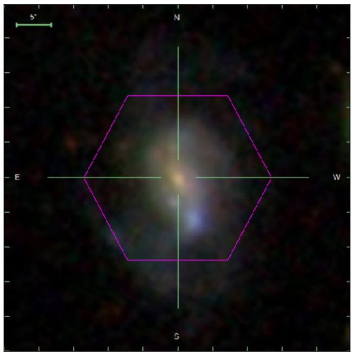

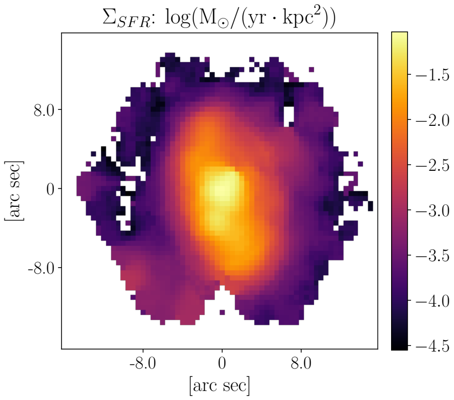
Σ_{SFR}: log(M$_{\odot}$/(yr · kpc^2))

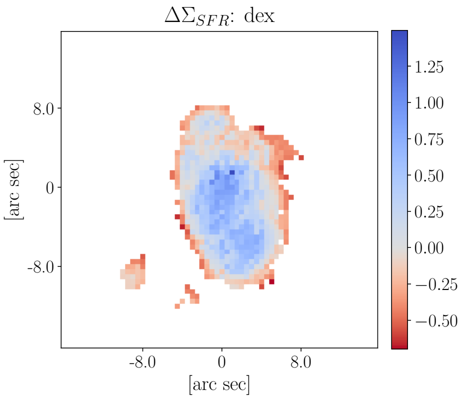
$\Delta\Sigma_{SFR}$: dex

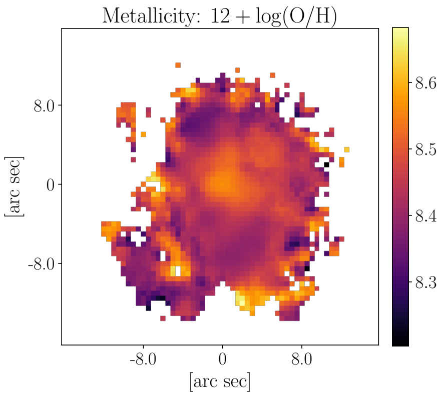
Metallicity: 12 + log(O/H)

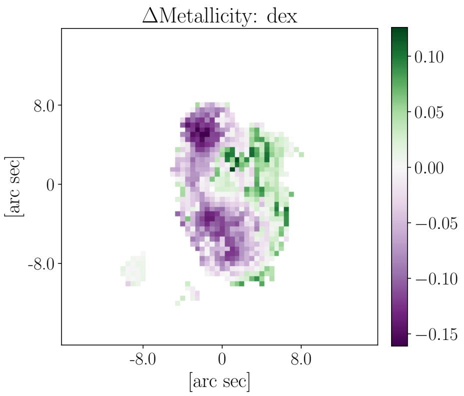
ΔMetallicity: dex

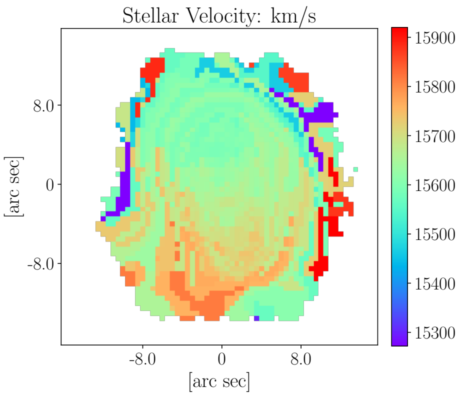
Stellar Velocity: km/s

Galaxy objID: 588007005271097606

plate-ifu: 8612-9101

RA: 253.289°

Decl: 38.8445°

z: 0.0521519

K03: SF

$\log M_*$: 10.5024 $\log M_\odot$

$\log SFR$: 0.586136 log(M$_\odot$/yr)

O/H(KE08): 8.99998

Δ SFR: 0.401419

manga-id: 1-95770

Match separation: 0.145953"

Companion Flag: 1

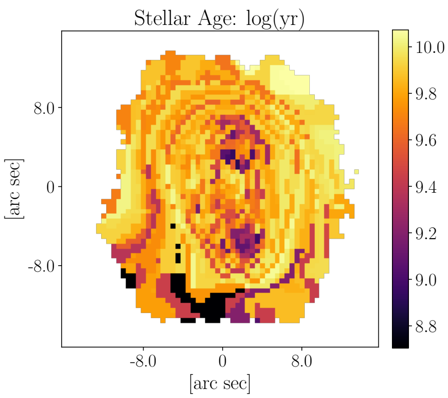
Stellar Age: log(yr)

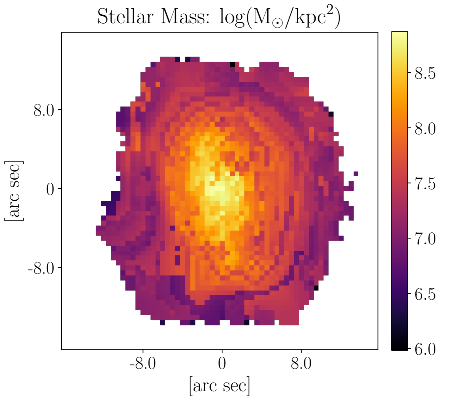
Stellar Mass: log(M$_\odot$/kpc^2)

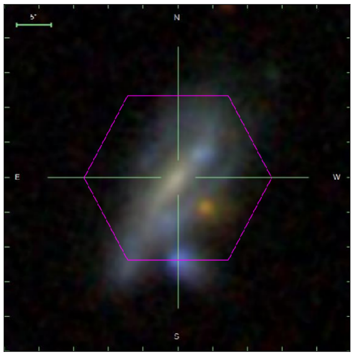

Σ_{SFR}: $\log(\mathrm{M}_\odot/(\mathrm{yr}\cdot\mathrm{kpc}^2))$

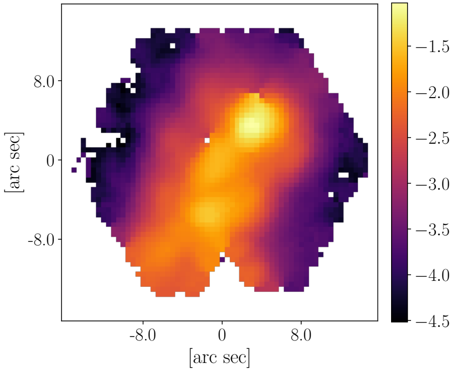

$\Delta\Sigma_{SFR}$: dex

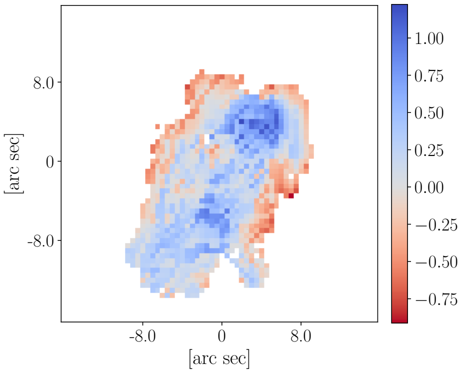

Metallicity: $12 + \log(\mathrm{O/H})$

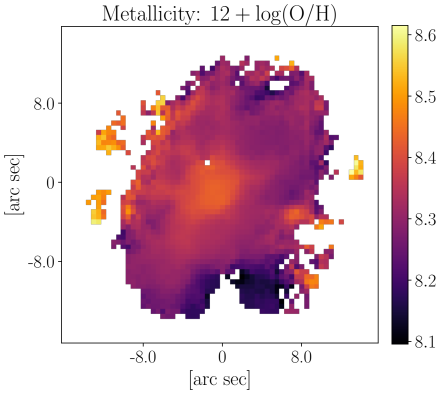

ΔMetallicity: dex

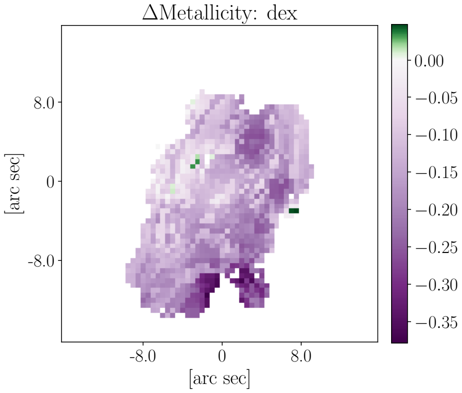

Stellar Velocity: km/s

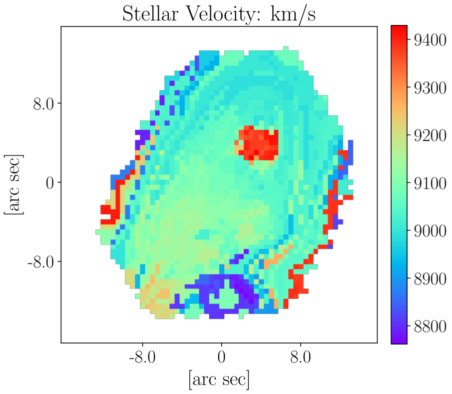

Stellar Age: log(yr)

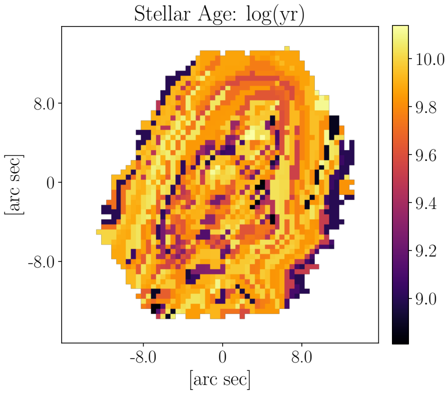

Stellar Mass: $\log(\mathrm{M}_\odot/\mathrm{kpc}^2)$

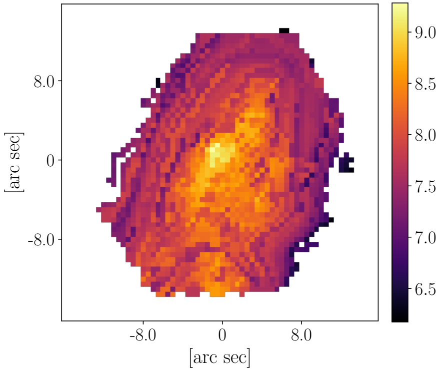

Galaxy objID: 588016892786901023

plate-ifu: 8455-9101

RA: 157.184°

Decl: 39.7786°

z: 0.0302909

K03: SF

$\log \mathrm{M}_*$: 10.219 $\log \mathrm{M}_\odot$

$\log \mathrm{SFR}$: 0.318246 $\log(\mathrm{M}_\odot/\mathrm{yr})$

O/H(KE08): 8.79566

Δ SFR: 0.417535

manga-id: 1-275176

Match separation: 0.166357"

Companion Flag: 1

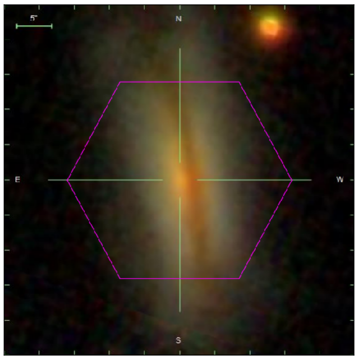

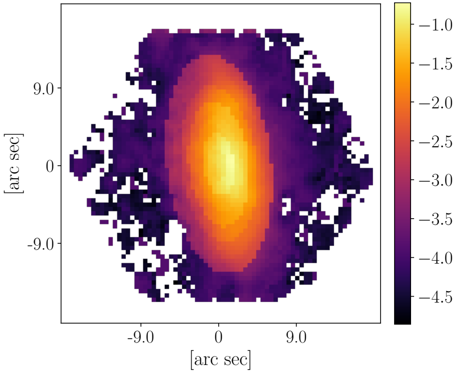
Σ_{SFR}: $\log(M_\odot/(yr \cdot kpc^2))$

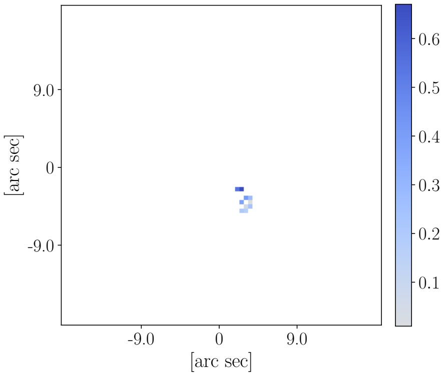
$\Delta\Sigma_{SFR}$: dex

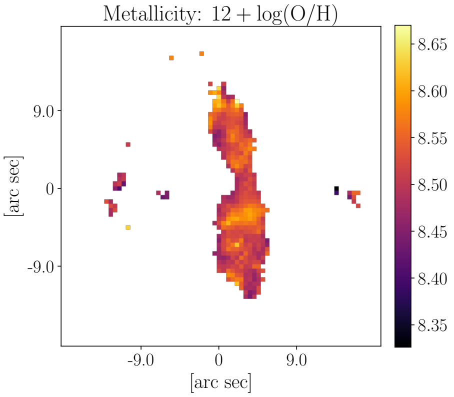
Metallicity: $12 + \log(O/H)$

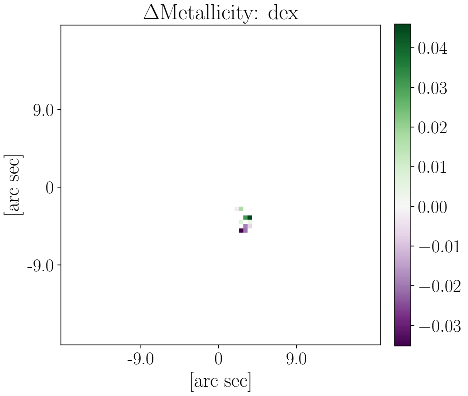
ΔMetallicity: dex

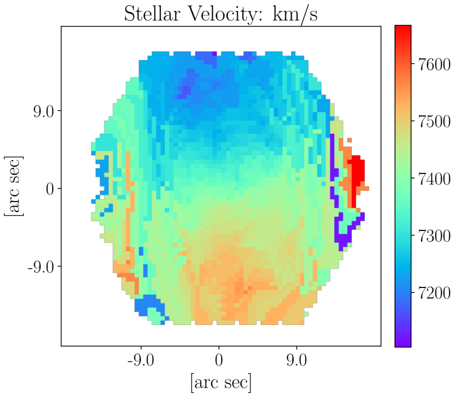
Stellar Velocity: km/s

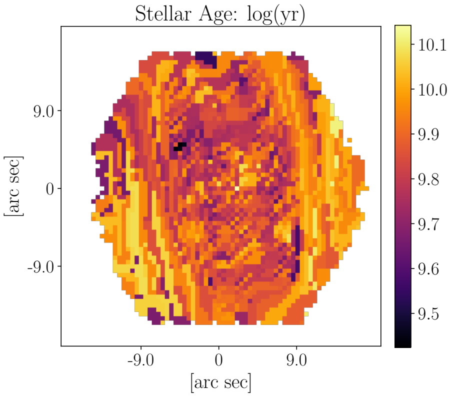
Stellar Age: log(yr)

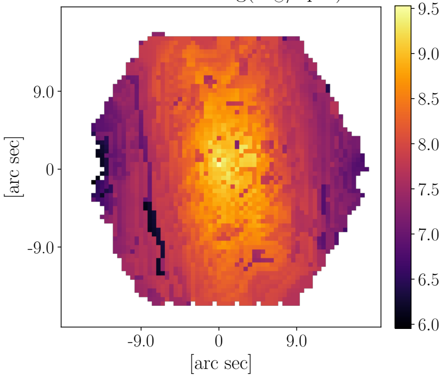
Stellar Mass: $\log(M_\odot/kpc^2)$

Galaxy objID: 588017110214508657
plate-ifu: 8253-12703
RA: 159.383°
Decl: 43.6538°
z: 0.0245746
K03: NULL
$\log M_*$: 10.4688 $\log M_\odot$
$\log SFR$: 0.331459 $\log(M_\odot/yr)$
O/H(KE08): nan
Δ SFR: nan
manga-id: 1-275456
Match separation: 0.186678”
Companion Flag: 0

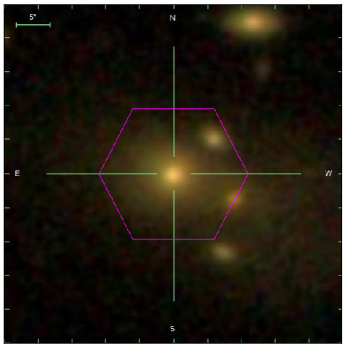

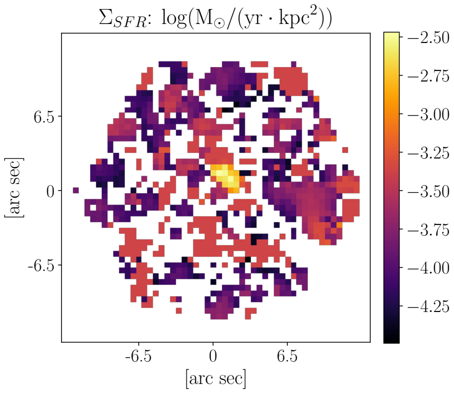

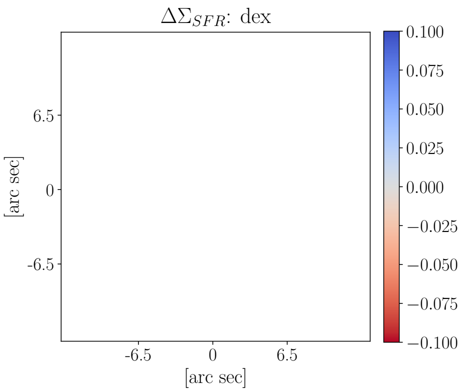

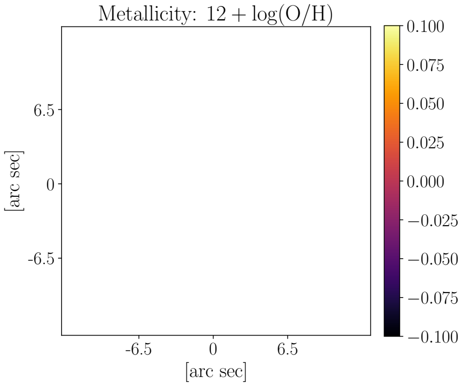

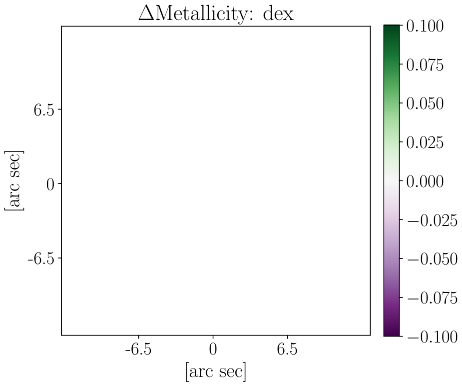

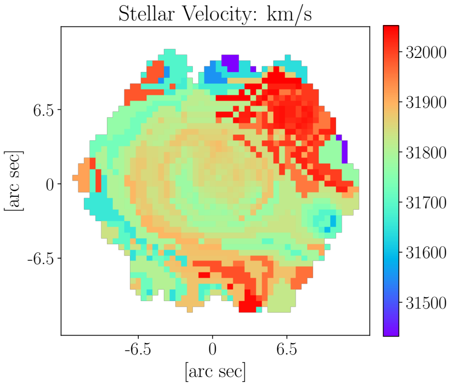

Galaxy objID: 588017605223776415

plate-ifu: 8317-6103

RA: 193.27°

Decl: 44.9604°

z: 0.106137

K03: NULL

$\log \mathrm{M}_*$: 11.1301 $\log \mathrm{M}_\odot$

$\log \mathrm{SFR}$: -0.669988 $\log(\mathrm{M}_\odot/\mathrm{yr})$

O/H(KE08): nan

Δ SFR: nan

manga-id: 1-259368

Match separation: 0.0562627”

Companion Flag: 1

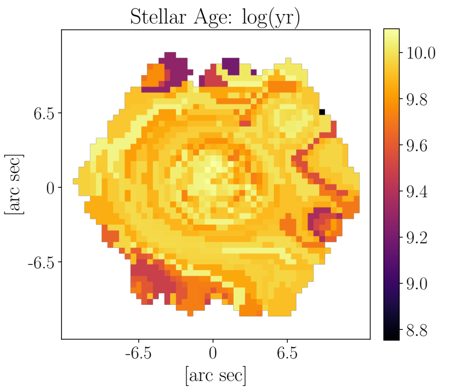

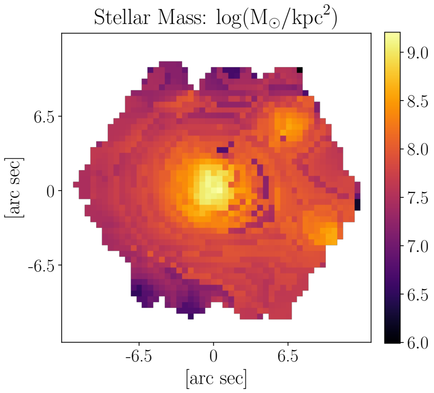

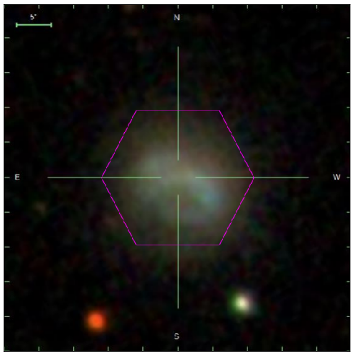

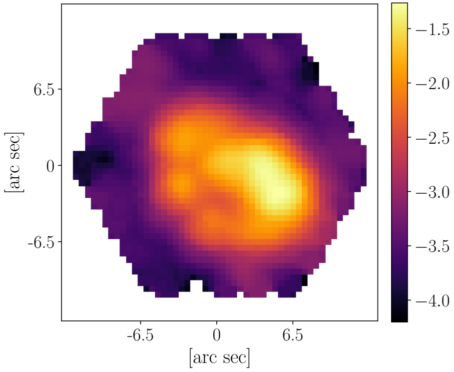
Σ_{SFR}: log(M$_\odot$/(yr · kpc^2))

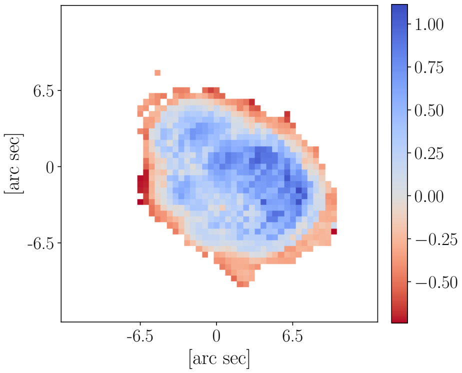
$\Delta\Sigma_{SFR}$: dex

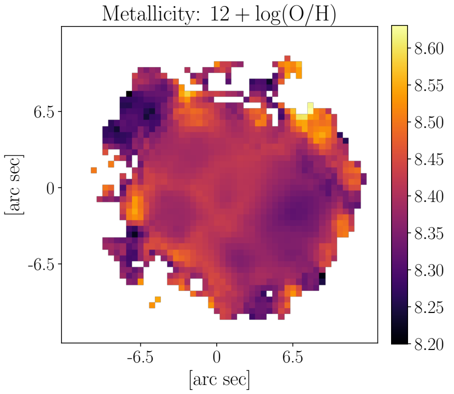
Metallicity: 12 + log(O/H)

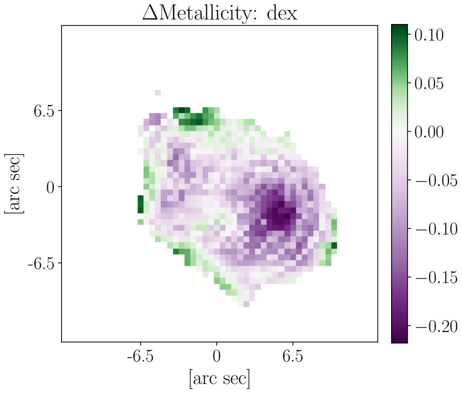
ΔMetallicity: dex

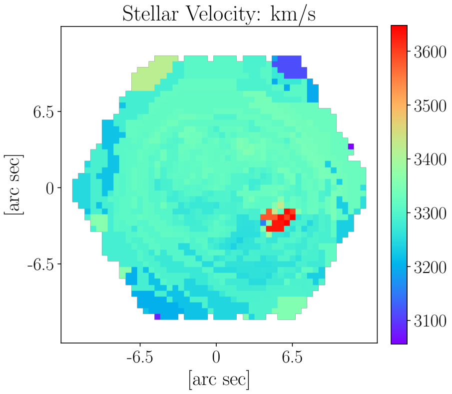
Stellar Velocity: km/s

Galaxy objID: 587725551192178920

plate-ifu: 8135-6101

RA: 115.242°

Decl: 39.3793°

z: 0.0110281

K03: NULL

log M$_*$: 9.14859 log M$_\odot$

log SFR : -0.901746 log(M$_\odot$/yr)

O/H(KE08): nan

Δ SFR: -0.0268595

manga-id: 1-43148

Match separation: 2.73435”

Companion Flag: 0

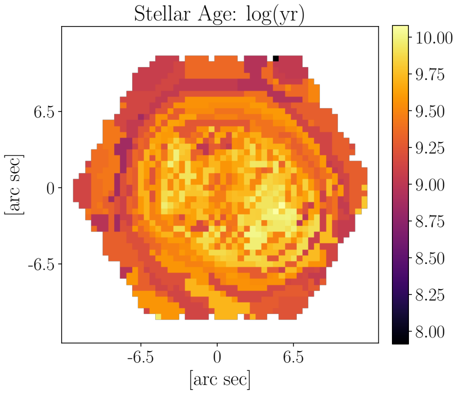
Stellar Age: log(yr)

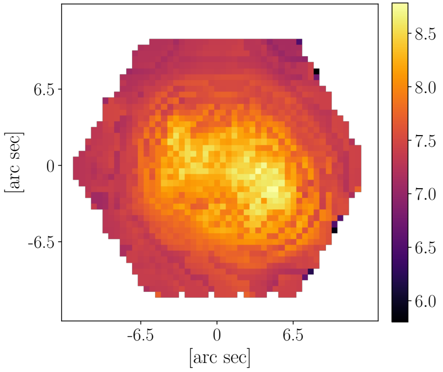
Stellar Mass: log(M$_\odot$/kpc^2)

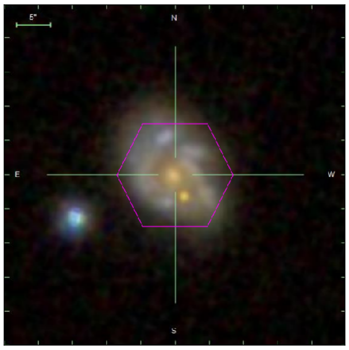

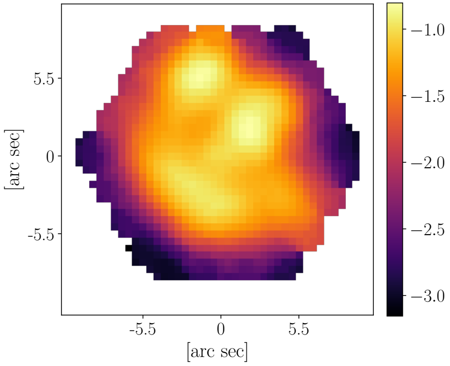
Σ_{SFR}: log(M$_\odot$/(yr · kpc^2))

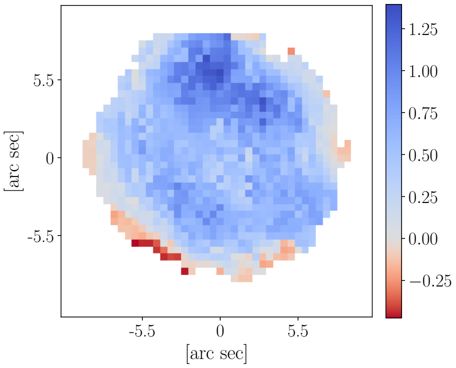
$\Delta\Sigma_{SFR}$: dex

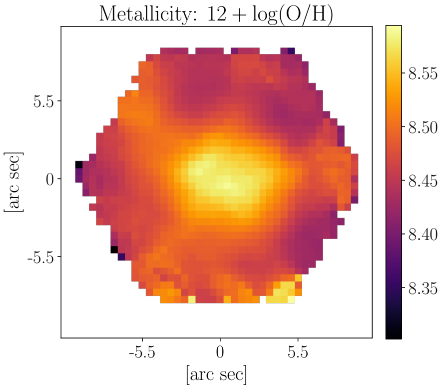
Metallicity: $12 + \log(O/H)$

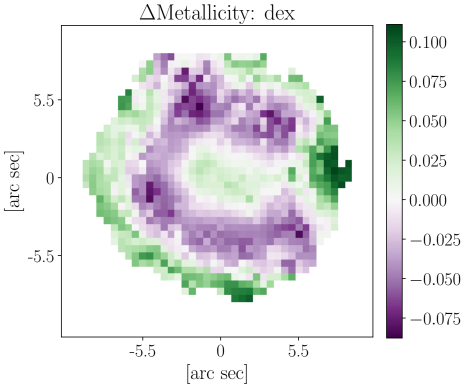
ΔMetallicity: dex

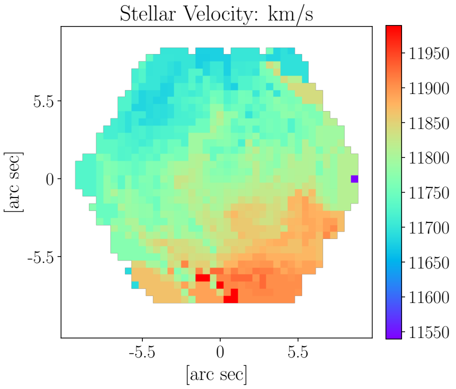
Stellar Velocity: km/s

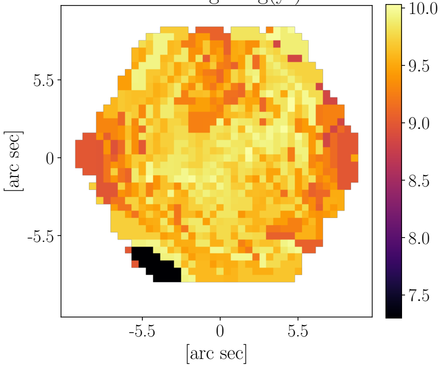
Stellar Age: log(yr)

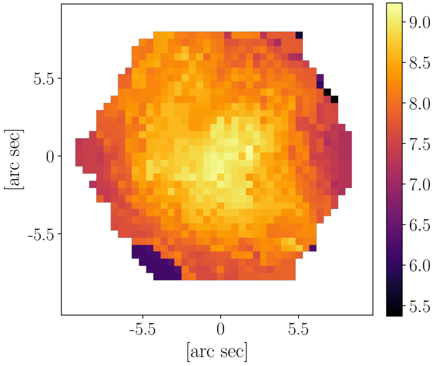
Stellar Mass: log(M$_\odot$/kpc^2)

Galaxy objID: 587725775604940809

plate-ifu: 8140-3701

RA: 116.177°

Decl: 42.3577°

z: 0.0393059

K03: SF

$\log M_*$: 10.55 $\log M_\odot$

log SFR : 0.872135 log(M$_\odot$/yr)

O/H(KE08): 8.95218

Δ SFR: -0.118458

manga-id: 1-43702

Match separation: 230.49”

Companion Flag: 0

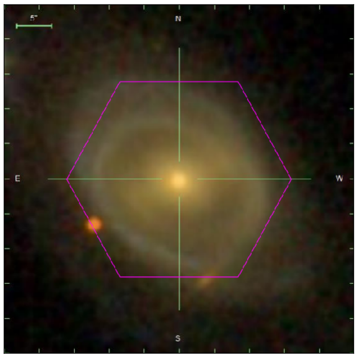

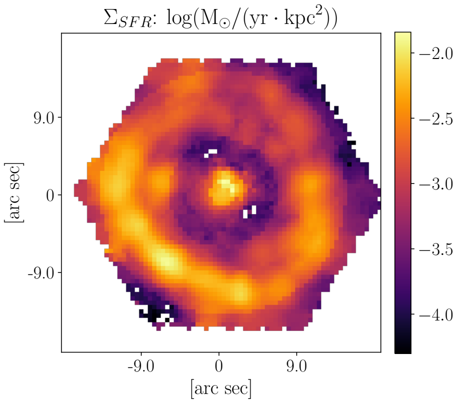
Σ_{SFR}: log(M$_\odot$/(yr · kpc^2))

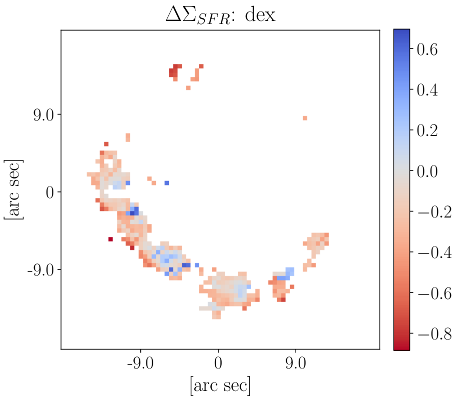
$\Delta\Sigma_{SFR}$: dex

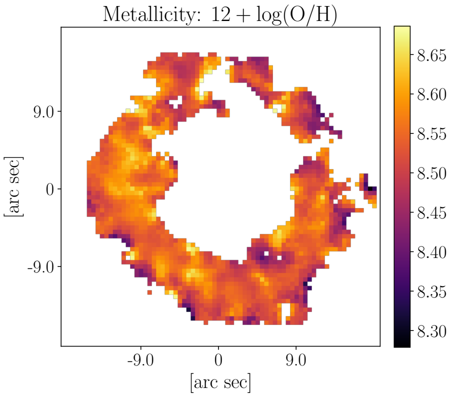
Metallicity: 12 + log(O/H)

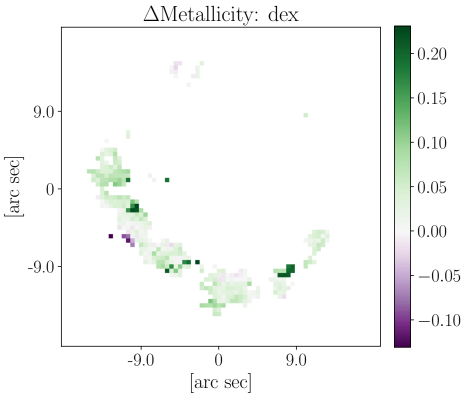
ΔMetallicity: dex

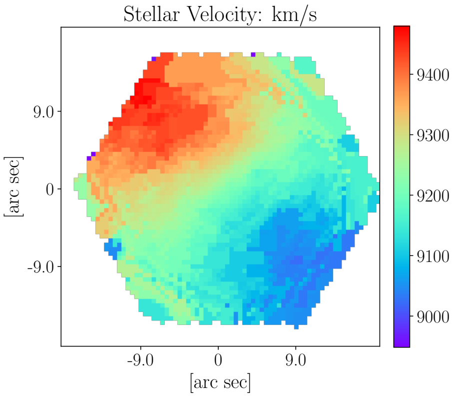
Stellar Velocity: km/s

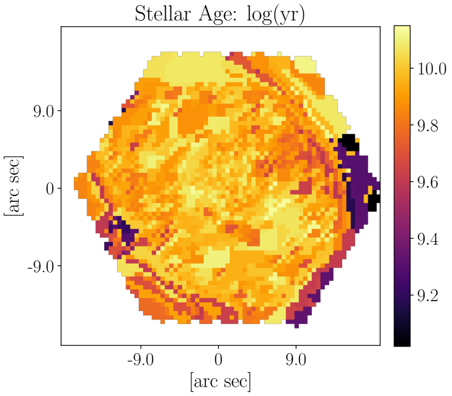
Stellar Age: log(yr)

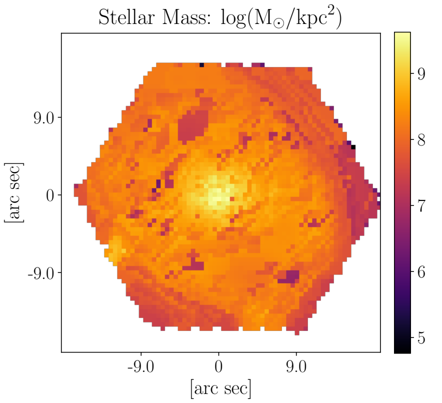
Stellar Mass: log(M$_\odot$/kpc^2)

Galaxy objID: 587730846891508132

plate-ifu: 8616-12702

RA: 322.306°

Decl: -0.294765°

z: 0.030791

K03: NULL

$\log M_*$: 10.7547 $\log M_\odot$

$\log SFR$: -0.201198 log(M$_\odot$/yr)

O/H(KE08): nan

Δ SFR: nan

manga-id: 1-289846

Match separation: 264.007”

Companion Flag: 0

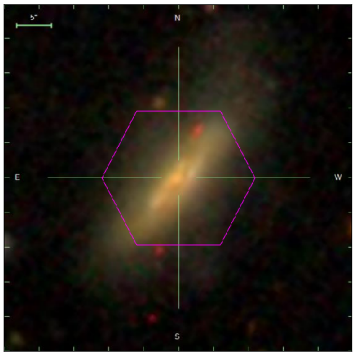

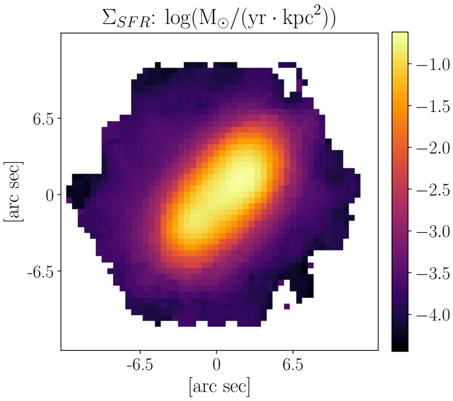
Σ_{SFR}: $\log(\mathrm{M_\odot}/(\mathrm{yr}\cdot\mathrm{kpc}^2))$

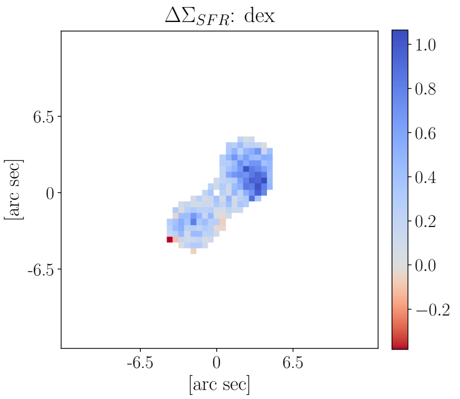
$\Delta\Sigma_{SFR}$: dex

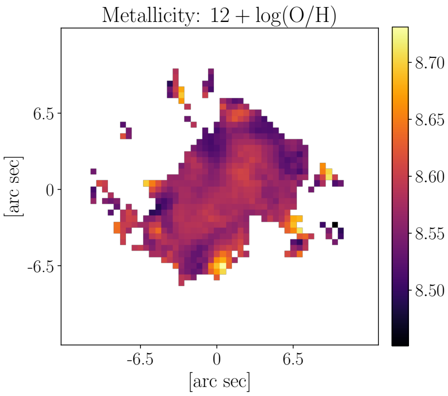
Metallicity: $12+\log(\mathrm{O/H})$

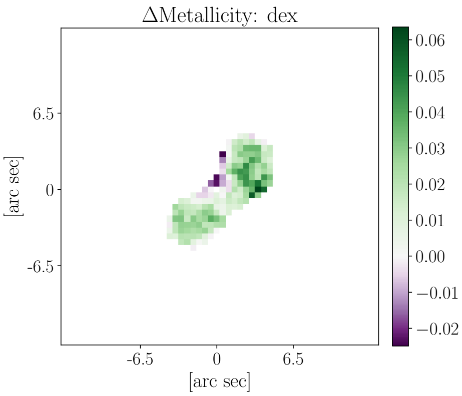
ΔMetallicity: dex

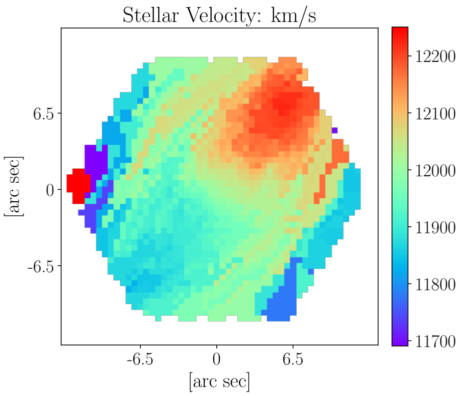
Stellar Velocity: km/s

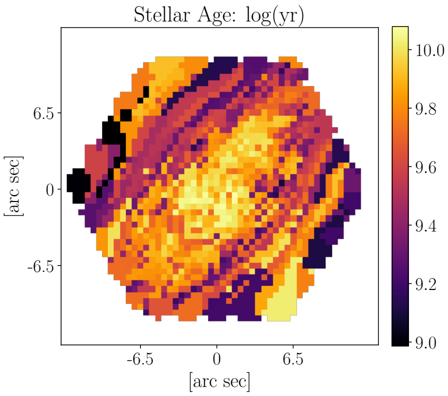
Stellar Age: log(yr)

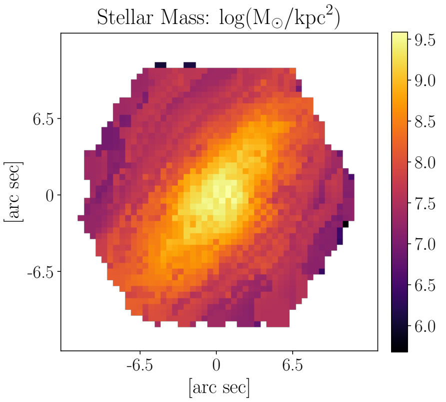
Stellar Mass: $\log(\mathrm{M_\odot}/\mathrm{kpc}^2)$

Galaxy objID: 587732054857220338

plate-ifu: 8250-6104

RA: 140.411°

Decl: 43.7262°

z: 0.0400622

K03: NULL

$\log \mathrm{M}_*$: 10.7532 $\log \mathrm{M}_\odot$

$\log \mathrm{SFR}$: 0.857882 $\log(\mathrm{M}_\odot/\mathrm{yr})$

O/H(KE08): nan

Δ SFR: nan

manga-id: 1-558926

Match separation: 408.198”

Companion Flag: 0

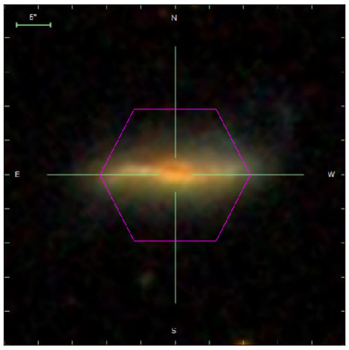

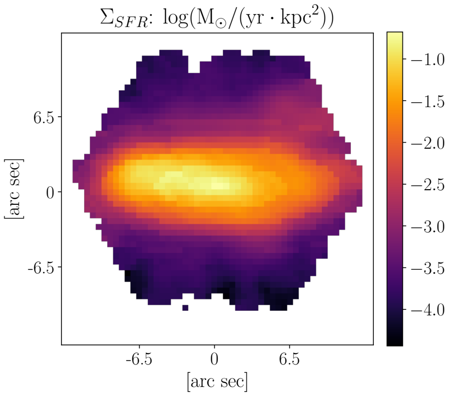
Σ_{SFR}: log(M$_\odot$/(yr · kpc^2))

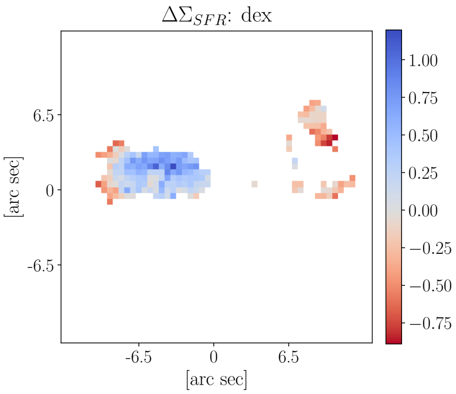
$\Delta\Sigma_{SFR}$: dex

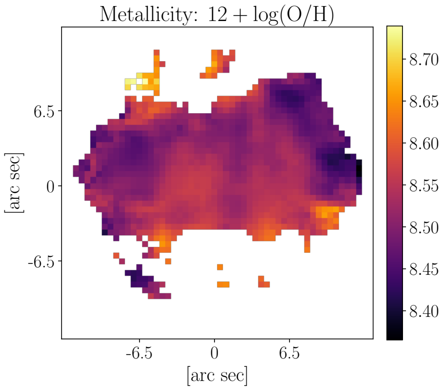
Metallicity: 12 + log(O/H)

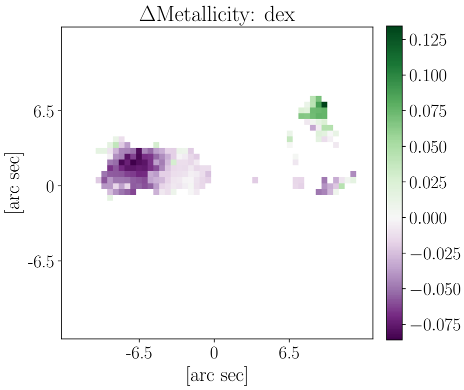
ΔMetallicity: dex

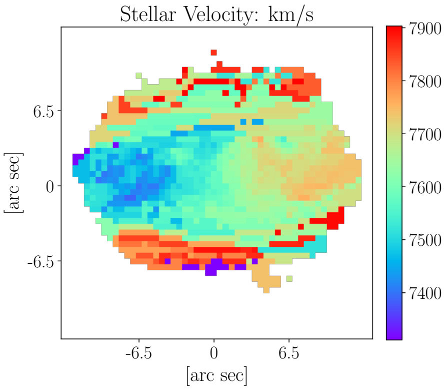
Stellar Velocity: km/s

Galaxy objID: 587733428701036711

plate-ifu: 8485-6103

RA: 233.033°

Decl: 49.1248°

z: 0.0252642

K03: SF

log M$_*$: 10.4611 log M$_\odot$

log SFR : 0.58674 log(M$_\odot$/yr)

O/H(KE08): 8.81232

Δ SFR: 0.061345

manga-id: 1-209221

Match separation: 320.355"

Companion Flag: 0

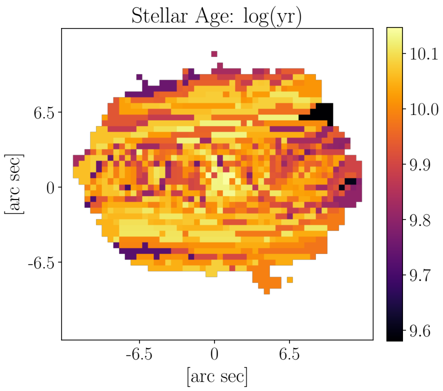
Stellar Age: log(yr)

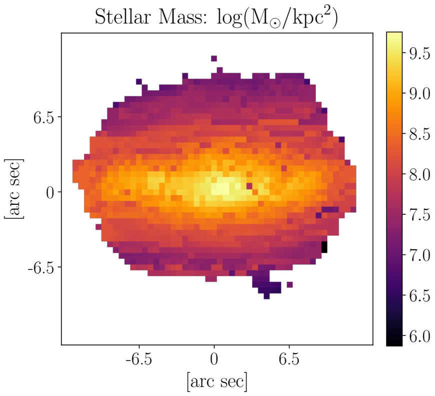
Stellar Mass: log(M$_\odot$/kpc^2)

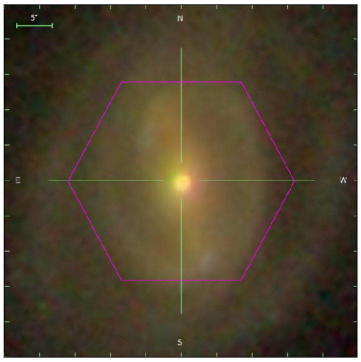

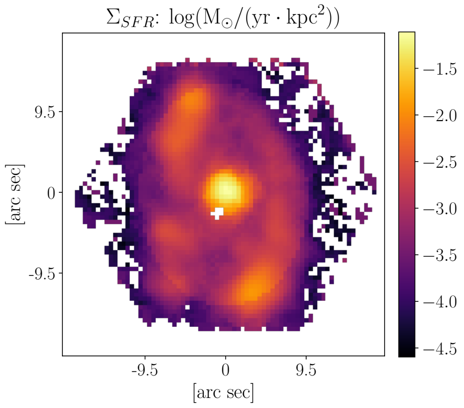

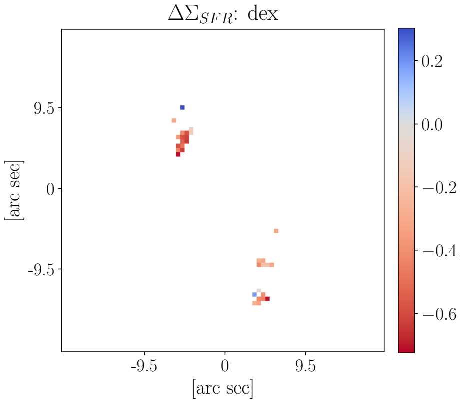

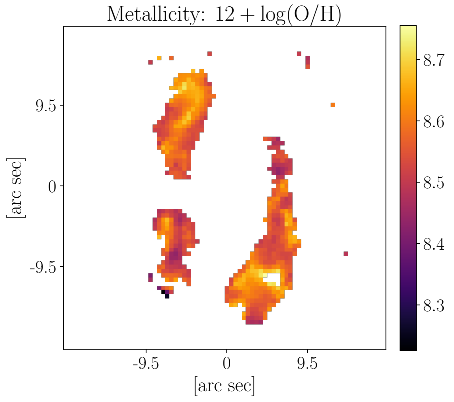

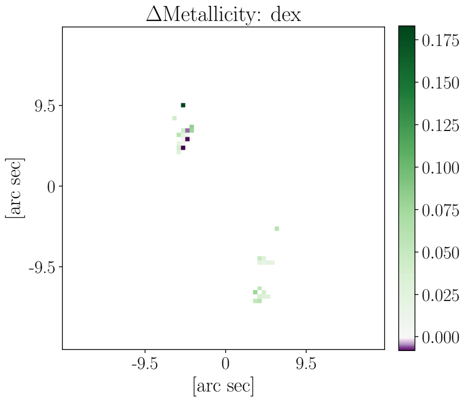

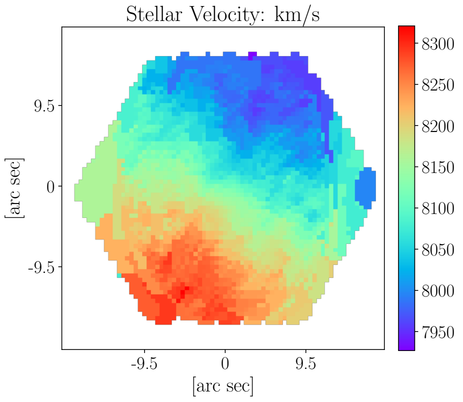

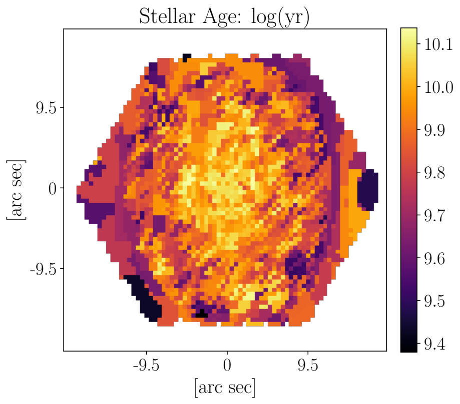

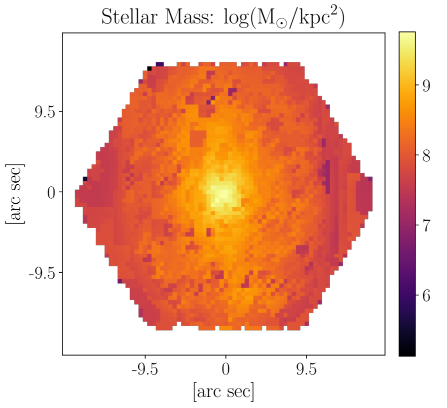

Galaxy objID: 587733609627124083

plate-ifu: 8602-12701

RA: 247.048°

Decl: 39.8219°

z: 0.0270692

K03: NULL

$\log M_*$: 10.7212 $\log M_\odot$

$\log SFR$: -0.287606 $\log(M_\odot/yr)$

O/H(KE08): nan

Δ SFR: nan

manga-id: 1-569169

Match separation: 277.736"

Companion Flag: 0

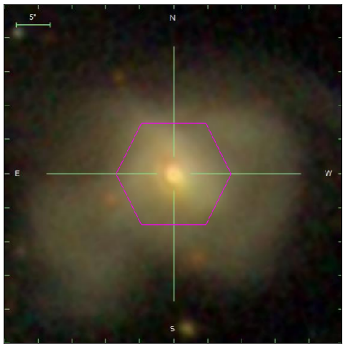

Σ_{SFR}: $\log(\mathrm{M}_\odot/(\mathrm{yr}\cdot\mathrm{kpc}^2))$

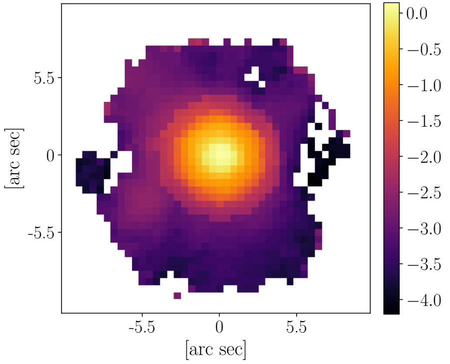

$\Delta\Sigma_{SFR}$: dex

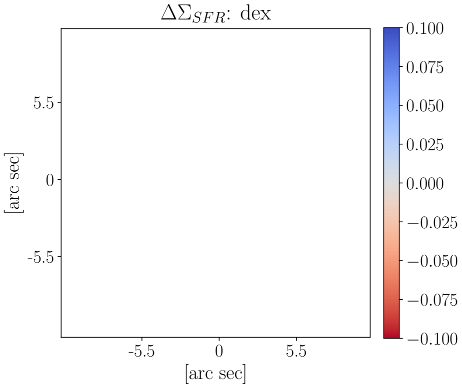

Metallicity: $12 + \log(\mathrm{O/H})$

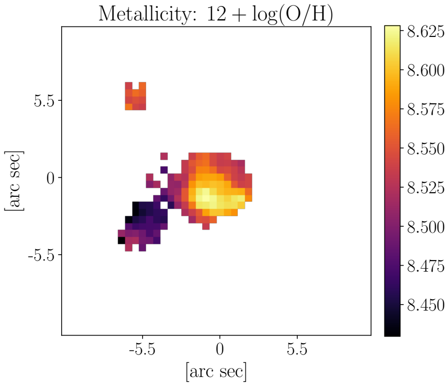

ΔMetallicity: dex

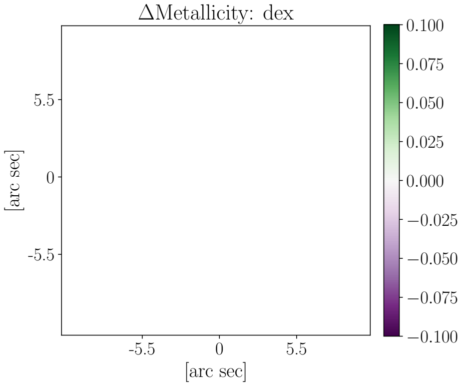

Stellar Velocity: km/s

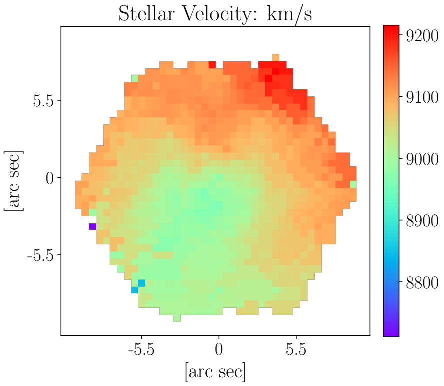

Galaxy objID: 587735665845469285

plate-ifu: 8595-3703

RA: 221.438°

Decl: 51.5808°

z: 0.0300276

K03: NULL

$\log \mathrm{M}_*$: 10.8864 $\log \mathrm{M}_\odot$

$\log \mathrm{SFR}$: 0.568961 $\log(\mathrm{M}_\odot/\mathrm{yr})$

O/H(KE08): nan

Δ SFR: nan

manga-id: 1-631278

Match separation: 262.605"

Companion Flag: 0

Stellar Age: log(yr)

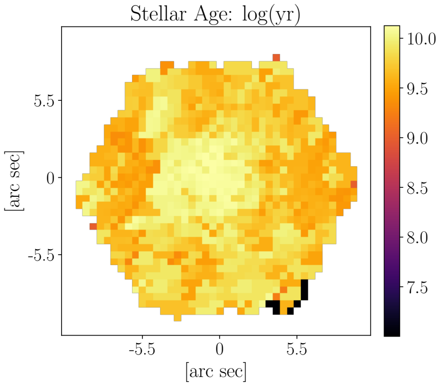

Stellar Mass: $\log(\mathrm{M}_\odot/\mathrm{kpc}^2)$

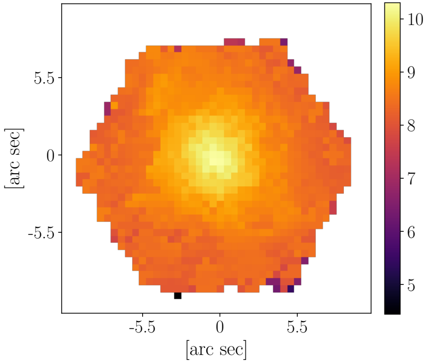

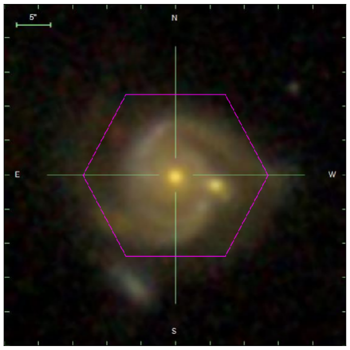

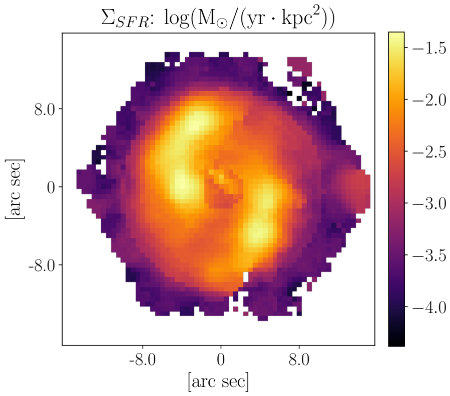

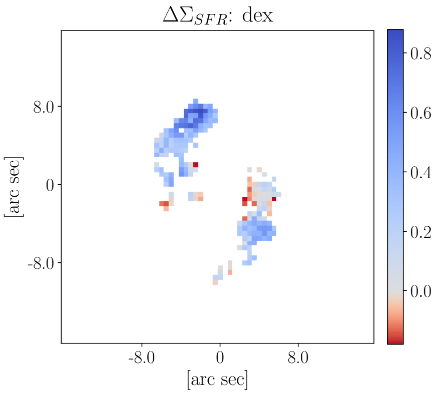

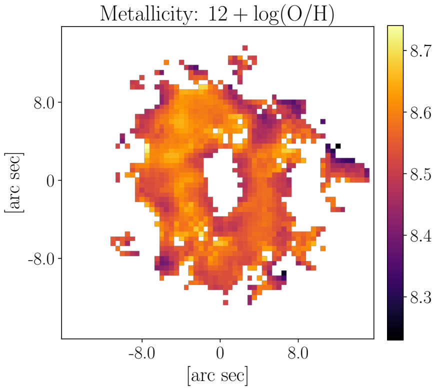

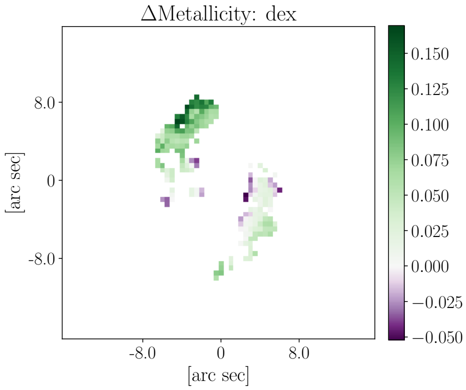

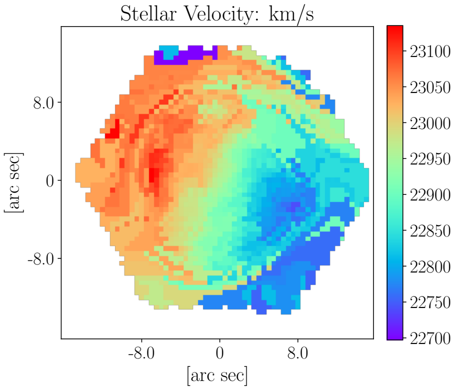

Galaxy objID: 587735696450519095

plate-ifu: 8591-9101

RA: 212.259°

Decl: 54.5562°

z: 0.0765382

K03: NULL

log M_* : 11.2279 log $M_\odot$

log SFR : 0.820902 log($M_\odot$/yr)

O/H(KE08): nan

Δ SFR: nan

manga-id: 1-629057

Match separation: 36.6477"

Companion Flag: 1

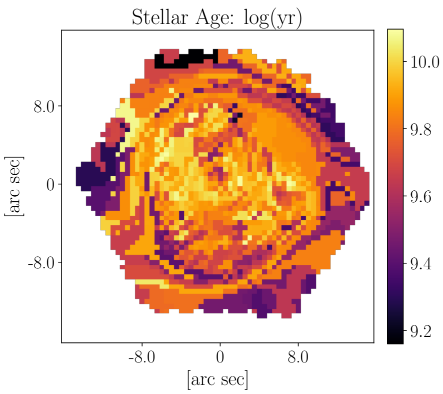

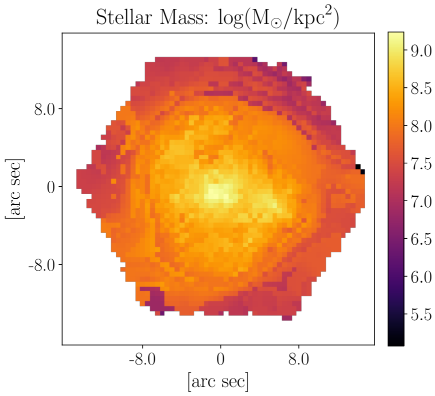

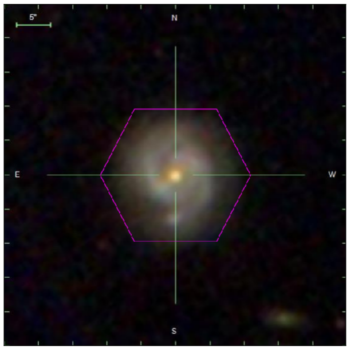

Σ_{SFR}: log(M$_\odot$/(yr · kpc^2))

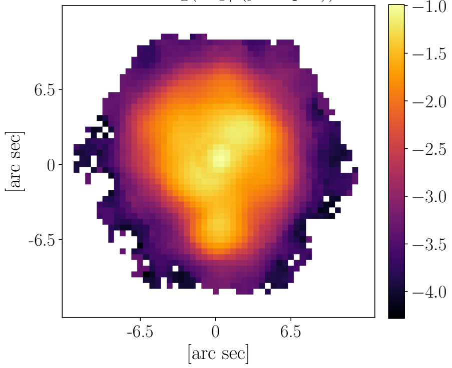

$\Delta\Sigma_{SFR}$: dex

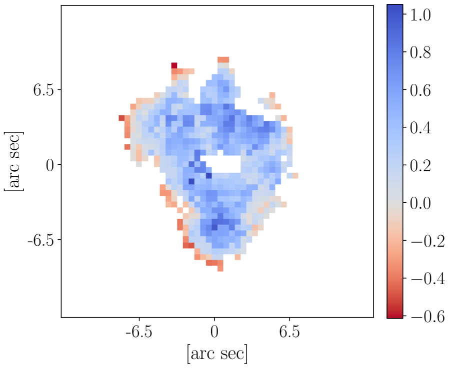

Metallicity: 12 + log(O/H)

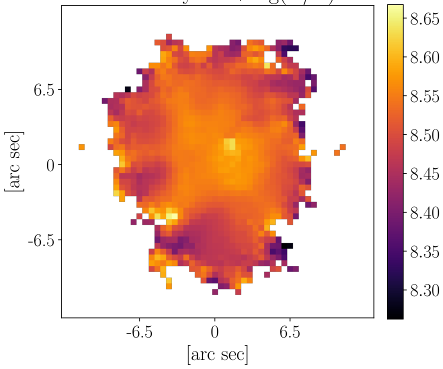

ΔMetallicity: dex

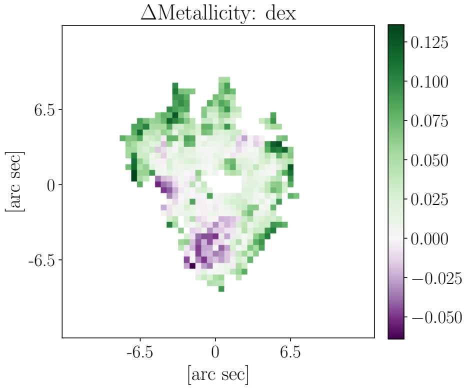

Stellar Velocity: km/s

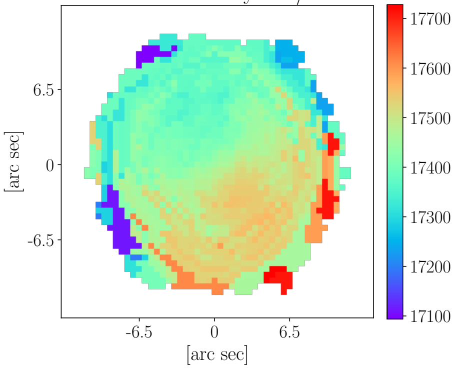

Galaxy objID: 587736620396642354

plate-ifu: 9041-6104

RA: 236.756°

Decl: 30.5332°

z: 0.0581667

K03: SF

log M$_*$: 10.7706 log M$_\odot$

log SFR : 0.699825 log(M$_\odot$/yr)

O/H(KE08): 8.96176

Δ SFR: 0.529841

manga-id: 1-264543

Match separation: 5.86524"

Companion Flag: 0

Stellar Age: log(yr)

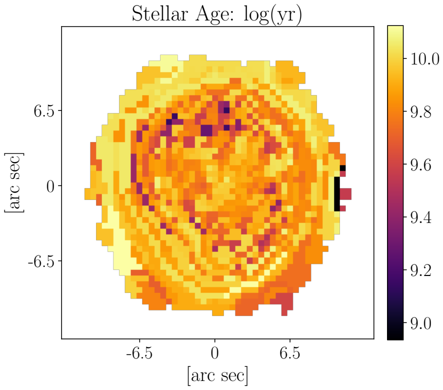

Stellar Mass: log(M$_\odot$/kpc^2)

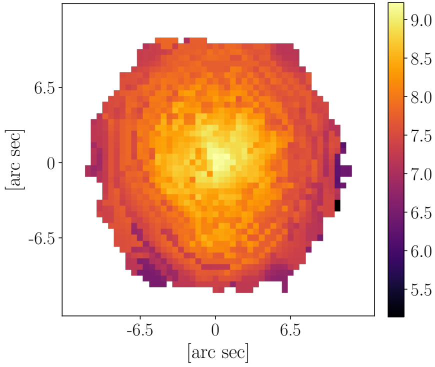

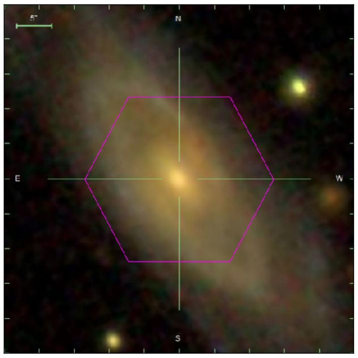

Σ_{SFR}: $\log(\mathrm{M}_\odot/(\mathrm{yr}\cdot\mathrm{kpc}^2))$

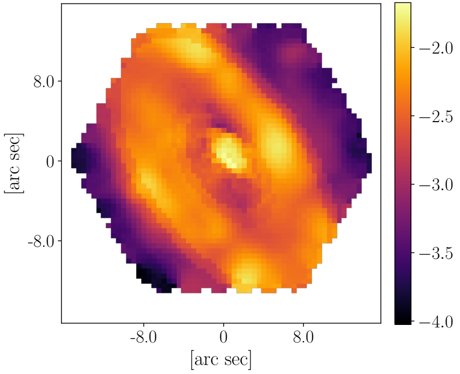

$\Delta\Sigma_{SFR}$: dex

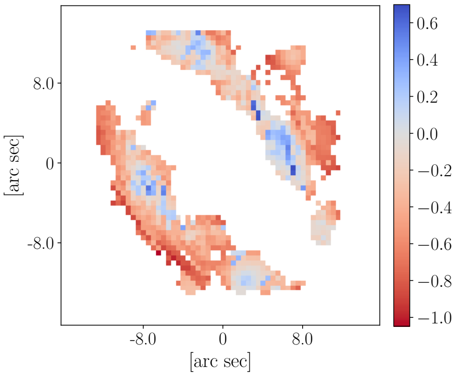

Metallicity: $12 + \log(\mathrm{O/H})$

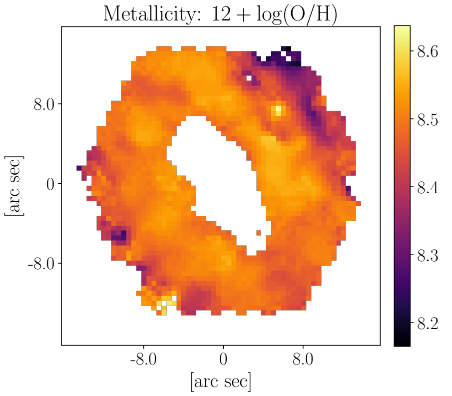

ΔMetallicity: dex

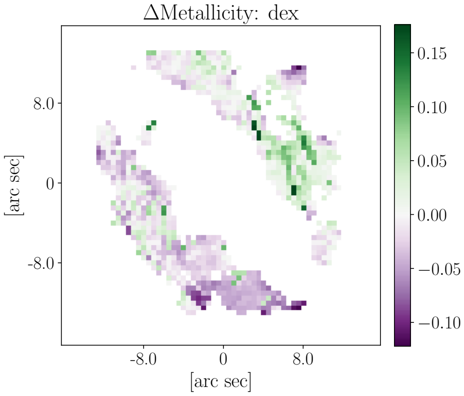

Stellar Velocity: km/s

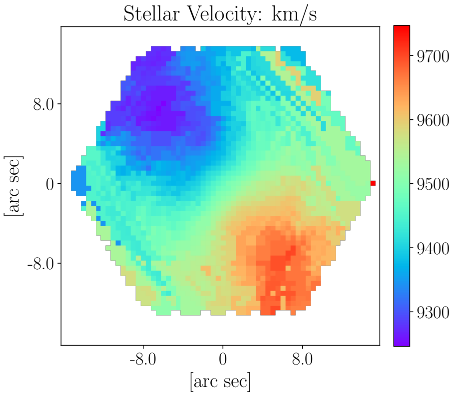

Stellar Age: log(yr)

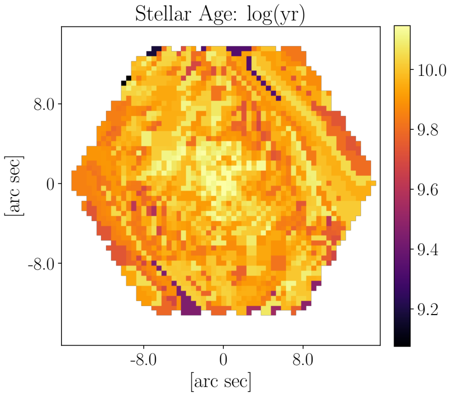

Stellar Mass: $\log(\mathrm{M}_\odot/\mathrm{kpc}^2)$

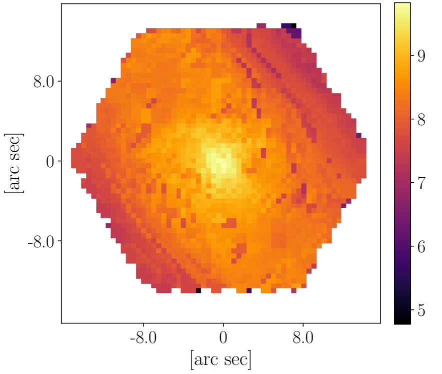

Galaxy objID: 587737810104353002
plate-ifu: 8134-9102
RA: 116.28°
Decl: 46.0724°
z: 0.0315717
K03: NULL
$\log \mathrm{M}_*$: 10.8245 $\log \mathrm{M}_\odot$
$\log \mathrm{SFR}$: 0.163564 $\log(\mathrm{M}_\odot/\mathrm{yr})$
O/H(KE08): nan
Δ SFR: nan
manga-id: 1-339163
Match separation: 238.703”
Companion Flag: 0

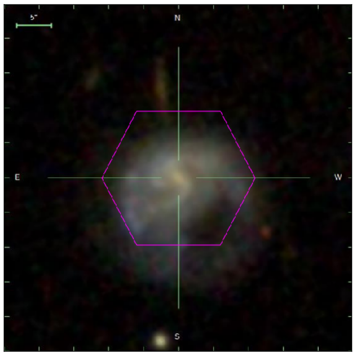

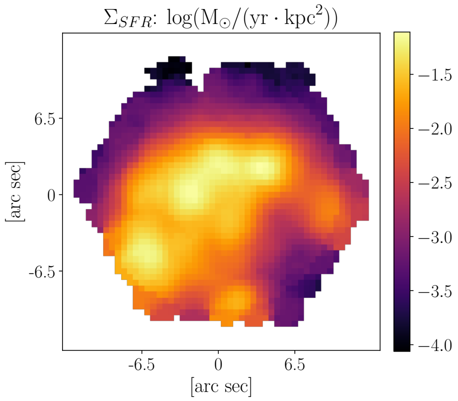
Σ_{SFR}: log($M_\odot$/(yr · kpc^2))

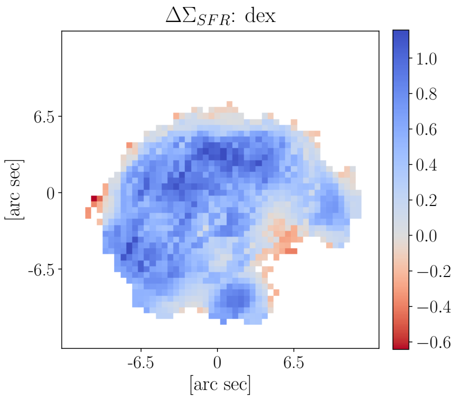
$\Delta\Sigma_{SFR}$: dex

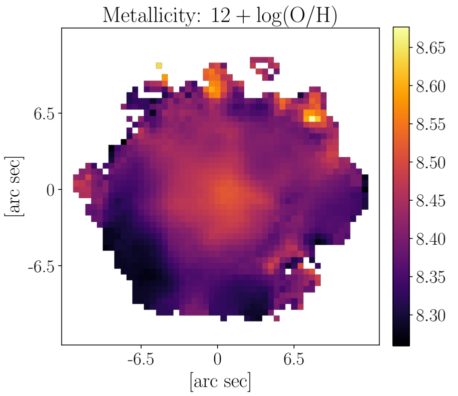
Metallicity: $12 + \log(O/H)$

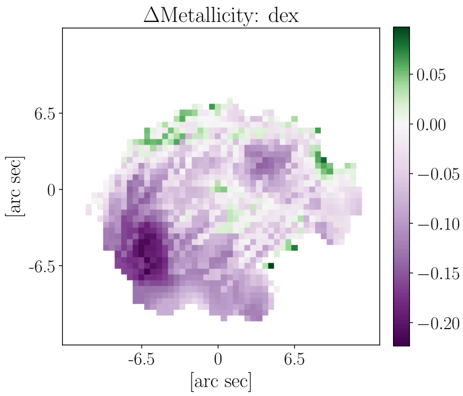
ΔMetallicity: dex

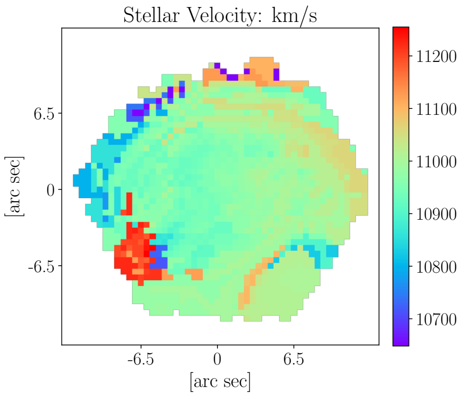
Stellar Velocity: km/s

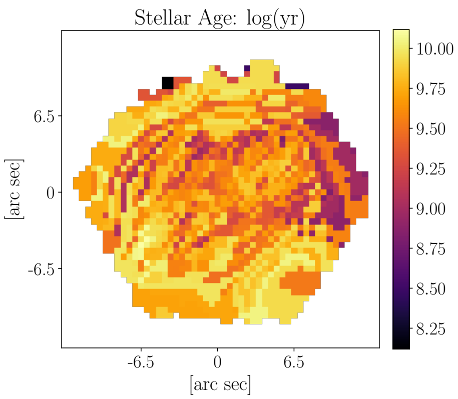
Stellar Age: log(yr)

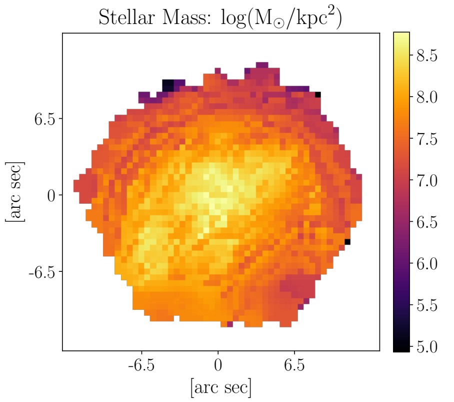
Stellar Mass: log($M_\odot$/kpc^2)

Galaxy objID: 587738196649378146

plate-ifu: 8134-6103

RA: 114.768°

Decl: 48.1291°

z: 0.0365246

K03: NULL

$\log M_*$: 10.1901 $\log M_\odot$

$\log SFR$: 0.52031 $\log(M_\odot/yr)$

O/H(KE08): nan

Δ SFR: nan

manga-id: 1-548075

Match separation: 40.3526”

Companion Flag: 0

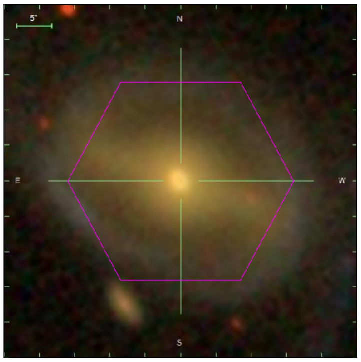

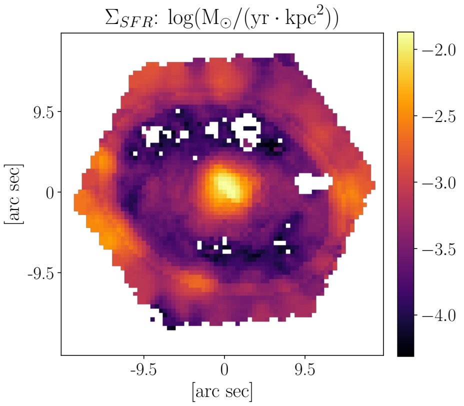

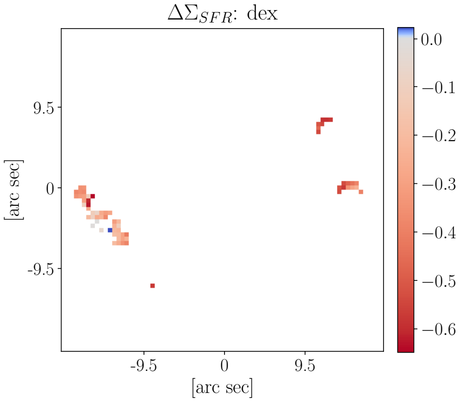

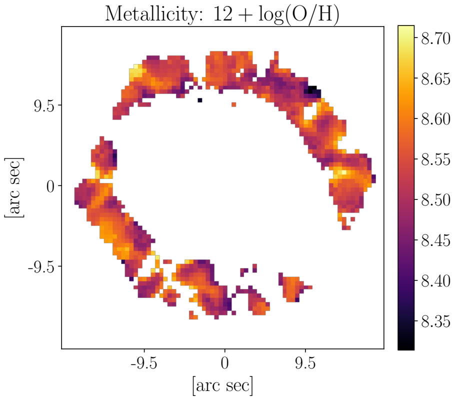

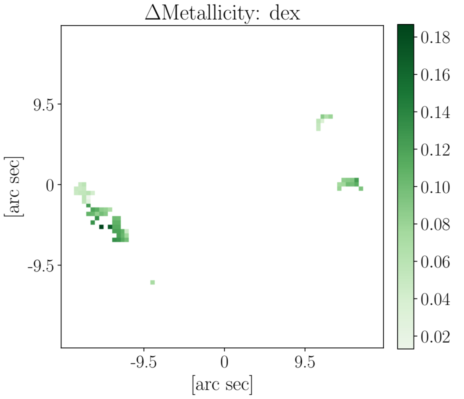

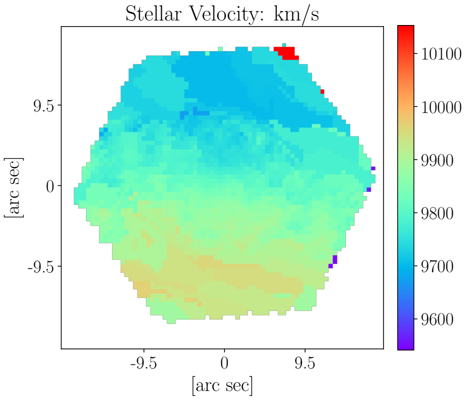

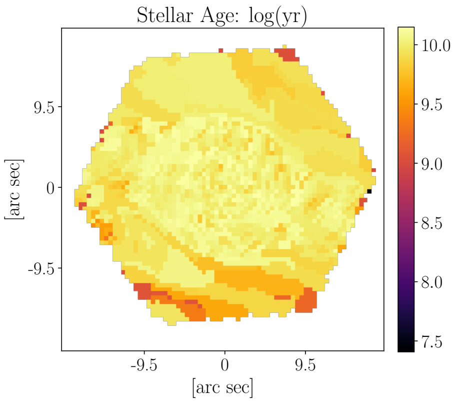

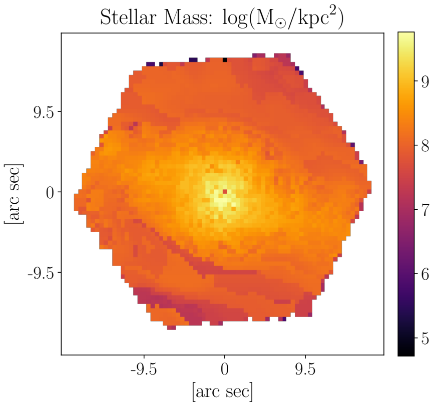

Galaxy objID: 587738196652982624
plate-ifu: 8712-12704
RA: 121.055°
Decl: 55.3977°
z: 0.0327574
K03: NULL
$\log \mathrm{M}_*$: 10.8799 $\log \mathrm{M}_\odot$
$\log \mathrm{SFR}$: -0.472428 $\log(\mathrm{M}_\odot/\mathrm{yr})$
O/H(KE08): nan
Δ SFR: nan
manga-id: 1-379708
Match separation: 151.806”
Companion Flag: 0

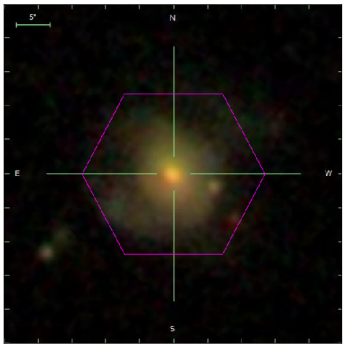

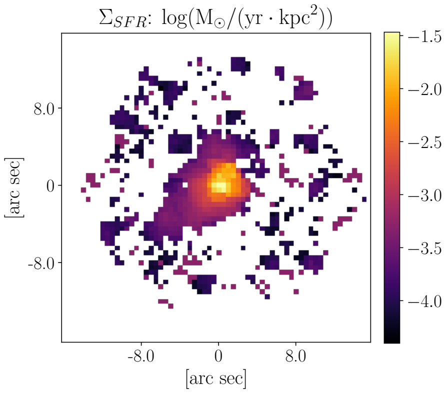

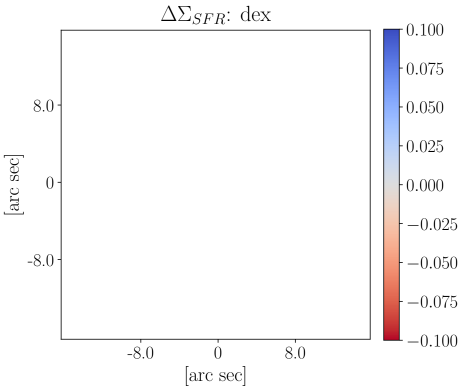

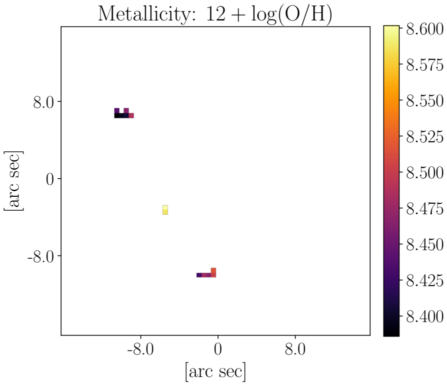

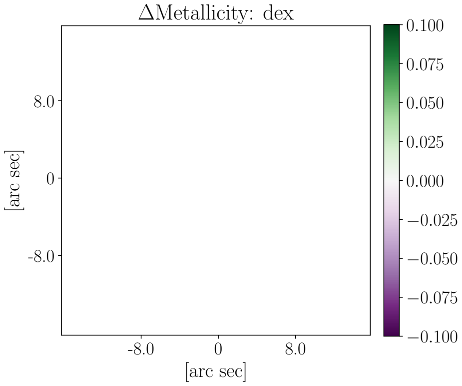

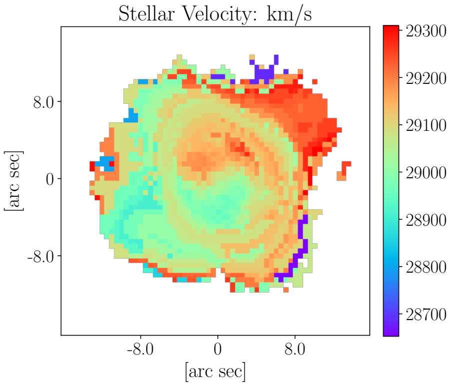

Galaxy objID: 587738948271538407

plate-ifu: 8939-9101

RA: 125.228°

Decl: 23.7292°

z: 0.0969256

K03: NULL

$\log \mathrm{M}_*$: 11.0981 $\log \mathrm{M}_\odot$

$\log \mathrm{SFR}$: -0.264041 log(M$_\odot$/yr)

O/H(KE08): nan

Δ SFR: nan

manga-id: 1-556714

Match separation: 44.0774"

Companion Flag: 0

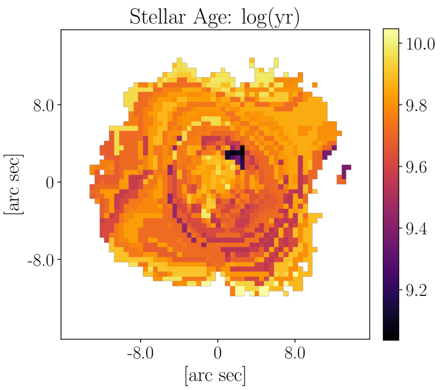

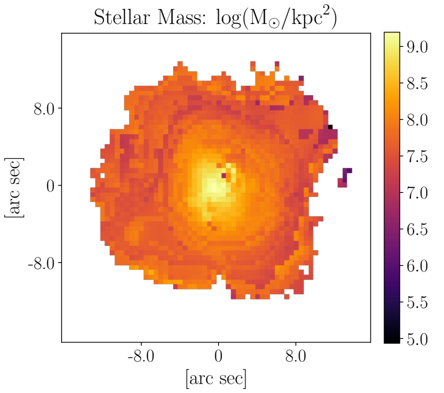

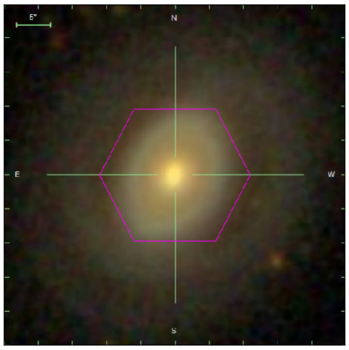

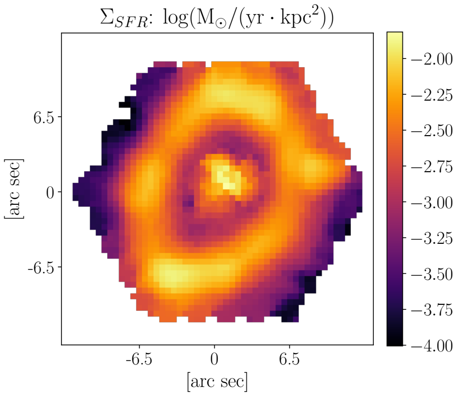
Σ_{SFR}: $\log(\mathrm{M}_{\odot}/(\mathrm{yr} \cdot \mathrm{kpc}^2))$

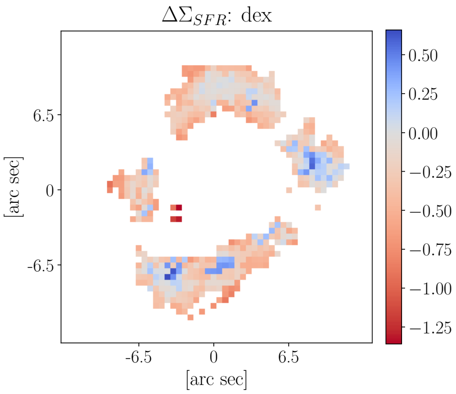
$\Delta\Sigma_{SFR}$: dex

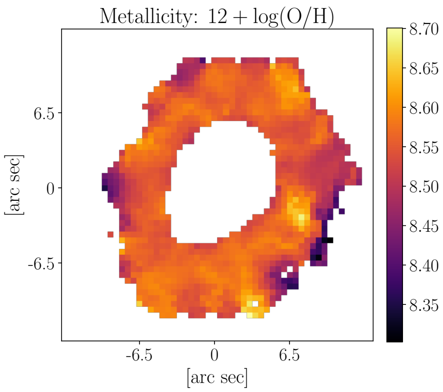
Metallicity: $12 + \log(\mathrm{O/H})$

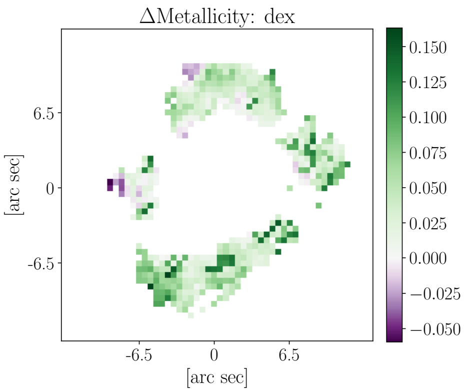
ΔMetallicity: dex

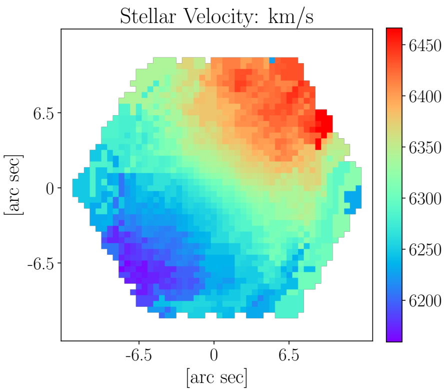
Stellar Velocity: km/s

Galaxy objID: 587742012741845202

plate-ifu: 8450-6101

RA: 172.143°

Decl: 21.0107°

z: 0.0210181

K03: NULL

$\log \mathrm{M}_*$: 10.4407 $\log \mathrm{M}_{\odot}$

log SFR : -0.529102 $\log(\mathrm{M}_{\odot}/\mathrm{yr})$

O/H(KE08): nan

Δ SFR: nan

manga-id: 1-491047

Match separation: 246.729”

Companion Flag: 0

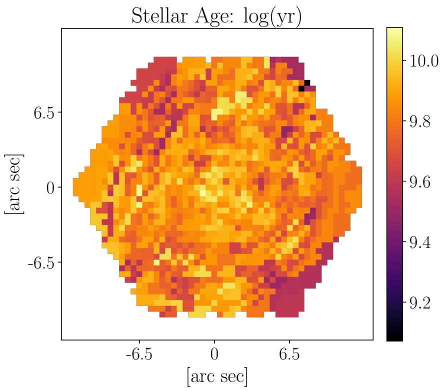
Stellar Age: log(yr)

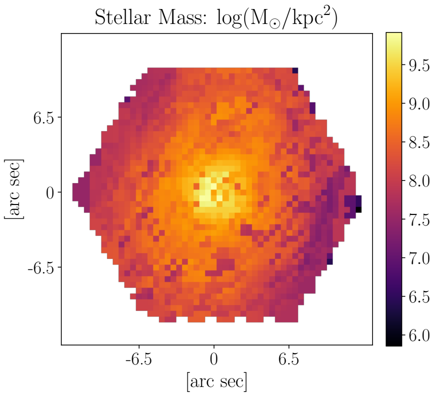
Stellar Mass: $\log(\mathrm{M}_{\odot}/\mathrm{kpc}^2)$

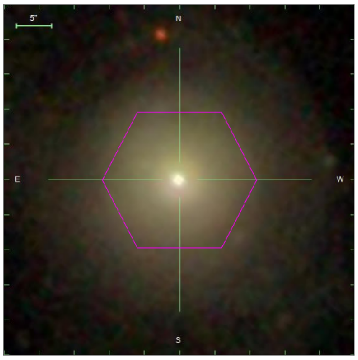

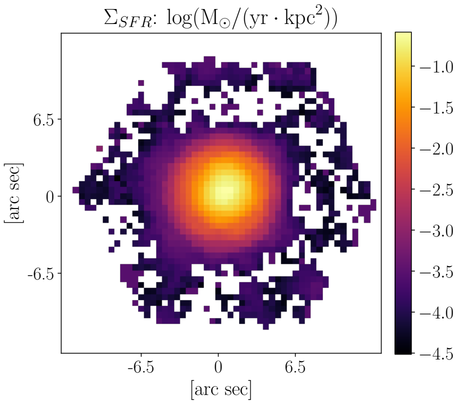
Σ_{SFR}: log(M$_\odot$/(yr · kpc^2))

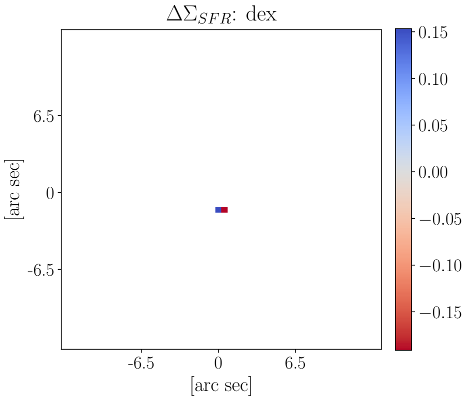
$\Delta\Sigma_{SFR}$: dex

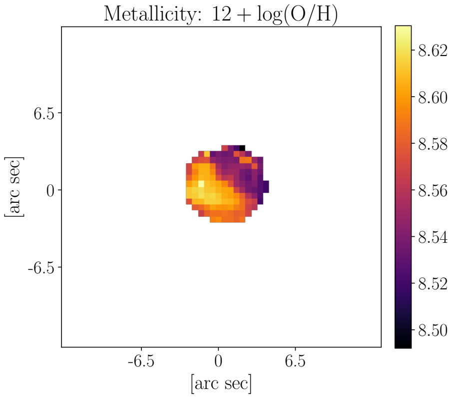
Metallicity: 12 + log(O/H)

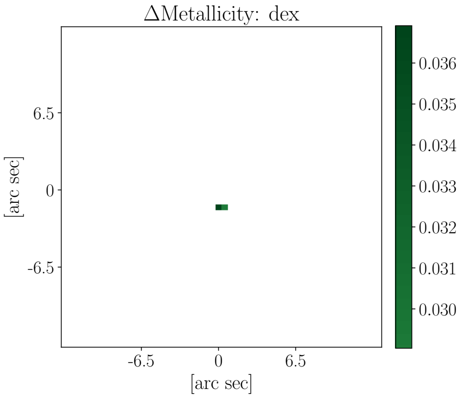
ΔMetallicity: dex

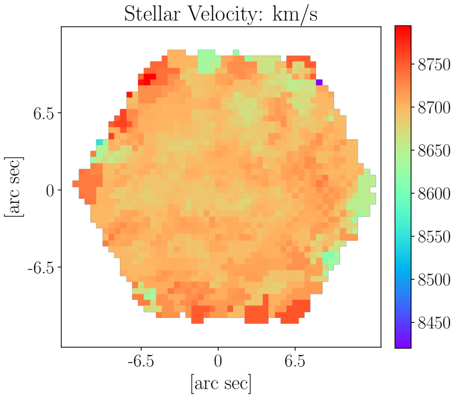
Stellar Velocity: km/s

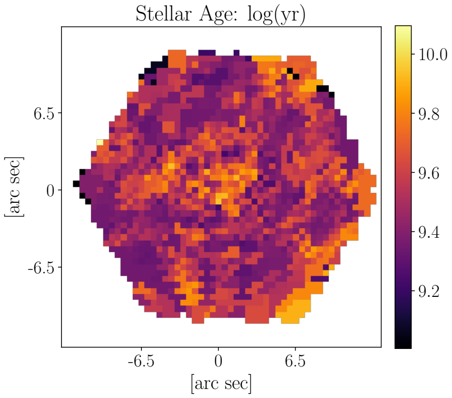
Stellar Age: log(yr)

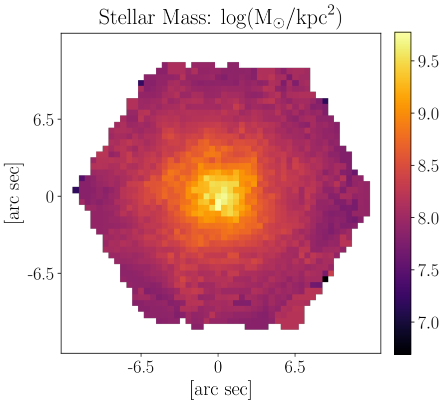
Stellar Mass: log(M$_\odot$/kpc^2)

Galaxy objID: 588013383265616039
plate-ifu: 8440-6104
RA: 135.759°
Decl: 40.434°
z: 0.0289817
K03: NULL
$\log \mathrm{M}_*$: 10.5681 $\log \mathrm{M}_\odot$
$\log \mathrm{SFR}$: -0.085546 log(M$_\odot$/yr)
O/H(KE08): nan
Δ SFR: nan
manga-id: 1-216976
Match separation: 102.922”
Companion Flag: 0

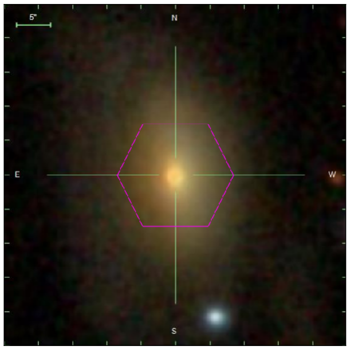

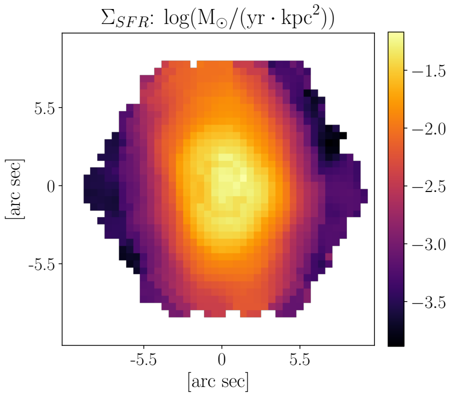
Σ_{SFR}: log(M$_\odot$/(yr · kpc^2))

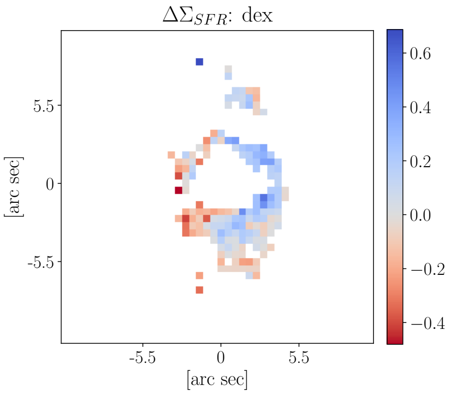
$\Delta\Sigma_{SFR}$: dex

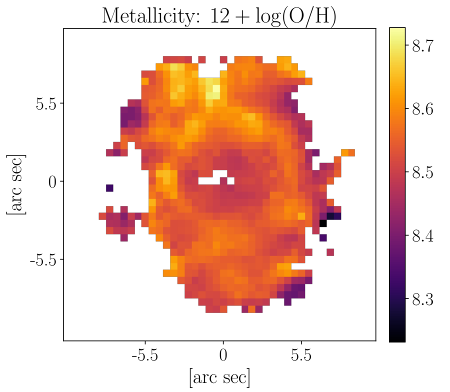
Metallicity: 12 + log(O/H)

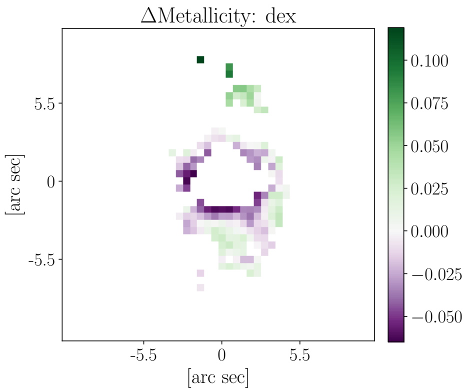
ΔMetallicity: dex

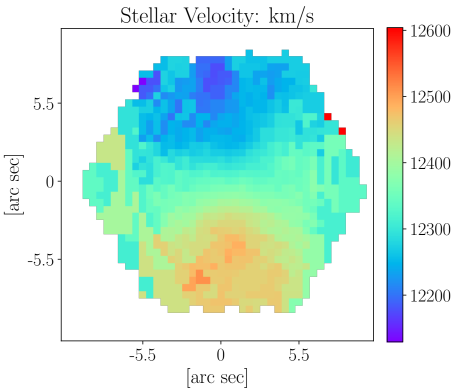
Stellar Velocity: km/s

Galaxy objID: 588017605757501605

plate-ifu: 8261-3701

RA: 183.127°

Decl: 45.6855°

z: 0.0411717

K03: NULL

log M$_*$: 10.7906 log M$_\odot$

log SFR : 0.364432 log(M$_\odot$/yr)

O/H(KE08): nan

Δ SFR: -0.0611125

manga-id: 1-575838

Match separation: 124.02"

Companion Flag: 0

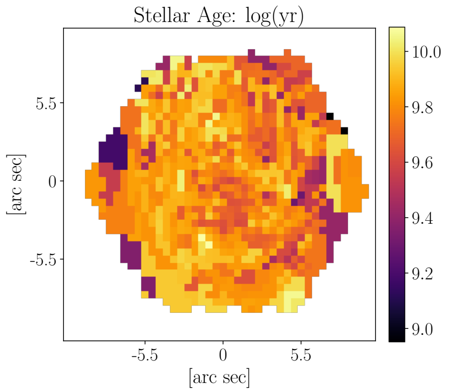
Stellar Age: log(yr)

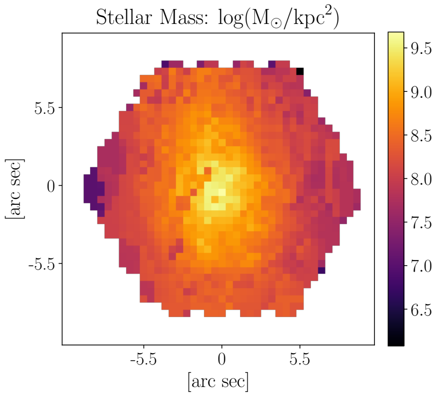
Stellar Mass: log(M$_\odot$/kpc^2)

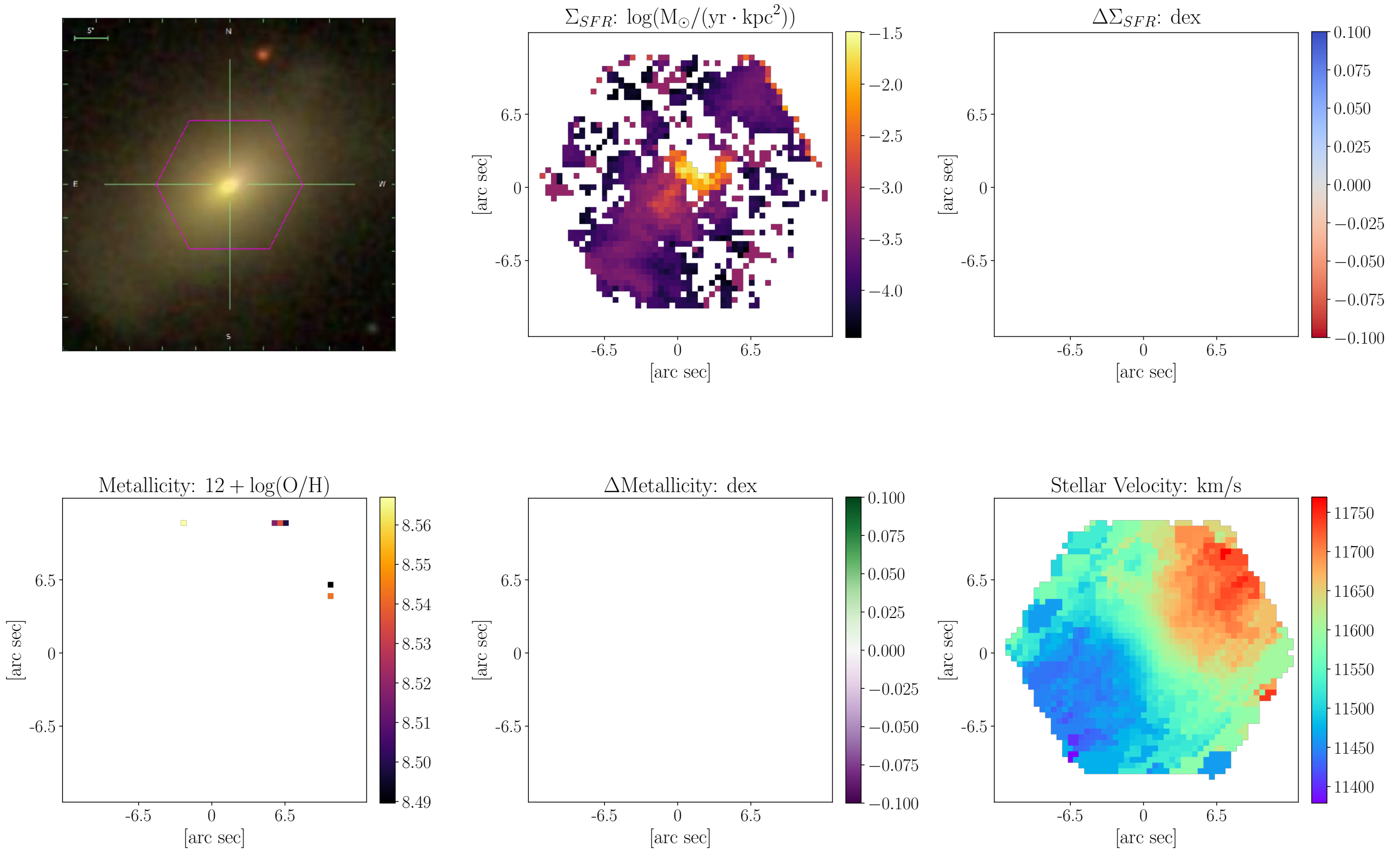

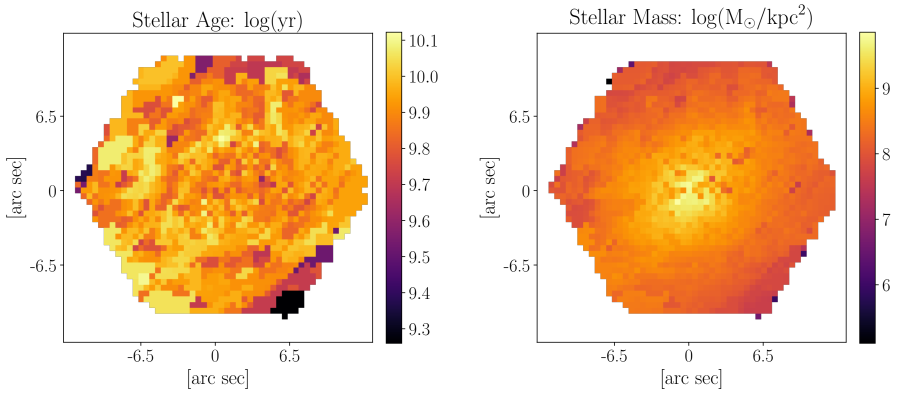

Galaxy objID: 588017626155253939

plate-ifu: 8262-6104

RA: 184.685°

Decl: 44.7812°

z: 0.0384971

K03: NULL

$\log \mathrm{M}_*$: 10.9852 $\log \mathrm{M}_\odot$

$\log \mathrm{SFR}$: -0.916429 $\log(\mathrm{M}_\odot/\mathrm{yr})$

O/H(KE08): nan

Δ SFR: nan

manga-id: 1-258653

Match separation: 160.7”

Companion Flag: 0

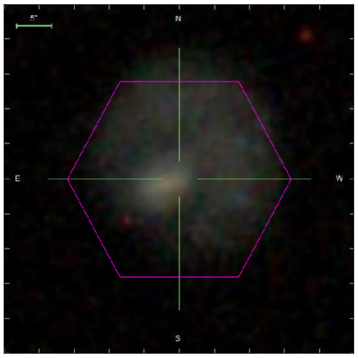

Σ_{SFR}: log(M$_\odot$/(yr $\cdot$ kpc^2))

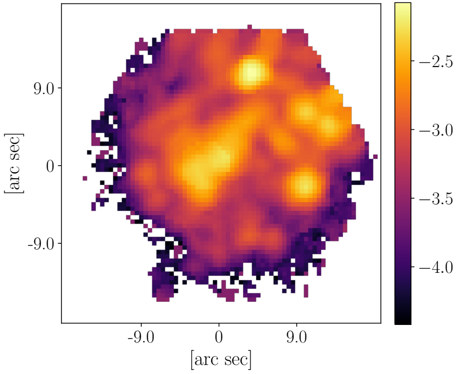

$\Delta\Sigma_{SFR}$: dex

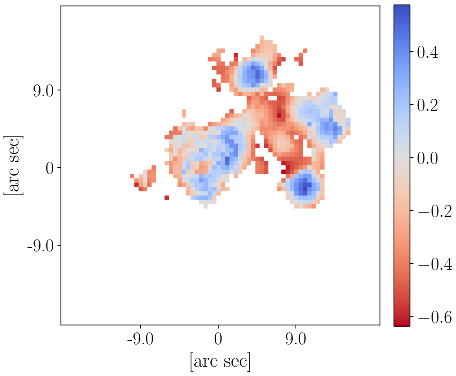

Metallicity: $12 + \log(\mathrm{O/H})$

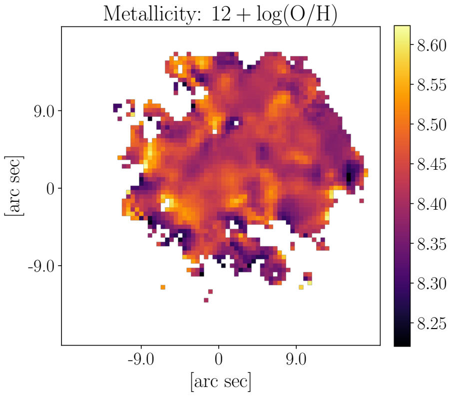

ΔMetallicity: dex

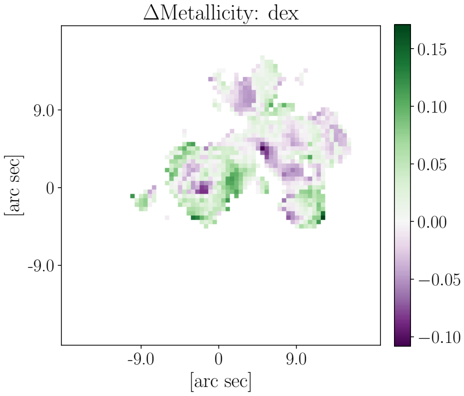

Stellar Velocity: km/s

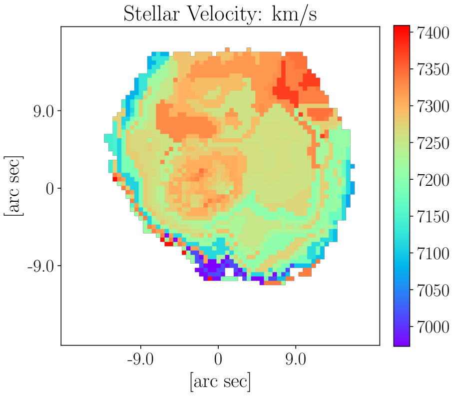

Stellar Age: log(yr)

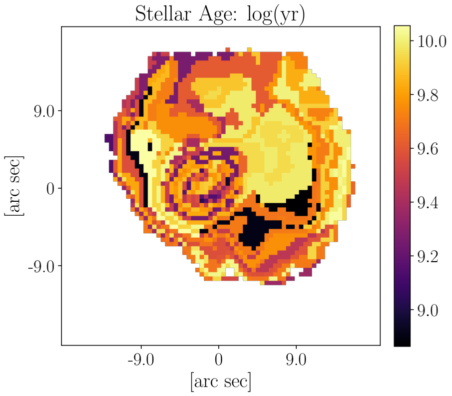

Stellar Mass: log(M$_\odot$/kpc^2)

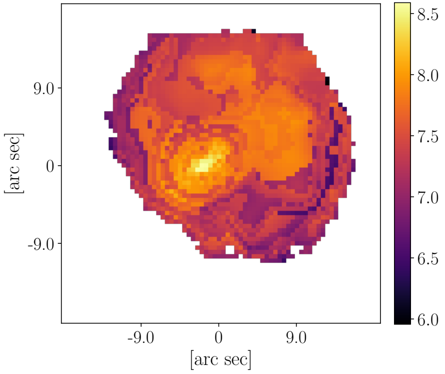

Galaxy objID: 588017979437678762
plate-ifu: 8447-12705
RA: 207.844°
Decl: 38.3103°
z: 0.0242737
K03: SF
$\log \mathrm{M}_*$: 9.64707 $\log \mathrm{M}_\odot$
$\log \mathrm{SFR}$: -0.724774 $\log(\mathrm{M}_\odot/\mathrm{yr})$
O/H(KE08): nan
Δ SFR: -1.00955
manga-id: 1-405261
Match separation: 10.2593"
Companion Flag: 0

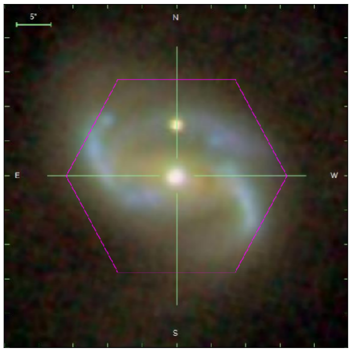

Σ_{SFR}: log(M$_\odot$/(yr · kpc^2))

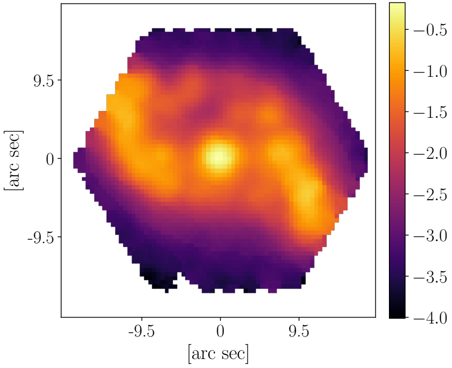

$\Delta\Sigma_{SFR}$: dex

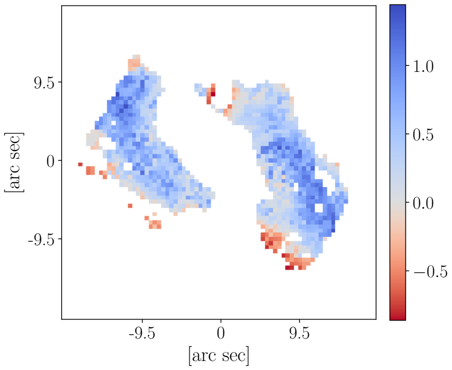

Metallicity: 12 + log(O/H)

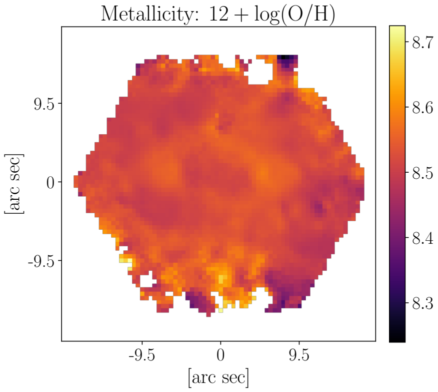

ΔMetallicity: dex

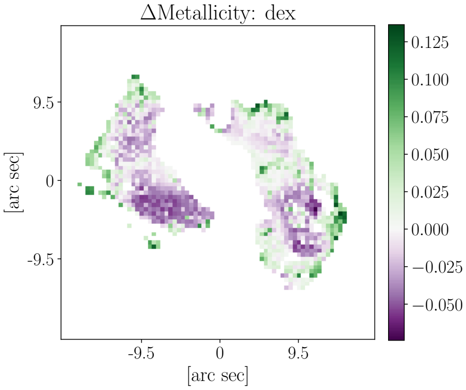

Stellar Velocity: km/s

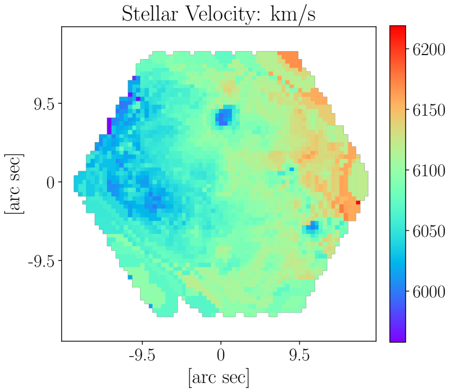

Galaxy objID: 588297863652966513

plate-ifu: 8257-12701

RA: 165.496°

Decl: 45.228°

z: 0.0202728

K03: NULL

$\log \mathrm{M}_*$: 10.6122 $\log \mathrm{M}_\odot$

$\log \mathrm{SFR}$: 0.79793 log(M$_\odot$/yr)

O/H(KE08): nan

Δ SFR: nan

manga-id: 1-277290

Match separation: 173.899"

Companion Flag: 1

Stellar Age: log(yr)

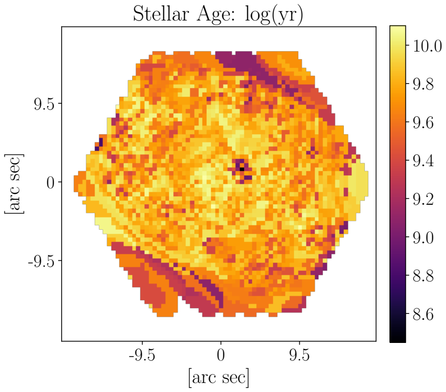

Stellar Mass: log(M$_\odot$/kpc^2)

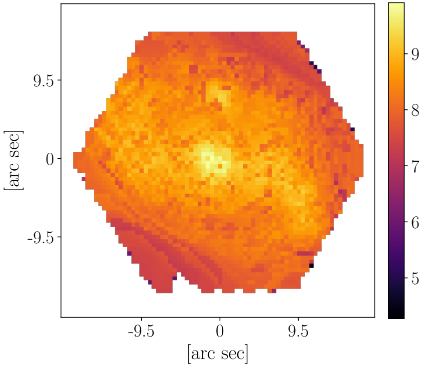

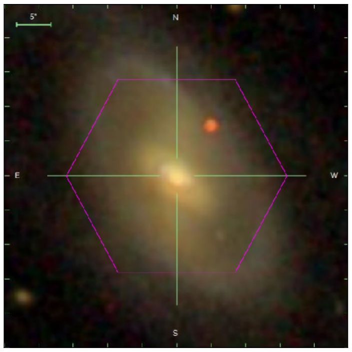

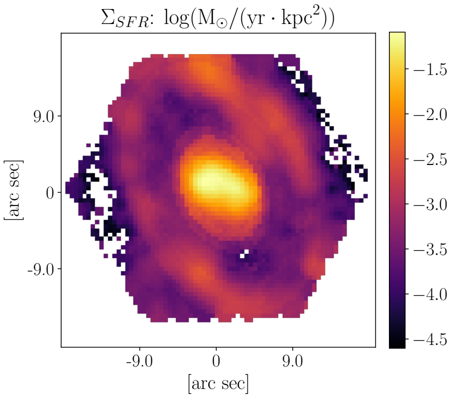

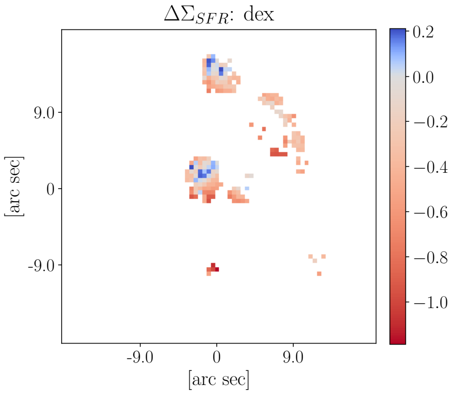

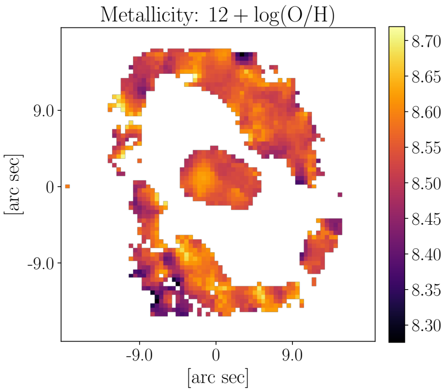

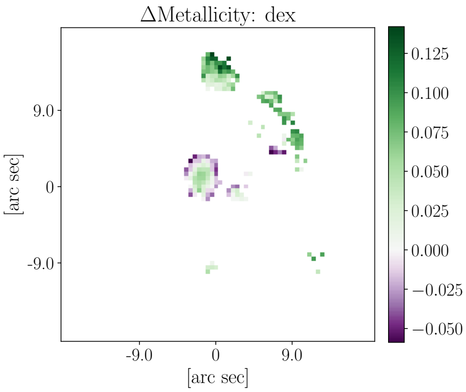

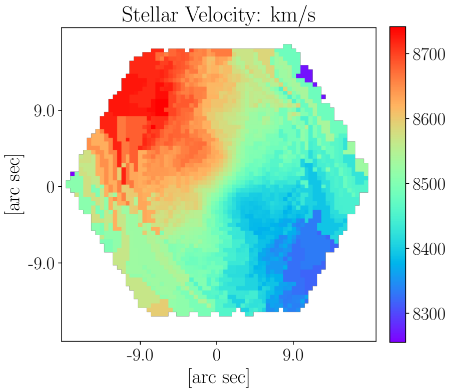

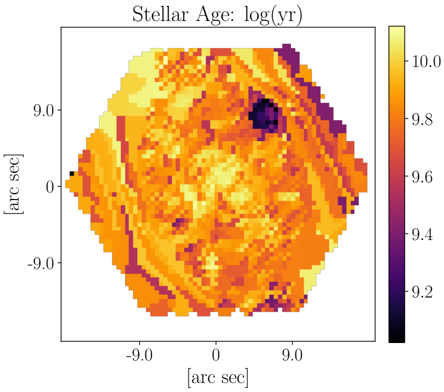

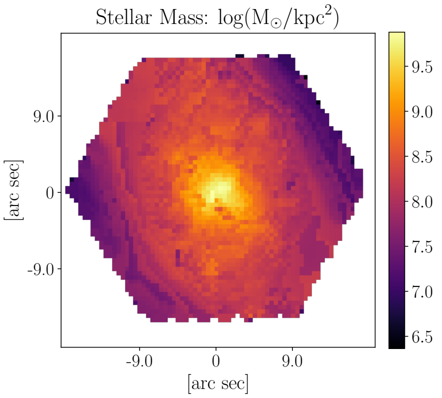

Galaxy objID: 588298664114520231
plate-ifu: 8465-12705
RA: 198.236°
Decl: 47.4566°
z: 0.0284565
K03: NULL
$\log \mathrm{M}_*$: 10.7953 $\log \mathrm{M}_\odot$
$\log \mathrm{SFR}$: -0.00887437 $\log(\mathrm{M}_\odot/\mathrm{yr})$
O/H(KE08): nan
Δ SFR: nan
manga-id: 1-285004
Match separation: 282.245”
Companion Flag: 0

Bibliography

Abolfathi B., et al., 2018, The Astrophysical Journal Supplement Series, 235, 42

Abraham R. G., van den Bergh S., Glazebrook K., Ellis R. S., Santiago B. X., Surma P., Griffiths R. E., 1996, The Astrophysical Journal Supplement Series, 107, 1

Abraham R., Bergh S. v. d., Nair P., 2003, The Astrophysical Journal, 588, 218

Aguado D. S., et al., 2019, The Astrophysical Journal Supplement Series, 240, 23

Allen J. T., et al., 2015, Monthly Notices of the Royal Astronomical Society, 446, 1567

Alonso-Herrero A., Rosales-Ortega F. F., Sánchez S. F., Kennicutt R. C., Pereira-Santaella M., Díaz . I., 2012, Monthly Notices of the Royal Astronomical Society: Letters, 425, L46

Alonso M. S., Tissera P. B., Coldwell G., Lambas D. G., 2004, Monthly Notices of the Royal Astronomical Society, 352, 1081

Alonso S., Mesa V., Padilla N., Lambas D. G., 2012, Astronomy & Astrophysics, 539, A46

Arp H., 1966, Astrophysical Journal Supplement, 14, 1

Banerji M., et al., 2010, Monthly Notices of the Royal Astronomical Society, 406, 342

Barnes J. E., 1988, Astrophysical Journal, 331, 699

Barnes J. E., Hernquist L. E., 1991, The Astrophysical Journal, 370, L65

Barnes J. E., Hernquist L., 1996, Astrophysical Journal, 471, 115

Barrera-Ballesteros J. K., et al., 2015, Astronomy & Astrophysics, 579, A45

Barrera-Ballesteros J. K., et al., 2016, Monthly Notices of the Royal Astronomical Society, 463, 2513

Barton Gillespie E. J., Geller M. J., Kenyon S. J., 2000, The Astrophysical Journal, 530, 660

Barton Gillespie E. B., Geller M. J., Kenyon S. J., 2003, The Astrophysical Journal, 582, 668

Barton E. J., Geller M. J., Kenyon S. J., 2000, The Astrophysical Journal, 530, 660

Baugh C. M., Cole S., Frenk C. S., 1996, Monthly Notices of the Royal Astronomical Society, 283, 1361

Bell E. F., 2008, The Astrophysical Journal, 682, 355

Bell E. F., et al., 2004, The Astrophysical Journal, 608, 752

Bershady M. A., Jangren A., Conselice C. J., 2000, The Astronomical Journal, 119, 2645

Bershady M. A., Verheijen M. A. W., Swaters R. A., Andersen D. R., Westfall K. B., Martinsson T., 2010, The Astrophysical Journal, 716, 198

Bertin E., Arnouts S., 1996, Astronomy & Astrophysics Supplement, 117, 393

Bertola F., Capaccioli M., 1975, The Astrophysical Journal, 200, 439

Blanc G. A., et al., 2013, The Astronomical Journal, 145, 138

Blanton M. R., Kazin E., Muna D., Weaver B. A., Price-Whelan A., 2011, The Astronomical Journal, 142, 31

Bolatto A. D., Wolfire M., Leroy A. K., 2013, Annual Review of Astronomy and Astrophysics, 51, 207

Bolatto A. D., et al., 2017, The Astrophysical Journal, 846, 159

Bolton A. S., et al., 2012, The Astronomical Journal, 144, 144

Bournaud F., Jog C. J., Combes F., 2005, Astronomy & Astrophysics, 437, 69

Bournaud F., et al., 2011, The Astrophysical Journal, 730, 4

Bower R. G., Lucey J. R., Ellis R. S., 1992, Monthly Notices of the Royal Astronomical Society, 254, 601

Boylan-Kolchin M., Ma C.-P., Quataert E., 2008, Monthly Notices of the Royal Astronomical Society, 383, 93

Braine J., Combes F., 1992, Astronomy & Astrophysics, 269, 7

Brinchmann J., Ellis R. S., 2000, The Astrophysical Journal, 536, L77

Brinchmann J., Charlot S., White S. D. M., Tremonti C., Kauffmann G., Heckman T., Brinkmann J., 2004, Monthly Notices of the Royal Astronomical Society, 351, 1151

Brodie J. P., et al., 2014, The Astrophysical Journal, 796, 52

Brooks A. M., Governato F., Booth C. M., Willman B., Gardner J. P., Wadsley J., Stinson G., Quinn T., 2007, The Astrophysical Journal, 655, L17

Bundy K., et al., 2015, The Astrophysical Journal, 798, 7

Calura F., Pipino A., Chiappini C., Matteucci F., Maiolino R., 2009, Astronomy & Astrophysics, 504, 373

Cano-Díaz M., et al., 2016, The Astrophysical Journal, 821, L26

Capelo P. R., Volonteri M., Dotti M., Bellovary J. M., Mayer L., Governato F., 2015, Monthly Notices of the Royal Astronomical Society, 447, 2123

Cappellari M., et al., 2011, Monthly Notices of the Royal Astronomical Society, 413, 813

Cardelli J. A., Clayton G. C., Mathis J. S., 1989, The Astrophysical Journal, 345, 245

Carroll B. W., Ostlie D. A., 2007, An Introduction to Modern Astrophysics, 2 edn. Pearson: Addison Wesley, San Francisco

Casasola V., Bettoni D., Galletta G., 2004, Astronomy & Astrophysics, 422, 941

Casteels K. R. V., et al., 2014, Monthly Notices of the Royal Astronomical Society, 445, 1157

Cattaneo A., Blaizot J., Devriendt J., Guiderdoni B., 2005, Mon. Not. R. Astron. Soc, 364, 407

Chabrier G., 2003, Publications of the Astronomical Society of the Pacific, 115, 763

Chandrasekhar S., 1943, Astrophysical Journal, 97, 225

Chiosi C., Carraro G., 2002, Monthly Notices of the Royal Astronomical Society, 335, 335

Chown R., et al., 2019, Monthly Notices of the Royal Astronomical Society, 484, 5192

Conselice C. J., 2006, The Astrophysical Journal, 638, 686

Conselice C. J., Bershady M. A., Jangren A., 2000, The Astrophysical Journal, 529, 886

Conselice C. J., Bershady M. A., Dickinson M., Papovich C., 2003, The Astronomical Journal, 126, 1183

Cooper M. C., Tremonti C. A., Newman J. A., Zabludoff A. I., 2008, Monthly Notices of the Royal Astronomical Society, 390, 245

Cortijo-Ferrero C., et al., 2017, Monthly Notices of the Royal Astronomical Society, 467, 3898

Cox T. J., Jonsson P., Primack J. R., Somerville R. S., 2006, Monthly Notices of the Royal Astronomical Society, 373, 1013

Cox T. J., Jonsson P., Somerville R. S., Primack J. R., Dekel A., 2008, Monthly Notices of the Royal Astronomical Society, 384, 386

Croom S. M., et al., 2012, Monthly Notices of the Royal Astronomical Society, pp no–no

D'Onghia E., Vogelsberger M., Faucher-Giguere C.-A., Hernquist L., 2010, The Astrophysical Journal, 725, 353

Daddi E., et al., 2007, The Astrophysical Journal, 670, 156

Darg D. W., et al., 2010, Monthly Notices of the Royal Astronomical Society, 401, 1043

Davies L. J. M., et al., 2015, Monthly Notices of the Royal Astronomical Society, 452, 616

De La Calleja J., Fuentes O., 2004, Monthly Notices of the Royal Astronomical Society, 349, 87

De Propris R., Melnick J., 2014, Monthly Notices of the Royal Astronomical Society, 439, 2837

De Propris R., Conselice C. J., Liske J., Driver S. P., Patton D. R., Graham A. W., Allen P. D., 2007, The Astrophysical Journal, 666, 212

Di Matteo T., Springel V., Hernquist L., 2005, Nature, 433, 604

Di Matteo P., Combes F., Melchior A. L., Semelin B., 2007, Astronomy & Astrophysics, 468, 61

Domínguez Sánchez H., et al., 2019, Monthly Notices of the Royal Astronomical Society, 484, 93

Donzelli C. J., Pastoriza M. G., 1997, The Astrophysical Journal Supplement Series, 111, 181

Dressler A., 1980, The Astrophysical Journal, 236, 351

Drory N., et al., 2015, The Astronomical Journal, 149, 159

Elbaz D., et al., 2007, Astronomy & Astrophysics, 468, 33

Ellison S. L., Patton D. R., Simard L., McConnachie A. W., 2008a, The Astronomical Journal, 135, 1877

Ellison S. L., Patton D. R., Simard L., McConnachie A. W., 2008b, The Astrophysical Journal, 672, L107

Ellison S. L., Patton D. R., Simard L., McConnachie A. W., Baldry I. K., Mendel J. T., 2010, Monthly Notices of the Royal Astronomical Society, 407, 1514

Ellison S. L., Patton D. R., Mendel J. T., Scudder J. M., 2011, Monthly Notices of the Royal Astronomical Society, 418, 2043

Ellison S. L., Mendel J. T., Patton D. R., Scudder J. M., 2013, Monthly Notices of the Royal Astronomical Society, 435, 3627

Ellison S. L., Sánchez S. F., Ibarra-Medel H., Antonio B., Mendel J. T., Barrera-Ballesteros J., 2018a, Monthly Notices of the Royal Astronomical Society, 474, 2039

Ellison S. L., Catinella B., Cortese L., 2018b, Monthly Notices of the Royal Astronomical Society, 478, 3447

Ellison S. L., Viswanathan A., Patton D. R., Bottrell C., McConnachie A. W., Gwyn S., Cuillandre J.-C., 2019, Monthly Notices of the Royal Astronomical Society, 487, 2491

Elmegreen D. M., Elmegreen B. G., Kaufman M., Sheth K., Struck C., Thomasson M., Brinks E., 2006, The Astrophysical Journal, 642, 158

Evans I. N., 1986, The Astrophysical Journal, 309, 544

Fensch J., et al., 2017, Monthly Notices of the Royal Astronomical Society, 465, 1934

Fu H., et al., 2018, Astrophysical Journal, 856, 93

García-Marín M., Colina L., Arribas S., Monreal-Ibero A., 2009, A&A, 505, 1319

Garnett D. R., 2002, The Astrophysical Journal, 581, 1019

Garnett D. R., Shields G. A., 1987, The Astrophysical Journal, 317, 82

Gil de Paz A., Madore B. F., 2002, The Astronomical Journal, 123, 1864

González Delgado R. M., et al., 2016, A&A, 590

Gunn J. E., et al., 2006, The Astronomical Journal, 131, 2332

Hambleton K. M., Gibson B. K., Brook C. B., Stinson G. S., Conselice C. J., Bailin J., Couchman H., Wadsley J., 2011, Monthly Notices of the Royal Astronomical Society, 418, 801

Hernquist L., 1989, Nature, 340, 687

Hopkins P. F., Quataert E., 2011, Monthly Notices of the Royal Astronomical Society, 415, 1027

Hopkins P. F., et al., 2009, Monthly Notices of the Royal Astronomical Society, 397, 802

Hsieh B. C., et al., 2017, The Astrophysical Journal, 851, L24

Hubble E., 1926, Astrophysical Journal, 64, 321

Huchtmeier W. K., Petrosian A., Krishna G., McLean B., Kunth D., 2008, Astronomy & Astrophysics, 492, 367

Huertas-Company M., et al., 2015, The Astrophysical Journal Supplement Series, 221, 8

Hwang H.-C., et al., 2018, The Astrophysical Journal, 872, 144

Illingworth G., 1977, The Astrophysical Journal, 218, 43

Iono D., Yun M. S., Mihos J. C., 2004, The Astrophysical Journal, 616, 199

Jian H.-Y., Lin L., Chiueh T., 2012, The Astrophysical Journal, 754, 26

Jogee S., et al., 2009, The Astrophysical Journal, 697, 1971

Kauffmann G., et al., 2003, Monthly Notices of the Royal Astronomical Society, 346, 1055

Kennicutt R. C., 1983, The Astrophysical Journal, 272, 54

Kennicutt R. C., 1998, Annual Review of Astronomy and Astrophysics, 36, 189

Kennicutt R. C., Tamblyn P., Congdon C. W., 1994, Astrophysical Journal, 435, 22

Kewley L. J., Dopita M. A., 2002, The Astrophysical Journal Supplement Series, 142, 35

Kewley L. J., Ellison S. L., 2008, Astrophysical Journal, 681, 1183

Kewley L. J., Dopita M. A., Sutherland R. S., Heisler C. A., Trevena J 2001, The Astronomical Journal, 556, 121

Kewley L. J., Groves B., Kauffmann G., Heckman T., 2006, Monthly Notices of the Royal Astronomical Society, 372, 961

Kewley L. J., Rupke D., Jabran Zahid H., Geller M. J., Barton E. J., 2010, The Astrophysical Journal, 721, L48

Kitzbichler M. G., White S. D. M., 2008, Monthly Notices of the Royal Astronomical Society, 391, 1489

Kobulnicky H. A., Kewley L. J., 2004, The Astrophysical Journal, 617, 240

Kroupa P., 2002, SCIENCE, 295, 82

Kuntschner H., et al., 2010, Monthly Notices of the Royal Astronomical Society, 408, 97

Lambas D. G., Tissera P. B., Alonso M. S., Coldwell G., 2003, Monthly Notices of the Royal Astronomical Society, 346, 1189

Lambas D. G., Alonso S., Mesa V., OMill A. L., 2012, Astronomy & Astrophysics, 539, A45

Lara-López M. A., Bongiovanni A., Cepa J., Pérez García A. M., Sánchez-Portal M., Castañeda H. O., Fernández Lorenzo M., Pović M., 2010, Astronomy and Astrophysics, 519, A31

Larson R. B., 1974, Monthly Notices of the Royal Astronomical Society, 169, 229

Larson R. B., Tinsley B. M., 1978, The Astrophysical Journal, 219, 46

Law D. R., et al., 2015, The Astronomical Journal, 150, 19

Law D. R., et al., 2016, The Astronomical Journal, 152, 83

Leitherer C., Ferguson H. C., Heckman T. M., Lowenthal J. D., 1995, Astrophysical Journal, 454, L19

Lequeux J., Peimbert M., Rayo J. F., Serrano A., Torres-Peimbert S., 1979, Astronomy and Astrophysics, 80, 155

Lin L., et al., 2004, The Astrophysical Journal, 617, L9

Lotz J. M., Primack J., Madau P., 2004, The Astronomical Journal, 128, 163

Lotz J. M., Jonsson P., Cox T., Primack J. R., 2008, Monthly Notices of the Royal Astronomical Society, 391, 1137

Lotz J. M., Jonsson P., Cox T. J., Primack J. R., 2010a, Monthly Notices of the Royal Astronomical Society, 404, 575

Lotz J. M., Jonsson P., Cox T. J., Primack J. R., 2010b, Monthly Notices of the Royal Astronomical Society, 404, 590

Ma C.-P., Greene J. E., McConnell N., Janish R., Blakeslee J. P., Thomas J., Murphy J. D., 2014, The Astrophysical Journal, 795, 158

Madau P., Dickinson M., 2014, Annual Review of Astronomy and Astrophysics, 52, 415

Malin D. F., Carter D., 1983, The Astrophysical Journal, 274, 534

Mannucci F., Cresci G., Maiolino R., Marconi A., Gnerucci A., 2010, Monthly Notices of the Royal Astronomical Society, 408, 2115

Marino R. A., et al., 2013a, Astronomy & Astrophysics, 559, A114

Marino A. F., Milone A. P., Lind K., 2013b, The Astrophysical Journal, 768, 27

Massey P., 1998, in Gilmore G., Howell D., eds, The Stellar Initial Mass Function (38th Herstmonceux Conference). p. 17, `http://articles.adsabs.harvard.edu/pdf/1998ASPC..142...17M`

Mcgaugh S. S., 1991, The Astrophysical Journal, 380, 140

Mendel J. T., Simard L., Ellison S. L., Patton D. R., 2013, Monthly Notices of the Royal Astronomical Society, 429, 2212

Michel-Dansac L., Lambas D. G., Alonso M. S., Tissera P., 2008, Mon. Not. R. Astron. Soc, 386, 82

Mihos J. C., Dubinski J., 1998, The Astrophysical Journal, 494, 183

Mihos J. C., Hernquist L., 1996, The Astrophysical Journal, 464, 641

Montuori M., Di Matteo P., Lehnert M. D., Combes F., Semelin B., 2010, Astronomy and Astrophysics, 518, A56

Moreno J., Torrey P., Ellison S. L., Patton D. R., Bluck A. F., Bansal G., Hernquist L., 2015, Monthly Notices of the Royal Astronomical Society, 448, 1107

Moreno J., et al., 2019, Monthly Notices of the Royal Astronomical Society, 485, 1320

Mouhcine M., Gibson B. K., Renda A., Kawata D., 2008, Astronomy & Astrophysics, 486, 711

Muzzin A., et al., 2013, The Astrophysical Journal, 777, 18

Nikolic B., Cullen H., Alexander P., 2004, Monthly Notices of the Royal Astronomical Society, 355, 874

Noeske K. G., et al., 2007a, The Astrophysical Journal, 660, L43

Noeske K. G., et al., 2007b, The Astrophysical Journal, 660, L47

Oemler A. J., 1974, The Astrophysical Journal, 194, 1

Osterbrock D. E., Ferland G. J., 2006, Astrophysics of Gaseous Nebulae and Active Galactic Nuclei, 2 edn. University Science Books

Pagel B. E. J., Edmunds M. G., 1981, Annual Review of Astronomy and Astrophysics, 19, 77

Pan H.-A., et al., 2018, The Astrophysical Journal, 868, 132

Pannella M., et al., 2009, The Astrophysical Journal, 698, L116

Patton D. R., Ellison S. L., Simard L., McConnachie A. W., Mendel J. T., 2011, Monthly Notices of the Royal Astronomical Society, 412, 591

Patton D. R., Torrey P., Ellison S. L., Mendel J. T., Scudder J. M., 2013, Monthly Notices of the Royal Astronomical Society: Letters, 433, 59

Patton D. R., Qamar F. D., Ellison S. L., Bluck A. F. L., Simard L., Mendel J. T., Moreno J., Torrey P., 2016, Monthly Notices of the Royal Astronomical Society, 461, 2589

Pawlik M. M., Wild V., Walcher C. J., Johansson P. H., Villforth C., Rowlands K., Mendez-Abreu J., Hewlett T., 2016, Monthly Notices of the Royal Astronomical Society, 456, 3032

Pearson W. J., Wang L., Trayford J. W., Petrillo C. E., Van Der Tak F. F. S., 2019, A&A, 626, 18

Pérez-Montero E., Contini T., 2009, Monthly Notices of the Royal Astronomical Society, 398, 949

Perez J., Michel-Dansac L., Tissera P., 2011, Monthly Notices of the Royal Astronomical Society, 417, 580

Perret V., Renaud F., Epinat B., Amram P., Bournaud F., Contini T., Teyssier R., Lambert J.-C., 2014, Astronomy & Astrophysics, 562, A1

Pettini M., Pagel B. E. J., 2004, Monthly Notices of the Royal Astronomical Society, 348, L59

Pilyugin L. S., Grebel E. K., Mattsson L., 2012, Monthly Notices of the Royal Astronomical Society, 424, 2316

Powell L. C., Bournaud F., Chapon D., Teyssier R., 2013, Monthly Notices of the Royal Astronomical Society, 434, 1028

Renaud F., Bournaud F., Kraljic K., Duc P.-A., 2014, Monthly Notices of the Royal Astronomical Society: Letters, 442, 33

Robaina A. R., et al., 2009, The Astrophysical Journal, 704, 324

Rodriguez-Gomez V., et al., 2015, Monthly Notices of the Royal Astronomical Society, 449, 49

Rodriguez-Gomez V., et al., 2017, Monthly Notices of the Royal Astronomical Society, 467, 3083

Rosales-Ortega F. F., Sánchez S. F., Iglesias-P Aramo J., Díaz A. I., Vílchez J. M., Bland-Hawthorn J., Husemann B., Mast D., 2012, The Astrophysical Journal Letters, 756, L31

Rupke D. S. N., Kewley L. J., Barnes J. E., 2010, The Astrophysical Journal, 710, L156

Salpeter E. E., 1955, Astrophysical Journal, 121, 161

Sánchez Almeida J., Sánchez-Menguiano L., 2019, preprint

Sánchez S. F., García-Lorenzo B., Jahnke K., Mediavilla E., González-Serrano J. I., Christensen L., Wisotzki L., 2006, New Astronomy Reviews, 49, 501

Sánchez S. F., et al., 2012a, A&A, 538, 8

Sánchez S. F., et al., 2012b, Astronomy & Astrophysics, 538, A8

Sánchez S. F., et al., 2013, Astronomy and Astrophysics, 554, A58

Sánchez S. F., et al., 2014, Astronomy and Astrophysics, 563, A49

Sánchez S. F., et al., 2016a, Revista Mexicana de Astronomia y Astrofisica, 52, 21

Sánchez S. F., et al., 2016b, Revista Mexicana de Astronomia y Astrofisica, 52, 171

Sanders R. L., Shapley A. E., Zhang K., Yan R., 2017, The Astrophysical Journal, 850, 136

Sauvage M., Thuan T. X., 1992, The Astrophysical Journal, 396, L69

Scalo J. M., 1986, Fundamentals of Cosmic Physics, 11, 1

Schade D., Lilly S. J., Crampton D., Hammer F., Le Fèvre O., Tresse L., 1995, The Astrophysical Journal, 451, L1

Schaller G., Schaerer D., Meynet G., Maeder A., 1993, A&As, pp 96,269

Schawinski K., et al., 2013, Monthly Notices of the Royal Astronomical Society, 000, 1

Schreiber C., et al., 2015, Astronomy & Astrophysics, 575, A74

Schweizer F., 1980, The Astrophysical Journal, 237, 303

Schweizer F., 1982, The Astrophysical Journal, 252, 455

Scudder J. M., Ellison S. L., Torrey P., Patton D. R., Mendel J. T., 2012, Monthly Notices of the Royal Astronomical Society, 426, 549

Scudder J. M., Ellison S. L., Momjian E., Rosenberg J. L., Torrey P., Patton D. R., Fertig D., Mendel J. T., 2015, Monthly Notices of the Royal Astronomical Society, 449, 3719

Sérsic J. L., 1963, Boletin de la Asociacion Argentina de Astronomia La Plata Argentina, 6, 4

Shields G. A., 1990, Annual Review of Astronomy and Astrophysics, 28, 525

Sillero E., Tissera P. B., Lambas D. G., Michel-Dansac L., 2017, Monthly Notices of the Royal Astronomical Society, 472, 4404

Simard L., et al., 2002, The Astrophysical Journal Supplement Series, 142, 1

Simard L., Mendel J. T., Patton D. R., Ellison S. L., McConnachie A. W., 2011, The Astrophysical Journal Supplement Series, 196, 11

Smee S. A., et al., 2013, The Astronomical Journal, 146, 32

Spindler A., et al., 2018, Monthly Notices of the Royal Astronomical Society, 476, 580

Spolaor M., Kobayashi C., Forbes D. A., Couch W. J., Hau G. K. T., 2010, Monthly Notices of the Royal Astronomical Society, 408, 272

Springel V., Hernquist L., 2005, The Astrophysical Journal, 622, L9

Strateva I., et al., 2001, The Astronomical Journal, 122, 1861

The Astropy Collaboration A., et al., 2013, Astronomy & Astrophysics, Volume 558, id.A33, 9 pp., 558

The Astropy Collaboration A., et al., 2018, The Astronomical Journal, Volume 156, Issue 3, article id. 123, 19 pp. (2018)., 156

Tim De Zeeuw P., et al., 2002, Monthly Notices of the Royal Astronomical Society, 329, 513

Tonnesen S., Cen R., 2012, Monthly Notices of the Royal Astronomical Society, 425, 2313

Toomre A., 1977, in Tinsley B. M., Larson R. B., Gehret D. C., eds, Evolution of Galaxies and Stellar Populations. p. 401, `http://articles.adsabs.harvard.edu/pdf/1977egsp.conf..401T`

Toomre A., Toomre J., 1972, The Astrophysical Journal, 178, 623

Torrey P., Cox T. J., Kewley L., Hernquist L., 2012, The Astrophysical Journal, 746, 108

Tremonti C. A., 2004, The Astrophysical Journal, 613, 898

Tremonti C. A., et al., 2004, The Astrophysical Journal, 613, 898

Utomo D., et al., 2017, The Astrophysical Journal, 849, 16

Veilleux S., Cecil G., Bland-Hawthorn J., 2005, Annual Review of Astronomy and Astrophysics, 43, 769

Violino G., Ellison S. L., Sargent M., Coppin K. E. K., Scudder J. M., Mendel T. J., Saintonge A., 2018, Monthly Notices of the Royal Astronomical Society, 476, 2591

Von Der Linden A., Best P. N., Kauffmann G., White S. D. M., 2007, Monthly Notices of the Royal Astronomical Society, 379, 867

Walterbos R. A. M., Greenawalt B., 1996, The Astrophysical Journal, 460, 696

White S. D. M., 1978, Monthly Notices of the Royal Astronomical Society, 184, 185

White S. D. M., 1979, Monthly Notices of the Royal Astronomical Society, 189, 831

White S. D., Rees M. J., 1978, Monthly Notices of the Royal Astronomical Society, 183, 341

Wild V., et al., 2014, Astronomy & Astrophysics, 567, A132

Wong K. C., et al., 2011, The Astrophysical Journal, 728, 119

Woods D. F., Geller M. J., 2007, The Astronomical Journal, 134, 527

Woods D. F., Geller M. J., Kurtz M. J., Westra E., Fabricant D. G., Dell'Antonio I., 2010, The Astronomical Journal, 139, 1857

Worthey G., 1994, The Astrophysical Journal Supplement Series, 95, 107

Wuyts S., et al., 2011, The Astrophysical Journal, 742, 96

Yang C., Gruendl R. A., Chu Y., Mac Low M., Fukui Y., 2007, The Astrophysical Journal, 671, 374

Yuan F.-T., Takeuchi T. T., Matsuoka Y., Buat V., Burgarella D., Iglesias-Páramo J., 2012, Astronomy & Astrophysics, 548, A117

Zaritsky D., Kennicutt R. C. J., Huchra J. P., 1994, The Astrophysical Journal, 420, 87

de Vaucouleurs G., 1948, Annales d'Astrophysique, 11, 247

van de Voort F., et al., 2018, Monthly Notices of the Royal Astronomical Society, 476, 122